UNIVERSITAT DE BARCELONA

Observational and theoretical perspective of massive star formation

José Ignacio Añez López

Tesi doctoral

Observational and theoretical perspective of massive star formation

José Ignacio Añez López

UNIVERSITAT DE
BARCELONA

Observational and theoretical perspective of massive star formation

Memòria presentada per optar al grau de doctor per la Universitat de Barcelona

Programa de doctorat en Física

Autor:
José Ignacio Añez López

Director/a:
Dr. Josep Miquel Girart Medina
i Dra. Gemma Busquet Rico
Tutor:
Dr. Alberto Manrique Oliva

Departament de Física Quàntica i Astrofísica
Facultat de Física

UNIVERSITAT DE BARCELONA

Gener 2021

«*¿Para qué llamar caminos a los surcos del azar?* »

Proverbios y cantares

Antonio Machado

Acknowledgments

Tras cinco años de trabajo he conocido a muchísimas personas increibles tanto a nivel profesional como personal así que agradecer a todas las que lo merecen es casi imposible pero trataré de hacerlo lo mejor posible. Quiero agradecer...

Als meus directors el Josep Miquel Girart i la Gemma Busquet per donar-me l'oportunitat de viure aquesta inoblidable experiència, per tota l'ajuda rebuda durant aquests anys i per mostrar-me el món de l'astronomia i la investigació. Al meu mentor el Chema Torrelles per tot el suport, ajuda i per ensenyar-me el costat més humà de la ciència. Al resto del grupo de radioastronomía de la Universitat de Barcelona, a Rosario López, Robert Estalella, Inma Sepúlveda, Carmen Juarez, Angels Riera (D.E.P.), gracias por escuchar y aguantar mis soporiferos ensayos and thanks also to Paolo Padoan, Zu-jia Lu and Veli-Matti Pelkonen for being there and dedicate your time to me.

A todos los compañeros del ICE y especialmente a Fina Ruiz, Guadalupe Masip, Angels Benet, Isabel Moltó, Josep Guerrero y Albert Bayona, os echaré de menos. También a todos los doctorandos, postdocs e investigadores del ICE, especialmente a Marina Lafarga, Anna Porredon, Fran Rivas, Juan Pedro López, Mariona Caixach, Jonathan Martín y todos los demás. La última etapa en la que nos hemos visto obligados a estar separados no emborrona los buenos ratos vividos. A Mayra Osorio, Guillem Anglada, Quique Macías, Ana Carla Díaz y a toda la gente del IAA por recibirme, enseñarme tanto y dejar que me asomara a la astronomía.

Thanks to Patrick Koch for hosting and teaching me so much in Taiwan and beyond, thanks also to Oscar Morata and to all people at the ASIAA, that summer in Taipei was unforgettable. Also thanks to Vivien Chen for kindly receiving me in Hsinchu. Thanks Lily, Elena and Cindy for show me your wonderful country and teach me a little bit of Chinese, Xièxiè. Thank you Qizhou Zhang, my experiences at the CfA were incredible and the learning immeasurable. To Fabio Santos, Giles Novak and Nicholas Chapmann, my time in the Northwester University was more than enriching. Muchas gracias a Manuel Fernández, tu visita al ICE fue un soplo de aire fresco, gracias por tu cercanía. Gracias también a Adriana Rodriguez por esas chelas tan necesarias.

Gracias Violeta y Jonathan por acogerme y a todos los habitantes del paraiso. A Isa y Jordi por tantas interesantísimas charlas y a toda la comunidad sureña. Gracias a todos por ser mi familia en Barcelona. Gracias también a Miriam, Lorena, Pilar, Angel, Edu, por estar siempre ahí. Gracias a la Jipi, a Mariluz y a Manolo por ser esa acción a distancia, siempre presente. Si estoy aquí en parte es gracias a vosotros.

Papá, Mamá, gracias por haberme apoyado a emprender el camino que me ha llevado hasta aquí y por confiar en mi incondicionalmente. Infinitas gracias hermanita, tu sabiduría me inspira. Gracias Juanki, Tita, a toda la familia y especialmente a la Yaya y al Tité, porque a veces la mejor lección es el ejemplo.

Por último, muchas gracias Nùria. Gracias por se mi punto de apoyo, por tu amor y paciencia.

Índice general

Índice de figuras

Índice de cuadros

Perspectiva observacional y teórica de la formación de estrellas masivas

Resumen

Las estrellas nacen, envejecen y mueren, pero debido a la escala temporal en la que esto sucede (de decenas a miles de millones de años) solo tenemos instantáneas del proceso evolutivo estelar. Gracias a los avances observacionales y a los modelos teóricos, tenemos una imagen bastante aproximada del proceso de formación de las estrellas como el Sol. Las estrellas se forman en nubes moleculares, las regiones más densas y frías del medio interestelar. Dichas nubes, lejos de ser uniformes, tienen una estructura compleja, destacandose estructuras filamentarias densas. Estos filamentos aparentemente se cruzan en regiones muy densas y relativamente compactas (∼0.1 pc) llamadas "hubs". Filamentos y hubs se pueden fragmentar en núcleos más densos cuyo colapso precede al nacimiento de las estrellas. En la formación de estrellas con masas similares a la del Sol la conservación del momento angular del material que cae hacia la proto-estrella provoca la formación del llamado disco de acrecimiento que transporta material desde la envoltura hacia la proto-estrella. Estos discos son las regiones de formación de planetas.

Las estrellas de alta masa, aquellas con masas por encima de 8 $M_{\odot}$ y luminosidades de más de 10^3 $L_{\odot}$, juegan un importante papel en el balance energético de las galaxias huésped. Sin embargo, el estudio de este tipo de estrellas supone un desafío debido a su rápida evolución, su gran distancia y que se encuentran atenuadas por el material circundante. Muchas teorías se han propuesto para explicar la formación de estrellas masivas pero la mayoría tienen en común que invocan al disco de acrecimiento para mediar en el trasporte de material desde la envoltura hasta la proto-estrella.

El campo magnético permea el material que forma las estrellas a todas las escalas, desde escalas galácticas, de nubes moleculares, escalas de núcleos proto-estelares hasta los disco sustentados rotacionalmente entorno a estrellas jóvenes. Sin embargo, aunque el campo magnético es clave en la formación de estrellas, su importancia en las primeras etapas de la formación de estrellas tanto de baja como de alta masa no está totalmente clara. Así por ejemplo, hay muchos indicios de que el campo magnético es esencial en la formación de filamentos. Además, se piensa que la fragmentación de las nubes moleculares también depende estrechamente del campo magnético. Los campos magnéticos también son importantes en el proceso de formación y evolución del disco de acreción. En el régimen milimétrico y submilimétrico, la principal manera de inferir el campo magnético es la observación de emisión polarizada proveniente de granos de polvo que han sido magnéticamente alineados.

En esta tesis, pretendemos contribuir a explicar el proceso de formación de estrellas masivas prestando especial atención al papel del campo magnético. Para ello, realizaremos un análisis multiescala con una doble aproximación, teórica y observacional. Por un lado investigaremos el proceso de acrecimiento a través de un disco de acrecimiento entorno a una estrella de alta masa. Nuestro objetivo es comprender si las estrellas masivas pueden formarse de manera similar a las de baja masa, es decir, acretando material de la envoltura hasta la proto-estrella a través de un disco de acrecimiento que evitaría el problema de la presión de radiación. Para ello, modelamos la imagen a 1.14 mm tomada con el "Atacama Large (Sub)Millimeter Array" (ALMA) con alta resolución angular hacia el disco de acrecimiento entorno a GGD 27–MM1. Con este objetivo, usaremos los modelos desarrollados por D'Alessio y col. (2006) y que se han aplicado con éxito a discos protoplanetarios alrededor de estrellas de baja masa. Por otro lado, estudiaremos el proceso de fragmentación en una nube oscura infrarroja (IRDC G14.225-0.506). Pretendemos entender el papel del campo magnético en dicho proceso de fragmentación. Para ello, estudiaremos observaciones de emisión polarizada tomadas con el "Caltech Submillimeter Observatory" (CSO) hacia

dos hubs físicamente idénticos pero que presentan distinto nivel de fragmentación.

El papel del campo magnético en el proceso de fragmentación: el caso de G14.225-0.506

En este primer trabajo, estudiamos la fragmentación de una nube oscura infrarroja que presenta una estructura filamentaria y dos hubs. Prestaremos especial atención al campo magnético presente en el entorno de los hubs y trataremos de relacionarlo con los distintos niveles de fragmentación que presentan estos hubs. Para poder llevar a cabo este estudio presentamos el resultado de las observaciones del CSO a 350 μm hacia ambos hubs, Norte y Sur, en la nube oscura infrarroja G14.225-0.506 (desde aquí G14.2). También mostramos el análisis de la polarización y gradiente de intensidad haciendo uso del método desarrollado por Koch, Tang y Ho (2012a) y Koch, Tang y Ho (2012b).

La nube oscura infrarroja G14.2 está situada a 1.98 kpc (Xu y col., 2011) y pertenece a una extensa (77×15 pc) y masiva ($> 10^5$ $M_\odot$) nube molecular localizada al Suroeste de la región HII Galactica M17 (Elmegreen y Lada, 1976). Observaciones de gas denso (Busquet y col., 2013; Chen y col., 2019b) revelan una red de filamentos compuestos por un sistema de dos hubs. Los hubs están asociados con una rica población de protoestrellas y objetos estelares jóvenes (Povich y Whitney, 2010; Povich y col., 2016). Dichos hubs muestran una mayor densidad, temperatura, mayor dispersión de velocidad respecto los filamentos, lo que sugiere que son regiones de actividad estelar.

En el hub del Norte encontramos un campo magnético con una distribución uniforme y con dirección Este-Oeste. Además, el ajuste Gaussiano de la distribución de ángulos de posición presenta el pico en 105±12°, prácticamente perpendicular a la dirección del filamento principal (100°). Sin embargo, en el hub del Sur el campo magnético muestra una distribución bimodal donde una componente tiene dirección Noreste-Suroeste y la otra Noroeste-Sureste.

En cuanto al gradiente de intensidad, en el hub del Norte, muestra un único mínimo local que coincide con el núcleo MM1a detectado previamente con el “Submillimeter Array"(SMA). Además, la orientación predominante del campo magnético (Este-Oeste), se desvía ligeramente al aproximarse al mencionado núcleo lo que sugiere una correlación entre campo magnético y material en colapso. En el hub del Sur, el gradiente de intensidad revela dos mínimos reflejando la distribución bimodal del campo magnético donde cada componente apunta a cada uno de los mínimos del gradiente de intensidad.

Unas de las principales herramientas utilizadas para el análisis ha sido el ángulo $|\delta|$, ángulo entre la orientación del campo magnético y la dirección del gradiente de intensidad, y Σ_B, bautizado como “la significación del campo magnético” y que evalúa la importancia del campo magnético en presencia del campo gravitatorio y frente a la presión hidrostática. El análisis de los mapas $|\delta|$ y Σ_B en el hub Norte indica que, en las inmediaciones del hub, la gravedad domina sobre el campo magnético. Esto se ve reflejado en el hecho de que el gradiente de intensidad es paralelo a las líneas del campo magnético, lo que sugiere que el campo magnético está siendo arrastrado por la acción de la gravedad o bien que el campo magnético está canalizando el material hacia la cresta central.

También hemos estimado la intensidad del campo magnético encontrando valores mayores en el hub del Norte que en el del Sur. Esto apoya la idea de que los diferentes niveles de fragmentación que presentan los hubs dependen de las diferencias en el campo magnético.

El modelado del disco de acrecimiento entorno a la protoestrella masiva GGD 27-MM1

En este segundo proyecto, descendemos hasta escalas de discos de acrecimiento para entender como las estrellas masivas se forman y evolucionan. En este trabajo hemos usado observaciones de ALMA a una longitud de onda de 1.14 mm con muy alta resolución angular ($\approx$ 40 mas[1]) que resuelven el disco entorno a la estrella masiva GGD 27–MM1. El disco se dispone perpendicularmente al espectacular jet[2] de 10 pc de longitud que emana de la fuente, conocido como HH 80–81. Motivados por el parecido de este sistema a los que encontramos en baja masa, hemos modelado la emisión del disco haciendo uso de los modelos desarrollados por D'Alessio y col. (2006) para estrellas de baja masa. El principal objetivo es investigar si las suposiciones que son válidas para discos entorno a estrellas de baja masa se podrían extrapolar al caso de estrellas masivas. Por ejemplo, los discos entorno a estrellas de baja masa son mucho menos masivos que la estrella central y esto los hace gravitacionalmente estables. En el caso de alta masa no está claro si los discos son estables (Maud y col., 2019) o inestables (Motogi y col., 2019; Zapata y col., 2019).

El disco se modeló usando los modelos de disco irradiado y acrecimiento α desarrollados por D'Alessio y col. (1998), D'Alessio y col. (1999), D'Alessio, Calvet y Hartmann (2001) y D'Alessio y col. (2006), que se han usado con éxito para modelar discos entorno a estrellas de masa baja e intermedia (e.j.; McClure y col., 2013; Osorio y col., 2014; Osorio y col., 2016; Macías y col., 2018). Las estructuras de temperatura y densidad se calculan de forma auto consistente una vez que se han fijado los parámetros estelares (radio R_*, masa M_* y temperatura T_*), el contenido de polvo (abundancias y distribución de tamaño de grano), viscosidad (α) y la tasa de acrecimiento. La opacidad del polvo se calcula teniendo en cuenta tanto la absorción como la auto-dispersión. La densidad superficial, como es común en los modelos de disco basados en acrecimiento α, se calcula como $\Sigma = \dot{M}_{\rm acc}\Omega/3\pi\alpha c_{\rm s}(T_{\rm c})^2$. El resto de parámetros que describen el modelo son el radio del disco ($R_{\rm disk}$) y la inclinación (i). El disco se considera estacionario, simétrico respecto al eje de giro y geométricamente delgado. La auto gravedad se considera despreciable comparada con la gravedad estelar y se asume rotación Kepleriana y equilibrio hidrostático en la dirección vertical. El modelo asume que el gas y el polvo están bien mezclados y termalizados por lo que se calcula una única temperatura como función de la posición.

Aunque no hay suficientes datos observacionales a distintas frecuencias con alta resolución angular para construir una distribución espectral de energía del disco, tenemos amplio conocimiento de la región que nos proporciona una serie de restricciones observacionales que nos sirven para acotar los rangos de exploración con el modelo. La morfología observada con las presentes observaciones es consistente con una inclinación de 49° y con un radio exterior de 240 ua. Inicialmente hemos usado la distancia de 1.7 kpc (Gómez y col., 2003), que indica una luminosidad bolométrica de $\sim 2.0\times10^4$ $L_\odot$. Sin embargo, más adelante adoptamos una distancia de 1.4 kpc que permite ajustar mucho mejor los datos al modelo. Esta distancia es compatible con el valor que hemos obtenido a partir del análisis de los datos de GAIA DR2 combinados con datos polarimétricos en el infrarojo cercano. La masa dinámica total del sistema estrella-disco, que se puede obtener a partir de las observaciones de líneas moleculares, está dentro del rango 21–31 $M_\odot$. La tasa de acrecimiento obtenida a partir de la tasa de pérdida de masa inferida para el jet (Carrasco-González y col., 2012) es de $\dot{M}_{\rm acc}$ $\sim 8\times10^{-5}$ $M_\odot$ yr^{-1}. Finalmente, un radio interior del disco mayor de 20 ua queda descartado ya que de lo contrario, con la actual resolución angular, se habría resuelto.

Considerando las restricciones observacionales hemos elaborado múltiples mallas de modelos variando los parámetros del disco y de la estrella. Posteriormente las mallas se refinaron hasta en-

[1] milisegundos de arco, del inglés milli-arc-sec

[2] Eyección de material a alta velocidad y muy colimado

contrar el mejor modelo. Como resultado hemos encontrado un disco muy masivo de unas $\sim 5 M_{\odot}$ que representa entorno a un 25 % de la masa estelar. Dicha masa es consistente con la masa dinámica calculada. El disco tiene un radio de ∼170 ua con una inclinación de 49º. Hemos comparado la estructura de temperatura y densidad obtenida con nuestro modelo con funciones potenciales y mostramos que el sistema GGD 27–MM1 es una plantilla potencial para futuros estudios similares en otras protoestrellas de alta masa. Concretamente, hemos encontrado un disco acampanado con una escala de altura máxima de ∼13 ua y un perfil de temperatura que va desde ∼150 K a las afueras del disco hasta ∼1400 K en el borde interior del disco. El análisis del parámetro de Toomre Q evaluado a la temperatura del plano medio del disco indica que el disco es estable hasta un radio $R_{\rm disk} \simeq 100$ ua. Este trabajo muestra que los modelos de D'Alessio se pueden usar como primera aproximación y además obtener varias predicciones observacionales para discos entorno a estrellas masivas.

Así mismo, reportamos la presencia de una fuente compacta no resuelta en el centro del disco de acrecimiento con un radio de 4 mas (∼5.6 ua) y una temperatura de brillo de $\sim 10^4$ K. Probablemente se trata de gas ionizado de origen incierto por ahora. Podría provenir de una incipiente y extremadamente compacta región HII o bien de la base del radiojet HH 80–81. Observaciones con mayor resolución angular ayudarían a determinar la naturaleza de esta fuente compacta.

Conclusiones Generales

Esta tesis pretende proporcionar una visión global del proceso de formación estelar en el régimen de alta masa. Desde el proceso de fragmentación hasta escalas de discos tomando como hilo conductor el campo magnético. La fragmentación de una nube se cree que es fuertemente dependiente del campo magnético de la nube y simulaciones MHD predicen bajo nivel de fragmentación en entornos altamente magnetizados. Nuestro resultado en G14.2 apoyan estas predicciones. Además, en un escenario donde el campo magnético es suficientemente intenso como para inhibir significativamente la fragmentación de un grumo masivo, la formación de núcleos masivos es plausible, lo que podría ser el preámbulo de una estrella masiva. Por otra parte, la presencia de un disco de acrecimiento es clave para que la estrella pueda crecer más allá de $\sim 10\ M_{\odot}$. El trabajo hecho durante esta tesis confirma este escenario y también muestra que el disco estudiado (GGD 27-MM1) tiene una estructura similar a la que se encuentra entorno a estrellas de baja masa, pero de mayor tamaño y masa. Sin embargo, este hecho está en aparente contradicción con lo que se espera encontrar en un entorno fuertemente magnetizado: el campo magnético inhibirá eficientemente o suprimirá la formación de un disco apoyado rotacionalmente mediante un catastrófico frenado magnético. Este hecho sugiere fuertemente que algún proceso difusivo del campo magnético debe tener lugar, probablemente en las primeras etapas, es decir, durante la formación de un núcleo masivo en el centro de un grumo.

Observational and theoretical perspective of massive star formation

Abstract

Stars are born, age and die, but due to the timescale in which this happens (from tens to billions of years) we only have snapshots of the stellar evolutionary process. Thanks to observational advances and theoretical models, we have a fairly approximate image of the formation process of stars like the Sun. Stars form in molecular clouds, the densest and coldest regions of the interstellar medium. These clouds, far from being uniform, have a complex structure. They have an intricate network of dense filamentary structures. These filaments apparently intersect in very dense and relatively compact regions (∼0.1 pc) called " hubs ". Filaments and hubs can fragment into denser cores whose collapse precedes the birth of stars. In the formation of Sun–like stars, the conservation of the angular momentum of the material falling towards the protostar causes the formation of the so-called accretion disk that transports material from the envelope to the protostar. These disks are the planet-forming regions.

High-mass stars, those with masses above 8 $M_{\odot}$ and luminosities greater than 10^3 $L_{\odot}$, play an important role in the energy balance of host galaxies. However, studying this type of stars is challenging due to their rapid evolution, their large distances and that they are attenuated by large amount of surrounding material. Many theories have been proposed to explain the formation of massive stars, but most have in common that they invoke the accretion disk to mediate the transport of material from the envelope to the protostar.

The magnetic field permeates the material that makes up stars at all scales, from galactic scales, to molecular clouds, to protostellar core scales to rotationally supported disks around young stars. However, although the magnetic field is key in star formation, its importance in the early stages of both low-mass and high-mass star formation is not entirely clear. For example, there are many indications that the magnetic field is essential in the formation of filaments. Furthermore, the fragmentation of molecular clouds is also thought to be highly dependent on the magnetic field. Magnetic fields are also important in the process of accretion disk formation and evolution. In the millimeter and submillimeter regime, the main way to infer the magnetic field is by observing polarized emission from dust grains that have been magnetically aligned.

In this thesis, we are aimed to better understand the massive star formation process paying special attention to the role of the magnetic field. To do this, we will carry out a multi-scale analysis with a double approach, theoretical and observational. Specifically on one hand, we will investigate the accretion process through an accretion disk around a high-mass star. Our goal is to understand whether massive stars can be formed in a similar way to low-mass stars, that is, accreting material from the envelope to the protostar through an accretion disk that would avoid the radiation pressure problem. To do this, we modeled the 1.14 mm image taken with the "Atacama Large (Sub) Millimeter Array" (ALMA) with high angular resolution towards the accretion disk around GGD 27–MM1. To this end, we will use the models developed by D'Alessio et al. (2006) and which have been successfully applied to protoplanetary disks around low-mass stars. On the other hand, we will study the fragmentation process in an infrared dark cloud (IRDC G14.225-0.506). We intend to understand the role of the magnetic field in this fragmentation process. To do this, we will study polarized emission observations taken with the "Caltech Submillimeter Observatory" (CSO) towards two physically identical hubs but with different levels of fragmentation.

The role of the magnetic field in the fragmentation process: the case of G14.225-0.506

In this first work, we study the fragmentation of an infrared dark cloud that has a filamentary structure and two hubs. We will pay special attention to the magnetic field present in the environment of the hubs and we will try to relate it to the different levels of fragmentation that these hubs present. In order to carry out this study, we present the result of the CSO observations at 350 μm towards both hubs, North and South, in the infrared dark cloud G14.225-0.506 (from here G14.2). We also show the analysis of polarization and intensity gradient making use of the method developed by Koch, Tang, and Ho (2012a) and Koch, Tang, and Ho (2012b).

The infrared dark cloud G14.2 is located at 1.98 kpc (Xu et al., 2011) and belongs to an extensive (77×15 pc) and massive ($> 10^5$ $M_\odot$) molecular cloud located southwest of the HII Galactic region M17 (Elmegreen and Lada, 1976). Dense gas observations (Busquet et al., 2013; Chen et al., 2019b) reveal a network of filaments composed of a system of two hubs. The hubs are associated with a rich population of protostars and young stellar objects (Povich and Whitney, 2010; Povich et al., 2016). These hubs show a higher density, temperature, and greater velocity dispersion than the surrounding filaments, which suggests that they are regions of stellar activity.

In the North hub we find a magnetic field with a uniform distribution along the east-west direction. Further, the Gaussian fit of the position angle distribution shows the peak at 105°± 12°, practically perpendicular to the direction of the main filament (100°). However, in the southern hub the magnetic field shows a bimodal distribution where one component has a Northeast-Southwest direction and the other Northwest-Southeast.

The intensity gradient in the North hub shows a single local minimum that coincides with the MM1a core previously detected with the Submillimeter Array (SMA). Furthermore, the predominant orientation of the magnetic field (East-West), deviates slightly when approaching the mentioned core. In the South hub, the intensity gradient reveals two minima reflecting the bimodal distribution of the magnetic field where each component points to each of the minima of the intensity gradient.

One of the main tools used for the analysis has been the angle $|\delta|$, angle between the orientation of the magnetic field and the direction of the intensity gradient, and Σ_B, known as "the magnetic field significance" and that assesses the importance of the magnetic field in the presence of the gravitational field and against hydrostatic pressure. Analysis of the maps $|\delta|$ and Σ_B in the North hub indicates that, in the vicinity of the hub, gravity dominates the magnetic field. This is reflected in the fact that the intensity gradient is parallel to the magnetic field lines, which suggests that the magnetic field is being pulled by the action of gravity or that the magnetic field is channeling the material towards the central ridge.

We have also estimated the intensity of the magnetic field finding higher values in the North hub than in the South hub. This supports the idea that the different levels of fragmentation exhibited by hubs depend on differences in magnetic field.

Modeling the accretion disk around the high-mass protostar GGD 27-MM1

In this second project, we descend to accretion disk scales to understand how massive stars form and evolve. In this work we have used ALMA observations at a wavelength of 1.14 mm with very high angular resolution (≈ 40 mas) that resolve the disk around the massive star GGD 27-MM1. The disk is arranged perpendicular to the spectacular 10 pc long jet emanating from the source, known as HH 80–81. Motivated by the similarity of this system to those found in low

mass, we have modeled the emission of the disk using the models developed by D'Alessio et al. (2006) for low mass stars. The main objective is to investigate whether the assumptions that are valid for disks around low-mass stars could be extrapolated to the case of massive stars. For example, disks around low-mass stars are much less massive than the central star and this makes them gravitationally stable. In the case of high-mass, it is not clear whether the disks are stable (Maud et al., 2019) or unstable (Motogi et al., 2019; Zapata et al., 2019).

The disk was modeled using the irradiated disk and accretion α models developed by D'Alessio et al. (1998), D'Alessio et al. (1999), D'Alessio, Calvet, and Hartmann (2001), and D'Alessio et al. (2006), which have been used successfully to model disks around stars low and intermediate mass (eg; McClure et al., 2013; Osorio et al., 2014; Osorio et al., 2016; Macías et al., 2018). The temperature and density structures are calculated in a self-consistent way once the stellar parameters (radius R_*, mass M_* and temperature T_*), the dust content (abundances and distribution of grain size), viscosity (α) and the accretion rate. The dust opacity is calculated taking into account both absorption and self-scattering. The surface density, as is common in accretion-based disk models α, is calculated as $\Sigma = \dot{M}_{\rm acc}\Omega$ / 3 $\pi\alpha c_{\rm s}$ $(T_{\rm c})^2$. The rest of the parameters that describe the model are the radius of the disk ($R_{\rm disk}$) and the inclination (i). The disk is considered steady, axisymmetric, and geometrically thin. Self-gravity is considered negligible compared to stellar gravity, and Keplerian rotation and hydrostatic equilibrium in the vertical direction are assumed. The model assumes that gas and dust are well mixed and thermally couple so a single temperature is calculated as a function of position.

Although there are not enough observational data at different frequencies with high angular resolution to construct a spectral energy distribution of the disk, we have extensive knowledge of the region that provides us with a series of observational constrains that help us to limit the exploration ranges with the model. The morphology observed with the present observations is consistent with an inclination of 49° and an outer radius of 240 au. Initially we used a distance of 1.7 kpc (Gómez et al., 2003), which yields an observed bolometric luminosity of $\sim 2.0 \times 10^4$ $L_\odot$. However, we later adopted a distance of 1.4 kpc that allows a much better fitting to the data. This distance is compatible with the value obtained with the Gaia DR2 data combined with near infrared polarimetric data. The total dynamic mass of the star–disk system, which is be obtained from observations of molecular lines, is in the 21–31 $M_\odot$ range. The mass accretion rate obtained from the inferred mass loss rate for the jet (Carrasco-González et al., 2012) is $\dot{M}_{\rm acc} \sim 8 \times 10^{-5}$ $M_\odot$ yr^{-1}. Finally, an inner radius of the disk greater than 20 au is ruled out since otherwise with the current angular resolution it would be resolved.

Considering the observational constraints we have elaborated multiple model grid varying the parameters of the disk and the star. Subsequently the grid have been refined to find the best model. As a result we have found a very massive disk of about ~ 5 $M_\odot$ which represents around 25 % of the stellar mass. This mass is consistent with the calculated dynamic mass. The disk has a radius of ∼170 au with a 49º of inclination. We have compared the temperature and density structure obtained with our model with potential functions and show that the GGD 27–MM1 system is a potential template for future similar studies in other high-mass protostars. Specifically, we have found a flared disk with a maximum scale height of ∼13 au and a temperature profile that goes from ∼150 K on the outside of the disk to ∼1400 K on the inner edge of the disk. Analysis of the Toomre parameter Q evaluated at the midplane temperature of the disk indicates that the disk is stable up to a radius $R_{\rm disk} \simeq 100$ au. This work shows that D'Alessio's models can be used as a first approximation and also obtain various observational predictions.

Likewise, we report the presence of a compact unresolved source in the center of the accretion disk with a radius of 4 mas (∼5.6 au) and a brightness temperature of $\sim 10^4$ K. It is probably ionized gas of uncertain origin. It could come from an incipient and extremely compact region HII

or from the base of the radio jet HH 80–81. Observations with higher angular resolution would help determine the nature of this compact source.

General Conclusions

This thesis aims to provide an overview of the star formation process in the high-mass regime. From the fragmentation process up to disk scales taking the magnetic field as the conductive thread. The fragmentation of a cloud is believed to be strongly dependent on the magnetic field of the cloud and MHD simulations predict low level of fragmentation in highly magnetized environments. Our result in G14.2 supports these predictions. Furthermore, in a scenario where the magnetic field is strong enough to significantly inhibit the fragmentation of a massive lump, the formation of massive core is plausible, which could be the preamble to a massive star. On the other hand, the presence of an accretion disk is key for the star to grow beyond $\sim$10 $M_{\odot}$. The work done during this thesis confirms this scenario and also shows that the disk studied (GGD 27-MM1) has a similar structure to that found around low-mass stars but of greater size and mass. However, this fact is in apparent contradiction to what is expected to be found in a strongly magnetized environment: the magnetic field will efficiently inhibit or suppress the formation of a rotationally supported disk through catastrophic magnetic braking. This fact strongly suggests that some diffusive process of the magnetic field must take place, probably in the early stages, that is, during the formation of a massive core in the center of a clump.

Chapter 1

Introduction

Stars are born, grow old and die but due to the long time scale of this process, from tens to thousand of millions of years, we only have snapshots of the process. Through detailed observations and theoretical works, models have been developed to explain the process of formation and evolution of stars, at least for stars with masses smaller than $\sim 8\ M_{\odot}$. However, the equivalent process to form stars above that limit (high-mass stars) is unclear. Nevertheless, these massive stars play a fundamental role, physically and chemically influencing the development of the galaxy that houses them throughout their life cycle. In addition, they are capable of triggering the formation of new generations of stars through their ejections and supernova events. The study of high-mass star formation is an extra challenge due to they are located at large distances (typically > 2 kpc) and they form in clusters deeply embedded within giant molecular clouds. In fact, the process by which a molecular cloud fragments giving rise to stellar cluster is an open question as well.

Nowadays, the development of new observatories, in particular radio interferometers like ALMA and VLA, is increasing the knowledge about the formation of high-mass stars, allowing us to discover equivalents characteristics to those of their low-mass siblings. These telescopes have made it possible to discover that the presence of circumstellar disk around low-mass stars is ubiquitous. In addition, the number of disks found around massive stars is growing in the last half decade, gaining strength the hypothesis that massive stars are also formed through an accretion disk.

During this dissertation I will discuss the process of high-mass star formation and compare it to the formation of low-mass stars. I will also discuss the fragmentation process of molecular clouds that leads to the formation of stellar clusters, with special attention to the role of the magnetic field.

1.1. Molecular clouds

It is well established that molecular clouds, which occupy a small fraction of the volume of the interstellar medium (ISM), are the principal sites of active star formation in our Galaxy. They are the coolest ($T_{\rm k} \sim 10 - 30$ K) and densest ($n(\rm H_2) \sim 10^3 - 10^5$ cm^{-3}) regions of the ISM and such environment allows the formation of molecules inside. In fact, molecular clouds are composed primarily of molecular hydrogen (H_2) with traces of other molecules (CO, NH_3, H_2O, etc...), but because molecular hydrogen lacks easily excitable transitions (i.e. rotational) under the prevailing conditions in molecular clouds, it is more convenient to use others molecules to trace the molecular clouds (see Fig. 1.1 as an example of different molecular cloud tracers). Among all the molecules detected in the ISM, approximately 200[1], the CO molecule, due to its abundance, its high dissociation energy (which makes it very resistant) and the characteristic temperature of its

[1] https://cdms.astro.uni-koeln.de/classic/molecules

rotational transitions (similar to the typical kinetic temperature of molecular clouds, T_k ~10 K), is the most important for the study of molecular clouds. The CO molecule has several isotope with observable transitions (^{13}CO, C^{18}O, C^{17}O) which are usually optically thin and thus they are very useful to obtain physical parameters in molecular clouds. For instance, the mass of a molecular cloud is usually inferred from the luminosity in the ^{12}CO or ^{13}CO J=1–0 transition.

Molecular clouds are not homogeneous volumes. In fact, recent observations demonstrate the prevalence of filamentary structures in molecular clouds (e. g., Molinari et al., 2010; André et al., 2014; Dhabal et al., 2018) and it is thought that they play an important role in the star formation process by favoring the fragmentation and the formation of dense cores. Filaments often intersect in high-density regions associated with star formation, known as hub–filament systems (e. g., Myers, 2009; Busquet et al., 2013). Nowadays, the mechanism and the ingredients that play a role in the fragmentation process are open questions. The main process is thought to be controlled by density and temperature, appealing to balance between thermal support and gravity for pure thermal Jeans fragmentation (e. g., Myhill and Kaula, 1992; Burkert, Bate, and Bodenheimer, 1997; Girichidis et al., 2011). Other ingredients have been called to be crucial in this process, such as turbulence (e. g.,entropy fluctuations, Keto, Field, and Blackman, 2020), mechanical feedback from protostellar objects through outflows and jets that can affect the earliest phases of the fragmentation process as well (e. g., Federrath et al., 2014; Cunningham et al., 2018), angular momentum (e. g., Chen et al., 2019a), and magnetic field (see Sec.1.3 for further details). If we consider only gravity and turbulence, excluding the rest of the ingredients, the collapsing clump should fragment into many cores, as many as the result of dividing the total mass by the Jeans mass (Dobbs, Bonnell, and Clark, 2005). However, fragmentation can be suppressed by the increase in temperature due to the gravitational energy radiated away from the densest portion of the clump that collapses first (Krumholz, 2006), or by magnetic support (Hennebelle et al., 2011).

In short, the fragmentation of molecular clouds is the starting point for the formation of stellar clusters and massive stars, and during this process gravity faces the rest of the ingredients (turbulence, stellar feedback and magnetic pressure) which are opposed to collapse. The observational and modeling study of the fragmentation process is therefore crucial for understanding how the star formation process originates, specially for high-mass stars.

1.2. (Low-mass) star formation process

Star formation, as we have previously established, takes place in molecular clouds, which are the coldest and densest places in the Galaxy. The process involves multiple scales, from the clouds themselves (typically spanning several pc), through the clumps (~0.3 - 3 pc) to the dense prestellar cores scale (~0.01 - 0.2 pc). Traditionally, the star formation process theory is divided into low- and high-mass stars. Usually, the criteria is the final star mass, being stars with masses smaller and larger than 8 $M_\odot$ considered as low-mass (and intermediate-mass) and high-mass stars, respectively. Protostars that will form low-mass stars have luminosities dominated by the accretion and can form from cores that have masses of order the thermal Jeans mass. However, protostars that will form stars above this value (massive stars) show luminosities that can be dominated by nuclear burning unless they present very high accretion rate, and if they form from molecular cores, those cores are significantly above the thermal Jeans mass (McKee and Ostriker, 2007).

Low-mass stars form from the collapse of dense gravitationally bound prestellar cores, when the gravitational pull generated by their own large reservoir of mass surpasses the gas thermal pressure. The collapse of such cores and the growth of the resulting protostars has been reviewed by several authors (Andre, Ward-Thompson, and Barsony, 2000; Larson, 2003; McKee and Ostriker, 2007), and here I will summarize the main stages (see Fig. 1.2 and 1.3). After the beginning of the

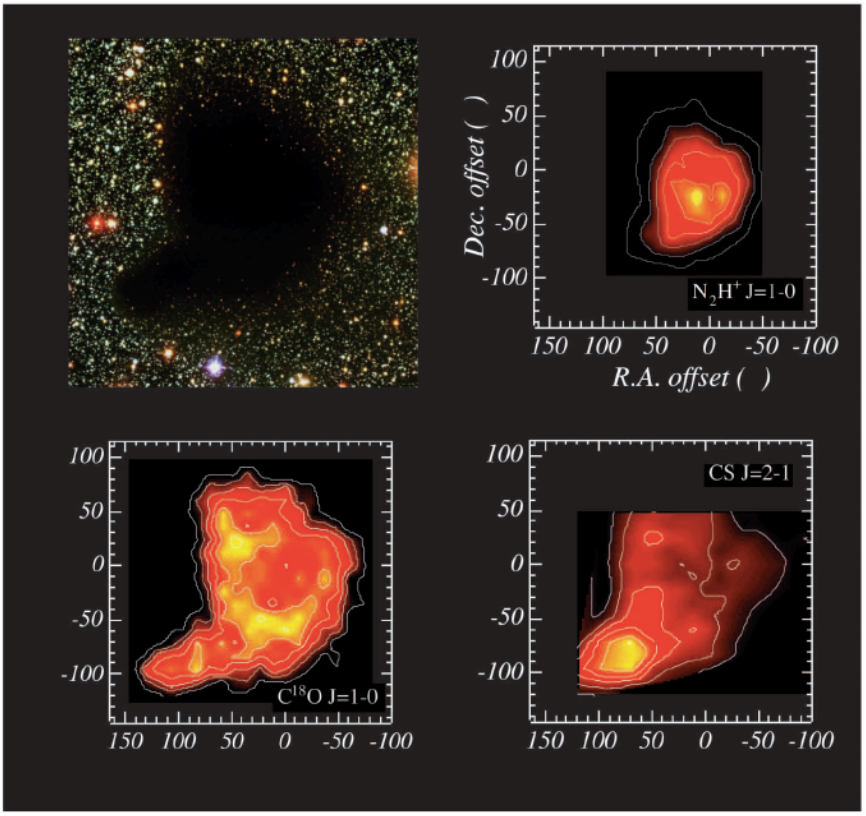

Figure 1.1: Barnard 68 molecular cloud observed at optical wavelength (upper left panel) and traced by different molecules (Lada et al., 2003).

collapse and the formation of a central protostar (Class 0), during the first $\sim 10^4$ years, the protostar is extremely faint in the optical and near-IR and have a large submillimeter luminosity (see Fig. 1.3 upper row). At this stage, protostars gain mass by accreting matter from the envelope through the accretion disk. Simultaneously to accretion, some of this matter is ejected by a jet, which is perpendicular to the disk, creating a molecular outflow and removing angular momentum (see Fig. 1.2 upper-right picture). Then, the protostar increases its temperature (Class I) becoming visible at infrared wavelengths (see Fig. 1.3 second row from up). At this stage, between $\sim 10^4 - 10^5$ years, the outflow has cleaned up part of the envelope matter and part of the radiation from the protostar can escape. During the Class II phase, the envelope is almost entirely dissipated, the optically thick disk is shown and the peak emission locates at near-infrared wavelengths (see Fig. 1.3 third row from up, and Fig. 1.2 bottom-left picture). Finally ($\sim 10^7$ years), the protostar enters the pre-main sequence (Class III) with the peak emission in the visible (see Fig. 1.3 bottom row), at which point the envelope is dissipated and a young star (or stars) and a protoplanetary disk remains (see Fig. 1.2 bottom-right picture).

The star formation process of low-mass stars has been studied in detail, as well as the formation and evolution of the circumstellar disks around them. Next, I will explain the main physical properties of circumstellar disks.

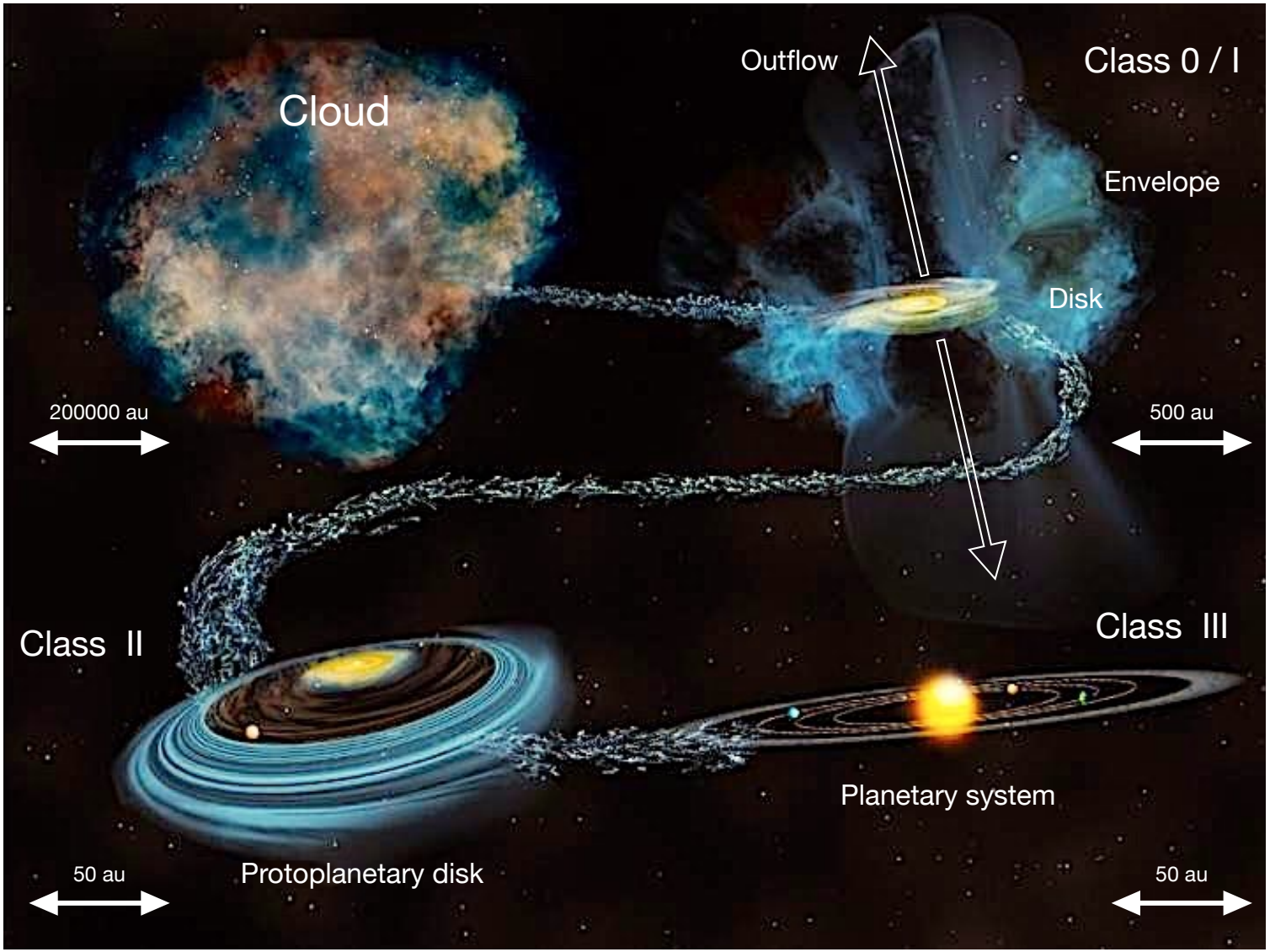

Figure 1.2: Illustration of the star-formation cycle. The dense molecular cloud (top-left) collapses to form a young protostar (Class 0/I) embedded in its envelope (top-right), which evolves to eventually become a star/protoplanetary disk system (bottom-left), which are the seed for planet formation (bottom-right). Image Credit: adapted from Bill Saxton (NSF/AUI/NRAO)).

1.2.1. Circumstellar disk

The vast difference in size between the rotating cloud cores and the final star ensures that most of the mass is accreted through a rotationally supported disk due to the angular momentum conservation. Accretion through an accretion disk is a key point for the development of the protostar itself and for the formation of a planetary system. Its function is to transport material from the envelope toward the protostar surface, and by means of this transport of material the gravitational potential energy is transformed into kinetic energy that powers collimated jets, which release angular momentum. As the star-disk system evolves, after the dissipation of the stellar envelope (~0.5 Myr; Williams and Cieza, 2011), the evolved accretion disk (a.k.a. protoplanetary disk), which now contains only a few percent of the stellar mass, keeps evolving mainly due to the accretion toward the central star, disk photoevaporation, and formation of larger bodies (planets or planetesimals) inside. Although, recently, there are clues that point to an early formation of large bodies in the discs (see below).

During the protostellar evolution, the emission from optical to millimeter wavelengths changes significantly (see Fig. 1.3). The dissipation of the envelope and the presence of the disk causes changes in the SED when its emission manages to escape through the attenuated envelope. In fact, during the Class II stage, there is an excess of far-IR and submillimiter emission respect to the stellar black body emission, which is associated with the emission from the disk.

From the observational point of view, high angular resolution observations at long wavelengths (from microns to millimeters) are necessary to resolve the star-disk system (solid angles of sub-arcsec), and in this way to capture thermal emission that occurs at typical temperatures of 100 K in the accretion disks. Radio interferometry meets the aforementioned requirements, in addition to filtering out the extended emission from the stellar envelope, which allows to image the disk. Indeed, great progress has been made during the past decade especially due to the development of the Atacama Large (Sub)Millimeter Array (ALMA), providing sub-arcsec angular resolution, high sensitivity, and high-image fidelity. This unprecedented characteristic has made it possible to discover, almost omnipresent, substructures in the circumstellar disks (rings, spiral arms, etc...) of which the most famous example is the HL Tau disk (see Fig. 1.4).

Observationally, we can resort to different tracers that show us multiple characteristics of the disks. Recently, Andrews (2020) presents a scheme of the disk structure in which different disk tracers are highlighted (see Fig. 1.5). On one hand, (sub)millimeter and centimeter emission traces the dust continuum emission which corresponds to the thermal emission of dust grains whose sizes range between micrometers and centimeters. These observations are sensitive to temperature and surface density in the optically thick and thin regime, respectively. On the other hand, scattered light caused by micrometric dust grains suspended in the atmosphere of the disk can be observed in the near infrared. In addition, spectral line emission at (sub)millimeter wavelength of molecular rotational transition is sensitive to the temperature and to density in the optically thin regime. Besides, such an observation allows inferring the velocity field of the molecular gas.

Next, I will describe the main physical properties of accretion disks and the most common way to obtain them.

- **Mass & density.** Protoplanetary disk, composed of gas and dust, are the birthplace of planets. Therefore, the knowledge of its available mass reservoir is key to understanding the evolution of the disks and the formation of planets in them. Besides, one would expect there to be consistency between the total mass of planetary systems and the total mass (gas + dust) observed in disks. However, many studies suggest that few disks have enough mass to produce planetary systems (e. g., Cieza et al., 2019; Williams et al., 2019; Andrews, 2020). A possible explanation is found in the uncertainties in disk mass estimation, such as the opacity

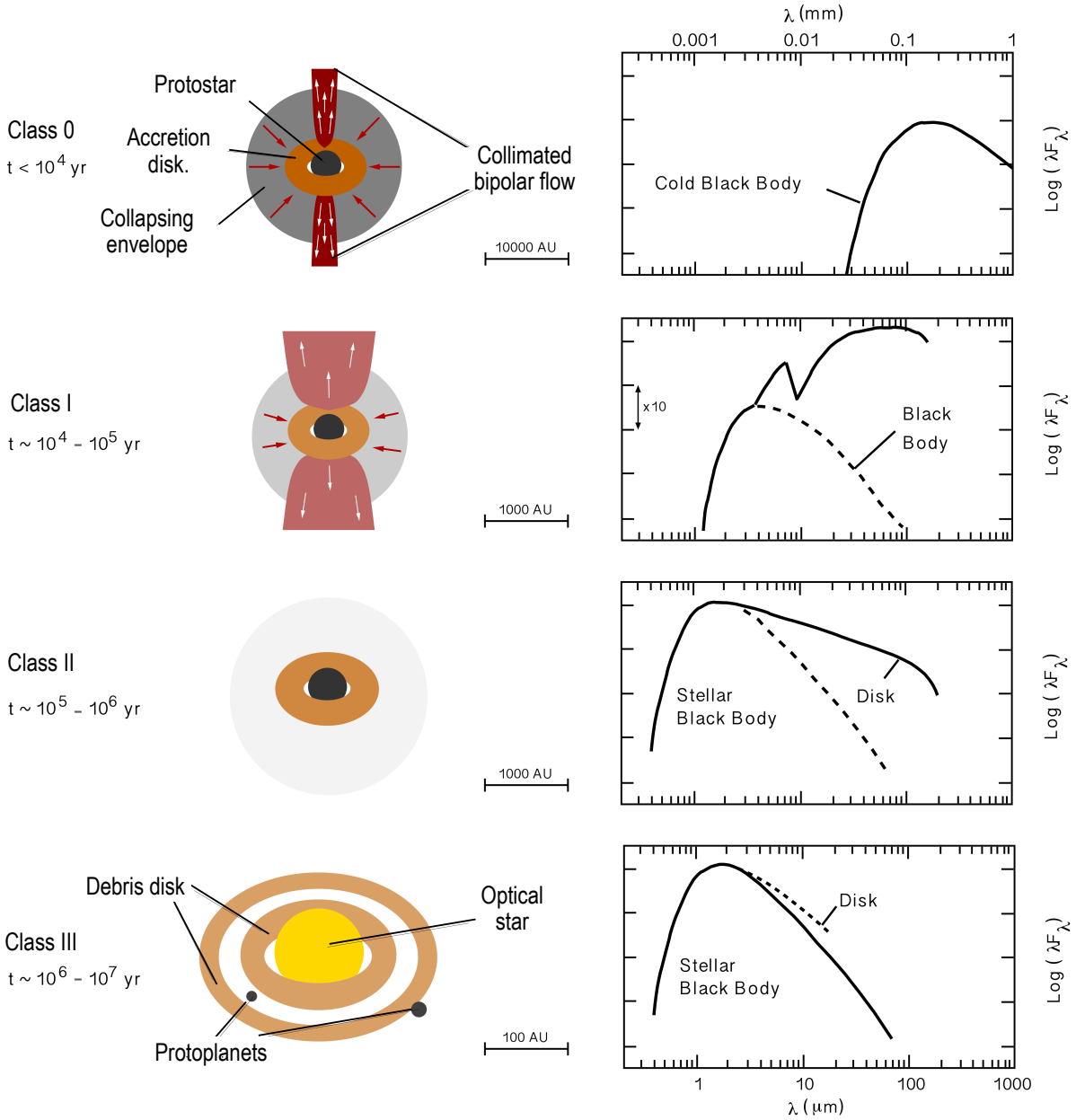

Figure 1.3: Illustration showing the protostellar evolution, from top to bottom Class 0, I, II and III, and its impact in the SED. Image Credit: Enrique Macias PhD thesis (2016)

estimation and scattering contribution for the mass of the particles or the CO fraction for the gas mass case (see below for further details). Nevertheless, another reason that is gaining strength lately is that the formation of planets takes place earlier than expected [2]. Annular structures, narrow emission rings or depleted gaps around pre-main sequence stars (Class II), interpreted as sign of planet formation, are ubiquitous (see e. g., Andrews et al., 2018; Huang et al., 2018). However, very recently Segura-Cox et al. (2020) noted that this type of structures (rings and gaps) are also observed in a very young Class I protostar (< 0.5 Myr), and in Alves et al. (2020), the authors reported features from a giant planet within a disk cavity around a Class I/II YSO, concluding that the formation of the star, disk and the planet is possibly happening simultaneously. In conclusion, the apparent mass deficit usually measured in disks could be due to we would be observing the excess material after planets (or planetesimals) formation.

The optimal dust mass diagnosis is the luminosity of the millimeter continuum emission which, in the optically thin regime, is proportional to the opacity absorption (κ_ν) and surface density (Σ):

$$I_\nu \propto \kappa_\nu B_\nu(T)\Sigma_\nu, \tag{1.1}$$

where $B_\nu(T)$ is the Planck function at temperature T. Therefore, uncertainties are introduced due to the estimation of opacity absorption, which is based on assumption about properties of particle. In addition, the assumption of optically thin emission could not to be accurate in some cases. If the contribution of scattering is ignored, optical depth could be underestimated (Zhu et al., 2019). Regarding the gas mass, the more common tracer in disks is the CO molecule or some optically thin isotopologues (^{13}CO, C^{18}O). In this case, the main source of uncertainty comes from the fraction H_2/CO (X_{CO}) considered. In general, these observational methods seem to lead to an underestimation of the mass of the disk (gas+dust), so we could consider these measurements as lower limits. Interferometric observations at (sub)millimeter wavelengths show typical masses in range 10^{-3} - 10^{-1} $M_\odot$ (e. g., Williams and Cieza, 2011; Andrews et al., 2018).

Density estimates are affected by the same ambiguities experienced by masses: the estimation of opacity absorption in the case of the dust density and X_{CO} for the gas, together with the underestimation of the optical depth. For large samples, different values have been found for dust density through different modeling techniques: $\Sigma_{\rm dust} \propto r^{-0.9}$ (Andrews et al., 2009; Andrews et al., 2010); $\Sigma_{\rm dust} \propto r^{(-0.8,0.8)}$ (Isella, Carpenter, and Sargent, 2009; Tazzari et al., 2017). Regarding the gas density, CO is the most widely used gas tracer for protoplanetary disk, and its optically thin isotopologue ^{13}CO and C^{18}O. One possibility is to compare spatially resolved emission with thermo-chemical models (e. g., Zhang et al., 2019).

- **Radius.** Disk size is strongly dependent of the tracer and of the definition of radius. It is usual to define the radius to include 90% (or another percentage) of the luminosity of the chosen tracer. It is also common to estimate the radius using radial profile models and/or Gaussian fit where the radius will be defined by the half width at half maximum (e. g., Busquet et al., 2019). Interferometric observations at (sub)millimeter wavelengths show typical disk radii between 10-200 au (Andrews et al., 2010; Andrews et al., 2018; Segura-Cox et al.,

[2] About half a decade ago, ALMA opened the door to high-angular resolution observations that are changing the paradigm of accretion disks. Images like HL Tau disk show us signs of planetary formation in a star in transition between Class-I and Class-II. Until then, the formation of planets were thought to occur during the latest stages of protostellar evolution, i. e., during the Class II phase

2016; Maury et al., 2019; Tobin et al., 2020). However, disk size based on scattered light images is larger (Garufi et al., 2018), while CO line emission traces disks with radii between ~100-500 au (e. g., Ansdell et al., 2018).

- **Temperature.** The main heating source of an accretion disk is the irradiation from the central star, which falls on the dust in the disk atmosphere and which in turn re-emits towards the disk midplane (D'Alessio et al., 1998). The efficiency of this mechanism depends on the central star spectrum, the vertical distribution of the material and its microphysical properties (D'Alessio et al., 1999; D'Alessio et al., 2006; Dullemond, Dominik, and Natta, 2001; Dullemond, van Zadelhoff, and Natta, 2002). Other important heating sources are: viscous dissipation (D'Alessio et al., 1998), irradiation from the envelope (D'Alessio, Calvet, and Hartmann, 1997), spiral shocks (Rafikov, 2016) and radioactivity (Cleeves et al., 2013).

  A fairly popular method to obtain the temperature profile is through the infrared SED modeling, although the main drawback of such modeling is the degeneracy of the models. On the other hand, the disk surface temperature can be probed with optically thick molecular lines. For instance, we can relate the J =2–1 CO line brightness temperature with gas temperature if we assume local thermodynamic equilibrium (Weaver, Isella, and Boehler, 2018). Furthermore, some authors propose a method to directly measure the temperature in the midplane of the disk from an optically thick molecular line, attending to the spatial morphology of the line. By recognizing certain patterns in such spatial distribution, it is possible to infer the midplane temperature (e. g., Rosenfeld et al., 2013; Dullemond et al., 2020).

  The estimation of the temperature profile in the disk is also very important to determine the radial position of the so-called snow-line, i.e., the radius from which the conditions of temperature and pressure allow the existence of volatile compounds such a water (H_2O), carbon dioxide (CO_2) and ammonia (NH_3) to condense in a solid state. It is though that processes that occur around the snow line facilitate the formation of planetesimals. For example, beyond the snow-line there are more icy pebbles available to form planets (e.g.; Drążkowska and Alibert, 2017).

- **Formation.** The disk forms after the initial collapse of the molecular core as a natural consequence of the angular momentum conservation (Terebey, Shu, and Cassen, 1984). The formation proves to be fast in purely hydrodynamic models, even large (> 100 au) and gravitationally unstable structures appear (Yorke and Bodenheimer, 1999). If the effects of the magnetic field are considered, using magnetohydrodynamic (MHD) models, what is known as the magnetic braking catastrophe occurs (Galli et al., 2006). The solution seems to be found when considering dissipative effects in non-ideal magnetohydrodynamic models (see Section 1.3 for more details). However the exact recipe that reproduces early disk formation during the accretion phase is still under debate.

  Observationally, restricting the ingredients involved in disk formation requires observations of the earliest stages of the disk. However, during the so-called Class 0 phase the disk is deeply embedded in the protostellar envelope. Therefore, it was not until the arrival of new generations of interferometers that we were able to explore the interior of these envelopes. Recently, statistical studies of very young protostars based on surveys have been carried out (Segura-Cox et al., 2018; Sheehan et al., 2020; Tobin et al., 2020). For example, in Maury et al. (2019) they conclude that it is more common to find disks smaller than those predicted by purely hydrodynamic models and favor magnetized models.

- **Dynamics.** The dominant factor in the kinematic structure of a disk is orbital motion with expected contribution from magnetic fields, viscous transport, pressure support, self-gravity

and winds. Interferometric molecular line emission observations of low-mass YSOs show that the velocity field is consistent with Keplerian rotation (Simon, Dutrey, and Guilloteau, 2000; Simon et al., 2017).

In conclusion, the knowledge of the main physical processes that govern disk evolution is crucial to understand the planet formation. Among the main physical phenomena stand out viscous accretion, dust settling and coagulation, dynamical interactions with (sub)stellar companions and forming planets, and photoevaporation by UV and X-ray radiation (see Williams and Cieza, 2011).

1.2.2. Disk model

In addition to the observational studies of disks, theoretical and modeling studies have proven to be a very important tool to unravel the physical processes that take place during their formation and development.

It is well established that the absorbing surfaces of circumstellar disk are curved upward away from the disk mid-plane (flared disk; Kenyon and Hartmann, 1987), therefore the irradiation of the disk by the central star tends to dominate the heating of the disk for large radii (Calvet et al., 1991; Calvet et al., 1992). Due to the cross-dependence between degree of flaring and temperature structure, a self-consistent density and temperature structure must be calculated iteratively (Kenyon and Hartmann, 1987; D'Alessio et al., 1998; D'Alessio et al., 1999; D'Alessio, Calvet, and Hartmann, 2001; D'Alessio et al., 2006).

In this thesis (Chapter 3), we use the D'Alessio irradiated accretion disk model (D'Alessio et al., 1998; D'Alessio et al., 1999; D'Alessio, Calvet, and Hartmann, 2001; D'Alessio et al., 2006), which has been successfully used in the past to fit SEDs and (sub)millimeter images of protoplanetary disks (e. g., Calvet et al., 2005; Hughes et al., 2009; Espaillat et al., 2011; McClure et al., 2016; Rubinstein et al., 2018). This model assumes that the disk is in steady state and geometrically thin; that is, radial energy transport is neglected and the vertical and radial structures are treated as decoupled problems. Disk is in vertical hydrostatic equilibrium. Since there can be turbulent and convective motions in the vertical direction, the assumption of hydrostatic equilibrium refers to the mean bulk motion of the gas and dust in the disk. The mass accretion rate, $\dot{M}$, is uniform both azimuth and radially and constant in time, and turbulent viscosity is described by the *alpha* viscosity prescription, $\nu_t = \alpha C_s H$, where α is assumed to be constant through the disk with the only constraint that $\alpha \leq 1$ (D'Alessio et al., 1998). A more detailed explanation of the model is provided in Chapter 3.

1.2.3. (High-mass) star formation process

We call massive stars those that exceed 8 $M_\odot$, have luminosities larger than 10^3 $L_\odot$ and spectral type O or early B-type. Furthermore, it is known that during their lifetime high-mass stars play an important role in the energy budget of their host galaxy due to their strong radiation, winds and supernova events. However, from an observational point of view, the study of high-mass star formation is challenging because of their fast evolution ($\sim 10^5$ yr) to the main sequence, their large distances and high obscuration. Furthermore, massive stars form in clusters, which makes their identification a non-trivial task. Thus, investigating high-mass star and cluster formation requires high angular resolution imaging at far-IR to (sub)millimeter and centimeter wavelengths.

Theoretically, for this sort of protostars the free-fall timescale is larger than the Kelvin-Helmholtz timescale. Therefore, high-mass protostars reach the Zero Age Main Sequence (ZAMS) while still accreting, raising the radiation pressure problem. It is thought that the strong radiation pressure could halt the infalling material under some conditions such accretion rates lower than

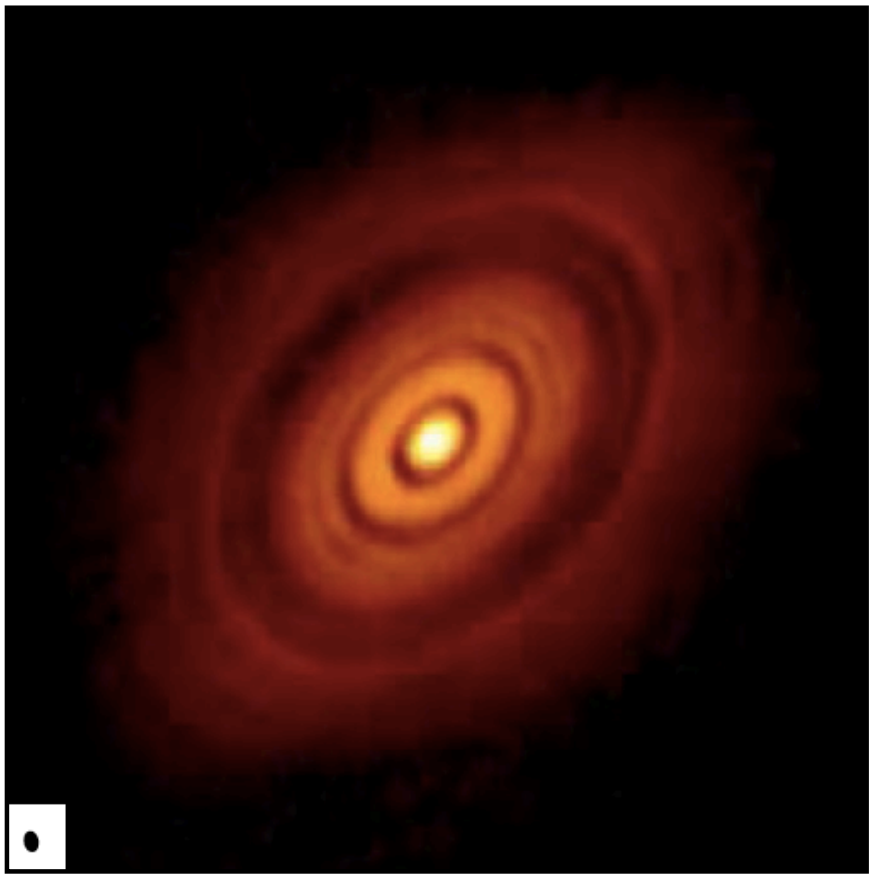

Figure 1.4: 1.3 mm ALMA continuum image of HL Tau. The synthesized beam is shown in the lower left of the panel (35.1 x 21.8 milliarcsecond). (ALMA Partnership et al., 2015)

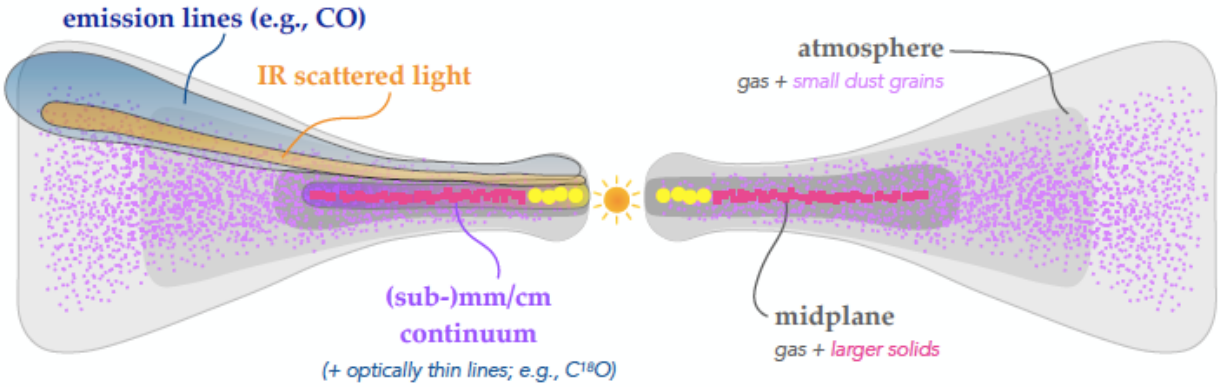

Figure 1.5: Scheme which describe the accretion disk tracers according the origin of the emission: molecular line, infrared scattered light and (sub)millimeter and centimeter continuum emission. Credit: (Andrews, 2020)

$\sim 10^{-3}$ $M_\odot$ yr^{-1} (Wolfire and Cassinelli, 1987). Besides, the radiation field of a massive protostar heats and eventually could ionizes the gas of its surrounding envelope creating a HII region (Spitzer, 1978). Some authors have proposed that the formation of a high-mass star through an accretion disk could mitigate the effects of radiation (see below).

Different theories have been proposed to explain the formation of massive stars. Among those that are under active debate we can highlight three: core accretion, protostar collision and competitive accretion. The *core accretion* is an extension of the low-mass star formation theory. Cores of dense gas form from clump fragmentation undergo gravitational collapse to form a single star or a multiple system (McKee and Tan, 2002; Hosokawa and Omukai, 2009). *Protostar collision* and coalescence in very dense stellar systems refers when the most massive stars are formed through a combination of gas accretion and stellar mergers (Bonnell and Bate, 2002). In *competitive accretion*, a massive protostar accretes material from the clump without it having formed a core. In this scenario, the massive star is formed together with a cluster of low-mass protostars (Bonnell and Smith, 2011; Murray and Chang, 2012; Hartmann, Ballesteros-Paredes, and Heitsch, 2012). Both sorts of theories, core accretion and competitive accretion, have in common that they both predict the formation of an accretion disk that channels the material towards the star in formation but the controversy remains about the existence of high-mass analogs of low-mass prestellar cores known as massive starless clumps, high-mass prestellar core or massive cold molecular cores. An alternative evolutionary scenario is proposed by Vázquez-Semadeni et al. (2009) and Vázquez-Semadeni, González-Samaniego, and Colín (2017): global hierarchical collapse theory suggests that high-mass protostars form within a low-mass prestellar core which grows from low- to high-mass and whose global collapse drives inflowing gas streams toward the protostar. Thus, in this scenario the high-mass stars precursors could be low-mass cores within massive infalling clumps, which is consistent with formation of massive cloud and massive clusters. Nevertheless, the key ingredient that could allow the accretion to continue once the central protostar has ignited is the accretion disk. Models including feedback due to radiation forces, photoionization, feedback from protostellar outflows and the ram pressure from large-scale gravitational infall show that as long as accretion flows through a disk it does not seem to be any barrier to forming massive stars (Tan et al., 2014; Kuiper and Hosokawa, 2018).

During the last decade, roughly flattened structures observed around massive stars have been proposed as potential accretion disks (e. g., Beltrán et al., 2011; Beltrán et al., 2014; Sánchez-Monge et al., 2014; Johnston et al., 2015; Sanna et al., 2019; Zapata et al., 2019). These large structures ($\geq$1000 au), that extend beyond the centrifugal barrier, with masses exceeding the central protostar mass, are more likely to correspond to rotating envelopes (so-called 'toroids') rather than true accretion disks. Due to the demanding needs of angular resolution and sensitivity, there are very few candidates for true rotationally supported accretion disks around massive stars with characteristics equivalent to those seen in low-mass stars. The best examples in literature are: Cepheus A HW2 (Patel et al., 2005); GGD27-MM1 (Girart et al., 2018); G11.92-0.61 (Ilee et al., 2018), and more recently Monoceros R2-IRS2 (Jiménez-Serra et al., 2020)

1.3. The magnetic field

Magnetic fields permeate star-forming material on every spatial scale, from the scales of entire galaxies (e. g., Lopez-Rodriguez et al., 2020), to the ~100 pc scale of molecular clouds (e. g., Planck Collaboration et al., 2015; Fissel et al., 2016; Santos et al., 2016), to the ~0.1 pc scale of protostellar cores (e. g., Girart, Rao, and Marrone, 2006; Girart et al., 2009; Ward-Thompson et al., 2018; Galametz et al., 2018), and all the way down to innermost regions of protostellar envelopes (~100 au scales) where planets form within rotationally supported disks around young stars. In

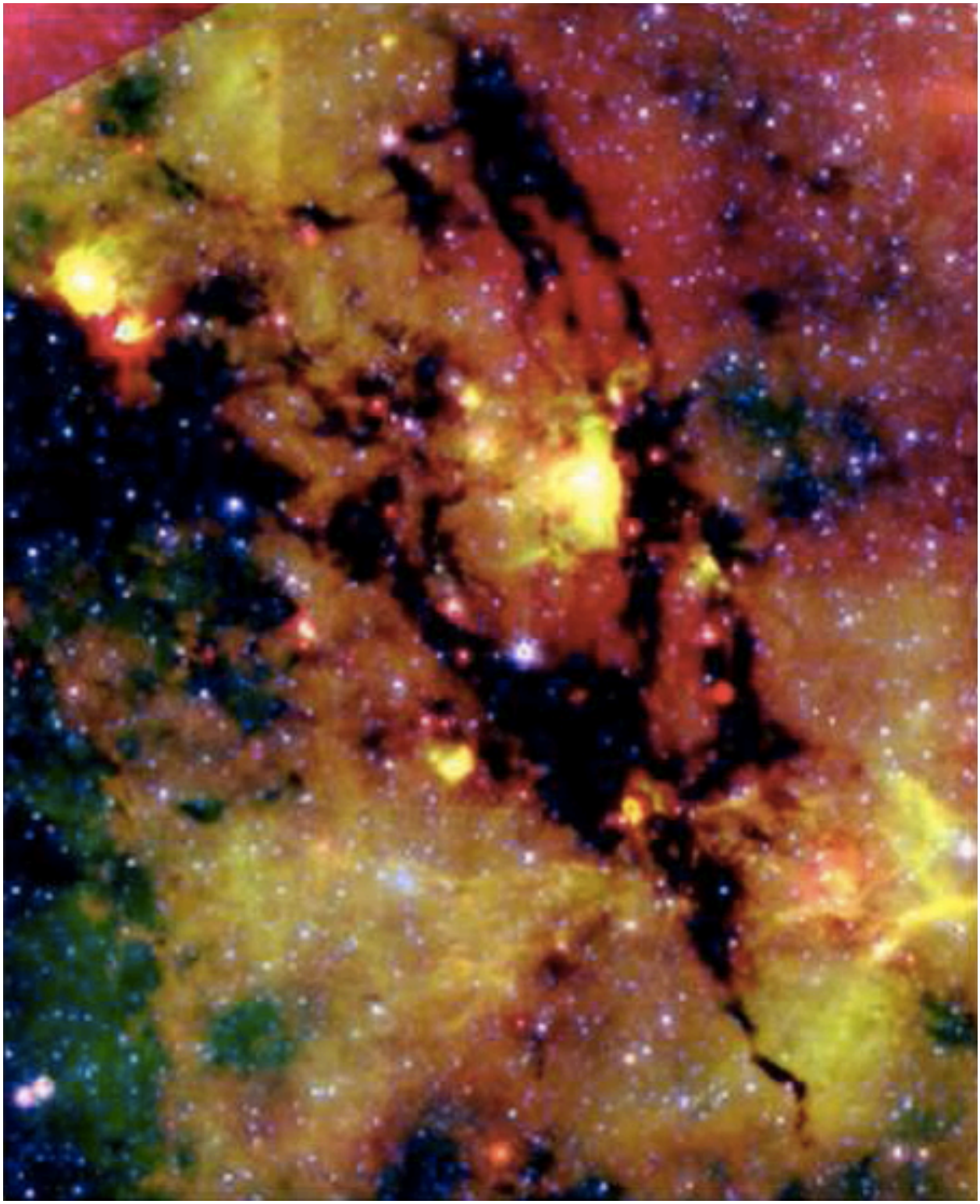

Figure 1.6: Archival Spitzer 4.5/8.0/24 μm(blue/green/red) three-color composite image of the IRDC G14.225-0.506 (Busquet et al., 2013).

the (sub)millimeter regime, these magnetic fields are mainly inferred by observing polarization from magnetically aligned dust grains (see Section 1.3.2 for further details). Various theories have been explored to explain the alignment of dust grains with the magnetic field; the most common of these is the theory that grains can be aligned by torques conveyed by the local radiation field, the so-called "Radiative Alignment Torque" (RAT) theory (e. g., Dolginov and Mitrofanov 1976; Hoang and Lazarian 2016, see also Andersson, Lazarian, and Vaillancourt 2015 for a review of grain-alignment mechanisms).

There are many signs that the magnetic field is essential in the formation of filaments (Zhang et al., 2014; Pillai et al., 2015; Li et al., 2015; Van Loo, Keto, and Zhang, 2014; Planck Collaboration et al., 2015). Observationally, Tang et al. (2019) studied the magnetic field in filamentary infrared dark clouds (IRDC) and found local correlation in alignment between magnetic field and local velocity gradient. Moreover, the fragmentation of a cloud is though to strongly depends on the cloud magnetic field strength as well. MHD simulations show that in an scenario where magnetic field support dominates the dynamical evolution, low fragmentation level is presented (Hennebelle et al., 2011; Commerçon, Hennebelle, and Henning, 2011; Myers et al., 2013). However, in Palau et al. (2020) authors studied observational correlation between magnetic field properties and fragmentation level and they did not find apparent relation between magnetic field strength and fragmentation level. Thus, the role of the magnetic field in the fragmentation process is still a matter of debate and I will deal with it in Chapter 2 of this thesis.

Low-mass stars are known to form via the gravitational collapse of slowing rotating, magnetized dense molecular cores. Because the magnetic field is "frozen" into the charge carriers, magnetic flux must be dissipated in order to explain the magnetic fluxes observed in newly formed stars. Typically, a key parameter to measure the relative importance of the magnetic field versus the potential gravitational collapse is the mas-to-flux ratio, defined as the amount of mass within a magnetic flux tube. Mouschovias and Spitzer (1976) proposed a critical value below which magnetic force would prevent a cloud from gravitational collapse. Usually, the mass-to-flux ratio is given in terms of this critical value $\lambda = (M/\Phi)/(M/\Phi)_{crit}$ (Crutcher et al., 2004). Thus, $\lambda < 1$ indicates a cloud magnetically subcritical, so the magnetic field provides support to avoid global collapse. On the opposite, $\lambda > 1$ represents a cloud in magnetically supercritical state and starts to collapse. The ISM is strongly magnetized ($\lambda \sim 1$), whereas stars are weakly magnetized. How the mass-to-flux ratio increases so dramatically during star formation is one of the classic problems of star formation (Mestel and Spitzer, 1956). This so-called "magnetic flux problem" in star formation is that stars have very large values for the mass-to-flux ratio ($\sim 10^4 - 10^5$, in magnetic stars; $\sim 10^8$, in the Sun; Nakano (1983)). Besides, in order for the stellar embryo to accrete enough mass to grow into a star, some dissipation of the initial angular momentum must occur: this is the so-called "angular momentum problem". This is because as a cloud contracts its angular velocity should increase quadratically as its radius decreases ($\Omega \propto R^{-2}$) if angular momentum were conserved. Nevertheless, in a magnetized cloud rotation twist the 'frozen' magnetic field lines and transports angular momentum, as torsional Alfvén waves propagates, away from a cloud and thereby keeping the, otherwise potentially fierce, centrifugal forces small (Mouschovias, 1987; Mouschovias, 1991). This mechanism is known as magnetic braking. It is clear that the diffusion of magnetic flux and angular momentum must occur to explain the observed properties of protostellar environments, but how and when these processes occur is still not well understood. What is clear, however, is that studies of the interstellar magnetic field are critical if we want to answer these fundamental questions about star formation.

Regarding the protostellar disk formation, ideal MHD simulations have shown that a realistic magnetic field of moderate strength suppress, through catastrophic magnetic braking, the formation of a rotationally supported disk during the protostellar accretion phase of low-mass star formation

(e. g., Li, Krasnopolsky, and Shang, 2011). This result is in contradiction with the observed properties of disks around protostars (e. g., Maury et al., 2019). This is another evidence that some magnetic flux must be dissipated during the formation of a protostar. However, there is still a vivid debate on how this is produced. Several non-ideal MHD mechanisms have been proposed to allow the magnetic flux diffusion: Ohmic dissipation, ambipolar diffusion (e. g.,, Dapp, Basu, and Kunz, 2012), Hall effect, turbulent reconnection (Lazarian, Vishniac, and Kowal, 2009). Other works suggest that a misaligned field with the rotation axis may help the formation of disk in a weakly magnetized cloud (Krumholz, Crutcher, and Hull, 2013). If we suppose a population formed by ions, electrons and neutral particles then, in the ambipolar diffusion density regime both ions and electrons are well tied to the magnetic field. On the other hand, in the Hall density regime, electrons remain linked to the magnetic field while ions are not. Finally, in the Ohmic dissipation regime, at the highest densities, both electrons and ions are released from magnetic field by collisions, which dissipates magnetic energy. Ambipolar diffusion in the context of disk formation allow the magnetic field lines that are tied to the ions to drift relative to the bulk neutral material (Li et al., 2014) and Hall effect can increase the angular momentum of a collapsing, magnetized flow through the so-called "Hall spin-up" (Wardle and Ng, 1999).

Once the disk is formed, magnetic fields are still expected to modify the gas dynamics, shape and evolution of the disk, which may have consequences on planet formation. Models have shown that including a poloidal magnetic field in an irradiated accretion disk influences emission, being weaker magnetized disk more emissive, and optical depth being larger for disks with higher magnetized (Tapia and Lizano, 2017). Besides, the origin of the omnipresent jets in YSO's, that remove angular momentum from the disk-star system allowing its formation, is linked to the magnetic field through magneto-rotational phenomena: magnetic fields attached to the accretion disk will carry gas that will be thrown out (see Li et al., 2014, for a recent review).

The main observational way to study the magnetic field is by detecting the polarized radiation of the regions observed. In the following subsection, I first explain the nature of the polarized light and different sources of polarization that we can observe in star-forming regions. Then I explain how we can derive the magnetic field strength and how to quantitatively derive the importance of the magnetic field with respect to gravity.

1.3.1. The nature of polarized light

Polarized light from astronomical sources was observed for the first time in the middle of the last century (Hall, 1949). Since then, the importance of polarimetric observations has increased and today they are one of the best tools for mapping the magnetic field (see Sec. 1.3.2).

We can consider polarized light in terms of the electric field component of the wave (Eq. 1.2).

$$\begin{cases} \vec{E_x}(t) & = E_{ox}(t)\cos[(\vec{kz}-\vec{\omega t})-\epsilon_x(t)]\vec{i} \\ \vec{E_y}(t) & = E_{oy}(t)\cos[(\vec{kz}-\vec{\omega t})-\epsilon_y(t)]\vec{j}. \end{cases} \tag{1.2}$$

The most general representation is that of elliptical light. The end point of the vector $\vec{E}$ is envisioned continuously sweeping along the path of an ellipse having a particular shape (the circle and line being special cases).

$$\left(\frac{E_y}{E_{oy}}\right)^2+\left(\frac{E_x}{E_{ox}}\right)^2-2\left(\frac{E_x}{E_{ox}}\right)\left(\frac{E_y}{E_{oy}}\right)\cos\epsilon=\sin^2\epsilon. \tag{1.3}$$

Equation 1.3 is the equation of an ellipse making an angle α with the (E_y, E_x)-coordinate system (see Fig. 1.7) where:

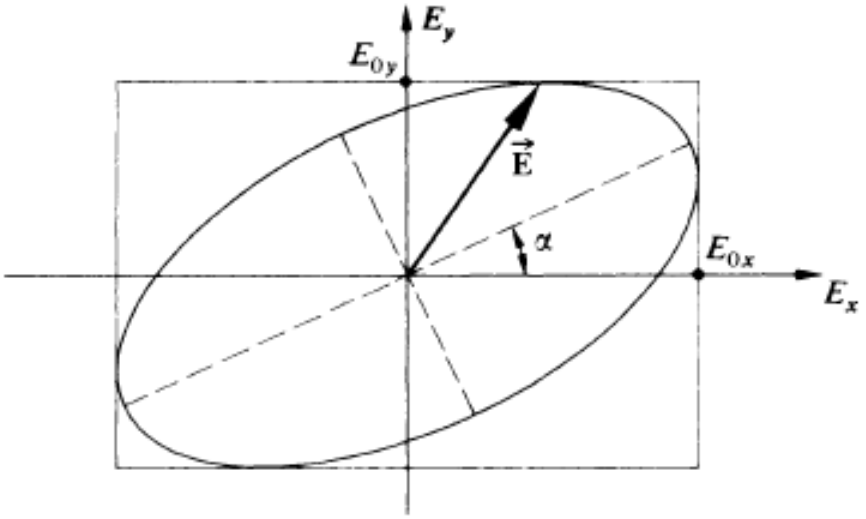

Figure 1.7: General case of polarized beam. Elliptical light, the end point of the electric field vector sweeps out an ellipse as it rotates once around.

$$\tan(2\alpha) \;= \frac{2E_{ox}E_{oy}\cos\epsilon}{E_{ox}^2 - E_{oy}^2} \tag{1.4}$$

In 1852 G.G. Stokes introduced four quantities that are functions only of observable of the electromagnetic wave and are known as the Stokes parameters. The operational definition of the Stokes parameters is given by the following relations:

$$\begin{cases} \delta_0 = & 2I_0 \\ \delta_1 = & 2I_1 - 2I_0 \\ \delta_2 = & 2I_2 - 2I_0 \\ \delta_3 = & 2I_3 - 2I_0, \end{cases} \tag{1.5}$$

and considering the Equation 1.2 we can express them in terms of the electric field component:

$$\begin{cases} \delta_0 = & \left\langle E_{ox}^2 \right\rangle + \left\langle E_{oy}^2 \right\rangle \\ \delta_1 = & \left\langle E_{ox}^2 \right\rangle - \left\langle E_{oy}^2 \right\rangle \\ \delta_2 = & \left\langle 2E_{ox}E_{oy}\cos\epsilon \right\rangle \\ \delta_3 = & \left\langle 2E_{ox}E_{oy}\sin\epsilon \right\rangle. \end{cases} \tag{1.6}$$

The degree of polarization is defined as $P = \frac{I_P}{I_P + I_N}$ where I_P and I_N are the flux density of polarized and unpolarized light respectively. The degree of polarization can be expressed in terms of the Stokes parameters as:

$$P = \left(\delta_1^2 + \delta_2^2 + \delta_3^2\right)^{\frac{1}{2}} / \delta_0, \tag{1.7}$$

and we can express Equation 1.4 in terms of the Stokes parameters as well:

$$\alpha = 1/2 \arctan \frac{\delta_2}{\delta_1} \tag{1.8}$$

It is usual to find the Stokes parameters ($\delta_0, \delta_1, \delta_2, \delta_3$) represented by I, Q, U and V respectively.

1.3.2. Dust polarization

An optical device, material or medium whose input is natural light (unpolarized) and whose output is some form of polarized light is a polarizer. There are several ways to polarize light but since this is not the main scope of this thesis I will only provide a brief overview of two of them, which are more related for our purpose.

Dichroism. The term dichroism describes the selective absorption of one of the two orthogonal polarization state of an incident beam. The dichroic medium itself is physically anisotropic, producing a preferential absorption of one field component while being essentially transparent to the other. An example of a device of this kind is a grid of parallel conducting wires (see Fig. 1.8). If we imaging a unpolarized beam going through the grid, the electric field component parallel to the grid ($\vec{E}_{\parallel}$) drives the conduction of electrons along the length of each wire, thus generating a current, heating the wires (Joule heat) and dissipating the energy of the field, resulting in little or no transmission of $\vec{E}_{\parallel}$. On the other hand, in the perpendicular direction ($\vec{E}_{\perp}$) the electrons cannot move very far and the field component is mostly unaltered and it propagates.

In ISM it is commonly accepted that dust grains rotate with their long axis perpendicular to the magnetic field through a mechanism that is not yet clear (see below). When unpolarized radiation goes through the dusty medium the output beam will be linearly polarized perpendicular to the dust grain long axis and thus parallel to the magnetic field. This effect is observed at visible and near-infrared wavelengths. However, if we observe at longer wavelengths (far-infrared, submillimeter and millimeter), we will observe the dust thermal emission. This emission will present an electric field that will oscillate preferably in the direction of the long axis of the dust grain and thus it is also linearly polarized but parallel to the dust grain major axis and thus perpendicular to the magnetic field (Stein, 1966; Cudlip et al., 1982; Hildebrand, 1988).

The mechanism that dominates the alignment of the dust grains is an open question today (see e. g., Andersson, Lazarian, and Vaillancourt, 2015, for a review). Below I will briefly describe the different mechanisms by which dust grains are believed to line up: paramagnetic relaxation, mechanical alignment, and radiative alignment. Davis and Greenstein (1951) proposed as an alignment mechanism the paramagnetic relaxation, whereby the magnetic energy would reach a minimum, or point of maximum stability, when the axis of rotation of the dust grain is aligned with the local magnetic field. The paramagnetic relaxation occurs when the initial misalignment between the internal grain field and the local field generates a torque which opposes such misalignment. Very soon after, Gold (1952b) and Gold (1952a) suggested a mechanical alignment caused by the passage of a gaseous flow through the elongated dust grains that would orient the axis of rotation perpendicular to the flow. Finally, Dolginov and Mitrofanov (1976) proposed that an anisotropic radiation field could align the dust grains through the angular momentum transfer, a.k.a. Radiative Alignment Torque (RAT), which takes place in the scattering of light by a dust grain. This last mechanism is considered the one that best explains the polarization observations in the ISM, although likely there are specific regimes in which each of the mechanism may dominate (Andersson, Lazarian, and Vaillancourt, 2015).

Polarization by scattering. The scattering of light by molecules produces linearly polarized light in the plane perpendicular to the incident beam. The reason is that the molecule behaves like a dipole and thus it does not radiate in the direction of its axis. Since the $\vec{E}$ field of the incident wave induces vibration in the molecules parallel to it, the consequence is that he scattered light in the forward direction is completely unpolarized, becoming increasingly more polarized as the angle increases. When the direction of observation is normal to the incident beam the light is completely linearly polarized. It is though that this effect can be observed in regions where dust grains and density are large enough (e. g.,polarization in protoplanetary disks; Kataoka et al., 2017), although this is a topic under debate.

Recently, Guillet et al. (2020) point out that the orientation of polarized light in the plane of the sky (POS) is highly dependent on the grain size (**a**) present in the disk. Thus, the thermal linear polarized emission could be perpendicular or parallel to the magnetic field depending if we are in the Rayleigh ($\lambda >>$ **a**) or in the Mie regime ($\lambda \sim$ **a**).

In conclusion, the polarized thermal emission from dust grains is, until now, the main tracer of the magnetic field in star-forming regions. However, we should keep in mind the rest of processes that can generate polarized light, and stay tuned as this is a boiling field. Besides, in any case it is tracing the magnetic field in the plane of sky (POS) since before a field parallel to the line of sight (LOS) the total polarized flux would be zero.

1.3.3. Molecular line polarization

In the range of action of a magnetic field, rotational lines of molecules with a strong magnetic dipole split in magnetic sub-levels. This rotational radio frequency transitions will split into linearly and elliptically polarized component slightly separated in frequency. This is the so-called Zeeman effect. The measure of this split is the only way to measure the magnetic field strength in the LOS. Furthermore, if the magnetic sub-levels are unequally populated, what occurs in the presence of anisotropic radiation field (Goldreich and Kylafis, 1981), then the line is linearly polarized and the linear polarization vector should reveal the magnetic field direction (Goldreich and Kylafis, 1981; Goldreich and Kylafis, 1982). This is the so-called Goldreich-Kylafis (GK) effect that happens if optical depth of molecular cloud is the order of unity and radiatives rates are equal or larger than collisional rates. In this thesis I will not delve further into these methods since it escapes the objective of the work although they are worth mentioning because of their importance.

1.3.4. Magnetic field properties from observations

.

Polarized emission observed of both starlight background (visible and near-infrared) and dust thermal (far-infrared, submillimeter and millimeter) allow us to measure $\vec{E}_{POS}$, although, as stated in Sect. 1.3.2 it does not provide a measurement of the magnetic field strength.

Different methods have been proposed to estimate the magnetic field strength based on dust polarization emission. Davis (1951a) and Chandrasekhar and Fermi (1953a) (DCF) describe a method to estimate the magnetic field strength assuming that turbulent motions have a visible effect on the distribution of the magnetic field in the plane of the sky, that is, magnetic field strength is proportional to the velocity dispersion and inversely proportional to the dispersion in polarization position angles. Later, Ostriker, Stone, and Gammie (2001) propose the following equation (Eq. 1.9), which retrieves the DCF equation for the case $Q = 1$. These authors suggest that, using Q$\approx$ 0.5, DCF method provide an accurate measurement of the B_{POS} when polarization angle dispersion is relatively small ($\delta_{P.A.} \leqslant 25°$)

$$B_{POS} = Q\sqrt{4\pi\rho}\frac{\delta v_{los}}{\delta_{P.A.}}. \tag{1.9}$$

Heitsch et al. (2001) propose another variation in which the restriction for large angles is removed, and later Hildebrand et al. (2009) and Houde et al. (2009) apply a more sophisticated technique which uses an analytical derivation of the dispersion in polarization angles within a turbulent molecular cloud. Very recently, Skalidis and Tassis (2020) present a new variation of DCF method in which the authors consider anisotropic turbulent motions. Different authors tested their method using simulations and they found their method to produces more accurate results than both

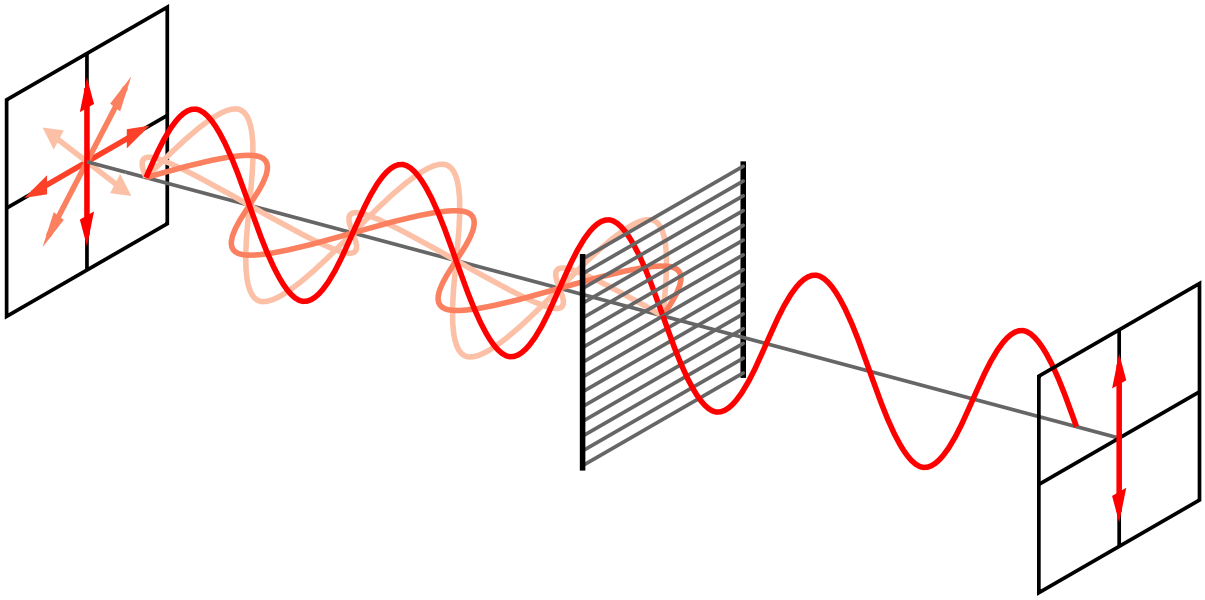

Figure 1.8: Polarization by dichroism illustration. Credits: CC BY-SA 3.0, https://commons.wikimedia.org/w/index.php?curid=724493

DCF and Heitsch methods as long as the sonic Mach number stay below ~ 4 (REFERENCE?). Above this limit, their method is still more accurate than DCF method and in general it presents stable relative deviation in sampled range.

In brief, the DCF method has proven not to be very accurate for calculating magnetic field strength and consequently many variations of this method have been proposed.

Koch, Tang, and Ho (2012a) and Koch, Tang, and Ho (2012b) proposed a method in the framework of ideal magnetohydrodynamic (MHD), based on the relative orientation between the local magnetic field and the gradient of the intensity emission, which provides an estimate of the magnetic field strength. Through this relative orientation, these authors obtain the so-called magnetic field significance (see Eq. 2.5), which is a measure of the relative importance of the magnetic field tension force and the other forces involved. The method has been used to test the role of the magnetic field in star formation process in molecular cloud (Koch, Tang, and Ho, 2013; Koch et al., 2014; Koch et al., 2018) and more recently in the fragmentation of molecular cloud process (Tang et al., 2019).

$$\Sigma_B \equiv \left(\frac{F_B}{|F_G + F_P|} \right), \tag{1.10}$$

The precision of these estimates is still a matter of debate. However, they provide valuable information that allows to evaluate the strength of the magnetic field with respect to the rest of the forces involved in the star formation process. In this thesis, I will make use of many of these methods (DCF, Heitsch, Koch) to estimate the strength of the magnetic field and will compare the results.

1.4. The objectives of the thesis and applied methodology

1.4.1. Motivation and goal of the thesis

This thesis originates from a scenario in which the arrival of new and more powerful instruments is facilitating the advancement of knowledge about the formation of stars. Instruments, such as ALMA, have provided astronomers with the ability to look inside protostellar envelopes and thus observe accretion disks in very early stages of star formation. However, due to the difficulties discussed in the previous sections, such a large distance, short evolution time, and the formation into a cluster, our knowledge about the formation of the most massive stars continues to have large gaps. From the theoretical point of view, a handful of models of high-mass star formation have been proposed. Among them, the most prominent are the so-called *competitive accretion* and *core accretion*. The latter proposes a scale up version of low-mass star formation however, this scenario involves theoretical drawbacks, such as the radiation pressure problem. One solution might be disk accretion, raising questions such as: are massive stars formed through an accretion disk? and if so, which are their properties?, are they planet-forming disks?.

One ingredient which is called to be key for the formation of stars is the magnetic field. It allows the formation of accretion disks and the ejection of material. However, its importance in the early stages of low- and high-mass star formation is not well understood yet. Some works point its importance during cloud formation and collapse, while others favor the dominant role of turbulence and gravity. Planck Collaboration et al. (2016) shows an apparent link between the morphology of the magnetic field and the formation of structures in the interstellar medium. In fact, magnetic field is thought to be crucial in the formation of filaments, which are closely linked to the formation of low- and high-mass stars. In addition, Zhang et al. (2014) find that the magnetic field is organized, pointing that it plays an important role during the formation of dense cores at sub-parsec scales in a massive star forming scenario. Furthermore, Pillai et al. (2020) find a correlation between the orientation of the magnetic field and gas flows in a star cluster of Serpens South. Besides, a relationship has also been found between the magnetic field and the fragmentation of molecular clouds that gives rise to cores and finally to star clusters. Through MHD simulations, a relationship between strong magnetization and low fragmentation level has been found (Hennebelle et al., 2011; Commerçon, Hennebelle, and Henning, 2011). However, in some cases this dependency could not be determined (Palau et al., 2020). Therefore it is worth asking What is the role of the magnetic field during the fragmentation process which gives rise to the stars clusters?.

In this thesis, we aim to contribute to explain the massive star formation process, paying special attention on the role that the magnetic field plays. To do that we will make a multi-scale analysis with a double approach, theoretical and observational.

In particular, we investigate the accretion process through an accretion disk around a high-mass star. Our goal is to understand if a massive star could be form in a similar way that a low-mass star, i.e., accreting material from the envelope through an accretion disk which would avoid the radiation pressure problem. For this purpose, we model the 1.13 mm ALMA image we obtained with high angular resolution of the accretion disk around GGD27-MM1, the source powering the impressive, 14 pc long and highly collimated radio jet HH 80–81. To do this, we take advantage of the apparent observational similarities between this disk-jet system and those observed in the low-mass regime and apply the models developed by D'Alessio et al. (2006).

On the other hand, we study the fragmentation process of the IRDC G14.225−0.506. We aim to investigate the role of the magnetic field in the fragmentation and in the gravitational collapse process. We take advantage of dust continuum and linear polarized emission observations car-

ried out with the Caltech Submillimeter Observatory (CSO) towards the physically twin hubs of this IRDC, but showing a different degree of fragmentation at millimeter wavelengths to test the magnetic field strength in both hubs.

The distribution of the thesis is detailed in the next section.

1.4.2. Outline and status project

In the following, I list the different projects that make up the thesis and their status.

- Chapter 2: In this chapter I present the work done with polarimetric observations towards G14.225-0.506 (G14.2), an IRDC located at ∼ 1.98 kpc. This work has led to a scientific article entitled (Añez-López et al., 2020b): *The role of the magnetic field in the fragmentation process: the case of G14.205-0.502*. The article is authored by N. Añez-López, G. Busquet, P. M. Koch, J. M. Girart, H. B. Liu, F. Santos, N. L. Chapman, G. Novak, A. Palau, P. T. P. Ho, and Q. Zhang and is published in Astronomy & Astrophysics, Volume 644, id.A52, 14 pp. You will find the manuscript in the following link:
https://www.aanda.org/articles/aa/abs/2020/12/aa39152-20/aa39152-20.html

- Chapter 3: In this chapter I present the work of modeling the accretion disk around the massive star GGD27-MM1. This work has led to a scientific article entitled (Añez-López et al., 2020a):
Modeling the accretion disk around the high-mass protostar GGD 27-MM1. The paper is authored by N. Añez-López, M. Osorio, G. Busquet, J. M. Girart, E. Macías, C. Carrasco-González, S. Curiel, R. Estalella, M. Fernández-López, R. Galván-Madrid, J. Kwon, J.M. Torrelles and is published in The Astrophysical Journal Volume 888, Issue 1, article id. 41, 15 pp. (2020). You will find the manuscript in the following link:
https://iopscience.iop.org/article/10.3847/1538-4357/ab5dbc

- Chapter 4: Conclusions, work in progress and future scientific challenges.

In addition to the projects which compose the thesis I have collaborated in the followings published works:

- "Characterizing the radio continuum nature of sources in the massive star-forming region W75N (B)", Rodríguez-Kamenetzky, Carrasco-González, Torrelles et al. (included Añez-López), 2020, MNRAS, 496, 3128. In the following link you will find the manuscript:
https://academic.oup.com/mnras/article-abstract/496/3/3128/5860292?redirectedFrom=fulltext

- "Unveiling a cluster of protostellar disks around the massive protostar GGD 27 MM1", Busquet, Girart, Estalella et al. (included Añez-López), 2019, A&A, 623, L8. In the following link you will fin the manuscript:
https://www.aanda.org/articles/aa/full_html/2019/03/aa33687-18/aa33687-18.html

- "Resolving the polarized dust emission of the disk around the massive star powering the HH 80-81 radio jet", Girart, Fernández-López, Li et al. (included Añez-López) 2018, ApJ, 856, L27. In the following link you will find the manuscript:
https://iopscience.iop.org/article/10.3847/2041-8213/aab76b

Chapter 2

The role of the magnetic field in the fragmentation process: the case of G14.225-0.506

2.1. Overview

Magnetic fields are predicted to play a significant role in the formation of filamentary structures and their fragmentation process to form stars and star clusters. We aim at investigating the role of the magnetic field in the process of core fragmentation toward the two hub-filament systems in the infrared dark cloud G14.225-0.506, which present different levels of fragmentation. We performed observations of the thermal dust polarization at 350 μm using the Caltech Submillimeter Observatory (CSO) with an angular resolution of 10″ toward the two hubs (Hub-N and Hub-S) in the infrared dark cloud G14.225-0.506. We additionally applied the polarization–intensity-gradient method to estimate the significance of the magnetic field over the gravitational force. The sky-projected magnetic field in Hub-N shows a rather uniform structure along the east-west orientation, which is roughly perpendicular to the major axis of the hub-filament system. The intensity gradient in Hub-N displays a single local minimum coinciding with the dust core MM1a detected with interferometric observations. Such a prevailing magnetic field orientation is slightly perturbed when approaching the dust core. Unlike the northern Hub, Hub-S shows two local minima, reflecting the bimodal distribution of the magnetic field. In Hub-N, both east and west of the hub-filament system, the intensity gradient and the magnetic field are parallel whereas they tend to be perpendicular when penetrating the dense filaments and hub. Analysis of the $|\delta|$- and Σ_B-maps indicates that, in general, the magnetic field cannot prevent gravitational collapse, both east and west, suggesting that the magnetic field is initially dragged by the infalling motion and aligned with it, or is channeling material toward the central ridge from both sides. Values of $\Sigma_B \gtrsim 1$ are found toward a north-south ridge encompassing the dust emission peak, indicating that in this region magnetic field dominates over gravity force, or that with the current angular resolution we can not resolve an hypothetical more complex structure. We estimated the magnetic field strength, the mass-to-flux ratio and the Alfvén Mach number, and found differences between the two hubs. The different levels of fragmentation observed in these two hubs could arise from the differences in the properties of the magnetic field rather than from different intensity of the gravitational field because the density in the two hubs is similar. However, environmental effects could also play a role.

2.2. Introduction

Recent observations show that filaments are prevailing structures in molecular clouds (e. g., Myers, 2009; Molinari et al., 2010; André et al., 2014; André et al., 2014; Rivera-Ingraham et al., 2016; Dhabal et al., 2018), but their formation mechanism and the effect of interplay between gravity, turbulence, and magnetic fields on the origin and evolution of filamentary structures remains unclear, and their specific role in the fragmentation process to form star clusters is still under debate. Several models have been proposed to explain the formation and evolution of filamentary structures, such as the magnetized filament (Inoue and Fukui, 2013; Van Loo, Keto, and Zhang, 2014). Others consider turbulent environments (Padoan et al., 2001; Moeckel and Burkert, 2015) and models which consider both turbulence and magnetic fields (Kirk et al., 2015; Federrath et al., 2016). One possible scenario is Global, Hierarchical Gravitational collapse (GHC; Gómez and Vázquez-Semadeni 2014; Smith, Glover, and Klessen 2014; Smith et al. 2016; Vázquez-Semadeni et al. 2019), according to which all scales accrete material from their parent structures, and filamentary accretion flows form as a natural consequence of the gravitational collapse of a highly inhomogeneous cloud.

Magnetic fields are believed to be important at cloud and core scales (e.g., Girart et al., 2009; Zhang et al., 2014; Li et al., 2015; Beltrán et al., 2019). In particular, observations suggest that magnetic fields in molecular clouds are perpendicular to the filaments (e. g., Sugitani et al., 2011; Palmeirim et al., 2013; Pillai et al., 2015; Santos et al., 2016; Planck Collaboration et al., 2016). There is also observational evidence of gas flows along the filaments that converge into the hubs (e. g., Kirk et al., 2013; Peretto et al., 2014; Williams et al., 2018; Chen et al., 2019b).

The infrared dark cloud G14.225-0.506 (hereafter IRDC G14.2), located at a distance of 1.98 kpc (Xu et al., 2011), is part of the extended (77×15 pc) and massive ($> 10^5$ $M_\odot$) molecular cloud discovered by Elmegreen and Lada (1976), located southwest of the Galactic HII region M17. Observations of the dense gas emission reveal a network of filaments constituting two hub–filament systems (Busquet et al., 2013; Chen et al., 2019b). The hubs are associated with a rich population of protostars and young stellar objects (Povich and Whitney, 2010; Povich et al., 2016), and appear more compact, warmer ($T_{\rm rot} \simeq$15 K), and show large velocity dispersion and larger masses per unit length than the surrounding dense filaments, suggesting they are the main sites of stellar activity within the cloud (Busquet et al., 2013).

The sky-projected magnetic field morphology in G14.2 has been mapped through interstellar polarization of background starlight at optical and near-infrared wavelengths (Santos et al., 2016). At large scales, Santos et al. (2016) find that the magnetic field in G14.2 is tightly perpendicular to the molecular cloud and to the dense filaments. The magnetic field strength was estimated using the Davis-Chandrasekhar-Fermi method to be in the range of $320 - 550$ μG, which lead to prevailing sub-alfvénic conditions, although the field strength does not seem to be sufficient to prevent the gravitational collapse of the hubs and filaments. These general features are suggestive of a scenario in which the magnetic fields played a significant role in regulating gravitational collapse on the ~30 to ~2 pc scale range.

Focusing on the hubs in G14.2, high-angular resolution observations (~1.″5) carried out with the Submillimeter Array (SMA) reveal that the two hubs are physically indistinguishable at 0.1 pc scales, despite clearly presenting a different level of fragmentation when observed with a spatial resolution of 0.03 pc: Hub-S being more fragmented than Hub-N (Busquet et al., 2016). Despite the presence of a bright Infrared Astronomical Satellite (IRAS) source ($L \simeq 10^4$ $L_\odot$) close to Hub-N, Busquet et al. (2016) show that all derived physical properties such as the density and temperature profiles, the level of turbulence, the magnetic field around the hubs, and the rotational-to-gravitational energy are remarkably similar in both hubs. The authors conclude that the lower

fragmentation level observed in Hub-N could result from the effects of UV radiation from the nearby HII region, evolutionary effects, and/or stronger magnetic field inside the hubs than originally derived.

The polarization of dust thermal emission at submillimeter wavelengths provides a method to study magnetic field properties (Hildebrand et al., 2000). It is thought that dust grains are aligned with their longer axis perpendicular to the magnetic field lines thus the emitted light appears to be polarized perpendicular to the field lines (see Lazarian, 2007; Andersson, Lazarian, and Vaillancourt, 2015, for reviews of grain alignment mechanisms). Therefore dust polarization measurements probe the plane of sky projected magnetic field structure in dense regions.

In this paper, we present CSO 350 μm polarimetric observations toward the two hubs in the IRDC G14.2. The paper is organized as follows. Section 2.3 describes the observations and data reduction process. In Section 2.4 we present the main results and we analyze the thermal dust polarized emission in Section 2.5. Finally, in Section 2.6 we discuss our findings and we list the main conclusions in Section 2.7.

2.3. Observations and data reduction

SHARP (Li et al., 2008) is a fore-optics module that adds polarimetric capabilities to SHARC-II, a 12×32 pixel bolometer array (Dowell et al., 2003). SHARP separates the incident radiation into two orthogonal polarization states that are then imaged side-by-side on the SHARC-II array. SHARP includes a half-wave plate (HWP) located upstream from the polarizing splitting optics. Polarimetric observations with SHARP involve carrying out chop-nod photometry at each of four HWP rotation angles. Observations carried out with SHARP prior to December 2011 suffered correlated noise, the treatment of which required special techniques (Chapman et al., 2013). The techniques used included χ^2 analysis followed by error inflating, or the use of generalized Gauss-Markov theorem. In December 2011, the "cold load mirrors" in SHARP (Li et al., 2008) were replaced with warm absorbers; and subsequent testing revealed that this increased the photon noise but largely eliminated the correlated noise problem. Accordingly, no treatment for correlated noise was applied to the present data set.

The wavelength of observation was 350 μm and the effective beam size was $\sim 10''$. We observed the IRDC G14.2 with 30 pointings to cover the entire cloud complex (see Appendix in this Chapter, Fig. 9 and Table 3 and 4). Observations were obtained remotely on June 09, 10, 11, 12, 14, and 17 of 2015. On each night, we observed the young stellar object IRAS 16293-2422 for initial focusing and pointing calibrations, and observed Neptune at the end of the operation for absolute flux calibration. We employed a $210''$ chop throw for calibration observations, and employed a $300''$ chop throw for target source observations.

The data were calibrated using the method presented in Davidson et al. (2011) and Chapman et al. (2013). The polarization intensity shown in the present paper has been debiased. SHARP data analysis is carried out in two steps. In the first step, each individual half-wave plate cycle is processed to obtain six 12×12 pixel maps, one for each of the Stokes parameters I, Q, U, and one for the corresponding error maps. Uncertainties are computed using the variance in the individual total and polarized flux measurements (Dowell et al., 1998; Hildebrand et al., 2000). In the second step of the data analysis, single-cycle maps are combined to form the final maps and the errors are propagated to the final maps. The sky rotation is taken into account by interpolating the single-cycle maps onto a regular equatorial-coordinate grid (Houde and Vaillancourt, 2007). Corrections for changing atmospheric opacity as well as for instrumental polarization and polarimetric efficiency are also made during this second analysis step (Kirby et al., 2005; Li et al., 2008). The

percentage and position angle of polarization and their associated errors are computed for each sky position through standard techniques (see Hildebrand et al., 2000).

A common problem of the chop-node mode technique arises when the emission of the reference (off-source) position is comparable in intensity to the emission from the target source. After careful inspection of the emission in the off-source positions using the 350 μm dust continuum map (Busquet et al., 2016; Lin et al., 2017a), we flagged scans in which the emission coming from the off-source position was larger, on average, than ∼20% of the intensity peak in the target source position. Following these criteria, we flagged 10 cycles toward Hub-N and 90 toward Hub-S, ∼ 11%, and ∼ 42% of the total, respectively.

We used Matplotlib[1] to calculate the histogram of polarization angles. This software allows the user to select different methods to calculate the optimal bin width and consequently the number of bins. While with the Freedman Diaconis (FD) estimator the bin width is proportional to the interquartile range and inversely proportional to the cube root of **a**, where **a** is the number of data points, with the Sturges Estimator the number of bins is the base 2 log of **a**. In this work, we used the 'auto' mode which selects the Sturges value for small datasets, while for larger datasets will usually default to FD which avoids the overly conservative behavior of FD and Sturges for small and large data sets, respectively. We note that because of the low sample size for polarization detections in Hub-S, the histogram of the polarization angles was built considering a lower number of bins.

2.4. Results

Figure 2.1 presents the sky-projected orientation of the magnetic field that is assumed to be traced by linear polarization. Red segments represent the magnetic field direction (polarization segments rotated by 90°) observed at 350 μm with an angular resolution of ∼ 10″. Thick segments denote a polarization signal larger than $3\sigma_{\rm P}$ and thin segments indicate a signal of between $2\sigma_{\rm P}$ and $3\sigma_{\rm P}$, where $\sigma_{\rm P}$ is the noise of the polarization signal. In addition, we only consider segments with a percentage of polarization larger than 0.3% and with intensity larger than 15% or 25% in Hub-N or Hub-S, respectively, of the Stokes I local peak emission. We applied a different intensity threshold because of the different peak intensity in every hub so as not to remove segments with a S/N of greater than 3-σ in hub-N or to keep apparently noisy segments in hub-S. In any case, due to the restrictions applied during the subsequent analysis, which only considers measurements near the peaks, the stricter cut does not affect our analysis. The uncertainties of the position angles detected with a S/N of 2-σ and 3-σ are 17° and 10° (Naghizadeh-Khouei and Clarke, 1993). Therefore, we used only values larger than 3-σ to compute the average uncertainty in each field. We find that these are 5.8° and 7.9° for Hub-N and Hub-S, respectively. In Fig. 2.1, blue segments show the magnetic field observed at infrared wavelengths (H-band) with the 1.6 m telescope of the Pico dos Dias Observatory (Santos et al., 2016). As shown in Fig. 2.1 (top panel), the magnetic field structure in Hub-N is rather ordered and uniform, that is, it is mostly along an east–west orientation and roughly perpendicular to the major axis of the hub–filament system direction (i. e., F10-E following the nomenclature of Busquet et al. 2013). This can be also seen in Fig. 2.2 (top panel), where we present the histogram of the B-field angles. It is clear that there is a prevailing orientation with a dominating single peak over a rather small and confined range in B-field angles (mostly between 90° and 120°).

We fit a Gaussian to the position angle distribution shown in this figure (the fit is shown as a red line). The peak is found at 105 ± 12°. For comparison, the direction perpendicular to filament

[1] https://docs.scipy.org

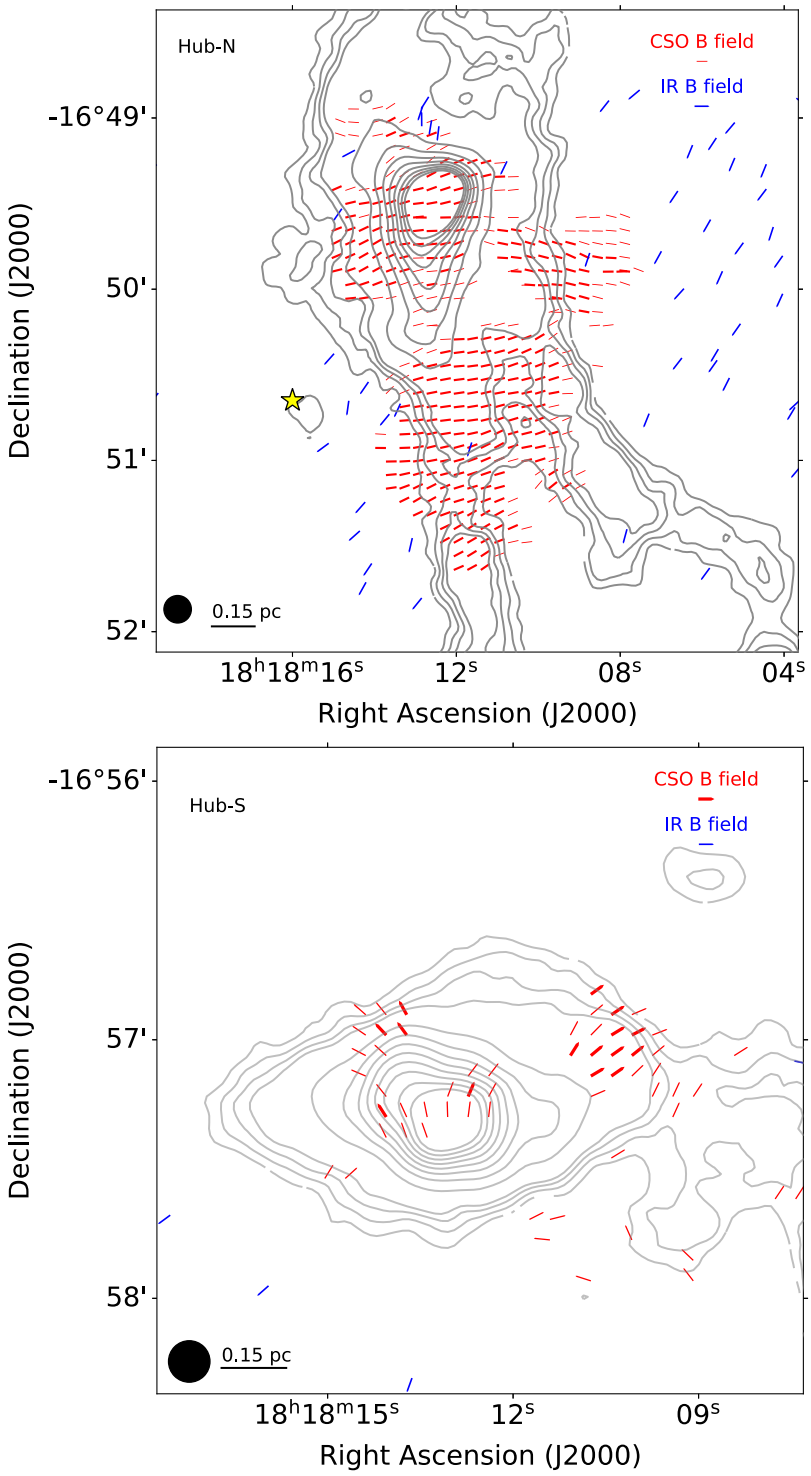

Figure 2.1: Polarization data toward Hub-N (top panel) and Hub-S (bottom panel) of the IRDC G14.2. Red segments depict the magnetic field (Nyquist sample) observed with the CSO at 350 μm obtained by rotating polarization vectors by 90°. The width illustrates segments above $3\sigma_p$ (thick segments) and between $2\sigma_p$ and $3\sigma_p$ (thin segments). Only segments over 15%/25% in Hub-N/Hub-S of Stokes I peak intensity are shown. Blue segments depict the magnetic field obtained from near-infrared (H-band) observations (Santos et al., 2016). Contours show the CSO 350 μm dust continuum emission (Busquet et al., 2016; Lin et al., 2017a; Lin et al., 2017b). Contour levels are 2, 4, 6, 8, 10, 20, 30, 40, 50, 60, 70, 80, 90 and 100 times the rms noise (~80 mJy beam^{-1}). The CSO beam (~10″) is shown in the bottom left corner of each panel. The yellow star (top panel) depicts the position of IRAS 18153-1651.

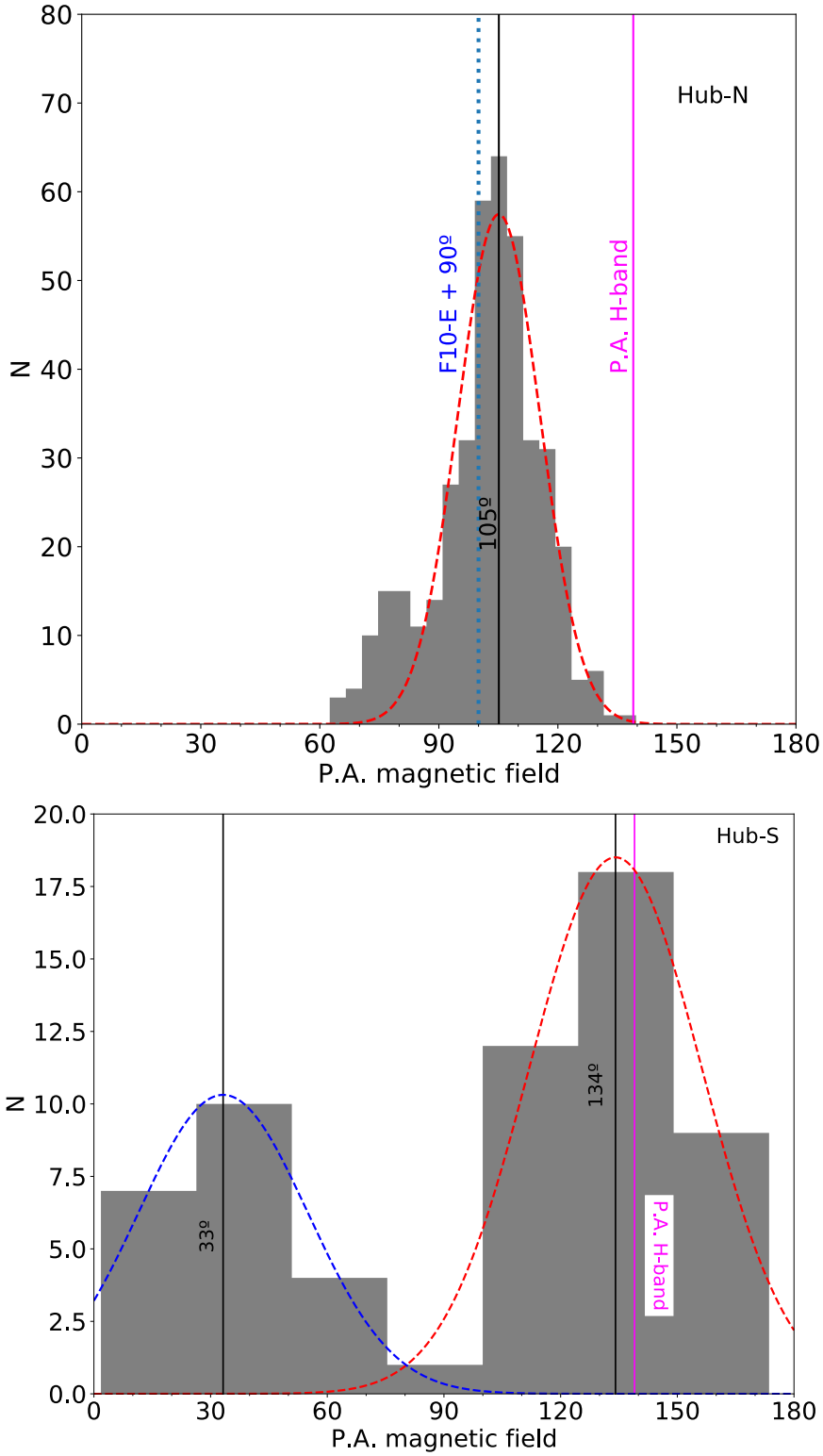

Figure 2.2: Histogram of the B-field position angles for Hub-N (top) and Hub-S (bottom). Distribution peaks at 105 ± 12°in Hub-N and 33 ± 25°/134 ± 26°in Hub-S, were obtained by Gaussian fit. The direction perpendicular to the main filament (i. e., F10-E, ∼ 100°, Busquet et al., 2013) is indicated by the dotted blue vertical line. The magenta solid line indicates the overall orientation of the polarization in the *H*-band (Santos et al., 2016).

F10-E (i. e., 100°) is also depicted in Fig. 2.2. From Fig. 2.1, it is clear that a direct point-by-point comparison between the magnetic field orientation inferred from the 350 μm dust polarization and the *H*-band observations cannot be conducted as there is no good spatial overlap between the two data sets. However, the overall orientation of the polarization in the *H*-band, including all detections over a larger field of view ($\sim 40' \times 40'$), is $139 \pm 16°$(see magenta line in Fig. 2.2, Santos et al., 2016), which indicates a relatively significant change of the magnetic field direction from cloud to filament scales.

Although the polarization data in Hub-S are scarce (see bottom panel of Fig. 2.1), the histogram shown in Fig. 2.2 (bottom panel) presents a bimodal distribution with two peaks: a dominant peak at 134±26° and a secondary peak around 33±25°(values obtained from a Gaussian fit, shown in this panel as a red and blue line). Such a bimodal distribution might be reflecting a "wing-like" magnetic field structure. There seem to be two wings coming into the main dust continuum peak (which is, presumably, the main gravitational center; see Fig. 2.1-lower panel), with one wing going from the northeast to the southwest and the other wing going from the northwest to the southeast. Despite the large uncertainty on the distribution of polarization angles, the direction of this second (and main) component peaking at ∼134° (west-center region in Fig. 2.1-bottom panel) is compatible with the main magnetic field orientation seen in Hub-N.

The polarization percentage map of Hub-N is shown in Fig. 2.3. The scarce data detection in Hub-S prevents us from building a similar map toward this region. In Hub-N, the lowest values, namely of $\sim$ 1% (see Table 2.1), are found toward the dust continuum peak. The high-angular-resolution SMA observations of Hub-N reveal a dominant dust continuum core (MM1a) with a mass of 13 $M_\odot$ and associated with H_2O maser activity (Busquet et al., 2016), and hence the core is undergoing gravitational collapse. Such depolarization may result from a polarization structure that is averaged out by the large CSO beam, similar to the case of the Orion KL region (Rao et al., 1998) and NGC 1333 IRAS 4B (Attard et al., 2009). Another very clear case is the successively higher resolution observations in W51, starting from BIMA (3″, Lai et al., 2001) to the SMA (0.7″, Tang et al., 2009) and ALMA (0.25″, Koch et al., 2018). Observing the region of depolarization in the BIMA data with the SMA revealed the collapsing core signature in the B-field structure in W51 e2, and observing the inner SMA depolarization region in W51 e2 with ALMA revealed the likely existence of a pseudo-disk B-field structure.

Figure 2.4 shows the polarization percentage as a function of the intensity normalized to the peak emission, $I/I_{\rm max}$, for both Hub-N (upper panel) and Hub-S (lower panel). The polarization percentages in Hub-N and Hub-S extend one order of magnitude, ranging from 1.2 % and 0.9 % to 16.0 % and 7.3 %, respectively (see Table 2.1), being slightly lower in Hub-S. Despite the relatively broad scatter of polarization percentages at the low-intensity contours, for both hubs there is an anticorrelation between the polarization percentage and the intensity. This anticorrelation can be fitted, without applying any weighting to the values, with power laws with indices of around −0.63 and −0.56 for Hub-N and Hub-S, respectively (see Table 2.1). In Fig. 2.4, we show the power-law fit considering all data points above $2\sigma_{\rm P}$ (blue and green lines in Fig. 2.4 for Hub-N and Hub-S) and only data above $3\sigma_{\rm P}$ (red and yellow lines in Fig. 2.4 for Hub-N and Hub-S). Table 2.1 reports the power-law indices considering these two data sets. Similar slopes have been found in the filamentary IRDC G34.43+00.24 (Tang et al., 2019) and at core scale in high-mass star-forming regions (e. g., Koch et al., 2018).

This dependence of the polarization fraction on the dust intensity is typically used to infer dust grain alignment efficiency in star-forming regions (see e. g., Whittet et al., 2008; Pattle et al., 2019). However, we stress that the observed depolarization toward the CSO dust peak in Hub-N may be due to beam smearing effects, which prevent us from drawing any firm conclusion on dust alignment efficiency.

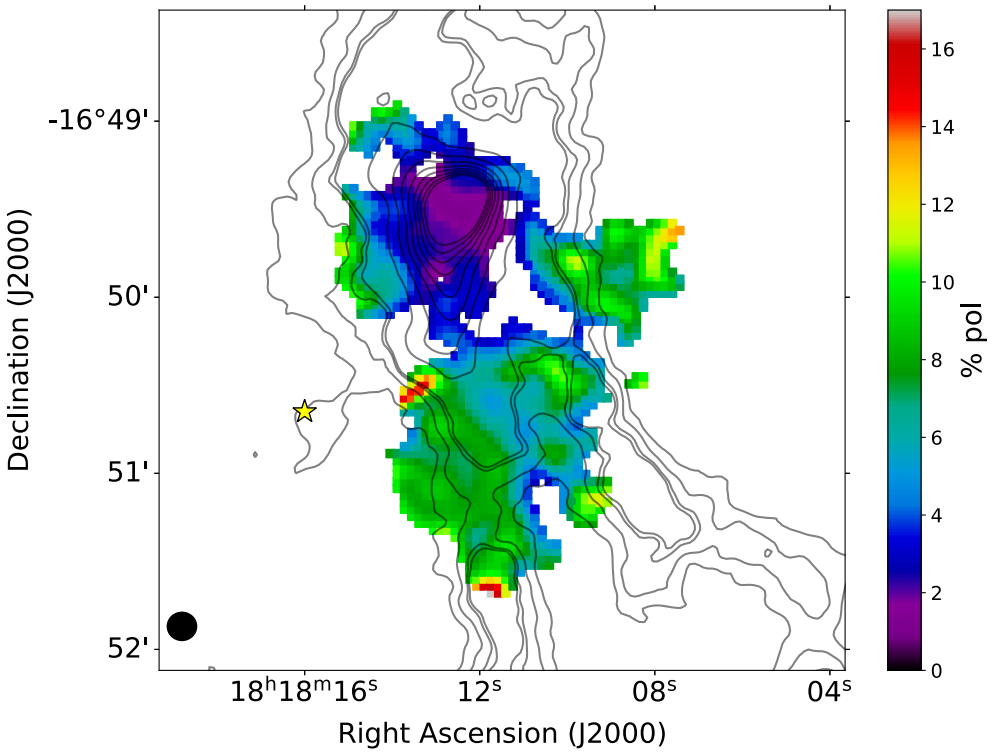

Figure 2.3: Polarization percentage map using data above $2\sigma_p$ and lower polarization threshold of 0.3%. Only segments over 15% of Stokes I peak intensity are considered. Contours and markers are the same as in Fig. 2.1.

Table 2.1: Polarization percentage properties

Field	Threshold [a] (σ_p)	Median (%)	Max (%)	Min (%)	Std [b] (%)	Slope [c]
Hub-N	3	7.2	16.0	1.2	2.5	−0.63
Hub-N	2	4.8	14.2	1.2	2.8	−0.73
Hub-S	3	3.8	7.1	1.5	1.2	−0.56
Hub-S	2	2.7	7.3	0.9	1.6	−0.68

[a] We only consider vectors with intensity greater than this threshold for the calculation of statistical values.
[b] Standard deviation of the polarization percentage distribution.
[c] Power-law index for fitting between normalized intensity and polarized emission percentage (see Fig. 2.4).

2.5. Analysis

2.5.1. Approach and Analysis Techniques

In this work, we applied the method developed by Koch, Tang, and Ho (2012a) and Koch, Tang, and Ho (2012b) to estimate the local magnetic field-to-gravity force ratio Σ_B. This method is motivated by the relationship between the magnetic field and the intensity gradient, and it begins with the force equation in the ideal magnetohydrodynamics (MHD) environment:

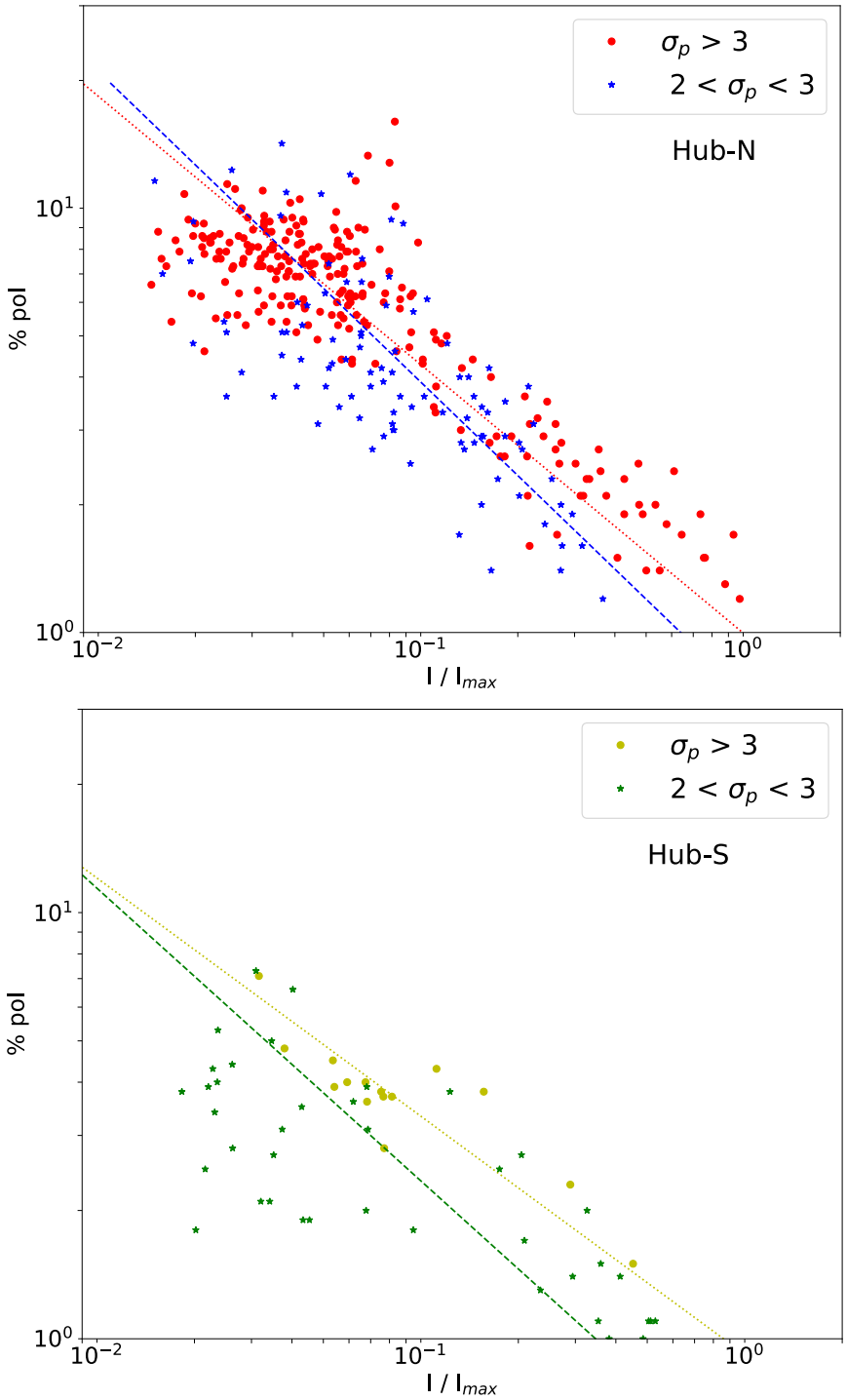

Figure 2.4: Polarization percentage as a function of the intensity normalized to the peak emission, $I/I_{\rm max}$ for Hub-N (upper panel) and Hub-S (lower panel), computed pixel by pixel. Red and Yellow circles show data $> 3\sigma_{\rm P}$ whereas blue and green stars show data between 2 and $3\sigma_{\rm P}$ for Hub-N/Hub-S. Red and yellow dotted lines and blue and green dashed lines show the power laws that best fit the data above $3\sigma_{\rm P}$ and the combined data, respectively (see Table 2.1). A lower intensity threshold of 3σ (σ = 0.08 Jy beam^{-1}) has been considered.

$$\rho\left(\frac{\partial}{\partial t}+\vec{v}\cdot\nabla\right)\vec{v}=-\nabla\left(P+\frac{B^2}{8\pi}\right)-\rho\nabla\phi+\frac{1}{4\pi}\left(\vec{B}\cdot\nabla\right)\vec{B}, \tag{2.1}$$

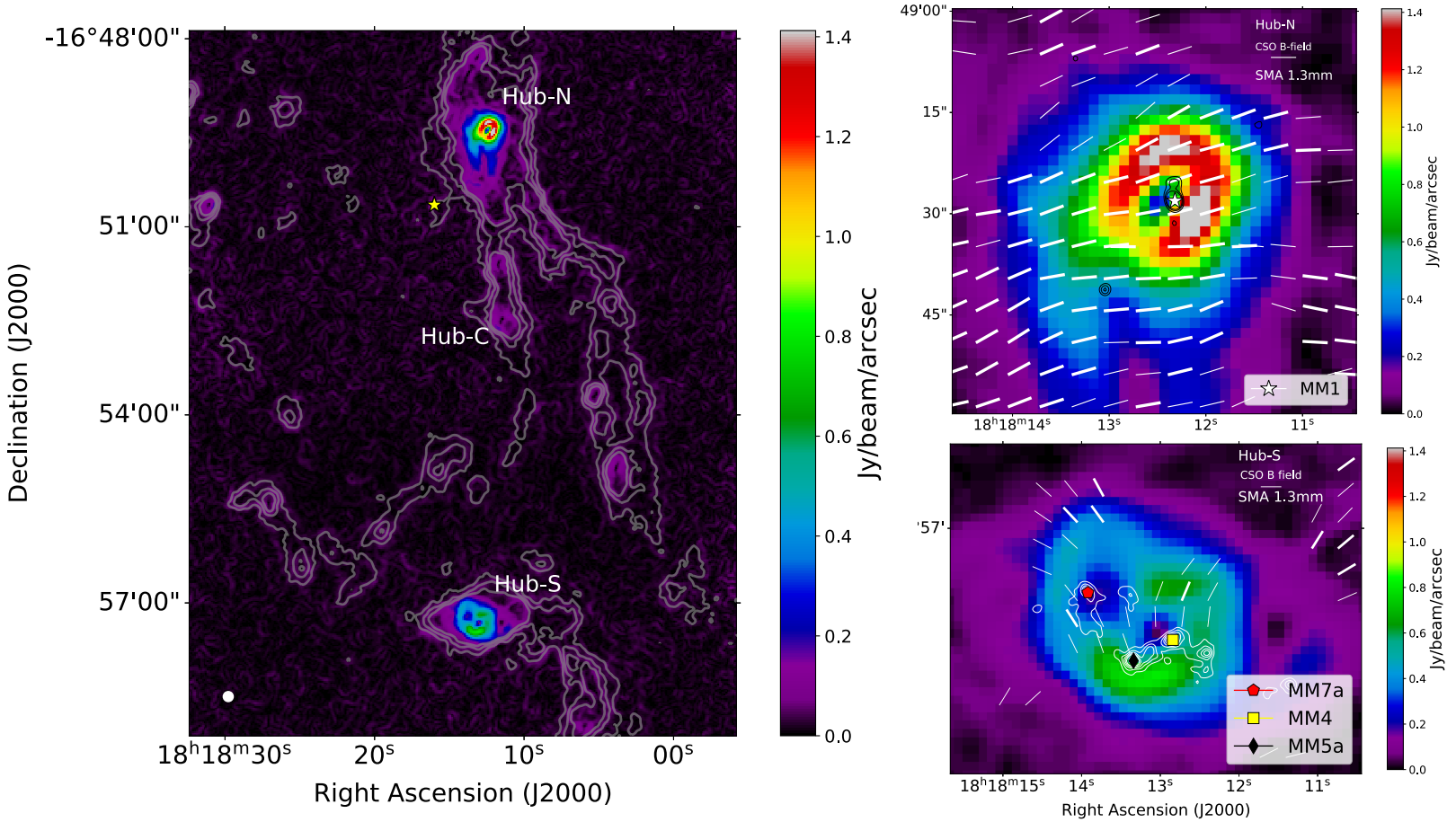

Figure 2.5: *Left:* CSO intensity gradient magnitudes at 350 μm in units of Jy beam^{-1} arcsec^{-1} (color scale) overlaid on the CSO dust continuum emission at 350 μm (contours, Busquet et al., 2016; Lin et al., 2017a). Contour levels are 3, 6, 9, and 12 times the rms noise, 80 mJy beam^{-1}. The yellow star depicts the position of IRAS 18153−1651. The white circle in the bottom left corner depicts the CSO beam size ($\sim 10''$). Hub-N, Hub-S and the Hub-C candidate identified by Chen et al. (2019b) are labeled. *Right:* Close-up images of the intensity gradient toward Hub-N (top panel) and Hub-S (bottom panel) overlaid on the SMA 1.3 mm dust continuum emission (black and white contours) at an angular resolution of $\sim 1\farcs5$ (Busquet et al., 2016). Contour levels range from 12σ to 30σ in steps of 6σ, and from 30σ to 60σ in steps of 15σ, in Hub-N and similar but starting from 6σ in Hub-S, where σ is the rms of the map, ~ 1 mJy beam^{-1}. White segments show the CSO B-field orientation, similar to Fig. 2.1. White star (right upper panel), red pentagon, black diamond and yellow square (right bottom panel) depict MM1a, MM7a, MM4 and MM5a cores, respectively.

where ρ is the dust density, $\vec{v}$ is the dust velocity, $\vec{B}$ is the magnetic field, P is the hydrostatic dust pressure, ϕ is the gravitational potential resulting from the total mass contained in the star-forming region and ∇ denotes the gradient. As shown by Koch, Tang, and Ho (2012a), we can transform Equation 2.1 into:

$$\rho v \frac{\partial v}{\partial s_v} \vec{e_{s_v}} + \rho v^2 \frac{\partial \vec{e_{s_v}}}{\partial s_v} = -\frac{\partial P}{\partial s_p} \vec{e_{s_p}} - \rho \frac{\partial \phi}{\partial s_\phi} \vec{e_{s_\phi}} + \frac{1}{4\pi} B^2 \frac{1}{R} \vec{n}, \tag{2.2}$$

where generalized coordinates s_v, s_P, s_ϕ, s_B along the directions of the unity vectors $\vec{e_{s_v}}$, $\vec{e_{s_P}}$, $\vec{e_{s_\phi}}$, and $\vec{e_{s_B}}$ are used, and the unity vector $\vec{n}$ is directed normal to a magnetic field line that is along $\vec{e_{s_B}}$. Here,$1/R$ is the curvature of the magnetic field line.

The interaction between hydrostatic pressure, gravitational potential, magnetic field force, and the resulting motion are described by Equation 2.2. In Koch, Tang, and Ho (2012a), the authors assume that the observed distribution of emission intensity is attributable to the transport of matter driven by a combination of the forces stated above. In other words, a change in emission distribution is the result of all combined forces. With this assumption, an emission intensity gradient measures the resulting direction of motion, expressed by the inertial term on the left-hand side of equations (2.1) and (2.2). With this, and identifying the various force terms in Equation 2.2 in an observed map in two dimensions (see Fig. 3 in Koch, Tang, and Ho, 2012a), and solving for the magnetic field, we can derive the following equation:

$$B = \sqrt{\frac{\sin\psi}{\sin\alpha} \left(\nabla P + \rho \nabla \phi\right) 4\pi R}, \tag{2.3}$$

where ψ and α are the angles in the plane of the sky between the orientation of local gravity and intensity gradient, and those between polarization and intensity gradient, respectively.

In addition, making use of the magnetic field tension force, and the gravitational and pressure forces:

$$\begin{aligned} F_B &= B^2/4\pi R \\ |F_G + F_P| &= |\rho \nabla \phi + \nabla P|, \end{aligned} \tag{2.4}$$

Equation 2.3 can be written as

$$\left(\frac{\sin\psi}{\sin\alpha}\right) = \left(\frac{F_B}{|F_G + F_P|}\right) \equiv \Sigma_B, \tag{2.5}$$

where Σ_B is a concept introduced by Koch, Tang, and Ho (2012a) to define the local magnetic field significance in the presence of gravity and any hydrostatic pressure. Σ_B evaluates the relative importance between the magnetic field tension force and the other forces involved. In star-forming regions, the thermal pressure term ∇P is typically small and negligible as compared to gravity. Therefore, Σ_B provides a criterion to distinguish a scenario where the magnetic field can prevent gravitational collapse and infall ($\Sigma_B > 1$) or not ($\Sigma_B < 1$). We note that all of the above equations can be evaluated locally at any position in a map where a magnetic field orientation is detected and where a local direction of gravity and an intensity gradient can be calculated based on a detected (dust) emission. These equations therefore allow us to construct maps of the magnetic field significance Σ_B and field strength B, and they provide a way of assessing where star formation is likely to preferentially occur.

The angle $|\delta|$ [2] ($= \pi/2$ - α; see Fig.3 in Koch, Tang, and Ho, 2012a) is the angle between a projected magnetic field orientation and an intensity gradient direction. Koch, Tang, and Ho

[2]For the purpose of the analysis here, it is sufficient to consider | delta | ≤ 90 deg. We note that the angle delta can additionally be given a sense of orientation, -90 deg ≤ delta ≤ 90 deg, as explained in Koch, Tang, and Ho, 2013.

(2012a) propose the angle $|\delta|$ as a diagnostic to measure the dynamical role of the magnetic field. In Koch, Tang, and Ho (2013), the authors develop the physical meaning of the angle $|\delta|$ by exploring its behavior at different scales across a large sample of about 30 sources observed with the SMA and the CSO. Further statistical evidence based on a sample of 50 sources is given in Koch et al. (2014). These latter authors conclude that a $|\delta|$–map always allows for an approximation of the more refined Σ_B map. Given the insufficient polarization data for Hub-S, except for its intensity gradient map, in the following sections we present the results obtained for Hub-N.

2.5.2. Polarization vs Intensity Gradient

We used the 350 μm dust continuum map presented in Busquet et al. (2016) and Lin et al. (2017a) to build an intensity gradient map. First we computed the numeric spatial derivative [3], from which we got X and Y vector components for every pixel. We then computed the vector magnitude encompassing the whole IRDC complex G14.2 (see Fig. 2.5). The highest values of the intensity gradient magnitudes are found toward the hubs. Obviously, at the peak of the dust emission, the intensity gradient magnitude decreases, which results in a ring-like morphology with maximum intensity gradient around the inner hole. As can be seen in Fig. 2.5, we can distinguish the filamentary structures detected in NH_3 by Busquet et al. (2013). Along the filaments, we find various regions where the intensity gradient slightly increases, coinciding with the dust clumps and the Hub-C candidate identified in N_2H^+ (Chen et al., 2019b).

This additionally captures systematic differences in the deviation of the magnetic field clock-wise or counterclock-wise from an intensity gradient, as e.g., in an hour-glass morphology that reveals characteristic positive and negative deviations.

[3] We used the Python tool numpy.gradient to compute the gradient map.

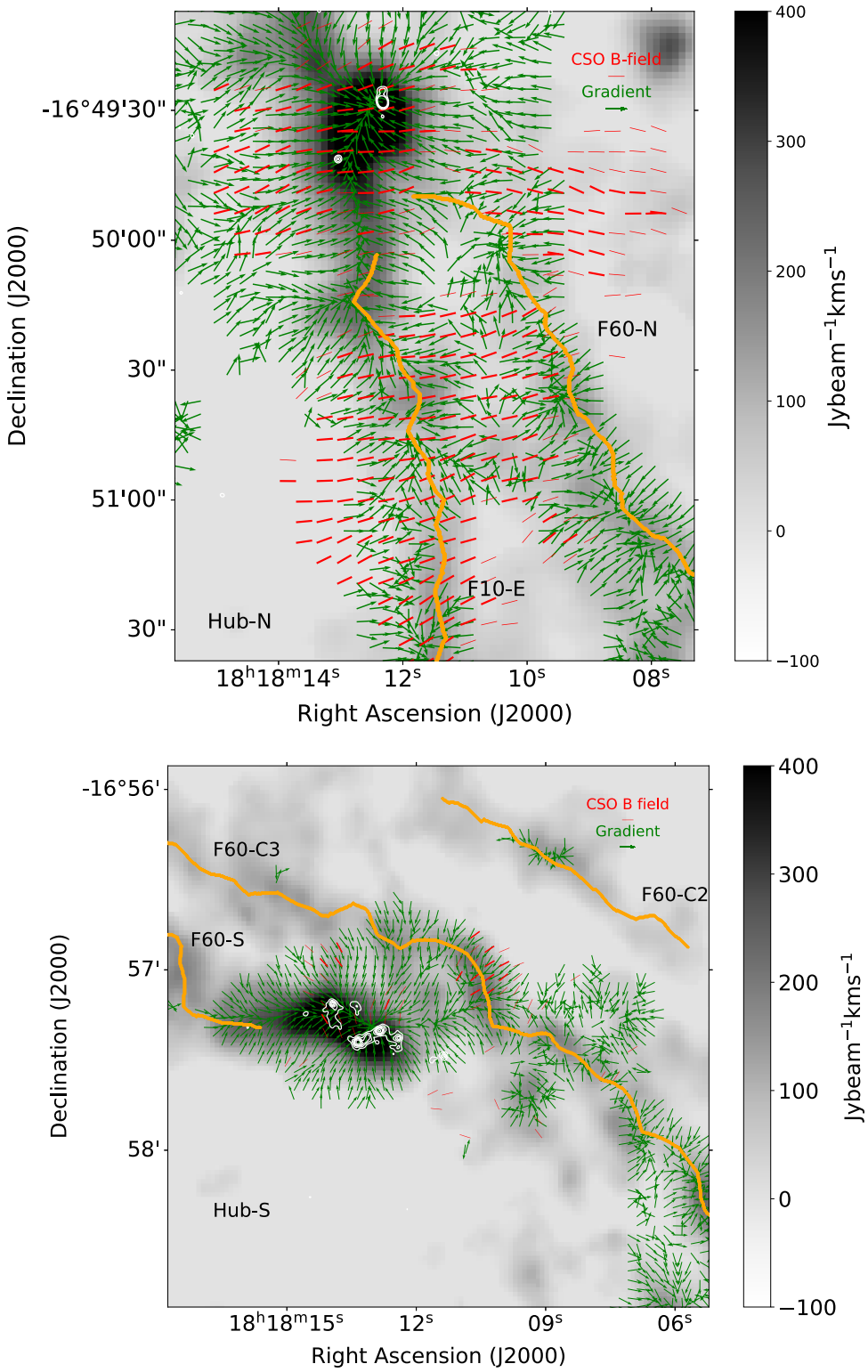

Figure 2.6: NH_3 moment 0 map (grey scale; Busquet et al., 2013) overlaid on the magnetic field segments (red) and the intensity gradient vectors (green, uniform length) from dust continuum for Hub-N (upper panel) and Hub-S (lower panel). We have restricted the representation of the gradient to the areas where the emission exceeds three times the rms noise of the continuum map. White contours correspond to the SMA 1.3 mm dust continuum emission (Busquet et al., 2016) similar to Fig. 2.5. The orange lines depict the spine of the filaments identified in N_2H^+ by Chen et al. (2019b) and they are labeled according to Busquet et al. (2013).

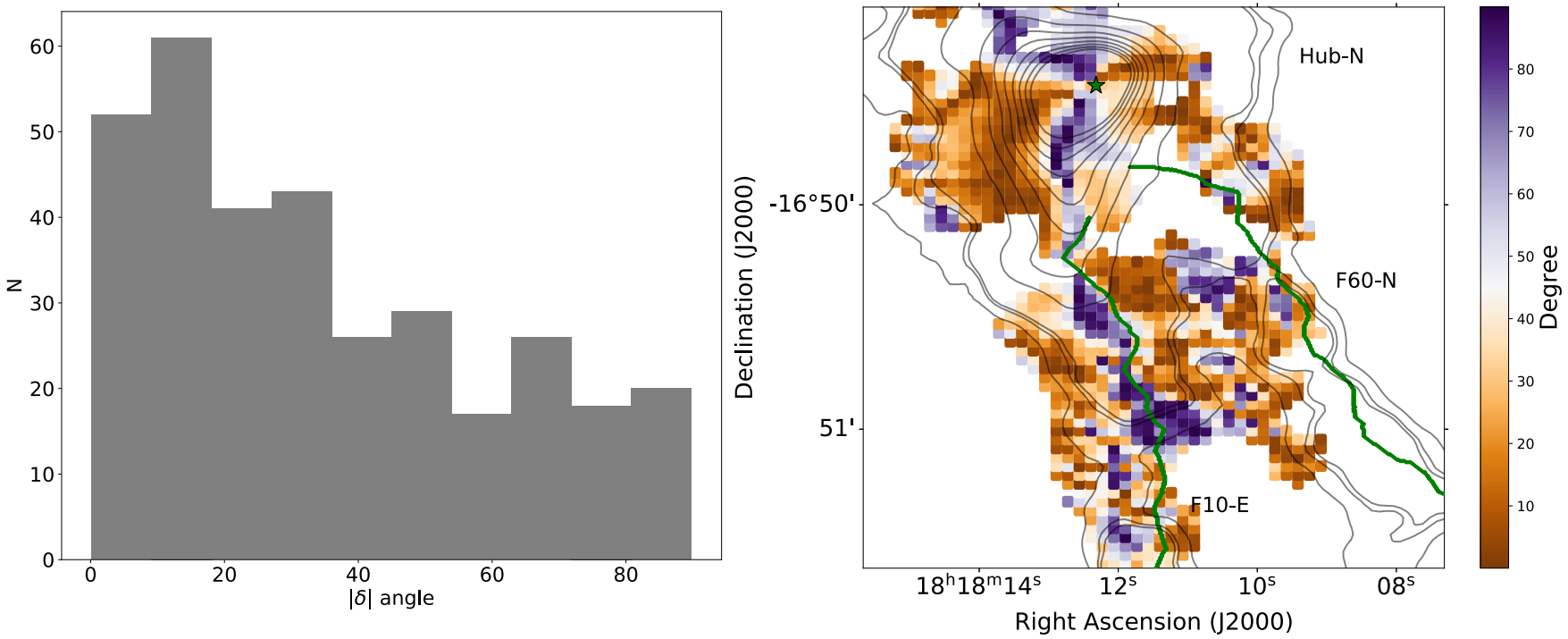

Figure 2.7: *Left:* Histogram of the absolute difference, $|\delta|$, between the position angles (P.A.s) of magnetic field and intensity gradient in the range from 0°to 90°. *Right:* $|\delta|$–map toward Hub-N (color scale) overlaid on the 350 μm dust emission. Contours levels range from 2σ to 10σ in steps of 2σ and from 10σ to 100σ in steps of 10σ, where σ is the rms noise of the map ($\sim$ 80 mJy beam^{-1}). The green star and the green solid line depict the MM1a core position and the spine of the filament, respectively, similar to Fig. 2.6.

The right panels in Fig. 2.5 show the close-up images of Hub-N (top panel) and Hub-S (bottom panel) overlaid with the SMA 1.3 mm dust continuum emission from Busquet et al. (2016). In addition, the magnetic field distribution observed with the CSO at 350 μm has been included. The high angular resolution ($\sim$ 1.″5) SMA 1.3 mm dust continuum images reveal that the two hubs present different levels of fragmentation. While Hub-N contains 4 mm condensations, Hub-S displays a higher fragmentation level, with 13 millimeter condensations within a field of view of 0.3 pc (Busquet et al., 2016, see also Table 2.2). Moreover, the spatial distribution of the 1.3 mm dust emission is significantly different in the two hubs. Hub-N presents a bright, centrally peaked dust condensation (MM1a according to the nomenclature of Busquet et al. 2016) with only a few and much fainter dust cores in its close vicinity (Busquet et al., 2016; Ohashi et al., 2016). On the other hand, as shown by Busquet et al. (2016) and Ohashi et al. (2016), the dust cores in Hub-S are more spread apart. They appear to be clustered in two different spatial locations, a snake-shape structure coinciding with the peak position of the CSO 350 μm emission, and the second group of dust cores located toward the north-east, following the elongation seen in the CSO 350 μm dust continuum map. This behavior is clearly reflected in the close-up images of the intensity gradient (see Fig. 2.5-right panels). While in Hub-N the intensity gradient displays a single local minimum coinciding with the bright dust continuum core MM1a, in Hub-S there are two clear minima, matching the spatial distribution at small scales. Interestingly, these close-up images reveal that the prevalent east-west magnetic field direction in Hub-N, slightly deviates when approaching the bright dust continuum core MM1a. Tang et al. (2019) find this kind of small deviation in G34 in the MM1 core, which is also the core with the most dominant magnetic field; it shows no fragmentation compared to the other cores in G34. Regarding Hub-S, Fig. 2.5 (bottom-right panel) shows that the two components of the bimodal distribution in B-field angles (see Fig. 2.2-bottom panel) resemble the two incoming wings which appear to converge towards the two local minima in the map of the magnitude of the intensity gradient. Specifically, the north-east component points toward MM7a, which is the most massive core ($\sim$ 10 $M_\odot$) of the north-east group whereas the second component (coming from the north-west and south east) points toward the snake-like structure, in which MM4 ($M \simeq 15$ $M_\odot$), and MM5a ($M \simeq 18$ $M_\odot$) are the most massive cores (Busquet et al., 2016). These results suggest a scenario in which the magnetic field in each hub is dragged by the collapsing cores, while at the same time the incoming wing-like and organized B-field morphology might be hinting accretion zones guided by the B-field.

We note that the intensity gradient can be a subtle tracer for changes in emission, and it can therefore localize weak (not yet resolved) maxima and minima in coarser emission. These local minima (such as in the case of Hub-N and Hub-S) can be signposts for fragmentation structures that can be detected and resolved with higher-resolution observations.

In order to see whether we are looking at the same depth in the two hubs, we estimated the optical depth at 350 μm. Adopting the physical parameters inferred by Busquet et al. (2016) (see their Table 5), we obtained similar values of the optical depth ($\tau_{350\mu m} \simeq 1.6$) in both hubs. Thus, we are confident that differences in the dust polarization are not due to different optical depths.

Figure 2.6 shows the dense gas emission traced by the NH_3 molecule toward the two hub-filament systems in G14 from Busquet et al. (2013), highlighting the extracted filament spine (orange line) identified through N_2H^+ emission by Chen et al. (2019b). We additionally overlaid the magnetic field segments (in red) and the intensity gradient vectors (in green). At large scales, and both east and west of Hub-N and its two associated filaments, the magnetic field is roughly perpendicular to the major axis of these dense structures, approximately following the direction of the intensity gradient. Close to the dense structures, the magnetic field appears to be still perpendicular to the direction of the filaments with only small variation close to the peak emission of Hub-N. In contrast, close to the filaments (specially toward F10-E), the intensity gradient ap-

pears to bend, becoming almost parallel to the filament spine, with the intensity gradient pointing toward Hub-N, that is, toward the gravitational potential (see Fig. 2.6 - top panel). In fact, locally converging intensity gradient directions also appear to trace the spine of the extracted filaments, that is, in many places intensity gradients converge from left and right towards a central line which overlaps or is near an extracted filament. We note that, because an intensity gradient map naturally identifies local and global minima and maxima, it will reveal structures similar to any filament-extraction routine that is searching for embedded denser structures. The bottom panel of Fig. 2.6 shows the same plot for Hub-S. At large distances of Hub-S, the magnetic field is perpendicular to filament F60-C3, following mostly the same direction as the intensity gradient. At some point, and when approaching the hub (i. e., the gravitational potential) the intensity gradient in both the eastern and western sides of Hub-S converge toward it. More specifically, the intensity gradient on the eastern side is perpendicular to F60-S and becomes parallel to the spine when entering the dense gas close to Hub-S where it penetrates the hub up to the group of dust cores located toward the northeast.

We observe the same behavior toward the west (~18h18m12s -16º57'20"), with the intensity gradient from the north-west and from the south-west, both pointing toward the snake-like structure. In this case, the magnetic field seems to follow the behavior of the gradient.

Figure 2.7 presents the results obtained from the analysis of the angle $|\delta|$. A significant number of values of $|\delta|$ are below 37° (about 60%), as shown in the histogram in the left panel, whereas the rest of the values are distributed roughly uniformly above this value. This is a consequence of the fact that around the main filament the intensity gradient follows the magnetic field lines leading to an elongated structure. This behavior is clearly seen in the pixel-by-pixel map for the angle $|\delta|$ shown in Fig. 2.7 (right panel). As can be seen in this figure, $|\delta|$ appears small in the outer zones, both from the east and from the west, of the central north–south ridge. This might indicate that the magnetic field is channeling material towards the central ridge from both sides and might also indicate that the B-field is initially dragged by the infalling motion and aligned with it. The rather uniform magnetic field together with small $|\delta|$ values also suggests that the magnetic field, the gravitational pull and possibly also large converging flows toward the ridge are all mostly aligned. It should be noted that larger deviations between the intensity gradient and the magnetic field, that is, larger values of $|\delta|$ occur along the inner spine of the north–south ridge. These are locations where gravity has not yet (fully) overwhelmed and forced the alignment of the magnetic field.

Figure 2.8 shows the Σ_B–map for the Hub-N, which represents the relative significance of the magnetic field tension force against gravity, following equation 2.5, where $\Sigma_B > 1$ or $\Sigma_B < 1$ indicate that the magnetic field can or cannot prevent the gravitational collapse, respectively. According to Fig. 2.8, $\Sigma_B < 1$ both east and west of the CSO 350 μm dust emission peak, and also throughout most of the inner hub area, and hence gravity dominates over the magnetic field force. Values of $\Sigma_B \simeq 1$ (and slightly larger) are found along a very confined structure, that is, along the north–south ridge, where $\Sigma_B > 1$ in several positions. We note the clear spatial correlation between $|\delta|$ and Σ_B-maps. Large values in $|\delta|$ generally also mean large values in Σ_B, and low values in $|\delta|$ are associated with low values in Σ_B . This fact confirms the angle $|\delta|$ as a diagnostic to measure the dynamical role of the magnetic field.

In summary, for Hub-N the analysis of the intensity gradient together with the $|\delta|$ and Σ_B maps indicate that, in general, gravity dominates the magnetic field. The intensity gradient is parallel to the magnetic field lines, both east and west of the dust emission peak, with the magnetic field being perpendicular to the major axis of the hub-filament system, suggesting that magnetic field is channeling material toward the central ridge or that the B-field is being dragged by gravity. On the other hand, this ridge appears to be dominated by the magnetic field ($\Sigma_B > 1$). When approaching the dust continuum peak, such uniform distribution is somewhat perturbed, with the magnetic field

being roughly perpendicular to the intensity gradient. In Hub-S, although the computation of the $|\delta|$ and Σ_B maps is less viable because of the more disconnected and isolated polarization detections, we clearly see that the magnetic field points toward each of the two minima identified in the intensity gradient map, which coincides with the most massive dust cores identified at high angular resolution. This scenario is compatible with the interpretation that the gravitational collapse is dragging the magnetic field toward the collapsing cores.

2.5.3. Magnetic Field Strength

In a previous work, Busquet et al. (2016) investigated the interplay between the different agents acting on the fragmentation process in the two hubs of the IRDC G14.2. These latter authors investigated the underlying density and temperature structure of these hubs and find remarkably similar physical properties. Additionally, all the inferred physical parameters, such as the level of turbulence and the magnetic field strength, are notably similar as well. However, it is important to point out that the magnetic field strength in Busquet et al. (2016) was obtained by scaling the magnetic field inferred from near-infrared $H-$band observations of interstellar polarization of background starlight (Santos et al., 2016), which traces the magnetic field in the diffuse gas surrounding the filaments and hubs of the IRDC complex. The CSO 350 μm dust polarization data provide the magnetic field distribution penetrating into the dense infrared-dark area, and therefore provide a more accurate estimation of the magnetic field strength deep into the hubs. It is important to mention that the magnetic field strength in Hub-N was estimated using a $3\sigma_p$ threshold whereas a threshold of $2\sigma_p$ was adopted for Hub-S as it contained fewer polarimetric detections. Furthermore, all calculations related to the magnetic field strength and derived magnitudes are restricted to an area of 0.15 pc in radius (centered on the phase center of the SMA maps) for consistency with Busquet et al. (2016).

Method I: Davis-Chandrasekhar–Fermi (DCF)

The magnetic field strength in the plane of the sky ($B_{\rm pos}$) can be estimated from the DCF technique (Davis, 1951b; Chandrasekhar and Fermi, 1953b) using Equation 2 of Crutcher et al. (2004):

$$B_{\rm pos} = Q\sqrt{4\pi\rho}\frac{\sigma_{\rm 1D,nth}}{\sigma_{\rm P.A.}} \approx 9.3\frac{\sqrt{n(\rm H_2)}\Delta v}{\langle\sigma_{\rm P.A.}\rangle}\,\mu G \tag{2.6}$$

where ρ is the gas density, $\sigma_{\rm 1D,nth}$ is the turbulent velocity dispersion, $\sigma_{\rm P.A.}$ is the dispersion in polarization position angles (in degrees), $n(\rm H_2)$ is the molecular hydrogen number density (in $\rm cm^{-3}$), $\Delta v = \sigma_{\rm 1D,nth}\sqrt{8\ln(2)}$ (in km $\rm s^{-1}$) is the FWHM line width. We included the numerical correction factor $Q = 0.5$ (Ostriker, Stone, and Gammie, 2001), which yields a good estimation of the $B_{\rm pos}$ strength when the dispersion in polarization angles is $< 25°$.

Table 2.2 reports the relevant physical parameters inferred in Busquet et al. (2016) that have been used to obtain the magnetic field strength, the mass-to-flux ratio and the Alfvén Mach number (see Section 2.5.4).

In Table 2.2 we list the magnetic field strength computed using the DCF technique for Hub-N/Hub-S, finding of 0.8/0.2 mG, respectively. The uncertainties in $B_{\rm pos}$ were estimated by propagating the errors in Δv, $n(\rm H_2)$ and $\sigma_{\rm P.A.}$ resulting in an error of a factor of ~2/1.5, i.e. ± 0.8/0.1 mG for Hub-N/Hub-S respectively. In Table 2.2, we also show the magnetic field angular dispersion for both Hub-N (~ 7.8°) and Hub-S (~ 29°) computed as the standard deviation. Due to large dispersion in Hub-S (larger than 25°), we can consider this result as an upper limit given the numerical

correction factor assumed (Q=0.5). In addition, further analyzing Hub-S is not yet conclusive with the present polarization data due to their rather disconnected and isolated detection.

We included the modified DCF technique developed by Heitsch et al., 2001, which is no longer dependent on low angle dispersion because it does not use the tangent angle approximation. Table 2.2 summarizes the estimation of the B-field strength in Hub-N, which reaches a slightly lower value than the previous approximation, $B_{\rm pos} \simeq 0.7$ mG. Regarding Hub-S, we find approximately the same value as with the DCF technique (0.1 mG).

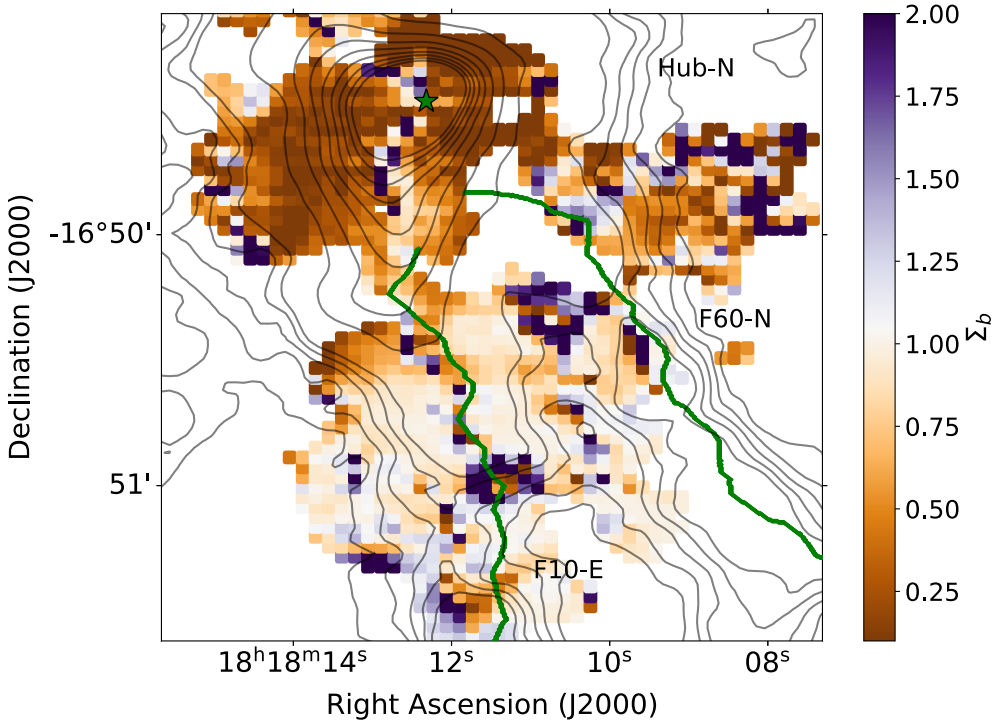

Figure 2.8: Spatial distribution of the B-field-to-gravity force ratio, Σ_B, toward Hub-N. Contour levels, symbols and lines are the same as in Fig. 2.7. We note that while in the hub there is a smooth transition of the values of Σ_B, in the boundaries of the hub and in the south of the map there are pixels with outliers. In these region there is a noisy intensity gradient (see Fig. 6), likely due to the absence of a dominant center of gravity at these positions.

Method II: Polarization - Intensity Gradient technique

According to the method illustrated in Section 2.5.1, we proceed to estimate the magnetic field strength based on the relative orientation between local magnetic field and the estimated local gravity field applying the following equation:

$$\left[\frac{B_{pos}}{G}\right] = \sqrt{\frac{sin\psi}{sin\alpha}\left(\nabla P + \rho \bigtriangledown \phi\right).4\pi R} = \sqrt{\Sigma_B\left(\nabla P + \rho\nabla\phi\right)4\pi R}. \quad (2.7)$$

where density (ρ) is in g cm^{-3}, gravitational potential gradient ($\nabla\phi$) is in cm s^{-2} , and B-field curvature radius (R) is in cm, resulting B-field in Gauss. Here, Σ_B is the magnetic field significance shown in Section 2.5.1. For simplicity, we neglected the pressure gradient (∇P) which is typically small compared to gravity potential.

Table 2.2: Physical properties of the two hubs

Source	$N_{\rm mm}$ [a]	$M_{0.15\rm pc}$ [b] ($M_\odot$)	$n_{0.15\rm pc}$ [b] ($\times10^5$cm^{-3})	$\sigma_{\rm 1D,nth}$ [c] (km s^{-1})	$\langle$ PA $\rangle$ [d] (°)	σ_{PA} [d] (°)	$B_{\rm DCF}$ [e] (mG)	$B_{\rm DCF}^{\rm mod}$ [f] (mG)	$B_{\rm P-IG}$ [g] (mG)	$\lambda_{\rm DCF/mod/P-IG}$ [h]	$\mathcal{M}_{\rm A-DCF/mod/P-IG}$ [h]
Hub-N	4	126	1.3	0.83 ± 0.04	~ 102	~ 7.8	~ 0.8	~ 0.7	~ 0.6	0.3 / 0.4 / 0.4	0.3 / 0.4 / 0.4
Hub-S	13	105	1.1	0.88 ± 0.02	~ 84	~ 29	~ 0.2	~ 0.1	–	1.1 / 1.6	1.1 / 1.6

[a] $N_{\rm mm}$ is the number of fragments detected at 1.3 mm within a field of view of 0.3 pc of diameter (Busquet et al., 2016).
[b] Mass and average density within a radius of 0.15 pc inferred by modeling the SED and the radial intensity profile (Busquet et al., 2016).
[c] Nonthermal turbulent component of the velocity dispersion obtained from NH_3 (1,1) data, averaged over the 0.15 pc area. (Busquet et al., 2013; Busquet et al., 2016).
[d] Average magnetic field position angle and dispersion computed as the standard deviation.
[e] Magnetic field in the plane of the sky estimated using the DCF method.
[f] Magnetic field in the plane of the sky estimated using the modified DCF method (Heitsch et al., 2001).
[g] Magnetic field in the plane of the sky estimated using the polarization–intensity gradient method (Koch, Tang, and Ho, 2012a)
[h] Mass-to-magnetic-flux ratio and Alfvén Mach number estimated using $B_{\rm DCF}$, $B_{\rm DCF}^{\rm mod}$, and $B_{\rm P-IG}$

Although we have restricted our calculations to an area of 0.15 pc of radius around the emission peak the gravitational potential at each point within this area is generated considering the contribution of all points on the map. The curvature C is computed from Eq. 2.8 (Koch, Tang, and Ho, 2012a, see q. 6).

$$C \equiv \frac{1}{R} = \frac{2}{d}\cos\left(\frac{1}{2}\left[\pi - \Delta PA\right]\right), \tag{2.8}$$

where d is the separation between two neighboring magnetic field segments and Δ PA is the difference between their position angles. The magnetic field strength is obtained using the average values of the volume density (see Table 2.2) over the area enclosed within 0.15 pc from the Hub-N center, together with Σ_B (0.7), and the field radius (1.3×10^{18} cm).

In Table 2.2 we present the estimation of the magnetic field strength in Hub-N obtained with this method, finding ~0.6 mG. This value is consistent with the magnetic field estimated through the DCF method (~0.8 mG, Sec 2.5.3). Regarding Hub-S, as we explain in the previous section, the present polarization data do not allow us to perform a similar study.

2.5.4. Mass-to-flux Ratio and Turbulence

The relevance of the magnetic force with respect to gravitational force can also be estimated by the mass-to-magnetic-flux ratio, stated in units of the critical value,

$$\lambda = \frac{(M/\Phi)_{\rm observed}}{(M/\Phi)_{\rm crit}} = 2.6\times10^{-21}\left[\frac{N(\rm H_2)}{\rm cm^{-2}}\right]\left[\frac{B_{\rm pos}}{\mu G}\right]^{-1}, \tag{2.9}$$

where we have applied a correction of one-third, which considers the statistical projection effects (see Crutcher et al., 2004).

In order to compare the role of the magnetic field between the two cores and to compare different magnetic field strength estimation as well, we used different $B_{\rm pos}$ values derived from both the standard DCF, the modified DCF relation, and the polarization–intensity gradient technique. We used the column density estimated by Busquet et al., 2016 within the 0.15 pc radius ($N(H_2)$= 1.1 or 0.9×10^{23} cm^{-2} for Hub-N or Hub-S, respectively)

The mass-to-flux ratio is calculated for the three different estimates of the magnetic field strength given in Table 2.2. For the Hub-N we obtain a value of λ between 0.3 and 0.4 (Table 2.2). For this hub, we can also calculate the mass-to-flux ratio using the Polarization-Intensity Gradient method, which is totally independent of the estimation of the magnetic field. From Eq. 8 in Koch, Tang, and Ho (2012b):

$$\left(\frac{M}{\Phi}\right)_{norm} = \left\langle \Sigma_B^{-1/2} \right\rangle \left(\frac{R}{R_o}\right)^{-3/2} \pi^{-1/2} \tag{2.10}$$

where R_0=R is the cloud radius.

Through this method we find a value of ~ 0.7 which is about twice the value found previously, but still subcritical, that is, the magnetic field can hold the gravitational collapse. For Hub-S, the resulting mass-to-flux ratio from Eq. 2.9 is between 1.1 and 1.6, which three to four times higher than in Hub-N. Hub-S is therefore magnetically supercritical. Regarding the absolute value of λ, this is probably underestimated because the magnetic field average along the line of sight is not taken into account, which is probably more severe around the hub center (e. g., Houde et al., 2009). Indeed, the Hub-N Σ_B map shows values lower than 1 in most of the hub. In addition, both hubs show clear signs of active and ongoing star formation revealed by the presence of H_2O and CH_3OH masers (Jaffe, Guesten, and Downes, 1981; Wang et al., 2006; Sugiyama et al., 2017), infrared sources (Povich et al., 2016), and molecular outflow activity (Busquet, private communication). This is an indication that the two hubs are supercritical.

Finally, to assess the importance of turbulence with respect to the magnetic field, we estimated the Alfvén Mach number, $\mathcal{M}_{\rm A}$, expressed as $\mathcal{M}_{\rm A} = \sqrt{3}\sigma_{\rm 1D,nth}/v_{\rm A}$, where $v_{\rm A} = B_{\rm tot}/\sqrt{4\pi\rho}$ is the Alfvén speed. The uncertainty in the Alfvén Mach number is the same as the uncertainty in $\sigma_{\rm P.A.}$. As can be seen in Table 2.2, $\mathcal{M}_{\rm A} < 1$ in Hub-N, indicating sub-Alfvénic conditions and therefore that magnetic energy dominates over turbulence. Similar results have been found in other IRDCs (e. g., Pillai et al., 2015; Soam et al., 2019). On the contrary, $\mathcal{M}_{\rm A} > 1$ in Hub-S (i. e., super-Alfvénic conditions), and therefore turbulence could play a more important role in this region.

2.6. Discussion

With the present study we show that the magnetic field orientation in Hub-N is relatively uniform along the east–west direction, being perpendicular to the major axis of the hub–filament system. Overall, based on the polarization–intensity gradient technique, we conclude that the magnetic field probably cannot prevent gravitational collapse, except in the north–south ridge where $\Sigma_B > 1$ in some positions. Hub-S, on the other hand, presents a bimodal magnetic field distribution, in which each component converges toward each local minimum identified with the intensity gradient map. At larger distances from the hub, the magnetic field appears perpendicular to the dense filaments.

Our aim is to investigate the relevance of the magnetic field in hub–filament systems and the fragmentation processes that they undergo to form star clusters. In this section, we first discuss our magnetic field strength estimation, which was derived using three different methods, and the role of the magnetic field at different scales, from the large-scale hub–filament system down to the 0.1 pc scale. We use this information to assess the role of the magnetic field in producing different fragmentation levels in these two hubs.

2.6.1. Magnetic field strength estimation

In this work we present three different estimations of the magnetic field strength based on the DCF (Davis, 1951b; Chandrasekhar and Fermi, 1953b), the modified DCF method presented by Heitsch et al., 2001, and the polarization–intensity gradient technique (Koch, Tang, and Ho, 2012a).

In Hub-N, the three estimates of the magnetic field lead to consistent results, with values of between 0.6 and 0.8 mG. The largest value is provided by DCF, as you would expect from an upper limit of the magnetic field (see Section 2.5.3).

To compare the magnetic field in both Hubs we use the DCF and modified DCF methods. Unlike the results found by Busquet et al. (2016), who found similar values for the magnetic field in both hubs, we find a stronger magnetic field in Hub-N than in Hub-S by a factor of approximately equal to or less than four. It is important to note that we only considered an area of 0.15 pc radius around the peak emission in both hubs. Therefore, we restrict the calculation to the area where we have more detections, especially in Hub-S.

2.6.2. Gravity and Magnetic field forces

Recent results obtained with the *Planck* satellite have shown that magnetic fields in the solar-neighborhood molecular clouds tend to be parallel to low density structures and perpendicular to high column density structures (Planck Collaboration et al., 2016; Soler, 2019). Numerical simulations under the scenario of global, hierarchical gravitational collapse (e. g., Gómez and Vázquez-Semadeni, 2014; Vázquez-Semadeni et al., 2019) predict that filaments gain their mass from their surrounding material that flows down to the gravitational potential (i. e., a clump or hub). The magnetic field is dragged by the collapsing material, following the accretion flow that feeds the filament, that is why the magnetic field tends to be oriented mostly perpendicular to the filaments (Gómez, Vázquez-Semadeni, and Zamora-Avilés, 2018). Within dense filaments, Gómez, Vázquez-Semadeni, and Zamora-Avilés (2018) point out that the magnetic field lines would bend, into the filament, due to the flow toward the hub showing a characteristic 'U' shape. Such longitudinal accretion flows along filaments have been actually observed in several filamentary regions (e. g., Kirk et al. 2013; Fernández-López et al. 2014, in Serpens South, Peretto et al. 2014, in SDC 13, Lu et al. 2018, in eight filamentary high-mass star-forming clouds), while magnetic fields oriented parallel to dense filaments have been recently observed in a few regions (Monsch et al., 2018; Liu et al., 2018; Pillai et al., 2020).

In this work, we assume that the intensity gradient of the 350 μm emission is an approximation of the inertial term in the MHD equation (left-hand term in Eq. 2.1) which can trace the flow of matter. Based on the kinematics of the N_2H^+ (1–0) line, Chen et al. (2019b) find large-scale velocity gradients along the filament, ~ 0.5 km s^{-1} pc^{-1}, indicative of inflow motions toward the two hubs that harbor deeply embedded protoclusters, with a mass accretion rate along the filaments of $\sim 10^{-4}\,M_\odot\,\mathrm{yr}^{-1}$. Figure 2.7 (right panel) shows the relative orientation between the position angles of the magnetic field and the intensity gradient in Hub-N. At large distances from the hub–filament system, the magnetic field is roughly parallel to the intensity gradient ($|\delta| \simeq 0$), becoming perpendicular as it enters the densest parts of both filament and hub. This situation is consistent with a scenario in which filaments are accreting gas material from their surrounding environment and the flow of matter onto the filament drags the magnetic field. Indeed, both east and west of Hub-N and F10-E, the gravity force dominates over magnetic fields (see Fig. 2.8), in agreement with numerical simulations under the scenario of GHC (e. g., Gómez, Vázquez-Semadeni, and Zamora-Avilés, 2018; Vázquez-Semadeni et al., 2019).

Despite the presence of inflow motions within the two filaments converging toward Hub-N (Chen et al., 2019b), the magnetic field in the dense regions appears to be perpendicular to the intensity gradient (i. e., perpendicular to the gas flow). From Fig. 2.6 (upper panel) it is clear that the magnetic field in the dense filament does not significantly change its orientation. This might be because the CSO observations lack the necessary resolution to fully resolve the spine of the filaments seen in N_2H^+ and could be indicative of an underlying complex B-field morphology. There

is a slight tendency of the magnetic field to appear distorted, although we cannot distinguish the U-shaped magnetic field structure predicted by Gómez, Vázquez-Semadeni, and Zamora-Avilés (2018). This could be explained by the lack of resolution in our CSO 350 μm observations, where $10''$ at 1.98 kpc corresponds to $\sim$ 0.1 pc, whereas the numerical simulations of Gómez, Vázquez-Semadeni, and Zamora-Avilés (2018) were performed with a spatial resolution of 1.2×10^{-4} pc. Under this hypothesis, the magnetic field is expected to be more complex at smaller scales.

Another plausible explanation for the lack of the U-shaped magnetic field could be found in terms of optical depth effects. The 350 μm polarization data might trace an upper layer and might not penetrate equally as deep as N_2H^+ and NH_3. In addition, simulations show that this U-shaped structure is more pronounced as density increases. It is interesting to mention that in the simulations of Gómez, Vázquez-Semadeni, and Zamora-Avilés (2018) the accretion flow within filaments takes place where the magnetic field is weaker. Our results from Fig. 2.8 suggest that the magnetic field seems to dominate over gravity along a north–south ridge encompassing the CSO 350 μm dust emission peak that harbors the primary dust core detected at high angular resolution (Busquet et al., 2016; Ohashi et al., 2016). This could indicate that the gas flow follows the magnetic field, or, alternatively, that the magnetic field structure inside filaments (i. e., at smaller scales) is much more complex (e. g., Li and Klein, 2019). Unfortunately, the current angular resolution does not allow us to disentangle the magnetic field structure within the dense filament. Therefore, dust polarization observations at higher angular resolution (e.g. ALMA) are required to further investigate the magnetic field structure within dense filaments and cores and its specific role in channeling material from the dense filament toward the embedded protocluster.

It is interesting to mention that in Fig. 2.8, and especially in Fig. 2.7, the region in which the relative orientation of the intensity gradient and the magnetic field is roughly parallel (i.e., $|\delta| \simeq 0$) seems to converge towards the position of the central dust continuum core MM1a (Busquet et al., 2016). This supports the idea that MM1a is accreting material from the environment east and west of the central core. In addition, as indicated by the velocity gradients detected along the filament's longer axis (Chen et al., 2019b), gas flows through the filament to the hub. Therefore, in Hub-N we have large-scale accretion from the east and west and an accretion flow through the filament to the hub in the south to north direction.

2.6.3. Fragmentation and magnetic field properties toward the hubs

In a previous study, Busquet et al. (2016) found that the two hubs in the IRDC G14.2 present different levels of fragmentation. By extrapolating the magnetic field strength obtained at infrared wavelengths that trace the diffuse gas to the dense hubs harboring a deeply embedded protocluster, Busquet et al. (2016) obtain similar values of the magnetic field, mass-to-flux ratio, and Alfvén Mach number in both hubs. Now, thanks to the submillimeter CSO polarization data we can penetrate deeper into the hub–filament system. As shown in Section 4.3, we find some differences in the magnetic field strength between both hubs, namely greater strength toward Hub-N. As a consequence, the mass-to-flux ratio and the Alfvénic Mach number are also different. While Hub-N seems to have sub-Alfvénic conditions, Hub-S presents super-Alfvénic conditions, indicating that turbulence plays a greater role than the magnetic field, at least at the scales traced by the CSO observations (~0.1 pc). These conditions are different from those inferred by Busquet et al. (2016), in which the magnetic field was estimated to be of the same order as in Hub-N and to display sub-Alfvénic conditions.

Palau et al., 2013 investigate the fragmentation of massive dense cores down to $\sim$ 1000 au by comparing high-angular-resolution and high-sensitivity observations with the radiation magneto-hydrodynamic simulations of Commerçon, Hennebelle, and Henning (2011). In this work, the

highly magnetized cores show low fragmentation while the weakly magnetized cores present a higher fragmentation level. Recently, Fontani et al. (2016) and Fontani et al. (2018) find that fragmentation is inhibited when the initial turbulence is low (sonic Mach number $\mathcal{M} \sim 3$), independently of the other physical parameters. In addition, these latter authors point out that a filamentary distribution of the fragments is favored in a highly magnetized clump, while other morphologies are also possible in a weaker magnetic field scenario. In any case, Fontani et al. (2016) show that the weakly magnetized simulations display more fragments.

In the two hubs of IRC G14.2, the different levels of fragmentation could be explained by the different values of magnetic field strength. Both hubs share some physical properties such as the internal structure of the envelope (temperature and density distribution) where the fragments are embedded, and similar Mach number, $\mathcal{M} \simeq 6$ (Busquet et al., 2016). The lower fragmentation level observed toward Hub-N, together with the homogeneous and well aligned magnetic field structure, the derived values of mass-to-flux ratio, and $\mathcal{M}_{\rm A}$, favors a scenario in which the magnetic field plays an important role in regulating the collapse and fragmentation processes in these two hubs, possibly by slowing down the star formation process.

In a very recent work, Palau et al. (2020) estimate the magnetic field strength and fragmentation level in a sample of massive dense cores, and find that fragmentation level seems to correlate with core density, although with significant scatter, while there is no correlation with magnetic field strength. The correlation of fragmentation level with density, which is consistent with previous works (e. g., Gutermuth et al., 2011; Palau et al., 2014; Mercimek et al., 2017; Sanhueza et al., 2019), suggests that gravity plays an important role in the fragmentation process. However, for those cores with similar densities in the Palau et al. (2020) sample, the magnetic field strength is greater in the cores with lower fragmentation, and the different magnetic field strengths could explain the scatter in the fragmentation-versus-density relation. Thus, the magnetic field seems to have a modulating effect to the dominant role of gravity. The work presented here is fully consistent with the results of Palau et al. (2020), as the two hubs in G14 present similar densities and the magnetic field seems to be larger for Hub-N where fragmentation is lower.

Finally, it is interesting to look at the immediate surroundings of these two hubs in order to investigate whether or not the environment could lead to different levels of fragmentation. On the one hand, the HII region IRAS 18153−1651 lies in the vicinity of Hub-N, with a bolometric luminosity of $\sim 10^4$ $L_\odot$ (Jaffe, Stier, and Fazio, 1982). Recent optical spectroscopic observations reveal that this IRAS source consists of two main sequence stars of spectral type B1 and B3 and that the HII indeed contains a recently formed star cluster (Gvaramadze et al., 2017). Moreover, Gvaramadze et al. (2017) report the discovery of an optical arc nebula located at the western edge of the IRAS source, which was interpreted as the edge of the photoionzing wind bubble blown by the B1 star. This one-sided appearance could result from the interaction between the bubble and the photoevaporation flow from the molecular gas associated with Hub-N and its associated filaments (Gvaramadze et al., 2017). The presence of this wind bubble powered by the HII region could compress the gas and produce the observed uniformity of the magnetic field, similarly to the Pipe Nebula where the highly magnetized regions with a uniform magnetic field arise from gas compression due to the collision of filaments (Frau et al., 2015), consistent with the findings of Busquet et al. (2013), where higher temperatures were measured at the eastern edge of Hub-N.

Regarding the dense gas surrounding the hubs, both hubs display a network of filaments that seem to converge into the hubs. However, in the northern part, the hub–filament system consists of a dominant filament in the north–south direction with a clear velocity gradient along the filament's longer axis that transports material into Hub-N (Chen et al., 2019b). Hub-S on the other hand presents a more complex network of filaments, with one filament coming from the east and another filament that approaches the northern part of the hub from the southwest with redshifted velocities

(Busquet et al., 2013; Chen et al., 2019b). We cannot discard that such a distribution is reflecting a projection effect, where the more complex filament distribution in the south (Busquet et al., 2016; Chen et al., 2019b) is smearing out the magnetic field observed by an averaging effect at the current CSO scale. Clearly, this scenario should be further investigated through interferometric observations (SMA, ALMA) with higher sensitivity polarization data to trace the magnetic field around the whole IRDC complex.

2.7. Summary and Conclusions

We present the results of CSO 350 μm dust polarization observations toward Hub-N and Hub-S in the IRDC G14.225-0.506 and an analysis of the polarization–intensity gradient using the method developed by Koch, Tang, and Ho (2012a). The main findings of this work can be summarized as follows.

1. Toward Hub-N, we find an almost uniform magnetic field orientation in the east–west direction, which is nearly perpendicular to the major axis of the hub-filament system. However, in Hub-S the magnetic field presents a bimodal distribution, with one component going from the northeast to the southwest and the other component going from the northwest to the southeast.

2. The intensity gradient in Hub-N presents a single local minimum coinciding with the bright dust continuum core MM1a, and the prevalent east–west magnetic field orientation slightly deviates when approaching the dust core. In Hub-S, the intensity gradient reveals two minima, reflecting the bimodal distribution of the magnetic field, as each component points toward one of the two intensity gradient minima. This result suggests a scenario in which the magnetic field is dragged by the collapsing cores.

3. The analysis of the $|\delta|$ and Σ_B maps in Hub-N indicates that, near the hubs, gravity dominates the magnetic field. The intensity gradient is parallel to the magnetic field lines both east and west of the hub, suggesting that the magnetic field is channeling material toward the central ridge or that the B-field is being dragged by gravity. We find that magnetic field segments do not change their direction into the filament. However, this could be due to the relatively coarse CSO resolution which falls short of resolving the B-field morphology in the close vicinity around the spine of the filaments. Combined with the velocity information from previous works, in Hub-N we see large-scale accretion from the east and west toward the central dust core and the accretion flow within the main filament (in the south–north direction) that feeds the hub.

4. We find higher values of the magnetic field strength in Hub-N than in Hub-S. This supports the idea that the different levels of fragmentation in these two hubs could result from differences in the magnetic field. However, we do not find an extreme difference between the magnetic field characteristics of the two hubs. Therefore, key differences could be found in the environment, perhaps in the influence of the nearby HII, region in Hub-N or in the more complex distribution of filaments in Hub-S.

In summary, our analysis of the magnetic field in the two hubs of the IRDC G14.2 reveals that the magnetic field could play a role in the fragmentation process and in the formation and evolution of dense filaments. Further observations of dust polarization with higher sensitivity and at higher angular resolution are needed to further investigate the magnetic field structure within the dense filaments and at core scales.

A. G14.2 observations details

In this section we expand the information on the CSO observations. Figure 9 shows the different pointings conducted toward the science target (in white), and off-beam positions (in magenta and cyan) for both Hub-N (upper panel) and Hub-S (bottom panel). The pointing coordinates of the science target are listed in Table 3.

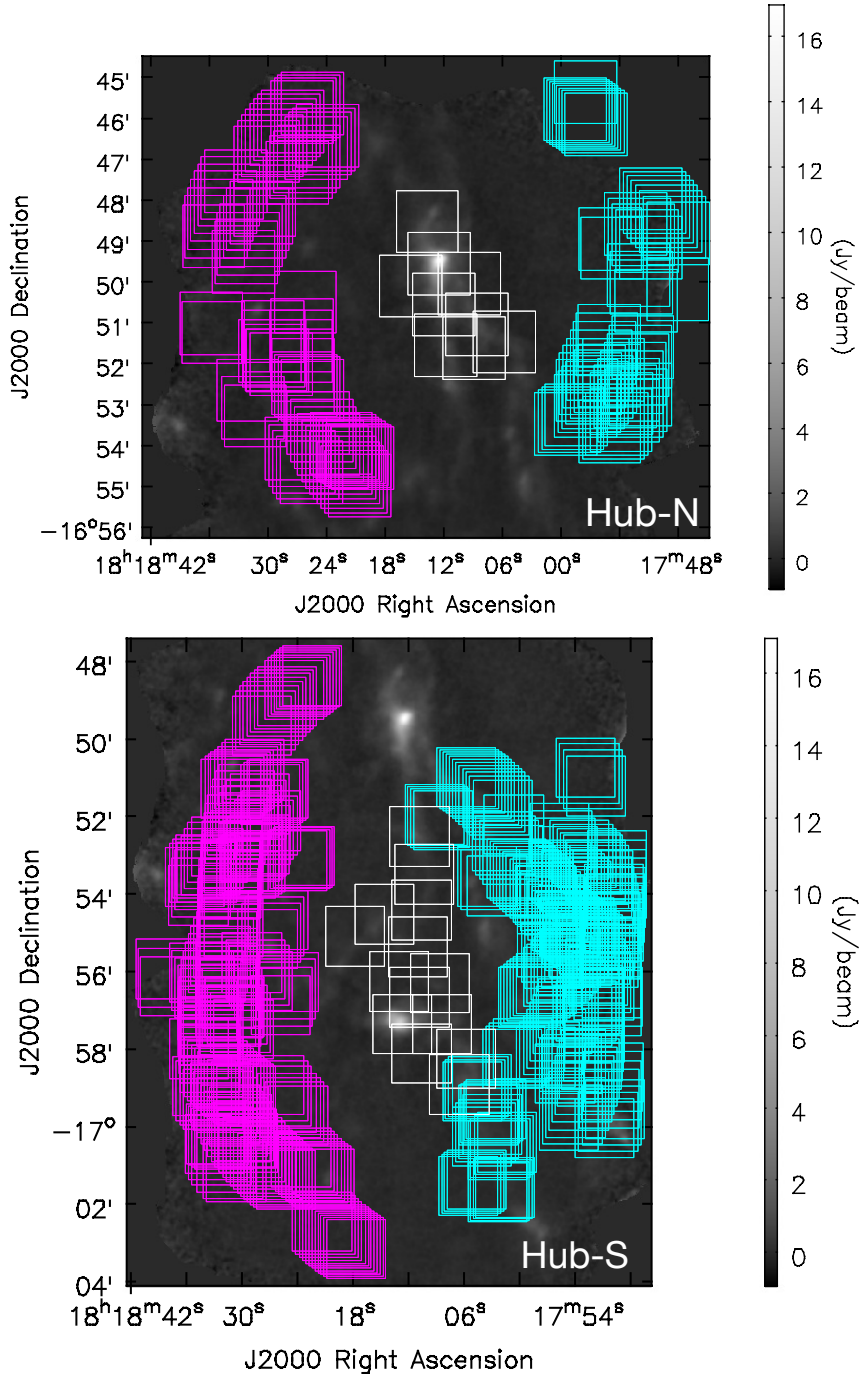

Figure 9: Pointings for SHARP observations. White square depict the fields of view that make up the mosaic about the source (corresponding to Table 3). Magenta and cyan square show the off-beam positions. Upper and bottom panel represents pointings toward the Hub-N and Hub-S respectively.

Table 3: Pointings of the CSO SHARP observations in G14.2

ID	R.A. (J2000)	Decl. (J2000)
Hub N		
g14 n1	$18^h18^m13^s630$	-16°48′30.″40
g14 n2	$18^h18^m12^s480$	-16°49′31.″90
g14 n3	$18^h18^m12^s060$	-16°50′31.″90
g14 n4	$18^h18^m11^s697$	-16°51′31.″90
g14 n5	$18^h18^m08^s615$	-16°51′01.″50
g14 n6	$18^h18^m08^s980$	-16°51′36.″00
g14 n7	$18^h18^m09^s451$	-16°50′01.″50
g14 n8	$18^h18^m15^s302$	-16°50′04.″50
g14 n9	$18^h18^m10^s705$	-16°48′48.″00
g14 n10	$18^h18^m05^s689$	-16°51′26.″99
Hub S		
g14 s1	$18^h18^m17^s080$	-16°57′19.″90
g14 s2	$18^h18^m12^s790$	-16°57′19.″90
g14 s3	$18^h18^m08^s450$	-16°57′19.″90
g14 s4	$18^h18^m05^s783$	-16°58′13.″81
g14 s5	$18^h18^m10^s632$	-16°58′05.″12
g14 s6	$18^h18^m10^s875$	-16°56′38.″16
g14 s7	$18^h18^m06^s554$	-16°58′53.″42
g14 s8	$18^h18^m15^s238$	-16°56′38.″16
g14 s9	$18^h18^m18^s996$	-16°56′43.″48
g14 s10	$18^h18^m13^s056$	-16°56′13.″81
g14 s11	$18^h18^m17^s541$	-16°55′56.″42
g14 s12	$18^h18^m14^s632$	-16°58′01.″65
g14 s13	$18^h18^m20^s571$	-16°56′06.″85
g14 s14	$18^h18^m14^s719$	-16°55′27.″92
g14 s15	$18^h18^m17^s645$	-16°55′03.″92
g14 s16	$18^h18^m14^s719$	-16°54′29.″42
g14 s17	$18^h18^m10^s956$	-16°55′20.″42
g14 s18	$18^h18^m10^s642$	-16°54′23.″42
g14 s19	$18^h18^m10^s329$	-16°53′27.″92
g14 s20	$18^h18^m10^s747$	-16°52′29.″42
g14 s21	$18^h18^m08^s760$	-16°56′15.″92

Table 4: Observing scans of CSO/SHARP observations

Integration ID 2015 June 09-10	Pointing	$\tau_{350\mu m}$	Source parallactic angle -Calibrator FWHM	Integration ID 2015 June 12-13	Pointing	$\tau_{350\mu m}$	Source parallactic angle -Calibrator FWHM
61848-61849	IRAS 16293-2422		∼12.5″	62023-62024	IRAS 16293-2422		11.5″
61850-61853	g14 s2	1.3-1.6	−30° – −23°	62028	IRAS 16293-2422		12″
61854-61857	g14 s2	1.6-1.9	−21° – −13°	62029-62032	g14 s14	0.8-1.2	−57° – −54°
61858-61861	g14 s2	1.0-2.0	−11° – −3°	62033-62036	g14 s15	1.2-1.4	−53° – −50°
61862-61865	g14 s2	2.0-2.1	1° – 9°	62037-62040	g14 s16	1.3-1.5	−48° – −44°
61866-61869	IRAS 16293-2422		∼12.0″	62041	IRAS 16293-2422		12.3″
61870-61873	g14 s2	2.1-2.4	21° – 28°	62042-62045	g14 s17	1.5-1.7	−41° – −35°
61874-61877	g14 s2	1.8-2.4	30° – 36°	62046-62049	g14 s18	1.8-2.2	−33° – −27°
61878-61881	g14 s2	1.8-2.0	38° – 43°	62050-62053	g14 s19	1.6-1.7	−25° – −18°
61882-61885	g14 s2	∼2.1	44° – 49°	62054-62057	g14 s19	1.2-1.5	−15° – −7°
61886-61889	g14 s2	2.1-2.3	50° – 53°	62058-62061	g14 s19	∼1.4	−4° – 4°
61890-61892	Neptune		∼8.8″	62066-62069	g14 s16	1.4-1.5	18° – 25°
2015 June 10-11				62077	Neptune		8.3″
61893-61898	IRAS 16293-2422		∼15″	62078-62081	g14 s15	1.3-1.6	41° – 45°
61899-61902	g14 n2	0.9-1.9	−44° – −39°	62082-62085	g14 s15	∼1.6	47° – 51°
61903-61906	g14 n2	0.7-1.9	−37° – −31°	62086-62089	g14 s15	1.6-1.7	52° – 55°
61907-61910	g14 n3	0.9-1.0	−29° – −22°	62090	Neptune		8.6″
61911-61914	g14 n3	∼1.0	−20° – −12°	2015 June 14-15			
61916-61919	g14 n5	0.8-1.0	2° – 10°	62092-62093	IRAS 16293-2422		11.7″
61924-61927	g14 n6	0.7-0.8	23° – 30°	62098-62101	g14 s20	1.2-1.3	−56° – −53°
61928-61931	g14 n6	0.6-0.8	32° – 37°	62106-62109	g14 s20	1.5-1.7	−47° – −42°
61932-61935	g14 n1	0.5-0.8	39° – 44°	62110-62113	g14 s20	∼1.5	−40° – −37°
61941-61944	g14 n1	0.3-0.8	62° – 55°	62114-62117	g14 s14	1.4-1.7	−33° – −27°
61947-61949	Neptune		∼8.8″	62118-62121	g14 s14	1.4-1.5	−24° – −17°
2015 June 11-12				62122-62125	g14 s18	1.6-1.8	−14° – −6°
61952-61953	IRAS 16293-2422		∼12.5″	62126-62129	g14 s18	1.7-2.0	−4° – 5°
61955-61958	g14 s2	0.5-0.6	−60° – −58°	62130-62133	g14 s17	1.6-2.0	8° – 15 °
61959-61962	g14 s1	0.5-0.6	−57° – −53°	62134-62137	g14 s17	1.5-1.7	18° – 25°
61963-61966	g14 s8	0.42-0.48	−52° – −49°	62138	IRAS 16293-2422		11.0″
61967-61968	IRAS 1693-2422		∼11.5″	62144-62147	g14 s21	1.2-1.6	38° – 43°
61969-61972	g14 s9	0.5-0.6	−44° – −40°	62148-62151	g14 s7	1.3-1.5	45° – 49°
61977-61980	g14 s3	0.6-0.7	−32° – −25°	62156-62159	g14 s7	0.6-1.2	55° – 58°
61981-61984	g14 s4	0.5-0.6	−24° – −16°	62161	Neptune		8.9″
61985-61988	g14 s5	∼0.7	−14° – −6°	2015 June 17-18			

Table 4: Observing scans of CSO/SHARP observations

Integration ID 2015 June 09-10	Pointing	$\tau_{350\mu m}$	Source parallactic angle -Calibrator FWHM	Integration ID 2015 June 12-13	Pointing	$\tau_{350\mu m}$	Source parallactic angle -Calibrator FWHM
61989-61992	g14 s6	0.6-0.8	-3° – 6°	62162-62163	IRAS 16293-2422		12.0″
61993-61996	g14 s10	0.6-0.7	9° – 16°	62162-62167	g14 n2	1.2-1.5	-52° – -48°
61997-62000	g14 s5	0.6-0.7	19° – 26°	62168-62171	g14 n7	∼1.4	-44° – -42°
62005-62008	g14 s11	0.6-1.3	37° – 40°	62172	IRAS 16293-2422		11.5″
62009-62012	g14 s3	0.6-0.7	44° – 48°	62173-62176	g14 n7	1.4-1.5	-38° – -33°
62013-62016	g14 s3	0.5-0.6	49° – 53°	62177-62180	g14 n8	1.4-1.6	-31° – -24°
62017-62020	g14 s13	0.5-0.6	54° – 57°	62181-62184	g14 n8	1.6-1.7	-22° – -14°
62021-62022	Neptune		8.8″	62185-62188	g14 n10	1.4-1.7	-11° – -3°
				62189-62192	g14 n10	1.4-1.5	0° – 8°
				62197	IRAS 16293-2422		12.2″
				62198-62201	g14 n10	1.5-1.7	23° – 30°
				62202-62205	g14 n10	1.5-1.7	32° – 38°
				62206-62209	g14 n10	1.4-1.5	40° – 45°
				62210-62213	g14 n10	1.5-1.6	46° – 50°
				62214-62217	g14 n7	1.5-1.7	51° – 55°
				62218-62221	g14 n7	1.5-1.7	56° – 59°

The observations of 2015 June 09-10, 10-11, and 11-12 (HST) are in the left column, while the observations of June 12-13, 13-14, and 17-18 (HST) are in the right column. The J2000 coordinates of the individual pointings can be found from Table 3. Each target source scan consist four integrations which were taken at the waveplate position angles 0°, 22.5°, 45°, and 67.5°, respectively. For target source scans, we list the parallactic angles during the observations. For calibration scans, we instead included the derived source FWHM instead of parallactic angle, which should be ∼12″ and ∼9″ for IRAS 16293-2422 and Neptune, respectively, as long as the seeing is good and the system is well calibrated.

Chapter 3

Modeling the accretion disk around the high-mass protostar GGD 27-MM1

3.1. Overview

Recent high-angular resolution ($\simeq$ 40 mas) ALMA observations at 1.14 mm resolve a compact ($R \simeq 200$ au) flattened dust structure perpendicular to the HH 80–81 jet emanating from the GGD 27-MM1 high-mass protostar, making it a robust candidate for a true accretion disk. The jet/disk system (HH 80–81/GGD 27-MM1) resembles those found in association with low- and intermediate-mass protostars. We present radiative transfer models that fit the 1.14 mm ALMA dust image of this disk which allow us to obtain its physical parameters and predict its density and temperature structure. Our results indicate that this accretion disk is compact ($R_{\rm disk} \simeq$ 170 au) and massive ($\simeq 5\ M_{\odot}$), about 20% of the stellar mass of $\simeq 20\ M_{\odot}$. We estimate the total of the star-disk system from the molecular line emission finding a range between 21 and 30 $M_{\odot}$, which is consistent with our model. We fit the density and temperature structures found by our model with power law functions. These results suggest that accretion disks around massive stars are more massive and hotter than their low-mass siblings, but they still are quite stable. We also compare the temperature distribution in the GGD 27–MM1 disk with that found in low- and intermediate-mass stars and discuss possible implications on the water snow line. We have also carried out a study of the distance based on Gaia DR2 data and the population of young stellar objects (YSOs) in this region, and from the extinction maps. We conclude that the source distance is within 1.2 and 1.4 kpc, closer than what was derived in previous studies (1.7 kpc).

3.2. Introduction

Understanding how high-mass stars form and evolve is one of the hot topics in astrophysics, due to the strong impact that these objects have in the life of a galaxy. However, the study of high-mass protostars is difficult due to their fast evolution ($\sim 10^5$ yr) to the main sequence, their large distances and high obscuration.

It is well known that low-mass stars are formed through an accretion disk that transports gas and dust from the envelope to the protostar and through a jet that removes the excess of angular momentum (Shu, Lizano, and Adams, 1987; McKee and Ostriker, 2007). Disks around nearby solar-type stars have been studied to great extent and detail (e.g. Williams and Cieza, 2011; Testi et al., 2014; Hartmann, Herczeg, and Calvet, 2016; Andrews et al., 2018), but at the moment the number of disks studies of more distant and massive stars is still comparatively very small.

Accretion disks around massive stars is a plausible mechanism that can alleviate the radiation pressure problem, hence allowing an accretion flow to continue once photo-ionization has started (e.g. Tan et al., 2014; Klassen et al., 2016; Kuiper and Hosokawa, 2018). However, their physical properties are still uncertain (see e. g., Beltrán and de Wit, 2016, for a recent review). Flattened, disk-like structures have been observed in a few massive young stars (Beltrán et al., 2011; Beltrán et al., 2014; Sánchez-Monge et al., 2014; Johnston et al., 2015; Sanna et al., 2019; Zapata et al., 2019). However, these structures are large (∼1000–10000 au) and have masses considerably larger than the central protostar and it is difficult to envisage them as real accretion disks. Therefore higher angular resolution and more sensitivity observations are required to better characterize the physical parameters and the role of these rotating structures (e.g. Maud et al., 2019; Ginsburg et al., 2019). Three of the best examples in the literature of massive protostars associated with a clearly defined jet and a compact (few hundred au) angularly resolved dusty disk candidate are: Cepheus A HW2 (Patel et al., 2005), GGD 27-MM1 (Girart et al., 2018), and G11.92-061 MM1a (Ilee et al., 2018).

The HH 80–81 objects (at a distance of 1.4 kpc; see Appendix in this Chapter) are associated with a spectacular (∼ 10 pc long) highly collimated radio-jet (Martí, Rodríguez, and Reipurth, 1993; Heathcote, Reipurth, and Raga, 1998; Masqué et al., 2015), which is powered by a massive early B-type protostar IRAS 18162−2048 (GGD 27-MM1, Fernández-López et al., 2011b; Girart et al., 2017). This protostellar radio-jet is the first one where polarized emission due to relativistic electrons has been detected, showing the presence of a magnetic field aligned with the jet (Carrasco-González et al., 2010; Rodríguez-Kamenetzky et al., 2017). Very Large Array (VLA) continuum observations at 7 mm reveal a cross-shaped morphology which was interpreted as two overlapping structures that could correspond to the radio-jet and a disk of ∼200 au of radius (Carrasco-González et al., 2012), in agreement with the upper limit imposed by the 1.3 mm continuum dust emission observations (Fernández-López et al., 2011b). The size of the putative disk coincides with theoretical predictions of the centrifugal radius based on the Spectral Energy Distribution (SED) fitting of some high-mass protostar regions (De Buizer, Osorio, and Calvet, 2005).

In addition, observed velocity gradients in the molecular gas perpendicular to the HH80-81 radio jet have been interpreted as rotating motions (Fernández-López et al., 2011a; Carrasco-González et al., 2012; Girart et al., 2017). Definitive evidence of a compact disk around IRAS 18162-2048 comes from ALMA observations at 1.14 mm with an angular resolution of ∼40 mas (∼56 au), which reveal a compact dust disk clearly perpendicular to the radio-jet (Girart et al., 2018, see Fig. 3.1).

Due to the similarities with disk-protostar-jet systems in low- and intermediate-mass protostars, in this paper we analyze the GGD 27–MM1 disk by applying models that have successfully explained disks around low-mass stars. The main goal is to investigate if the assumptions that are usually adopted for disks around low-mass stars can be roughly extrapolated to the case of massive stars. For example, disks around low-mass stars are much less massive than the central protostar and therefore they are usually gravitationally stable. In the high-mass case it is not clear if disks are stable (Maud et al., 2019) or unstable (Motogi et al., 2019; Zapata et al., 2019).

The paper layout is as follows. In Section 2 we present the ALMA observations of the disk around GGD 27–MM1, describing the disk model in Section 3. In Section 4 we present the main observational properties of the region. In Section 5 we explain the fit procedure and Sections 6 and 7 correspond to results and discussion, respectively. We list the main conclusions in Section 8 and present the new distance estimation in the Appendix in this Chapter.

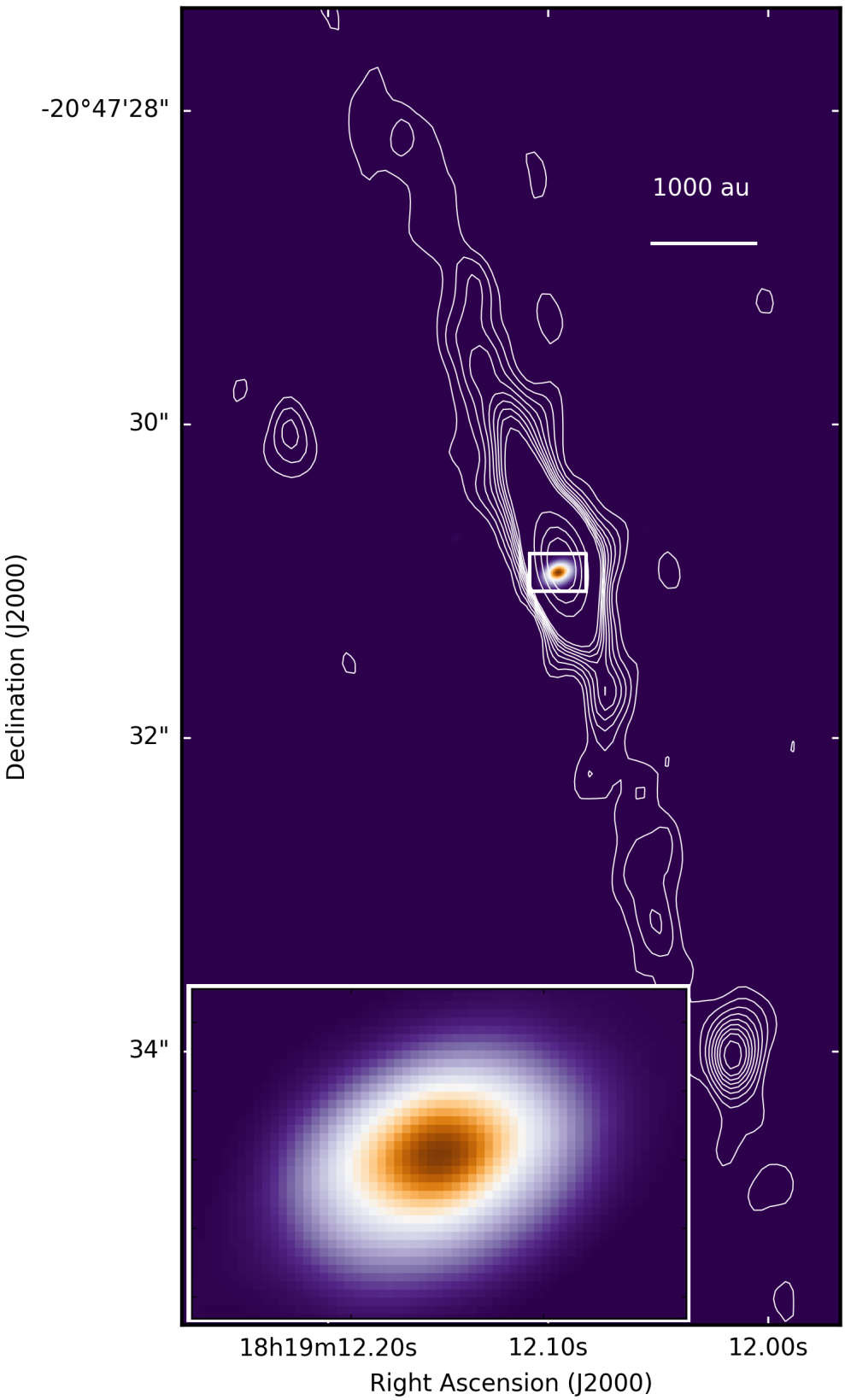

Figure 3.1: Disk and jet system of the massive star GGD 27 -MM1. The color image shows the dust continuum emission of the disk observed with ALMA at 1.14 mm with ~40 mas angular resolution (~56 au) (Girart et al., 2018, see also our Fig. 3.4). In contours it is shown the VLA image at 3.6 cm of the radio-jet observed with an angular resolution of ~0.4 arcsec (Carrasco-González et al., 2012).

3.3. ALMA Observations

In this work we use ALMA continuum observations at 1.14 mm (263.0 GHz; project ALMA #2015.1.00480.S). The Band 6 receiver with the correlator set in continuum mode (time division mode, TDM) covering the 253.0-257.0 GHz and 269.0-273.0 GHZ frequency ranges was used. The observations were carried out with 37 antennas in the c36-8/7 configuration, which provided baselines between 82 m and 11.05 km (13 to 5400 kλ). The Stokes I image toward GGD 27 -MM1 was generated using the resulting visibilities after the subtraction of the compact source (see Section 3.3.1). This was done using the CASA task *tclean* with a value of 0.5 for the robust Briggs weighting parameter. Because of a lack of visibilities between 150 and 300 kλ and in order to filter extended emission coming from the envelope, we used visibilities from baselines larger than 300 kλ (calibration of the data is described in Girart et al., 2018). The resulting synthesized beam has a full width at half maximum (FWHM) of 45.0 mas × 38.3 mas (PA = -62.4). The Stokes I rms noise is 60 μJy beam^{-1}. The ALMA#2015.1.00480.S project had also a science goal at Band 7 to observe several molecular lines in the 298-302 and 310-313 GHz frequency ranges (c40-6 configuration). Here we analyze the position-velocity diagrams of two of the brightest lines detected that better trace the disk kinematics, SO_2 $9_{2,8}$–$8_{1,7}$ and $19_{3,17}$–$19_{2,18}$ transitions. For these two molecular lines, the calibrated data were self-calibrated from the continuum by using all the available channels in the four observed spectral windows, except for the channels with the brightest line emission (e.g., H_2CO $4_{2,3}$-$3_{1,2}$). Velocity channel maps were obtained (after continuum subtraction) using *tclean* with natural weighting, which yielded a FWHM synthesized beam of $0.21''\times0.16''$ (PA = -87.1). The channel width was $\simeq$ 0.98 km s^{-1}. The rms noise achieved was 1.3 mJy beam^{-1} per channel. The other molecular lines detected will be presented in a forthcoming paper (Fernández-López et al. in prep.).

3.3.1. The compact (few au) source at the disk center

Figure 3.2 shows the real part of the observed visibilities as a function of the *uv* distance from the phase center (disk center). The flux density decreases steeply with increasing visibility radius, $r(u,v)$, for the shortest baselines ($r(u,v)\lessapprox$ 2000 kλ). At larger radii the flux density decreases more smoothly up to $r(u,v)\simeq$ 4000 kλ. At this point the flux density remains roughly constant with the visibility radius. This suggests that the emission from the longest baselines may be dominated by a very compact object. To check this possibility, we generated several images using only visibilities with a minimum visibility radius, $r(u,v)_{\rm min}$, between 3500 and 4750 kλ and with a robust weighting of 1. The values of the minimum visibility radius used and the resulting synthesized beam are given in Table 3.1. Maps including only baselines longer than 4000 kλ are devoid of artifacts due to the severe missing flux density from the disk. The compact source appears in maps with long visibilities radii (see Fig. 3.3).

A two dimensional Gaussian fit was performed to the different images obtained with different baseline ranges. The flux density and the deconvolved size obtained from the Gaussian fit are listed in Table 3.1. The images with visibilities radii ≥ 4000 kλ show an unresolved source with a flux density of ∼19 mJy at the center of the disk. We also performed a Gaussian fit to the visibilities using the same range of visibilities as before. The flux density and size of these fits are also shown in Table 3.1. The fits to the visibilities with $r(u,v)_{\rm min}$>4000 and >4250 kλ reveal that the emission arises from a very compact region with a radius of ∼4 mas (∼5.6 au). Given the relatively short range of visibilities used in this fit, further very high angular resolution observations (∼10 mas) are needed to better constrain its size. In any case, these values imply that the brightness temperature of this compact source is probably $\sim10^4$ K.

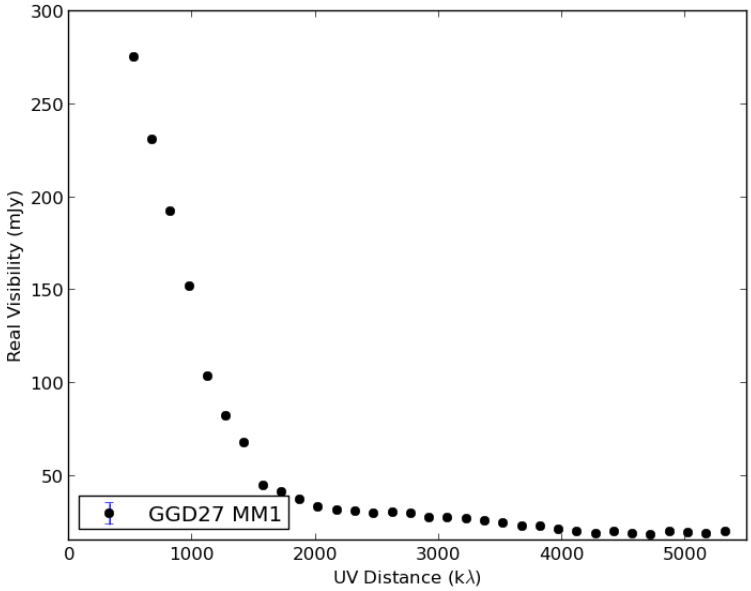

Figure 3.2: Annular average of the real part of the 1.14 mm ALMA visibilities, centered in GGD 27 MM1, as a function of the *uv* distance where the error bars are smaller than symbols.

The origin of the compact source cannot be due to the thermal emission of dust grains but rather to ionized gas (see Section 3.8.1). Therefore, this compact source was removed from the visibilities to obtain the map presented here, tracing only the dust emission from the accretion disk (Fig. 3.4).

3.4. Disk model

The disk was modeled using the irradiated α-accretion disk models created by D'Alessio et al. (1998), D'Alessio et al. (1999), D'Alessio, Calvet, and Hartmann (2001), and D'Alessio et al. (2006), which have been successfully used and further developed to model disks around low- and intermediate-mass stars (e.g.; McClure et al., 2013; Osorio et al., 2014; Osorio et al., 2016; Macías et al., 2018).

Table 3.1: Gaussian fit to the Compact Source

	Image plane			Visibility plane	
$r(u,v)_{\rm min}$ (kλ)	Synthesized Beam (mas×mas,°)	Flux density (mJy)	Deconvolved Size (mas×mas,°)	Flux density (mJy)	Size (mas)
3500	26.7×22.4, -63	28.5±0.2	16±1×7±1, 91±5	29.5±0.1	13.6±0.1
4000	23.8×20.9, -68	21.0±0.2	unresolved	20.8±0.1	4.7±0.5
4250	21.9×20.9, -59	20.1±0.2	unresolved	19.9±0.3	3.5±1.0
4500	21.6×19.8, 77	19.7±0.3	unresolved	19.3±0.4	failed [a]
4750	21.8×18.3, 67	19.1±0.4	unresolved	19.5±0.6	failed [a]

[a] Algorithm did not found solution probably due to the small range of visibilities.

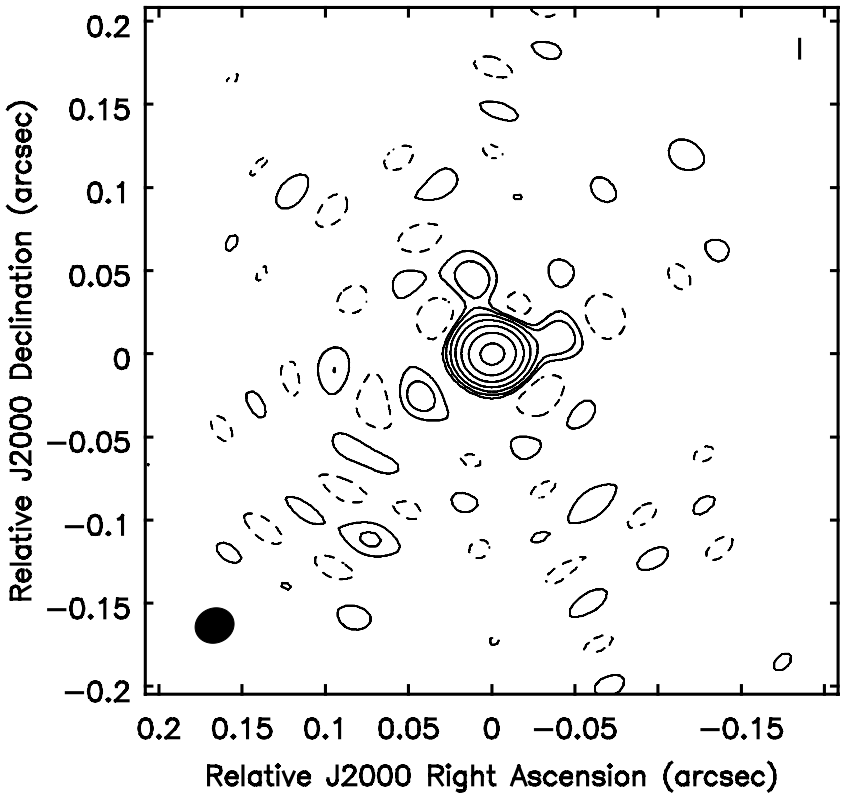

Figure 3.3: 1.14 mm ALMA image of GGD 27 MM1 obtained using only visibilities from baselines larger than ≥4000 kλ. Contour levels start at 4–σ, where σ is 0.06 mJy beam^{-1}, and then increase by a factor two at each contour. The emission shows a compact source with a brightness temperature $\sim 10^4$K, likely associated with free-free emission (see Section 3.8.1).

The models describe disks around stars with parameters typical of classical T Tauris; that is, an irradiated flared disk with two population of grains. These two populations aim at emulating the dust growth and vertical settling predicted by dust evolution models (Dullemond and Dominik, 2004). The code computes the vertical and the radial structure of the disk using the α-viscosity prescription and enforcing vertical hydrostatic equilibrium. In the past, these models have already been used to reproduce the spectral energy distribution (SED) of a possible disk around the high-mass protostar AFGL 2591-VLA 3 (Trinidad et al., 2003). Furthermore, the α-viscosity prescription has been also used to model quasi-steady selfgravitating disks around massive protostars under certain conditions ($H/R \leq 0.1$ and $M_{\rm disk}/M_* < 0.5$, with H the disk scale height, and R the radius of the disk; Forgan et al. 2016).

The model allows to set two populations of grains, with a power-law size distribution $n(a) \propto a^{-3.5}$, where a is the grain radius. Regarding the degree of settling, we used the epsilon parameter $\epsilon = \zeta_{\rm small}/\zeta_{\rm std}$, where $\zeta_{\rm small}$ and $\zeta_{\rm std}$ are the dust-to-gas mass ratio of the small grains and the initial standard value respectively (see D'Alessio et al., 2006). The relative abundances of the different dust components were adopted with a dust-to-gas ratio of 0.0065 corresponding to the measured abundances of silicates and graphites in the ISM (Draine and Lee, 1984; D'Alessio et al., 2006; Osorio et al., 2014). The remaining ratio up to the commonly used value of 0.01 would be water ice and other ices. These ices sould be sublimated at the high temperatures expected in the disk, so they should have a negligible contribution in the model (see Section 3.8.6.)

Other parameter related with the settling is $Z_{\rm big}$ that locates, as a function of the scale height (H), the border between both populations of grains, which was fixed as $Z_{\rm big}$=0.1H.

The main heating sources are the stellar irradiation and the viscous dissipation, which is parameterized through α (Shakura and Sunyaev, 1973) and it is assumed to be constant over the disk. The viscosity effective coefficient is defined as $\nu_t = \alpha c_{\rm s} H$, where $c_{\rm s}$ is the local sound speed, and H is the hydrostatic scale height of the gas:

$$\frac{H}{R} = \frac{c_{\rm s}\left(T_{\rm c}\right)}{R\Omega(R)} = \left[\frac{kT_{\rm c}R}{GM_{\rm tot}\mu m_{\rm H}}\right]^{1/2}, \tag{3.1}$$

where k is the Boltzmann constant, $T_{\rm c}$ is the disk mid-plane temperature, G is the gravitational constant, $M_{\rm tot}$ is the total mass (M_* + $M_{\rm disk}$) at every radius, μ=2.33 is the mean molecular weight and $m_{\rm H}$ is the hydrogen mass. Besides, the model considers accretion luminosity as part of the irradiation of the disk.

The temperature and density structure are calculated self-consistently once the stellar parameters (radius R_*, mass M_*, and temperature T_*), the dust content (abundances, distribution of grain sizes), viscosity (α), and disk mass accretion rate ($\dot{M}_{\rm acc}$) are set. The dust opacity includes absorption and isotropic self-scattering. In an α-accretion disk model the mass surface density is Σ=$\dot{M}_{\rm acc}\Omega/3\pi\alpha c_{\rm s}(T_{\rm c})^2$. The remaining parameters to describe the disk model are: the disk radius, $R_{\rm disk}$, and the inclination angle of the disk i.

The disk is considered to be steady, axisymmetric, and geometrically thin. Its self-gravity is neglected compared to the stellar gravity, and it is assumed to be in Keplerian rotation and in hydrostatic equilibrium in the vertical direction. The model assumes that dust and gas are well mixed and thermally coupled; thus, a unique temperature as a function of position in the disk is calculated.

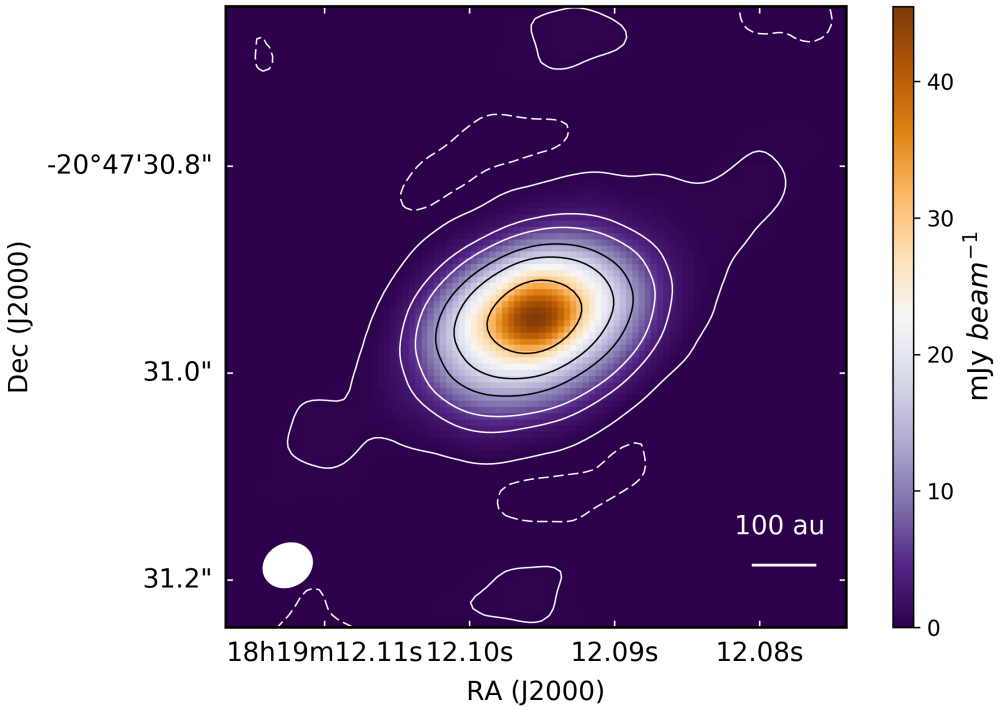

Figure 3.4: ALMA image at 1.14 mm of the GGD 27-MM1 disk. The contour levels are -5, 5, 50, 100, 200, 300, 500 times the rms noise (0.06 mJy beam^{-1}). The conversion factor from flux density to brightness temperature is ~8.9 K mJy^{-1} beam.

3.5. The GGD 27-MM1 disk-jet system

In this section we present the main observational properties that can be used to constrain the parameters of our disk model. Figure 3.4 shows the ALMA continuum image of the GGD 27–MM1 disk at 1.14 mm. We resolve the disk at this wavelength, obtaining a flux density of 351.30 ± 0.33 mJy and a peak intensity of 46 mJy beam^{-1} (see also Busquet et al., 2019). The morphology observed at this wavelength is consistent with an inclined disk (49°; 0° for a face-on disk) with a radius of ~240 au and PA= 113°. The brightness temperatures of the disk in the central region reaches a value of ~470 K (Girart et al., 2018). This is an indication of an important source of heating.

Although there are not enough data points at different frequencies with high angular resolution to build the SED of the disk, we have extensive knowledge of the region that provides us with a series of observational constraints regarding the physical parameters of our model, which are discussed below.

Bolometric luminosity. The observed value is ~2.0 ×10^4 $L_\odot$ for a distance of 1.7 kpc (Gómez et al., 2003). As shown in the Appendix in this Chapter the source distance is between 1.2 and 1.4 kpc, and therefore the luminosity can be re-calculated to be between ~1.0 ×10^4 and ~1.4 × 10^4 $L_\odot$. This luminosity must be considered an upper limit for the massive protostar GGD 27–MM1 since it comes mainly from the IRAS fluxes that probably encompasses other sources (Fernández-López et al., 2011b).

Dynamical mass. The total dynamical mass of the star-disk system can be obtained from the molecular line emission tracing the gas motions from the disk and assuming that they behave as a rotationally-supported disk (i.e., Keplerian velocity). We used the data cubes for the SO_2 $9_{2,8}$–$8_{1,7}$ and $19_{3,17}$–$19_{2,18}$ lines (see Section 3.3) to construct position-velocity (PV) maps, centered at the dust peak intensity with a position angle of 113°, i.e. along the major axis of the disk.

Figure 3.5 shows the resulting plots. The brightest blueshifted emission appears in the south-east side of the disk, while the redshifted emission arises from the north-west side of the disk. This is in agreement with previous lower angular resolution and less sensitive observations (Fernández-López et al., 2011a; Carrasco-González et al., 2012; Girart et al., 2017). We note that there is also significant red/blueshifted emission in the SW/NE side of the disk. This could be an indication of infall motions, although MHD simulation of disk formation and evolution shows that this can be also a projection effect for significant inclinations (e.g., Seifried et al., 2016). In order to constrain the dynamical mass from these PV maps, we followed the procedure given by Seifried et al. (2016). This procedure fits the Keplerian profile to the 5-σ contour emission, and was tested in synthetic ALMA molecular line PV maps generated from MHD simulations for disks around both low- and high-mass stars. It should best work for lines that fully resolve, spatially and kinematically, the Keplerian profile in the PV maps and for cases not too close to a face-on projection. The best fit obtained yielded an inclination corrected dynamical mass of 31±1 and 21±1$M_\odot$ for the SO_2 $9_{2,8}$–$8_{1,7}$ and $19_{3,17}$–$19_{2,18}$ lines, respectively. Since the line emission mostly arises from the outskirts of the dusty disk modelled in this paper, we can consider this dynamical mass as the combined mass of the star and the accretion disk. Thus we explored stellar mass values between 15 and 25$M_\odot$ and keep the total mass (star + disk) close to the dynamical mass.

Mass accretion rate. Carrasco-González et al. (2012) estimate the mass-loss rate in the jet using the formulation given by Reynolds (1986) (see Eq. 3.2), who model the free-free emission from an ionized jet adopting a power-law dependence with radius (see also Anglada, Rodríguez, and Carrasco-González, 2018):

$$\begin{aligned}\left[\frac{\dot{M}_{out}}{M_\odot yr^{-1}}\right] = \; & 1.9\times10^{-6}x_0^{-1}\left[\frac{v_{jet}}{1000kms^{-1}}\right]\left[\frac{S_\nu}{mJy}\right]^{0.75} \\ \times \; & \left[\frac{\nu}{GHz}\right]^{-0.45}\left[\frac{D}{kpc}\right]^{1.5}\left[\frac{\theta_0}{rad}\right]^{0.75}\end{aligned} \tag{3.2}$$

they assume a pure hydrogen jet with constant opening angle θ_0 ~19° (conical jet), terminal velocity $v_{\rm jet}$ (~1000 km s^{-1}), ionization fraction x_0 = 0.1, electron temperature $T_{\rm e}$=10^4 K, and that the jet axis is in the plane of the sky. They obtain a mass-loss rate of $\dot{M}_{\rm out}$ ~10^{-5} $M_\odot$ yr^{-1} for a distance of 1.7 kpc, ≃ 8×10^{-6} $M_\odot$ yr^{-1} for the corrected distance of 1.4 kpc (see Appendix in this Chapter). This value is in agreement with the value obtained from CO observations of the molecular outflow associated with the jet (Qiu et al., 2019). Assuming the accretion rate $\dot{M}_{\rm acc}$ of the disk onto the star to be ~10 times larger than the mass-loss rate (Bontemps et al., 1996), the mass accretion rate would be $\dot{M}_{\rm acc}$~8×10^{-5} $M_\odot$ yr^{-1}. However, Beltrán and de Wit (2016) (and references therein), obtain a ratio between the mass-loss rate and mass-accretion rate of approximately ~0.3 for disks in young high-mass stars. In this case the mass accretion rate would be lower, ~3×10^{-5} $M_\odot$ yr^{-1}.

Even though the mass accretion rate is not well determined using these methods, it allows to define a range of values to explore. Therefore, in our modeling we explored values of $\dot{M}_{\rm acc}$ in the ~1×10^{-5} to ~2×10^{-4} $M_\odot$ yr^{-1} range.

Stellar parameters. It is expected that most of the dynamical mass (21-31$M_\odot$) is stellar, otherwise the disk would be unstable and would show significant asymmetries (e.g., spiral structures) that are not observed with the present data. Such massive star, if it were in the main sequence, should develop an HII region, which is not detected with the present observations (see Sect. 3.8.1). A possible solution to mitigate this problem is to assume that the star is inflated, with low enough temperature for not producing stellar UV radiation and create an HII region.

In that sense, Hosokawa and Omukai (2009) found a dependence of the protostellar radius with the accretion rate. They obtain that, in general, the higher is the accretion rate, the larger is the stellar radius. Then the protostar has a lower maximum temperature for a certain stellar mass. This

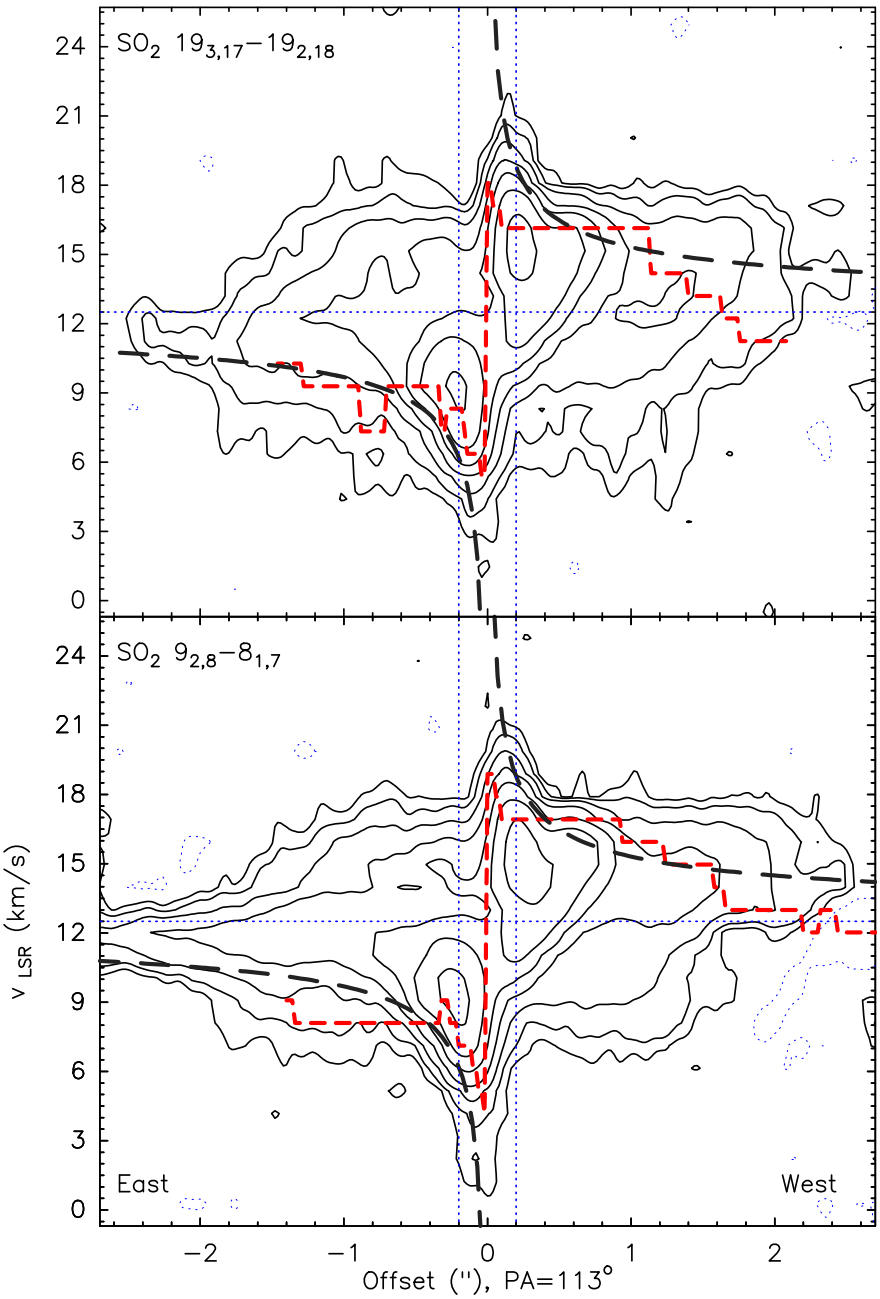

Figure 3.5: Position-velocity plots along the major axis of the disk for the SO_2 $9_{2,8}$–$8_{1,7}$ and $19_{3,17}$–$19_{2,18}$ lines. Contours are 2, 4, 8, 16, 32, 64 and 128 times the rms noise of the maps, 1.2 mJy beam^{-1}. The dashed black line shows the expected Keplerian profile for a 25 $M_{\odot}$. The red dashed line shows the best Keplerian fit to the data using the method proposed by Seifried et al. (2016) at 5-σ. The fit corresponds to a dynamical mass of 30 and 21 $M_{\odot}$ for SO_2 $9_{2,8}$–$8_{1,7}$ and $19_{3,17}$–$19_{2,18}$ lines, respectively.

fact causes a delay in the onset of the main sequence phase and therefore a delay in the formation of an HII region. Thus, because of the high accretion rate estimated, we decided to explore large stellar radii, between 10 and 30 $R_\odot$. Because the luminosity is known, this implies temperatures between 12000 and 18000 K. This is consistent with Johnston et al. (2013), who modeled the envelope and disk around the luminous star AFGL 2591-VLA3 (2.3×10^5 $L_\odot$), and find a stellar radius of 90 $R_\odot$ with a temperature of 13000 K.

Inner disk radius. Considering a sublimation temperature of 1400 K for the most refractory grains (D'Alessio et al., 2006) and the observed luminosity, we can locate the sublimation wall from $L_{\rm tot} = 4\pi\sigma T^4 R^2$ at ~ 12 au of radius. Because of the high spatial resolution of the observations (~56 au), an inner radius larger than ~20 au was discarded. Otherwise we should marginally resolve the inner wall of the disk. The sublimation temperature usually is assumed to cover a range from 1200-1500 K, thus we explored an inner radius range between 10 and 20 au instead to just using the 12 au that we calculated (see Table 3.2).

Settling degree and grain size. We can obtain some constraints about the settling of the larger dust grain at the mid-plane looking at the polarization emission due to scattering from large grains. Based on polarization observations, Girart et al. (2018) do not find signs of dust settling, and determine a dust maximum grain size (a_{max}) from 50 to 500 μm (see Section 3.8.2). We explored in our modeling cases with different settling degree, including the no settling case.

Taking into account the observational restrictions set out above, in the following we proceed to look for the set of parameters that best fit the observations.

3.6. The model-fitting procedure

We computed several grids of models varying the parameters of the disk and the star. Through these grids the parameters were refined until the best-fit model image.

The fitting procedure and analysis was done using Common Astronomy Software Applications (CASA) and Multichannel Image Reconstruction, Image Analysis, and Display (MIRIAD; Sault, Teuben, and Wright, 1995) data reduction software packages.

In order to properly compare the model with the ALMA data, synthetic visibilities were computed from the model images. This was done with the CASA *simutil* package. After that, *tclean* of CASA was used with the simulated visibilities to create a final image from the model adopting the same cleaning parameters used to create the observed ALMA image. In Fig. 3.6 we show the ALMA image (top panel), the modelled image (middle panel), and the residual map (bottom panel). The residual map was obtained by subtracting the model image from the observed one. Therefore positive values in the residuals show regions where the model underestimates the emission.

The radial intensity profile was computed averaging in concentric ellipses every 0.01 (~1/4 of the beam) with the inclination adopted in the disk model (see Fig. 3.7). The best fit parameters of the disk model were obtained initially by visual inspection of the radial intensity profile and then, from among this first selection we chose the best fit model based on minimum χ^2 of the residual map. In the case of the residual map, only pixels inside of ellipse with R=230 au were considered to calculate the χ^2 (see Fig. 3.4) to avoid contamination from the outskirts of the map. Appendix B in this Chapter shows the variation of the disk parameters with χ^2 (leaving the other parameters fixed).

3.7. Results

Table 3.2: Explored parameters range

Parameter	Values	Step
Star mass ($M_\odot$)	15 – 25	1
Temp. eff. (K)	12000 – 18000	1000
Star radius ($R_\odot$)	10 – 30	5
Acc. rate ($M_\odot$ yr^{-1})	1×10^{-5}– 2×10^{-4}	1×10^{-5}
Disk radius (au)	130 – 250	10
Inner radius (au)	10 – 20	1
Inclination(degrees)	44 – 54	1
a_{max} (μm)	100, 500 and 1000	-
α	0.1, 0.01 and 0.001	-

Table 3.3: Best fit model parameters

Parameter	Value	
$M_*(M_\odot)$	20	fitted
$T_{\rm eff}$ (K)	12000	fitted
R_* ($R_\odot$)	25	fitted
Distance (kpc)	1.4	adopted
$\dot{M}$ ($M_\odot$ yr^{-1})	7×10^{-5}	adopted/refined [a]
$M_{\rm disk}$ ($M_\odot$)	5	calculated
$R_{\rm disk}$ (au)	168	adopted/refined [a]
H_{100} (au)	7	calculated
$R_{\rm in}$ (au)	14	fitted
i (degree)	49	adopted/refined [a]
a_{max} (μm)	500	fitted
α	0.1	fitted

[a] Parameter with observational constrains and uncertainty.

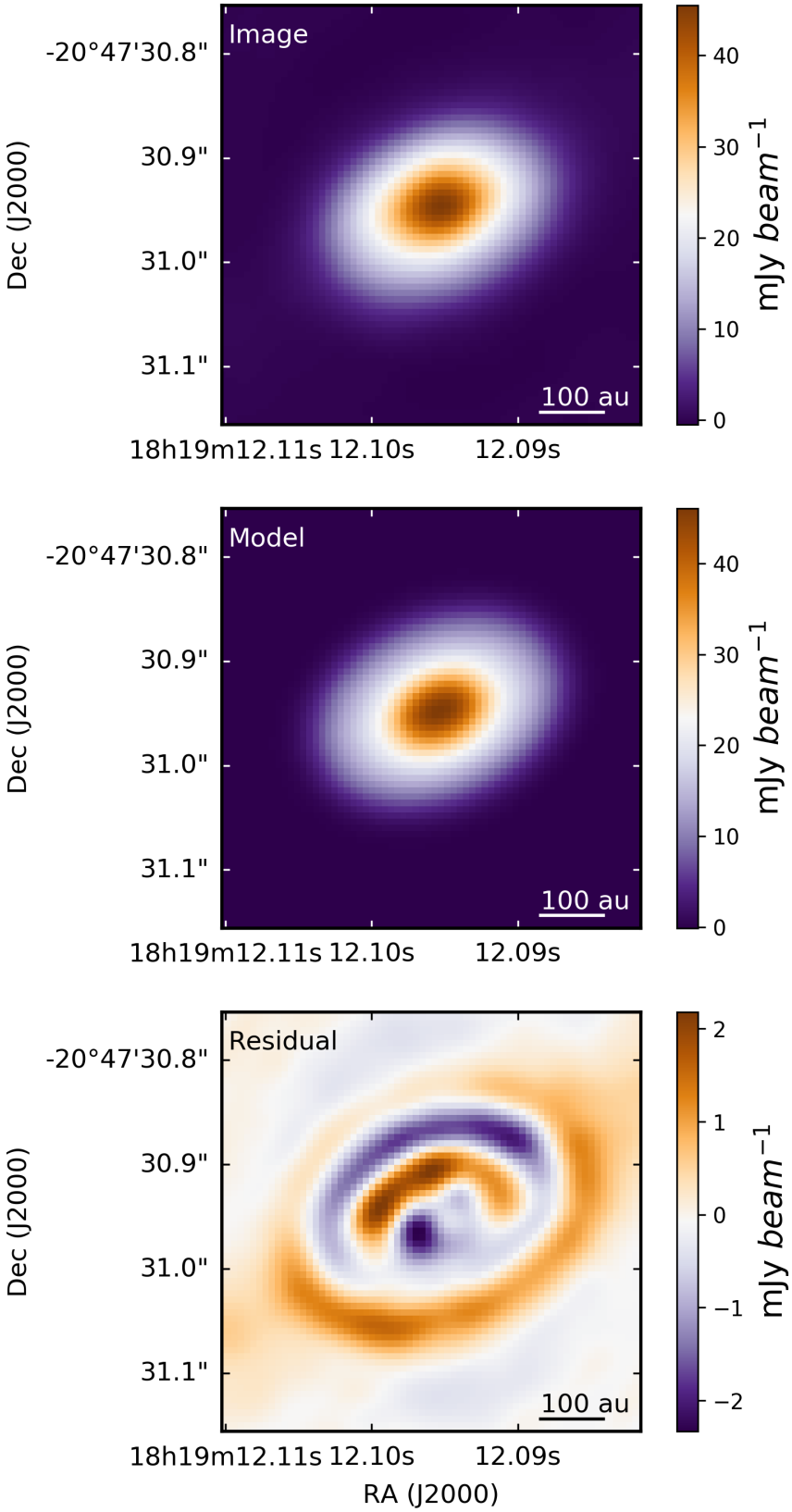

Figure 3.6: Observed ALMA 1.14 mm image (top panel), best fit disk model (middle plane), and the residual (image−model) map (bottom panel). The conversion factor from flux density to brightness temperature is ∼8.9 K mJy^{-1} beam.

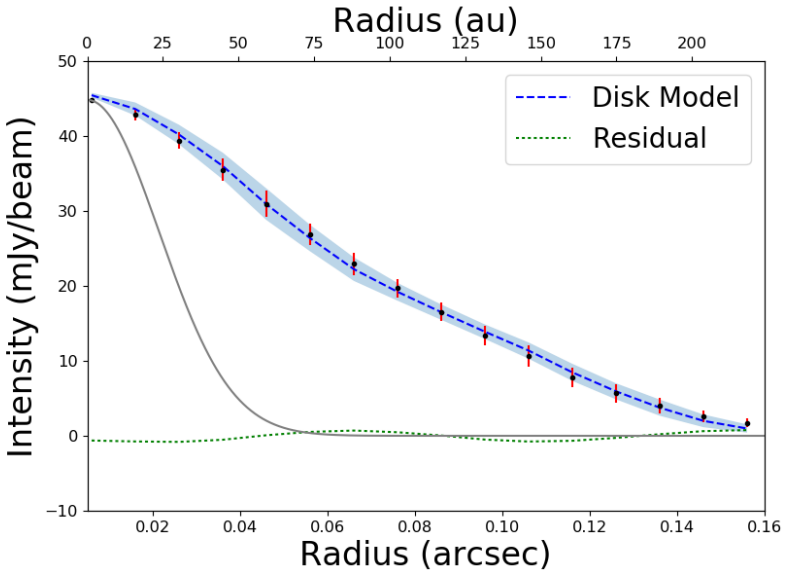

Figure 3.7: Averaged radial intensity profile at 1.14 mm. Dots represent the averaged value at each radius for the observed image and error bars represent the standard deviation. The blue dashed line is the averaged value at each radius for the disk model and the blue shadow is the standard deviation. The grey line depicts the synthesized beam of the ALMA observations. The dotted green line indicates the residual (difference between observed and modeled profile).

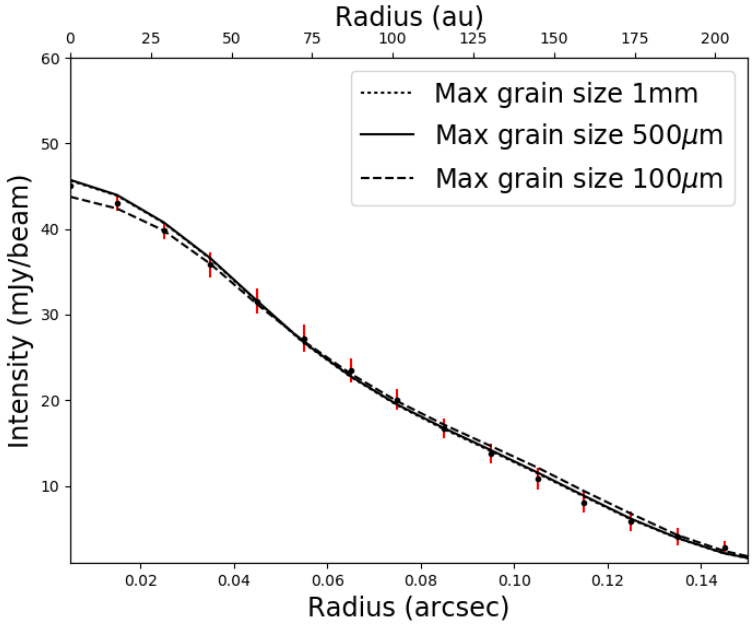

Figure 3.8: Radial intensity profile for three models with the same parameters given in Table 3.3, except a_{max} of 100 μm, 500 μm, and 1 mm.

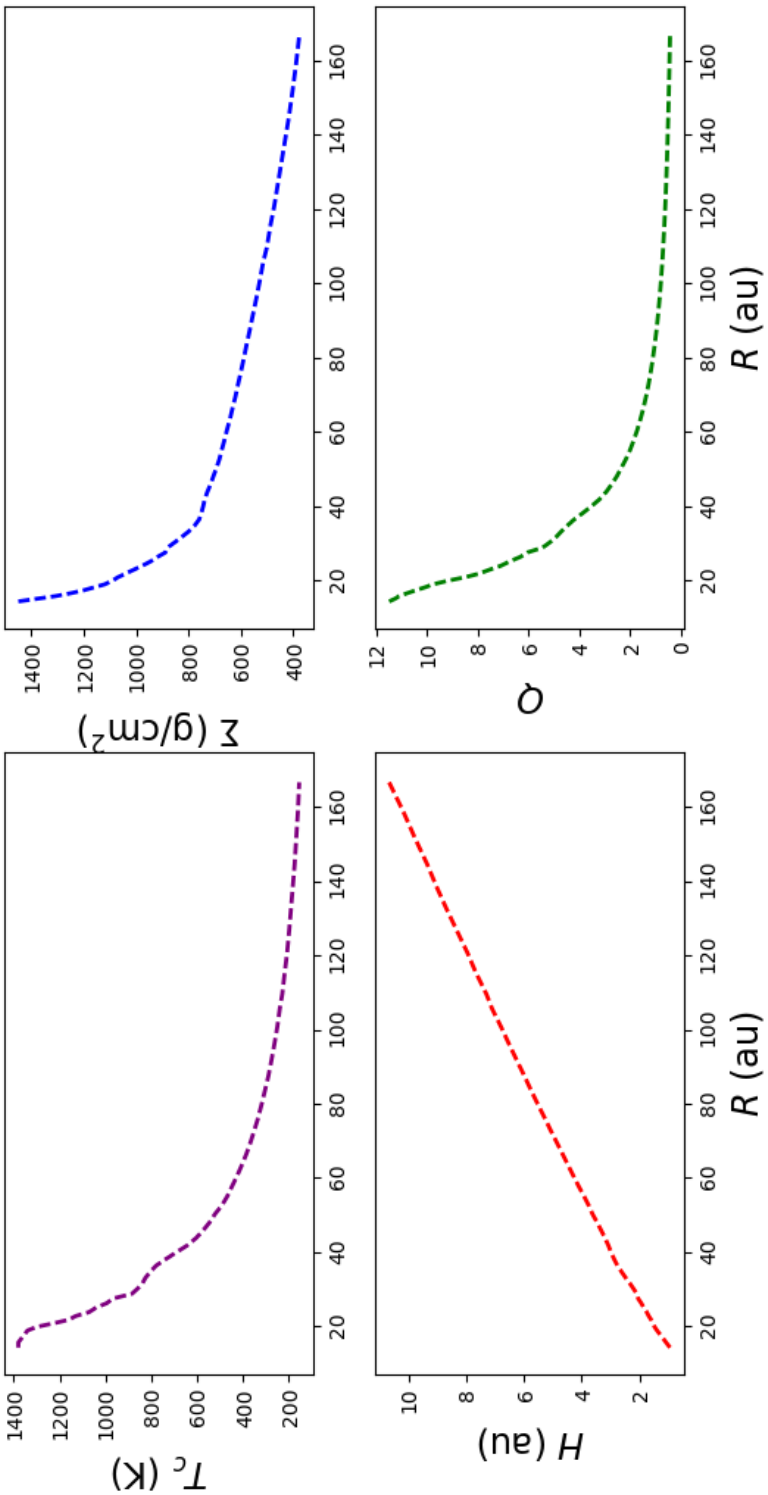

Figure 3.9: *Upper:* Temperature at the mid-plane (left) and surface density (right). *Bottom:* Scale height, H (left) and Toomre parameter Q, see Section 3.8.3 (right).

In this section we present the best fit model obtained after exploring a wide range of values in the space of parameters of the model presented in Section 3.4. The best fit parameters are shown in Table 3.3.

We found a massive disk of $\sim 5 M_{\odot}$, i.e. 20% of the stellar mass. The radius of the disk is ~170 au with an inclination angle of ~49° (angle between the rotation axis and the line of sight). The mass accretion rate, which in our model is a very sensitive parameter, resulted to be $\sim 7 \times 10^{-5}$ $M_{\odot}$ yr^{-1}. The total luminosity is $\sim 1 \times 10^{4}$ $L_{\odot}$ which is in agreement with the previous estimation (see Section 3.5). The stellar mass is 20 $M_{\odot}$ which together with disk mass (5 $M_{\odot}$), is consistent with the estimated dynamical mass for the star-disk system (21–30 $M_{\odot}$; see Section 3.5).

Regarding the composition of the disk in terms of grain size, different maximum size of grains according with results found in Girart et al. (2018) were tested (see Section 3.5). We did not find substantial differences between models with a_{max} of 100, 500 μm and with 1 mm (see Fig. 3.8). Only for small radii (< 0.05") the difference between the models is noticeable. The grain sizes of the best fit model goes from a minimum value of 0.005 μm to a maximum of 3 μm in the disk upper layer. For those grains settled in the disk mid-plane the grain sizes are between 5 μm and 500 μm.

The density and temperature profiles for the best fit model are shown in Fig. 3.9. We found a flared disk with a maximum scale height of ~13 au. The disk shows a temperature profile that goes from ~1400 K at the inner edge of the disk to ~150 K at the outer part. The small irregularities that can be seen in the internal part of the disk are caused by numerical effects and by the sublimation of the different dust components, which result in a step in the dust opacity, but they do not affect the results.

From the mass surface density (Σ) and using the total opacity of the model (absorption + self-scattering), $\chi = 0.13$ cm^2/g (opacity for a dust grain mixture with the physical properties described in Section 3.4 and with a grain size distribution which assumes grains with a maximum radius of 500 μm and considers the scattering effects), we obtain an optically thick disk at 1.14 mm for all radii, with $\tau = \Sigma\chi$ ranging from 50 to 170. In Busquet et al. (2019) they computed the mass of gas and dust of the disk assuming that the 1.14 mm dust continuum emission is optically thin and the temperature distribution is uniform (T_d=109 K). They estimated a disk mass for GGD 27 MM1 of $\sim 0.5 M_{\odot}$. This mass could be considered as a lower limit due to the optical thickness of the disk and to the fact that the opacity due to the self-scattering is not considered. We fitted the density and the temperature profiles with a power law functions ($\Sigma(R) \propto R^p$, $T(R) \propto R^q$) using the method of the minimum mean squared error (MSE). Here we present the coefficient and the power index. Equations 3.3 show the behaviour of the surface density, $\Sigma(R)$, and the temperature at the mid-plane, $T_c(R)$, approximated as power laws. The MSE of the fits are 0.023, and 0.034 respectively.

$$\begin{aligned} \frac{\Sigma(R)}{[\mathrm{g/cm^2}]} &\sim 500\left(\frac{R}{[100\ \mathrm{au}]}\right)^{-0.5} \\ \frac{T_c(R)}{[\mathrm{K}]} &\sim 300\left(\frac{R}{[100\ \mathrm{au}]}\right)^{-1} \end{aligned} \tag{3.3}$$

3.8. Discussion

In this work we have studied the ALMA image at 1.14 mm of the circumstellar disk around GGD 27 -MM1. We found a compact source coming from the inner radius (~4 mas/5.6 au) probably due to ionized gas. By modeling the dust continuum emission from the disk (with the compact source previously subtracted), we found a massive (~5 $M_{\odot}$) and compact (~170 au) disk. In the

following we discuss the implications of our results, while also analyzing the gravitational stability of the disk.

3.8.1. Ionized component

The compact source reported in Sect. 3.3.1 appears unresolved in the different images obtained with a minimum visibility radius of 4000 kλ (Fig. 3.3). The Gaussian fits in the visibility domain indicate that the source has a radius of ∼5.6 au and a brightness temperature of $\sim 10^4$ K. At such high temperature, the dust grains should be sublimated. Indeed, the expected temperature for the sublimation of silicates is ∼1400 K (D'Alessio et al., 2006). Therefore, the most plausible explanation is that this compact emission is tracing ionized gas, either from an incipient and extremely compact HII region or from the base of the HH 80–81 thermal radio-jet, best traced at cm-wavelengths (e.g., Carrasco-González et al., 2012). In fact, from the peak flux density measured at 1.3 cm at the center of the radio-jet (∼1 mJy; Carrasco-González et al., 2012), and the flux density measured at 1.14 mm ∼19 mJy (see Sec. 3.3.1), we estimated a spectral index of α ∼1.2 between these two frequencies. This value is within the range of spectral indices measured in thermal radio-jets associated with YSOs (e.g., Anglada, Rodríguez, and Carrasco-González, 2018). Higher resolution and multi-frequency observations would help determine the nature of this compact component in a conclusive way.

3.8.2. Restrictions from polarization

An important source of information about the composition of the disks in terms of grain size, grain shape, and grain distribution comes from polarimetric observation.

Polarization data allows to constrain the dust distribution in the disk (settling) and the maximum dust grain size. Girart et al. (2018) based on polarization models of Yang et al. (2017) conclude that dust settling has not yet occurred . Yang et al. (2017) compare two models with different thickness of the layer of large grains which are responsible for the scattering, and propose two models in which large grains can be found up to 0.1 H' and 1 H', where H' is the (dust) hydrostatic scale height, $H'(R) = H'_0(R/R_c)^{1.5-q/2}$ being R_c a characteristic radius of the disk (dust) density distribution, and q the temperature power law index.

Unlike the models of these authors, our models consider the dust settling changing the dust-to-gas mass ratio between two populations through the ϵ parameter as explained in Section 3.4. Small grains are in the upper layer and big grains are in the mid-plane. The position of the border between these two populations can be set through the parameter $Z_{\rm big}$.

In this work our best fit model has ϵ=1 (no dust settling) but it still has two dust populations with the border located at $Z_{\rm big}$=0.1H, where H is the pressure scale height of the gas at the mid-plane temperature (see Section 3.4).

We also reproduced the scenario suggested by Yang et al. (2017) to reproduce the polarization pattern observed by Girart et al. (2018). To do so, we tested a model with $Z_{\rm big}$ =1 H and ϵ =1. In this case we obtained a more massive disk (7 $M_\odot$) with larger mass accretion rate (1×10^{-4} $M_\odot$ yr^{-1}) than the model with $Z_{\rm big}$=0.1H ($M_{\rm disk} \sim 5\ M_\odot$ and $\dot{M}_{\rm acc} \sim 7 \times 10^{-5}\ M_\odot$ yr^{-1}; see Table 3.3), our fiducial best fit model, which shows a lower value of χ^2.

Furthermore, we have compared two- and one-population models. We tested models with a single dust grain population with a maximum grain size of 500 μm Due to the lower opacity to the stellar radiation of this dust population, the one-population models would require significantly higher disk masses, even comparable to the stellar mass. These masses are inconsistent with our

estimated dynamical mass (see Section 3.5, indicating that at least two dust populations are needed to fit the observations.

In summary, we have considered the results presented in Girart et al. (2018) concerning the size and distribution of grains. Moreover, taking into account the conceptual differences presented above (H, H'), we have explored values adjacent to them. We did not find substantial differences between both scenarios and therefore we can not favor either.

3.8.3. Stability of the disk

We have quantified the Toomre parameter of our model to check the stability of the disk against self-gravity perturbations. Figure 3.9 (bottom right) shows the Toomre parameter Q (Eq. 3.4) for a Keplerian disk evaluated at the disk mid-plane temperature.

$$\begin{aligned} Q &= \frac{c_s \Omega}{\pi G \Sigma} \\ \Omega &= \left(\frac{G M_{total}}{R^3}\right)^{1/2}, \end{aligned} \tag{3.4}$$

where c_s is the sound speed at the mid-plane temperature, Ω the Keplerian angular velocity, Σ the surface density of the disk, and G the gravitational constant.

We adopted the surface density and the temperature at the mid-plane as a function of the radius of our best fit model. The stability condition ($Q > 1$) is satisfied up to a radius $R_{\rm disk}$ ~100 au. A similar result has been found by Maud et al. (2019) in the massive O-type protostar G17.64+0.16, who reported a massive and stable disk for $R_{\rm disk} \leq 150$ au. Furthermore, Meyer et al. (2018) and Takahashi, Tsukamoto, and Inutsuka (2016) propose an update of the Toomre criterion in which the only necessary condition for disk instability is Q<0.6.

In addition, our best fit model satisfies the conditions proposed by Forgan et al. (2016) in order to apply the α-viscosity prescription model in self-gravitating disks; that is, $H/R < 0.1$ (see Fig. 3.9) and $M_{\rm disk}/M_* < 0.5$.

We note that due to the relatively high mass of the disk of our best model (5 $M_\odot$), self-gravity might play a non-negligible role. In order to explore the potential effects of including self-gravity, we compared our best fit model to the hydrodynamic simulations (including self-gravity) of massive star formation performed by Kuiper and Hosokawa (2018). Our model shows very similar results in terms of disk mid-plane temperature and disk's aspect ratio to this model (Fig. 6; Kuiper and Hosokawa, 2018), which indicates that including self-gravity would not change our results significantly.

3.8.4. Residual map

The values of the residual map are low when compared with the observed (residuals are below 5% of the peak intensity), but significant with respect to the rms noise level (σ ~0.06 mJy beam^{-1}), with an intensity range between ~2 and −2 mJy beam^{-1} (see Fig. 3.6). The main differences between the observed and modeled images arise from the outer parts of the disk, beyond 150 au, with an excess and a deficit of emission. This is illustrated in Fig. 3.10, where we show flux density-position cuts along the major and minor axis of the disk (observed and modeled). We also verified that the asymmetries were not caused by a mismatch in the inclination of the system or a shift in the disk centers. In Fig. 3.11 we present the model image and the residual map of the best fit model (i=49°; central panels) together with two models in which the inclination around the best fit has been modified (i=44° and 54°). In addition, we show in Fig. 15 the χ^2 as a function of the inclination for the best fit model varying the inclination angle in a range of 10° centered at 49°.

Although we cannot discard intrinsic asymmetries within the disk, a plausible explanation for this excess/defect of emission at the outer parts of the disk could be a small mismatch with the flaring angle and/or settling of the disk. To discriminate between possible intrinsic asymmetries and modeling, we would need ALMA high-angular observations at other frequencies as it has been carried out in low-mass YSOs (e.g., Carrasco-González et al., 2019; Macías et al., 2019).

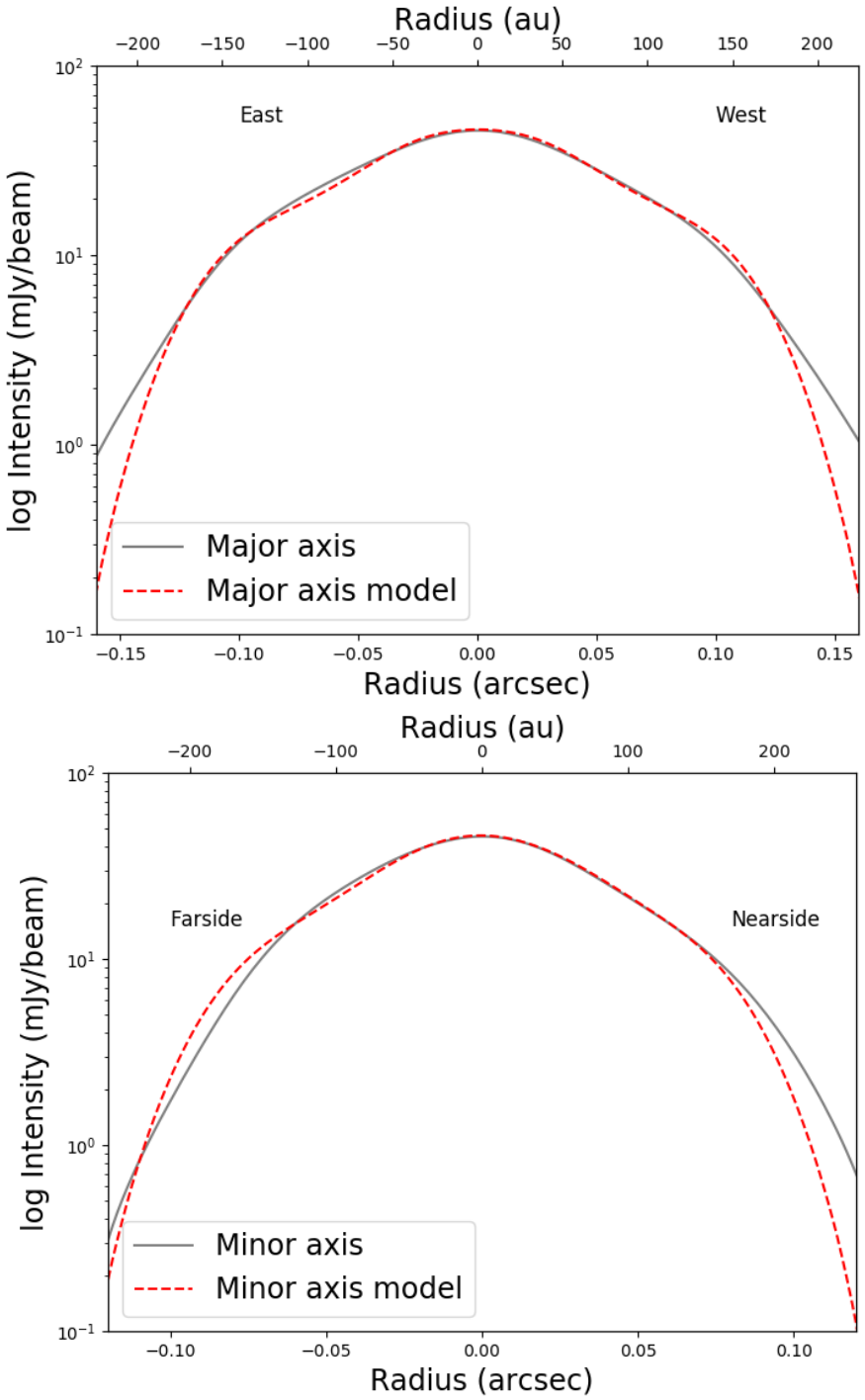

Figure 3.10: Cut along the major (top panel) and minor (bottom panel) axis. Solid grey and dashed red lines represent the observed image and model, respectively. The physical space scale (au) is corrected by inclination.

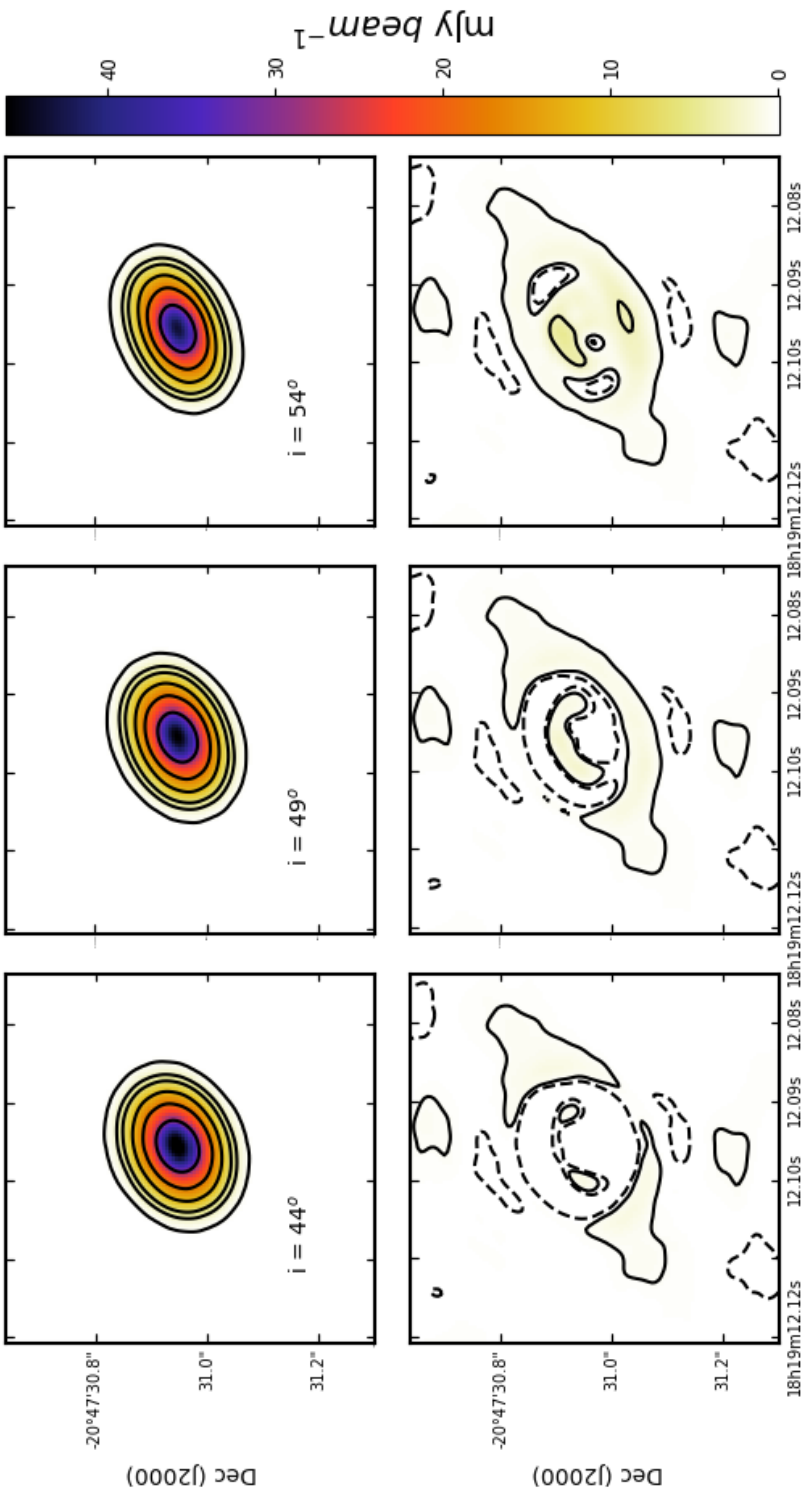

Figure 3.11: Models (top panels) and residuals (bottom panels) for the best fit model varying the inclination. Left panels correspond to i=44°, middle panels to i=49°, and right panels to i=54°. The contours levels are -5, 5, 50, 100, 200, 300, and 500 times the rms of the observed image (0.06 mJy beam^{-1}).

3.8.5. Mass accretion rate and evolutionary stage

Trinidad et al. (2003) used the D'Alessio model to fit the SED of AFGL 2591 VLA3, a massive disk-star system located in the Cygnus X region. They find that for all models, the main heating source was the stellar irradiation for radii larger than 20 au and the viscous dissipation for smaller radii. Furthermore, $\Sigma \sim \dot{M}_{\rm acc}/\alpha$ for radius larger than 20 au. In this scenario, they find a family of models that could explain the observed SED. This family of models correspond to a constant value of $\dot{M}_{\rm acc}/\alpha$, showing that the SED does not change as long as this ratio is maintained.

Our best fit model yields a rate $\dot{M}_{\rm acc}/\alpha \sim 1\times10^{-4}$ $M_\odot$ yr^{-1}. We tested if the radial intensity profile would be significantly affected by varying the accretion rate and alpha, while keeping $\dot{M}_{\rm acc}/\alpha$ constant. As we show in Fig. 3.12, the radial intensity profile at 1.14 mm is dramatically affected when the disk mass accretion rate is changed although the ratio $\dot{M}_{\rm acc}/\alpha$ stays constant. The main reason for this difference is because of the effects of the irradiation from the accretion luminosity. Therefore by not having this degeneration we are able to constrain the $\dot{M}_{\rm acc}$.

We would like to point out that the accretion rate could be variable with time. In fact, Martí, Rodríguez, and Reipurth (1998), based on multi-epoch VLA continuum observations, report a flux density decay of the two inner condensations in the HH 80–81 thermal radio jet. Such a flux density decay could be attributed to changes in the mass accretion rate, being higher in the past. Furthermore, GGD 27–MM1 is a young source that has a faint envelope and probably an incipient (hyper-compact) HII region. Some studies estimate that the timescale for the development of HII regions, with an accretion rate in the range $\sim10^{-4}$–10^{-3} $M_\odot$ yr^{-1}, is $\sim10^5$ years (e.g., Osorio, Lizano, and D'Alessio, 1999; Cesaroni, 2005). Considering the constant accretion rate of our best fit model (7×10^{-5} $M_\odot$ yr^{-1}), for it to reach a star mass of 25 $M_\odot$, its age would be $\sim4\times10^5$ yr, which is larger than the development time of an HII region. Thus, higher accretion episodes in the past are necessary to explain the present situation.

The GGD 27 complex includes two compact cores, MM1 and MM2, separated by ~7 arcsec (~10000 au). Fernández-López et al. (2011b) estimated masses of MM1 and MM2 at different scales (see their Table 6). These authors show that while in MM2 most of the mass (~75%) is found at envelope scale, in MM1 ~70% of the mass is already at disk scale. This fact would place MM1 in a more evolved stadium than MM2, being MM1 equivalent to a Class I low-mass star.

3.8.6. Temperature distribution in the GGD 27-MM1 disk: comparison with disks around low- and intermediate- mass stars and implications on the water snow line

In flared α-irradiated disk models, the temperature varies as a function of both the radial distance to the star and the height above the disk mid-plane. The mid-plane temperature decreases with increasing radius, typically as $T_c \propto R^{[-0.5,-1]}$ (e.g., D'Alessio et al., 1998). In the GGD 27-MM1 disk we found $T_c \propto R^{-1}$ (see Section 3.7).

Furthermore, because of the flared morphology of the disk, its surface is heated directly by the radiation from the star and the accretion shock, while the inner layers are heated by viscous dissipation, which heats mainly the disk mid-plane. The energy released by the star and the accretion shock generally exceeds the one released by viscous dissipation. As a result of these heating mechanisms, the surface of the disk is warmer than the regions closer to the mid-plane, but the temperature gradient becomes smoother, or even reversed (temperature increasing with decreasing height), near the mid-plane. In the latter case, the minimum temperature is not reached at the mid-plane but above it.

For disks in low-mass stars this vertical inversion only happens typically at radii $\leq$ 1 au and

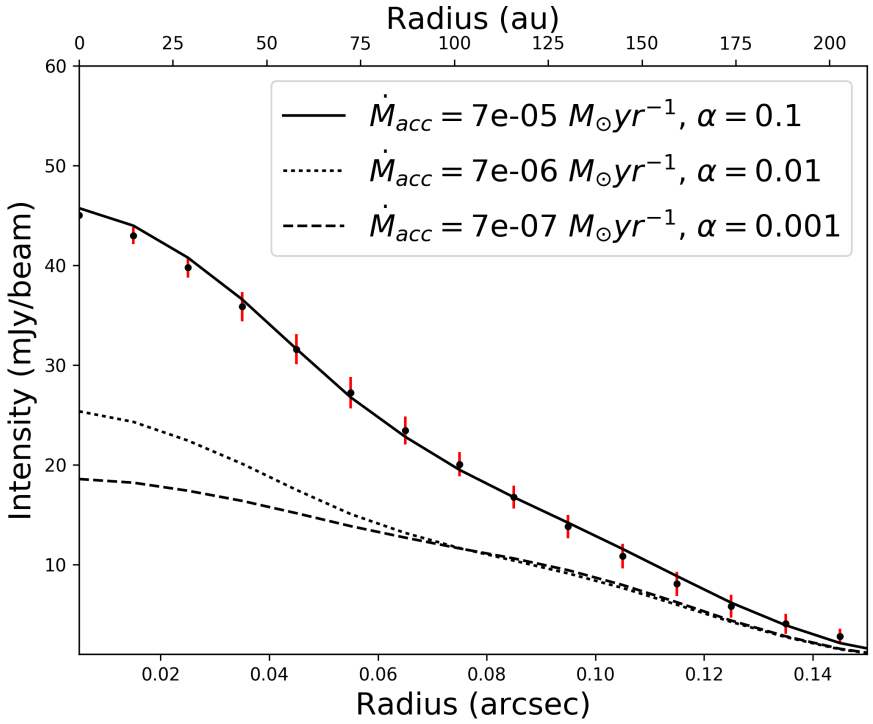

Figure 3.12: Averaged radial intensity profile of the best fit model (R_*=25 $R_\odot$, M_*=20$M_\odot$, $R_{\rm disk}$=170 au, i=49°, $T_{\rm eff}$=12000 K, distance=1.4 kpc, $R_{\rm in}$=14 au, a_{max} 500 μm) varying $\dot{M}_{\rm acc}$and α. Solid line: Disk mass accretion rate 7×10^{-5} $M_\odot$ yr^{-1}, α=0.1, $M_{\rm disk}$=5$M_\odot$. Dotted line: Disk mass accretion rate 7×10^{-6} $M_\odot$ yr^{-1}, α=0.01, $M_{\rm disk}$=8$M_\odot$. Dashed line: Disk mass accretion rate 7×10^{-7} $M_\odot$ yr^{-1}, α=0.001, $M_{\rm disk}$=9$M_\odot$.

heights ≤ 1 au (D'Alessio, Calvet, and Hartmann, 1997; D'Alessio et al., 1998). According to our modeling, in the case of the GGD 27–MM1 disk the vertical inversion of temperature occurs at all radii; for instance, near the star, at $R_{\rm disk} \simeq 30$ au, the inversion occurs at a height of ∼5 au and at a temperature of ∼240 K, while in the outermost regions, $R_{\rm disk} \simeq 150$ au, the inversion occurs at a height of ∼30 au and at a temperature of ∼120 K.

Typical disks around low-mass stars reach very low temperatures (∼20–30 K at ∼150 au; D'Alessio, Calvet, and Hartmann, 1997; Men'shchikov, Henning, and Fischer, 1999; Fogel et al., 2011; Tobin et al., 2018). Disks around intermediate-mass stars have slightly higher values of the minimum temperature (∼30–40 K at ∼150 au; Osorio et al., 2014). In contrast, according to our modeling, the GGD 27–MM1 disk is significantly warmer. Even at large distances from the star, close to the edge of the disk ($R_{\rm disk} \simeq 170$ au), its mid-plane temperature remains above ∼140 K (see Fig. 9) and at this radius the minimum temperature is ∼115 K at a height of ∼30 au. High temperatures have also been reported for disk candidates around other massive protostars (mid-plane $T_c \simeq 200$ K at $R_{\rm disk} \simeq 200$ au; Chen et al. 2016), using radiative transfer models which take into account radial and vertical temperature gradients. However in most cases, the temperatures have been inferred from vertically isothermal models that do not provide the temperature of the surface layer; also, it is unclear if some of the disk candidates are indeed real accretion disks or just elongated structures, since they are extremely large.

Due to the elevated temperatures of GGD 27–MM1 disk, condensation fronts, known as snow lines, of major volatile such as carbon monoxide, carbon dioxide and methane, are not expected to be present since these species sublimate at temperatures considerably lower (∼20–40 K, Zhang, Blake, and Bergin 2015) than the temperatures we find in the GGD 27–MM1 disk. Nevertheless, water ice sublimates at temperatures above 100 K, hence it is possible that the water snow line is present in the outer regions of GGD 27–MM1 disk. Since the water ice sublimation temperature depends on the density (e.g., Sandford and Allamandola, 1993; Osorio et al., 2009), taking into account the density and temperature distributions obtained in our modeling of the GGD 27–MM1 disk (see Section 3.7), we estimate that the water snow line would be located near the edge of the disk, at a radius of ∼170 au. At this radius, densities are 1×10^9–2×10^{11} cm^{-3} within a height of 30 au of the mid-plane, implying a range of water sublimation temperatures of 120–130 K, which is similar to the range of temperatures of ∼120–150 K predicted by our model.

It has been thought that water snow lines are important because they can trigger the growth of grains to pebbles and lastly to planets. They are also important because they mark the border between rocky planets formed inward of this line and giant gas planets formed outside. In the case of the GGD 27–MM1 disk, we expect the formation of gas planets to be hindered by the high temperatures of the disk, being restricted to radii near the disk edge. Consequently, we speculate that if the formation of gas planets were to occur in disks around massive protostars, in general, they would be formed at distances around hundreds of au. It is unclear, however, whether such giant planets could survive after the onset of an HII region around the massive star.

One should keep in mind that the planetary formation process in high-mass protostars, if it takes place, must be fast because the time scales for the formation of these stars are shorter than for low-mass stars. In principle, the time scale for planet formation is expected to be of the order of that of mass exchange in the accretion disk, roughly estimated as the disk mass divided by the accretion rate, resulting in 7×10^4 yr for the disk of GGD 27–MM1. This time scale is shorter than the values typically estimated for the grain coagulation process (∼10^6 yr, Testi et al. 2014), required for particles to become cores and eventually planetesimals ending in planets. However, some additional factors should be also taken into account: (i) the full disk lifetime is larger than the time scale of mass exchange in the disk, resulting in more available time for the final planetary mass to be assembled. In particular, in the GGD 27–MM1 disk, where infall is still significant,

the disk is still being replenished with new material from the surrounding envelope that makes its life longer; (ii) at later stages, hydrodynamic models show that the accretion of material onto planet embryos can largely exceed the accretion onto the star itself (Zhu et al., 2011), speeding up the planet formation; (iii) the density of particles in massive disks is much higher than in low-mass disks. Thus, the density of planetesimals would be higher and one would expect planet assembling to be faster than in the low-mass case, analogously to what happens in the formation of the star itself, which is a faster process for high-mass stars; (iv) lastly, for low-mass stars there is both theoretical (Lambrechts and Johansen, 2012) and observational evidence (HL Tau: Carrasco-González et al. 2016; TMC 1A: Harsono et al. 2018) suggesting that planet formation starts very early in the star-formation process. These results imply that the planetary formation process might be faster than initially thought and compatible with the time scales of massive star-formation.

Obtaining observational constraints on the location of the water snow line in the GGD 27–MM1 disk would be of major importance to inform about the plausibility of gas planet formation around this massive protostar. We note that in low-mass protostars, water snow lines are difficult to detect because they are commonly located at very small distances, of only a few au, from the star, requiring a very high angular resolution to detect them. Cieza et al. (2016) observed V883 Ori during an outburst, when an increase in luminosity drove the water snow line out to more than 40 au (∼0.1 arcsec at the distance of Orion), making the detection feasible. Since in the GGD 27–MM1 disk the water snow line is expected to be located at a radius of ∼170 au, resulting in a similar angular separation, ∼0.1 arcsec, at the distance of GGD 27–MM1, it would not require of a stellar outburst, as in the case of low-mass protostars, to become detectable. High angular resolution ALMA observations of the GGD 27–MM1 disk at several frequencies could help to constrain the presence of the water snow line by looking for spatial variations of the dust optical depth (e.g., Cieza et al., 2016).

3.9. Conclusions

We used ALMA continuum observations at 1.14 mm, obtained with an angular resolution of ∼40 mas, to model the accretion disk around the central massive early B-type protostar exciting the powerful HH 80–81 radio jet using α-viscosity prescription. We found an enclosed mass of 21–30 $M_\odot$, of which 5–7 $M_\odot$ can be attributed to the disk. This mass is consistent with the derived dynamical mass of 31 ± 1 $M_\odot$ and 21 ± 1 $M_\odot$ for the SO_2 $9_{2,8}$–$8_{1,7}$ and $19_{3,17}$–$19_{2,18}$ lines, respectively. The radius of the disk is ∼170 au, with an inclination angle of 49º. We compared the physical structure, temperature and density profiles, obtained with our model with power law functions, showing that the GGD 27–MM1 system is a potential template for future similar studies in other high-mass protostars. In particular, we obtained a flared disk with a maximum scale height of ∼13 au, and a temperature profile that ranges from ∼150 K at the outskirts of the disk up to ∼1400 K at the inner edge of the disk. The analysis of the Toomre Q parameter, evaluated at the disk mid-plane temperature, indicates that the disk is stable up to a radius $R_{\rm disk} \simeq 100$ au. This work shows that the D'Alessio models can be used as a first approximation in the modeling of accretion disks around massive protostars, providing in addition several observational predictions.

We also reported the presence of an unresolved compact source at the center of the accretion disk, with a radius of 4 mas (∼5.6 au at the source distance of 1.4 kpc) and a brightness temperature of $\sim 10^4$ K, most likely tracing ionized gas. The origin of this compact source is uncertain, it could arise from an incipient, extremely compact HII region or from the base of the HH 80–81 radio jet. Observations at higher angular resolution would help to determine the nature of this compact source.

Finally, we have estimated a distance of 1.2-1.4 kpc to the GGD 27 star-forming region based

on the Gaia DR2 catalogue combined with near-IR polarimetric data of the YSOs in the region and the extinction maps.

A. The distance to the LDN 291 cloud

The GGD 27 nebulosity and the objects associated to the region (e.g., HH 80-81, and the HH 80N star forming core Heathcote, Reipurth, and Raga, 1998; Girart et al., 1994; Girart et al., 2001; Masqué et al., 2011; Masqué et al., 2013) are located in the LDN 291 large molecular cloud complex (including the dark clouds LDN 306, 314, 315 and 322) that extends ~ 4 in Sagittarius (Lynds, 1962; Reipurth, Rodney, and Heathcote, 2008; Saito et al., 1999). The distances reported in the literature range between 1.5 and 2.4 kpc (e.g. Racine, 1968; Humphreys, 1978; Rodriguez et al., 1980). However, the most used value in the literature is 1.7 kpc. For this distance, the spatial scale of LDN 291 cloud complex is ~75 pc × 19 pc and the mass is ~1.2 $10^5 M_\odot$ (Saito et al., 1999).

A.1. Analysis

Here we present two different approaches to better estimate the distance to the LDN 291 / GGD 27 region. The two approaches rely on the Gaia DR2 catalogue (Gaia Collaboration et al., 2016; Gaia Collaboration et al., 2018). First, we used data from Gaia in combination with near-IR polarimetric data of the YSOs located in the GGD 27 region (Kwon et al., 2016). The second approach is to use the on-line *STILISM*[1] application (Capitanio et al., 2017; Lallement et al., 2018), which combines the Gaia data with extinction maps to obtain 3-D dust maps of the Galaxy.

Method 1: Young Stellar Objects in GGD 27 and Gaia

Figure 13 shows the polarization fraction as a function of the Gaia DR2 parallax for the YSOs in GGD 27 (from the Kwon et al. (2016) and This figure shows that the YSOs population with counterpart in GAIA have distances clearly smaller than the distance adopted in the literature, 1.7 kpc. Most of the YSOs have parallaxes between ~0.6 mas (1.67 kpc) and 1.2 mas (830 pc) but with significant uncertainties. However, there are two objects that have large parallaxes. One of them is [HL85] GGD 27-28 31 (Hartigan and Lada, 1985). It is located at a distance of 362 ± 58 pc but has very high polarization levels (26%, 42% and 57% in the *JHK* bands, respectively; Kwon et al., 2016). This star is located in front of the bright GGD 27 nebula, where high levels of circular polarization are detected. Therefore, the near-IR linear polarization is likely coming from the nebula and it is not related with the optical star. The other star, 2MASS J18185959-2045537, is located at 395 ± 31 pc and it exhibits no polarization in the near-IR, which indicates that this is a (cold) foreground star not related to the cloud. In order to estimate the distance we calculated for the YSOs the average value of the Gaia parallaxes weighted with the uncertainty:

$$< \pi_{\rm GGD27} >= \frac{\sum_i^N \pi_i/\sigma_i^2}{\sum_i^N 1/\sigma_i^2} \tag{5}$$

and the uncertainty is:

$$\sigma(<\pi>) = \sqrt{\frac{N}{\sum_i^N 1/\sigma_i^2}} \tag{6}$$

[1] https://stilism.obspm.fr

π_i and σ_i are the parallax for each star and its uncertainty, respectively, from the GAIA DR2 catalogue. We excluded four stars with parallaxes, within their uncertainties, larger than 0.9 mas (with distances less than $\simeq$ 1100 pc). Using the rest of the sample, we obtain an average, weighted by the uncertainty, parallax of 0.801 $\pm$ 0.106 mas. Therefore, the distance to the YSO cluster is 1248±166 pc.

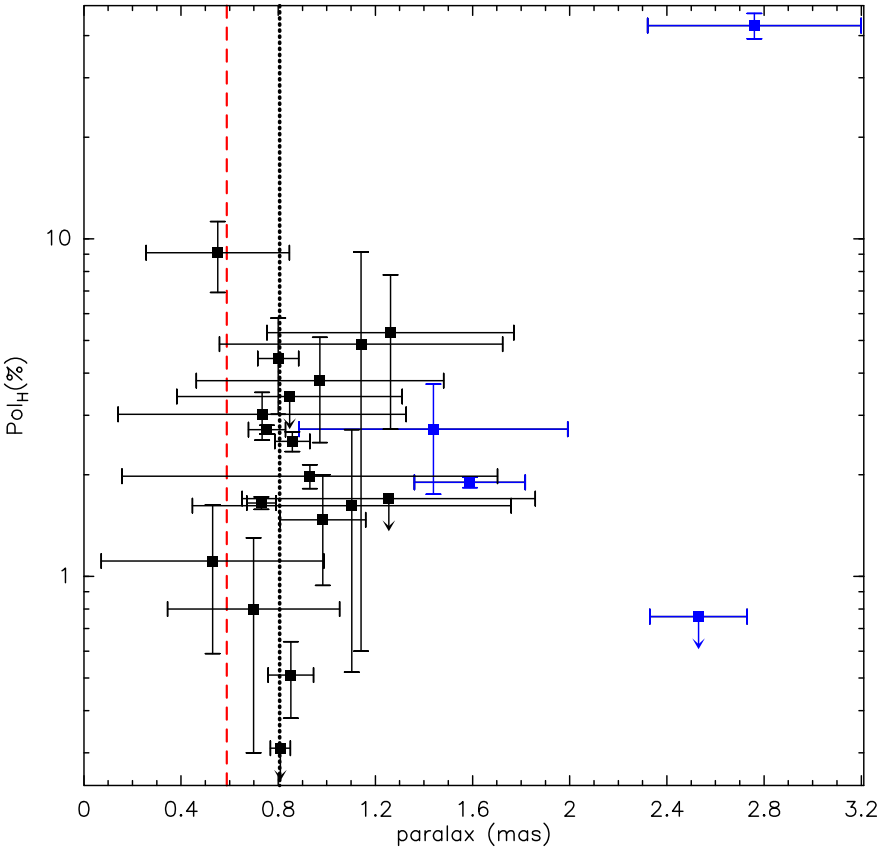

Figure 13: Gaia parallax (in mas) *versus* polarization fraction in the *H* band for the YSO stars that appear in any of the Kwon et al. (2016) and Qiu and Zhang (2009) catalogues. The blue color stars have distances smaller than ≃1100 pc (considering their error bars), suggesting that they are not associated with the cloud. These stars were not used in the cloud distances estimation. The black dashed vertical line shows the averaged parallax (weighted by the uncertainty) of the YSOs in GGD 27, 0.81 mas (1.25 kpc). The red dashed vertical line shows the parallax for the distance previously adopted in the literature, 1.7 kpc.

Method 2: Extinction-Gaia data – *STILISM*

A recent work (Danielski et al., 2018) has correlated the Gaia distances and the corrected version of G extinction with archival ground based data, specially with 2MASS and SDSS/APOGEA-DR14 (Capitanio et al., 2017; Lallement et al., 2018). This allows to derive 3D maps of the extinction as a function of the distance. We used the on-line tool that provides the cumulative reddening curve as a function of the distance for a given line-of-sight. Figure 14 shows the $E(B-V)$ extinction as a function of the distance toward the LDN 291 / GGD 27 region. It clearly shows two abrupt increases of the extinction, a small one ($E(B-V)$ ~0.2 mag or A_V ~0.6 mag) around 100 pc and a larger one ($E(B-V)$ ~0.7 mag or A_V ~2.0 mag) around 1200 pc. In order to fit the two abrupt extinction jumps, we used the following approach:

$$E(B-V) = \frac{A_0}{1+e^{-A_1(D-D_{\rm jump})}} + A_2 D + A_3, \quad (7)$$

where D is the distance, $D_{\rm jump}$ is the distance where the jump occurs and A_i (i = 0, ..., 3) are free parameters. We used a reduced χ^2 fit. The distance for the large jump is 1270 ± 65 pc. We also used this expression to estimate the first small extinction jump, obtaining a distance of 119 ± 15 pc.

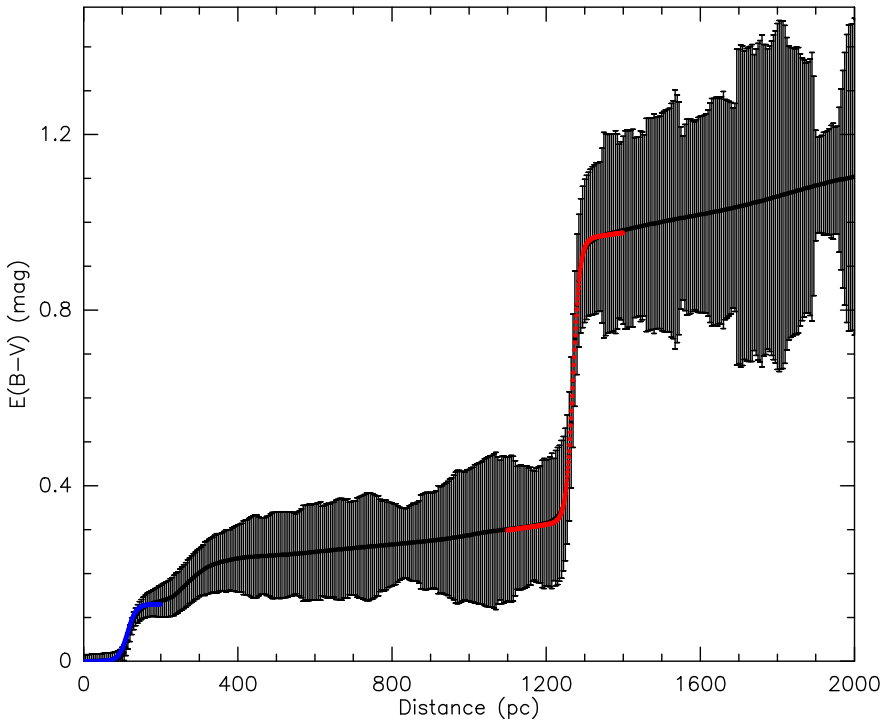

Figure 14: $E(B-V)$ extinction (in magnitudes) as a function of the distance toward the GGD 27 region obtained from the *STILISM* (Structuring by Inversion the Local Interstellar Medium) online application (Capitanio et al., 2017; Lallement et al., 2018). The blue and red lines are the fit to the visual extinction jump at 119 and 1270 pc, respectively.

Distance to the GGD 27 nebula/molecular cloud

The YSOs detected with Gaia are likely near the surface of the cloud, otherwise the cloud extinction would make them not visible at optical wavelengths. Indeed, most of the *Spitzer* YSOs from Qiu and Zhang (2009) do not have optical counterparts. The previous analysis indicates that the average distance within 1-σ uncertainty is between ~1100 to 1400 pc. The second method is even more very sensitive to the cloud's surface, giving a distance between 1200 and 1340 pc (also at 1 σ level). Therefore, combining both methods, we can constrain the distance to the GGD 27 region in the range of 1200 to 1400 pc.

B. Model robustness

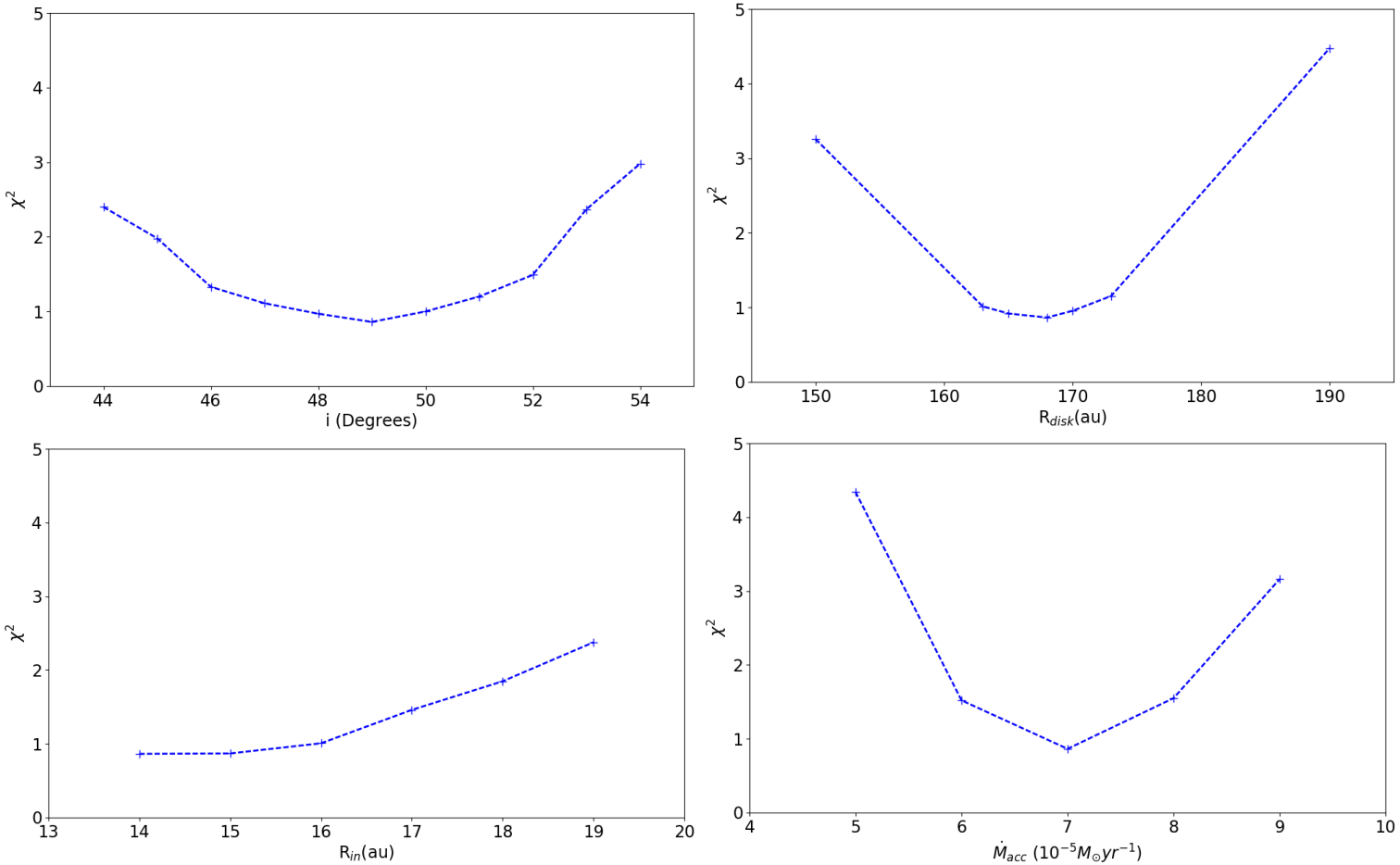

Figure 15: χ^2 for the best fit model varying inclination (upper left), R_{disk} (upper right), R_{in} (bottom left), $\dot{M}_{acc}$(bottom right).

As we already advanced in Section 3.6, Figure 15 shows how the χ^2 value changes when we vary the main parameters of the disk, while fixing the others to the best fit value. The same scale for the Y-axis (χ^2) is used in the four panels. The parameters under study were varied between ~10% and ~30% according to the observational restrictions (see Section 3.5). The four parameters show a minimum at the value of our best fit model. The panel shows that the model is much more sensitive to changes in inclination and disk radius, where the parameter variations are around 10%, compared to changes in the inner radius and accretion rate, where the variations are over 30%.

Regarding the inner radius, we situated the sublimation wall at 12 au (± 2 au), based on the luminosity and the dust sublimation temperature. Inward from this border the dust can not survive, thus we can not obtain a physically consistent model with an inner radius smaller than 14 au. In addition, an inner radius larger than ~20 au (~14 mas) is discarded because it should have been observed with the angular resolution of our ALMA observations.

Chapter 4

Conclusions and open challenges

In this thesis we present the results of a multi-scale study of the high-mass star formation process with a double approach, theoretical and observational. We aim to study the high-mass star formation process at molecular cloud scale and analyse the fragmentation process in hub-filament systems that precedes the formation of the stellar clusters where massive stars are born. It is though that thermal Jean fragmentation is the main mechanism controlling the fragmentation process. Yet, others ingredients, such as turbulence, protostellar feedback, angular momentum and magnetic fields, are also likely crucial as well, and regulate the way the fragmentation is produced, enhancing or inhibiting it. In this work, our goal is to investigate the role of the magnetic field in the fragmentation process and whether its morphology and strength are able to suppress or promote the fragmentation of a massive core. We also study the massive star formation process by going down to disk scales (few tens of au). It is though that high-mass stars can be formed through an accretion disk. This disk allows the star to keep accreting even when it has reached a mass of more than 10 $M_{\odot}$. We aim to better understand massive star formation at disk scales with a novel approach: we have used a disk model originally developed for low-mass stars. Our goal is to check whether this low-mass disk model can serve as a first approximation to extract the physical properties of a disk around a massive star. In the following we present the main conclusions of this thesis.

4.1. Role of the magnetic field in the fragmentation process: the case of the G14.225-0.506

In this chapter we studied the role of the magnetic field in the process of core fragmentation toward two apparently twin hubs (Hub-S, Hub-N) surrounded by a complex network of filaments in the infrared dark cloud G14.225-0.506. Despite the similarity in physical conditions at core scales (~0.1 pc), the two hubs present different levels of fragmentation at smaller scales (~0.03 pc). To perform this study we have observed the polarized thermal dust emission at 350 μmwith the CSO with an angular resolution of 10″ (~0.1 pc) toward the two hubs. In addition, we complemented these observations with the study of the magnetic field strength in both hubs with the aim of investigating whether the magnetic field is linked to the different levels of fragmentation found in these two hubs. We applied the polarization–intensity-gradient technique developed by Koch, Tang, and Ho (2012a) to investigate the relative significance of the magnetic field compared to gravity, and assess the magnetic field strength using the DCF method. The main conclusions are:

- We found that at core scale the morphology of the magnetic field is different for the two hubs. On one hand, toward Hub-N we find a nearly uniform magnetic field orientation in the

east-west direction, almost perpendicular to the major axis of the hub-filament system. In addition, the intensity-gradient in Hub-N presents a single local minimum coinciding with the bright dust continuum core MM1a. On the other hand, in Hub-S the magnetic field presents a bimodal distribution, with one component coming along north-east to the south-west direction and the other component coming along north-west to the south-east direction. In this hub, the intensity gradient reveals two minima, reflecting the bimodal distribution of the magnetic field, as each component points toward one of the two intensity gradient minima. The intensity-gradient analysis has proven to be very sensitive to intensity variations and therefore very useful for studying fragmentation. This result suggests a scenario in which the magnetic field is dragged by the collapsing cores.

- One of the main tools for the analysis are the $|\delta|$ angle, i. e., the angle between a projected magnetic field orientation and an intensity gradient direction, and Σ_B, the local magnetic field significance in the presence of gravity and any hydrostatic pressure. The analysis of the $|\delta|$-map and Σ_B-map in Hub-N indicates that, near the hub, gravity dominates the magnetic field. The intensity gradient is parallel to the magnetic field lines, both east and west of the hub, suggesting that the magnetic field is channeling material toward the central ridge or that the B-field is being dragged by gravity.

- We found higher values of the magnetic field strength in Hub-N than in Hub-S by a factor less than four, although the overall magnetic fields strength of the two hubs are not very different. We note that this is partially due to the lack of statistics in the polarization data of the Hub-S. In any case, our findings supports the idea that the different levels of fragmentation in these two hubs could result from differences in the magnetic field.

In short, the different levels of fragmentation observed in these two hubs could arise from the differences in the magnetic field properties rather than from different intensity of the gravitational field because the density in the two hubs is similar. However, environmental effects such as the influence of the HII region IRAS 18153−1651 with a bolometric luminosity of $\sim 10^4\ L_\odot$ (Jaffe, Stier, and Fazio, 1982), could also play a role.

4.2. Modeling the accretion disk around the high-mass protostar GGD 27-MM1

In this chapter we studied the accretion disk around a massive protostar. Our goal is to understand if a massive star can be formed through an accretion disk and, if so, whether this disk is similar to those found around low-mass young stars. To reach our goal we proposed to use the irradiated α-accretion disk models developed by D'Alessio et al. (2006) which has successfully explained the emission of accretion disks around low and intermediate mass young stars. We have modelled the ALMA 1.14 mm continuum emission of the accretion disk surrounding the high-mass early-B type star GGD 27-MM1 obtained with an angular resolution of ∼40 mas, which corresponds to ∼56 au at the source distance. Such angular resolution coupled with the extraordinary sensitivity of ALMA (rms $\approx 60\ \mu$Jy beam^{-1}) has allowed to resolve the disk around the massive protostar. We have taken advantage of the disk's impressive image and its apparent resemblance to low-mass disk-jet-star systems (see Fig. 4.1) to apply the disk models developed for T Tauri stars. Here are our main conclusions:

- We found an enclosed mass of 21–30 $M_\odot$, of which 5–7 $M_\odot$ can be attributed to the disk, around 25% of the central star mass, while the typical masses in the low-mass case are below

10% (e. g., Andrews et al., 2018). This mass is consistent with the derived dynamical mass of 31 ± 1 $M_\odot$ and 21 ± 1 $M_\odot$ for the SO_2 $9_{2,8}$–$8_{1,7}$ and $19_{3,17}$–$19_{2,18}$ lines, respectively. The radius of the disk is ∼170 au, with an inclination angle of 49º. The surface density ranges between 1400 and 400 g cm^{-2} and it can be fitted with a power law as a radius function ($r^{-0.5}$) similar to those found in disks around low-mass stars (e. g., Isella, Carpenter, and Sargent, 2009).

- We compared the physical structure, temperature and density profiles obtained with our model with power law functions, showing that the GGD 27–MM1 system is a potential template for future similar studies in other high-mass protostars. In particular, we obtained a flared disk with a maximum scale height of ∼13 au, and a temperature profile that ranges from ∼150 K at the outskirts of the disk up to ∼1400 K at the inner edge of the disk. This temperature is much more higher than the typical temperature in the low-mass case, which range between ∼300-10 K (e. g., Tazzari et al., 2017).

- The analysis of the Toomre Q parameter, evaluated at the disk mid-plane temperature, shows a value larger than 1, indicating that the disk is stable up to a radius $R_{\rm disk}$ ≃100 au. Despite being very massive, which could generate an unstable disk, the high temperature makes it remain in stable conditions until ≃ 100 au where the temperature is no longer so high.

- We estimated the water snow line location on the disk edge (∼170 au). It is though that water snow lines are important because they can trigger the growth of grains to pebbles and lastly to planets and because they mark the border between rocky planets formed inward of this line and giant gas planets formed outside. In the case of the GGD 27–MM1 disk, we expect the formation of gas planets to be hampered by high disk temperatures, being restricted to radii near the disk edge. Consequently, we speculate that if the formation of gas planets were to occur in disks around massive protostars, in general, they would be formed at distances around hundreds of au. It is unclear, however, whether such giant planets could survive after the onset of an HII region around the massive star.

- We also reported the presence of an unresolved compact source at the center of the accretion disk, with a radius of 4 mas (∼5.6 au at the source distance) and a brightness temperature of ∼10^4 K, most likely tracing ionized gas. The origin of this compact source is uncertain. It could arise from an incipient, extremely compact HII region or from the base of the HH 80–81 radio jet. Observations at higher angular resolution would help to determine the nature of this compact source.

- We have estimated a distance of 1.2-1.4 kpc to the GGD 27 star-forming region based on the Gaia DR2 catalogue combined with near-IR polarimetric data of the YSOs in the region and the extinction maps. Furthermore, our model of the GGD 27-MM1 accretion disk discards the initially reported distance in the literature (∼1.7 kpc), but suggesting a distance similar to the one obtained using the GAIA data.

In summary, we found a compact (∼170 au), very massive (∼5 $M_\odot$), and stable accretion disk. We also have found hints of the presence of an unresolved compact source at the center of the disk whose origin is unclear. This work shows that the D'Alessio models can be used as a first approximation in the modeling of accretion disks around massive protostars, providing in addition several observational predictions.

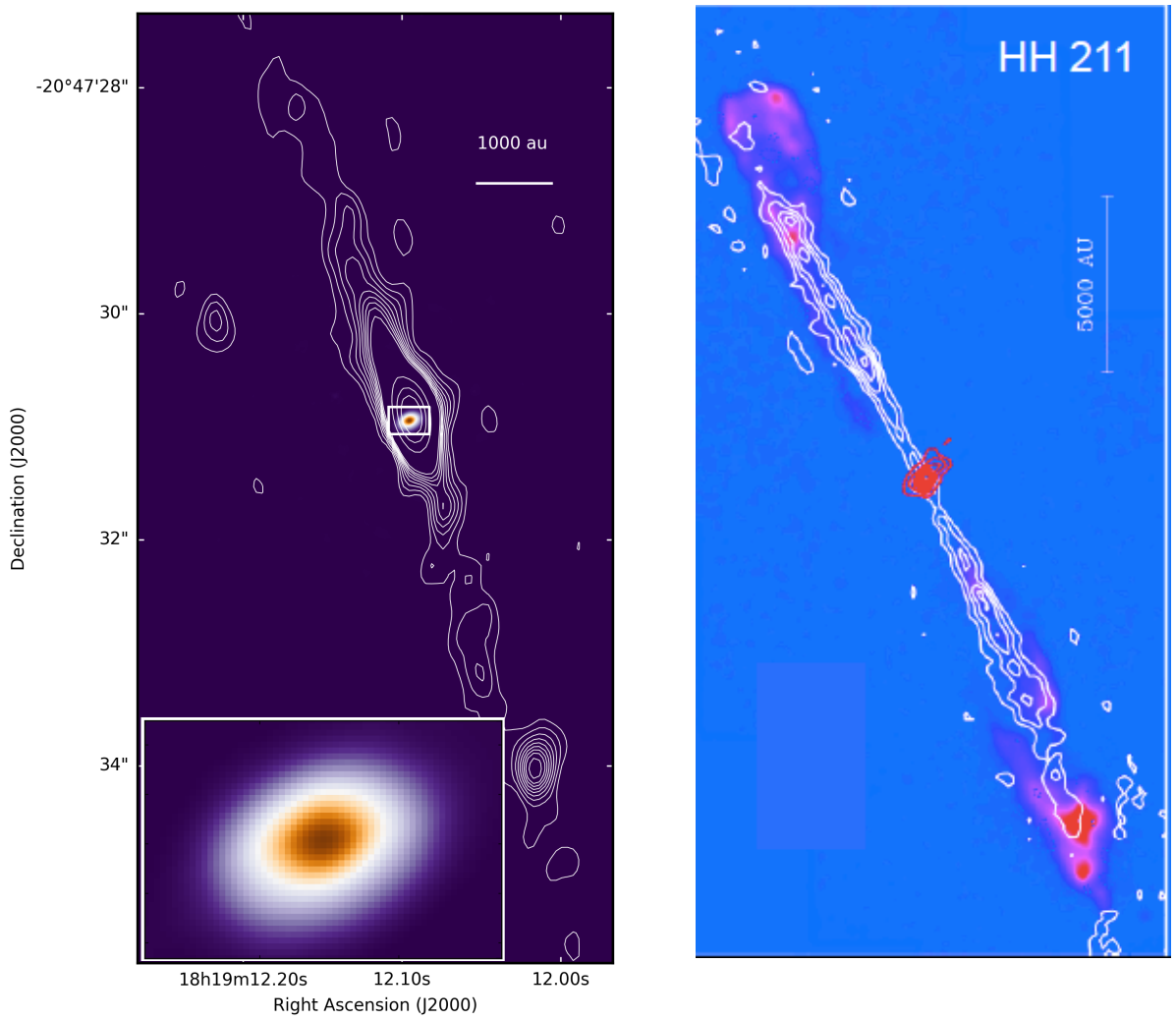

Figure 4.1: Left: HH 80–81 high-mass disk-jet system. The color image shows the dust continuum emission of the disk observed with ALMA at 1.14 mm with ~40 mas angular resolution (~56 au) (Girart et al., 2018). In contours it is shown the VLA image at 3.6 cm of the radio-jet observed with an angular resolution of ~0.4 arcsec (Carrasco-González et al., 2012). Right: HH 211 low-mass disk-jet system (Gueth and Guilloteau, 1999). CO J=2-1 emission (whithe contours) integrated for velocities lower than 2.2 km $s^{-1}$and larger than 18.2 km s^{-1}; and superimposed on the H_2 v=1–0 S(1) emission (colorscale; from McCaughrean, Rayner, and Zinnecker, 1994) and the 230 GHz continuum emission (red contours; contours are 10, 30 and 50 mJy/beam). The spatial scale is indicated in both panels.

4.3. General conclusions

This thesis aimed to provide a global vision of the formation process of high-mass stars, starting from the fragmentation of the IRDC G14.225-0.506 that gives rise to stellar clusters where low- and high-mass stars are formed, down to the accretion disk around the massive protostar GGD 27-MM1. The common thread is the magnetic field. The fragmentation of a cloud is though to strongly depend on the cloud magnetic field strength, and MHD simulations predict low fragmentation level in a highly magnetized environment. Our results in G14.2 support those predictions. Furthermore, in a scenario where magnetic field is strong enough to inhibit significantly the fragmentation of a massive core, the formation of dense and massive nuclei is plausible, which may lead to the formation of a massive star. The presence of a accretion disk is key for the star to grow more than $\sim$10 $M_{\odot}$. The work done in this thesis confirms this scenario and also shows that the disk studied (GGD 27-MM1) has a similar structure as those around low mass stars but it is larger and much more massive. However, this fact is in apparent contradiction with the expected outcome in a strongly magnetized core: the magnetic field will efficiently inhibit or suppress the formation of a rotational supported disk through "catastrophic magnetic braking". This strongly suggest that some diffusive processes of the magnetic field should occur, probably in an early stage, i.e., in the formation of a massive nuclei in the center of the core.

In the next sections we describe the open questions triggered by this thesis and we indicate possible lines of research for future work.

4.4. Open questions and future prospects

In this thesis, we aimed to answer several questions regarding the role of the magnetic field in the formation of high-mass stars and in particular in the fragmentation process of dense clumps. We also set out to understand the accretion process in high-mass stars by studying the accretion disk. Next we describe the questions that have been left open.

Regarding the IRDC **G14.225-0.506**:

- The analysis toward the IRDC G14.225-0.506 shows an uniform magnetic field structure in Hub-N, even in the densest regions. We speculate that the magnetic field is dragged by the collapsing material, following the accretion flow that feeds the filament, that is why the magnetic field tends to be oriented mostly perpendicularly to the filaments. However, we cannot rule out that it is the magnetic field that is channeling the material or even, a combination of both effects is taking place.

- Within dense filaments, it is expected, from MHD simulations, that the magnetic field lines would bend into the filament due to the flow toward the hub showing a characteristic 'U' shape (Gómez, Vázquez-Semadeni, and Zamora-Avilés, 2018). Actually, Pillai et al. (2020) recently reported a transition of the magnetic field orientation from perpendicular to parallel to the filament upon reaching a certain visual extinction ($A_V \geq 21$) at < 0.1 pc scale. This result provides observational evidence for gravity entraining the frozen-in large-scale magnetic field traced by near-infrared polarization data, and causing it to become parallel to the gas flow that is feeding the forming cluster. However, such magnetic field morphology is not appreciated in Hub-N with our angular resolution ($10''$, $\sim$0.1 pc). A possible reason for that is a lack of spatial resolution.

- Since a certain level of fragmentation has been observed in both hubs of the IRDC G14.225-0-506, studying the magnetic field at core scales will show its behaviour closer to the gravitational collapse zone. In the next section I will return to this idea to talk about the work we are currently developing.

- Finally, we found different magnetic field strength in both hubs, which can be related with the different fragmentation levels observed in these hubs. However, it is necessary to further analyse the magnetic field, specially in the Hub-S, where the current CSO data are very sparse.

In addition to these questions, there are other unknowns that could pose a scientific challenge. For example, which is the evolutionary state of the different fragments detected in the two hubs?, are these different between the two hubs?. Answering these questions is challenging and raises new questions as, how to measure the evolutionary state? through near/mid-IR observations?. If we cannot escape the image saturation due to the presence of massive stars, can we analyse the evolutionary state through the chemistry of the fragments? and if so, how to differentiate evolution versus density/temperature effects in the chemical composition?

Regarding the accretion disk around **GGD 27–MM1**:

- We successfully modeled the disk around a massive star using a model designed for low-mass stars. However, additional tests in other massive stars are necessary to determine if we are dealing with a unique case, or this type of jet-disk-star systems are common.

- We reported the presence of a compact source in the center of the disk with a brightness temperature estimated of $\sim 10^4$ K. We propose that such a compact, hot source could be an extremely compact HII region (a nano-HII region) or the base of the HH 80–81 radio jet. However, new observations will be necessary to decipher the origin of such emission.

- The model, because it was intended for low-mass stars, neglects the effect of the disk's autogravity. Certainly, it is necessary to develop a self-consistent model that considers self-gravitation and to compare the results.

- Our model does not include the effect of an envelope surrounding the protostar. We tested the effect of the envelope at millimeter wavelength, in terms of emission attenuation, and we found a negligible contribution. However, the envelope can provide an additional source of heating by absorbing and re-emitting the energy received from the central protostar. Therefore, it would be very interesting to include this effect in the model.

There are, of course, other interesting questions that are beyond the scope of this thesis but that undoubtedly can inspire future research.

Concerning the study of accretion disks, nowadays, dust continuum observation with ALMA have proved that ringed substructures and gaps, interpreted as symptoms of planetary formation, are ubiquitous in protoplanetary disks around low-mass stars (Carrasco-González et al., 2019; Cieza et al., 2019; Maury et al., 2019; Williams et al., 2019). Therefore, one might wonder if massive stars are capable of forming planetary systems and, therefore, if these substructures are present in massive disks as well. The advent of technology that will allow observations with very long baselines at longer wavelengths (e. g., ALMA band 3 and band 1) will allow to be more sensitive to substructures in massive disks. Besides, the high angular resolution that will be achieved will allow us to distinguish the strong jet emission at these frequencies. Thus, the

following questions arise: will we find structures similar to those observed in low-mass disks (e. g., HL Tau) in disks around massive stars? Are disks around massive stars able to form planetary systems? At what distance from the central star could such planets form? On what time scale would they be formed?

Our study of GGD 27-MM1 indicates that the snow line would be located in the outer zone of the disk (~170 au) and therefore from there, the formation of giant gas planets could be considered. More studies towards massive systems with high angular resolution and high sensitivity are needed to answer all these questions. Furthermore, new and more sensitive observations will help to narrow down the ranges of the physical parameters that serve as input values to the model. In this way, possible model degenerations could be reduced. Also, the new information will help update the model and to evaluate which factors must be considered in the massive case. For example, a more accurate estimate of the mass of the disk could conclude that self-gravity cannot be neglected in a more realistic model.

Another important open question is the role of the magnetic field in the formation and evolution of accretion disks. In addition, the detection of the magnetic field in disks presents an unrivaled scientific challenge. Today, several processes compete to explain the alignment of the dust grains and therefore to explain the polarization of the dust thermal emission. Besides, the density and opacity found in accretion disk environments poses great added difficulty.

Regarding future technological advances, nowadays ALMA covers the wavelength range between 3 mm up to 0.3 mm, observing at millimeter wavelengths where the brightest dust emission arises from millimeter-sized dust grains. In order to probe grain growth it is necessary to carry out observations of the dust thermal emission at cm wavelengths where dust opacity is dominated by centimeter-sized dust particles. In the near-/mid-term future, the arrival of the Square Kilometer Array (SKA) and the Next Generation Very Large Array (ngVLA) will allow to observe cm dust emission at higher angular resolution and sensitivity, similar to ALMA. Their angular resolution and sensitivity is essential to study the grain growth and planet formation in protoplanetary disks.

4.5. Current and future work

+ Further analysis of the IRDC **G14.225-0.506**

  During this chapter we have posed various questions derived from the study developed in this thesis. Therefore, in order to answer these open questions, further observations of dust polarization with higher sensitivity and/or at higher angular resolution are needed. We aim to further investigate the magnetic field structure within the dense filaments and at core scales and two lines of research are being developed in this regard.

  - On one hand, we are currently analysing polarimetric ALMA observation at millimeter wavelengths (1.3 mm) with an angular resolution of ~2″ (~4000 au at the source distance) toward both Hub-N (Fig. 4.2, panel A) and Hub-S (Fig. 4.3). We also count with single pointings observations toward the filamentary structure around Hub-N (see Fig. 4.2, panels B, C and D). We intent to develop an statistical analysis of the position angles at 1.3 mm and to compare them with the previous CSO 350 μm observations at ~10″. We also plan to apply the polatization-intensity-gradient method to the ALMA observation and to compute the magnetic field strength at core scale. We aim to test how magnetic field change (or not) at core scales compared with the cloud scale magnetic field.

- On the other hand, we participate in an observational campaign towards the two hubs and the filamentary region between them, making use of the Stratospheric Observatory for Infrared Astronomy (SOFIA). This work, led by Dr. Fabio Santos and of which I am a co-investigator, consists of polarimetric observations at 150 μmwith an angular resolution of $\sim 13''$ (similar to the CSO). These observations will allow us to apply the polarization-intensity-gradient technique in Hub-S and to obtain the magnetic field significance since with the current data of the CSO it was not possible. In addition, the field of view of this new observation includes the filamentary structure that connects the two hubs. Thus, we will analyse the magnetic field morphology and strength not only in hubs but also within the dense filaments converging toward the hubs.

Both works complete an ambitious multiscale study of the IRDC G14.225-0.506, which includes observations of polarization at optical, near-infrared, far-infrared (SOFIA), and millimeter (SMA) wavelengths, in addition to the works presented in this thesis.

Another possible line of research on the different levels of fragmentation detected in these two hubs falls to the assumption that both hubs are in different evolutionary states. Different evolutionary states could explain both the different levels of fragmentation and the different morphology of the magnetic field. Thus, to study the evolutionary state, we plan to obtain a molecular inventory at 1 mm and to derive the continuum spectral index toward two 0.1 pc-twin hubs with different level of fragmentation at 0.01 pc scales. The science goal is to evaluate the evolutionary state of the hubs. In order to achieve this, the approach is to characterize and look for chemical/dust differentiation of the fragments in each hub, and to study the overall kinematics of the hub-filament systems. I intent to characterize the dense cores previously detected with the SMA at 1.3 mm, through new SMA observation. By this observation, I will investigate the molecular population by looking for significant chemical differentiation between cores.

+ Further analysis of the high-mass protostar GGD 27–MM1

Several ideas for future work have emerged during the development of the modeling project of the accretion disk around GGD 27–MM1. For the near future, we propose the following works:

- The best fit model gives us an inner radius, the border from which the dust sublimates, of ~14 au. Considering the sublimation temperature of the most refractory grains (~1200 K) and the observed luminosity (~1.9×10^4 $L_\odot$; Fernández-López et al., 2011b) and assuming that sublimation is the mechanism responsible for producing the inner hole, we can locate the sublimation wall, where dust reaches its sublimation temperature, at ~12 au of radii. The 1.14 mm ALMA visibilities with baselines larger than 4000 kλ trace an unresolved ($R < 8$ au) source. The lower limit of the brightness temperature, ~1000 K, suggests that the emission is probably ionized gas associated with the base of the jet, or with an unresolved and incipient HII region (a nano-HII region). We plan ALMA observations at the highest angular resolution possible (~10 milli-arcsec at 860 μm to resolve for the first time the inner part of the dusty disk and to put stringent constraints on the nature of the extremely compact (~au scales) ionized gas around a 20 $M_\odot$ star. The precise determination of the radius of the inner dusty wall will allow a much better constrain of the mass accretion rate (currently affected

by a great uncertainty), since the radius of the wall, the sublimation temperature, and the mass accretion rate are strongly related (Nagel et al., 2013). Moreover, according to our model the mass accretion rate shows an inversely proportional behavior with the inner radius. To test the feasibility of these observations we have generated synthetic images from our best model of the disk including the presumed compact source by means of a Gaussian function (see Fig. 4.4)

- We aim to investigate the evolution of high-mass accretion disks and to study if they evolve in a similar way to the low-mass case. We propose to study the possible substructure present in the disk around GGD 27–MM1. We expect that ALMA observations in band 3/band 1 would give us greater contrast between rings and gaps (e. g.,, Fig. 4.5). In addition, we will need the highest angular resolution to avoid contamination due to the jet emission, which we expect will be very intense at these wavelengths.

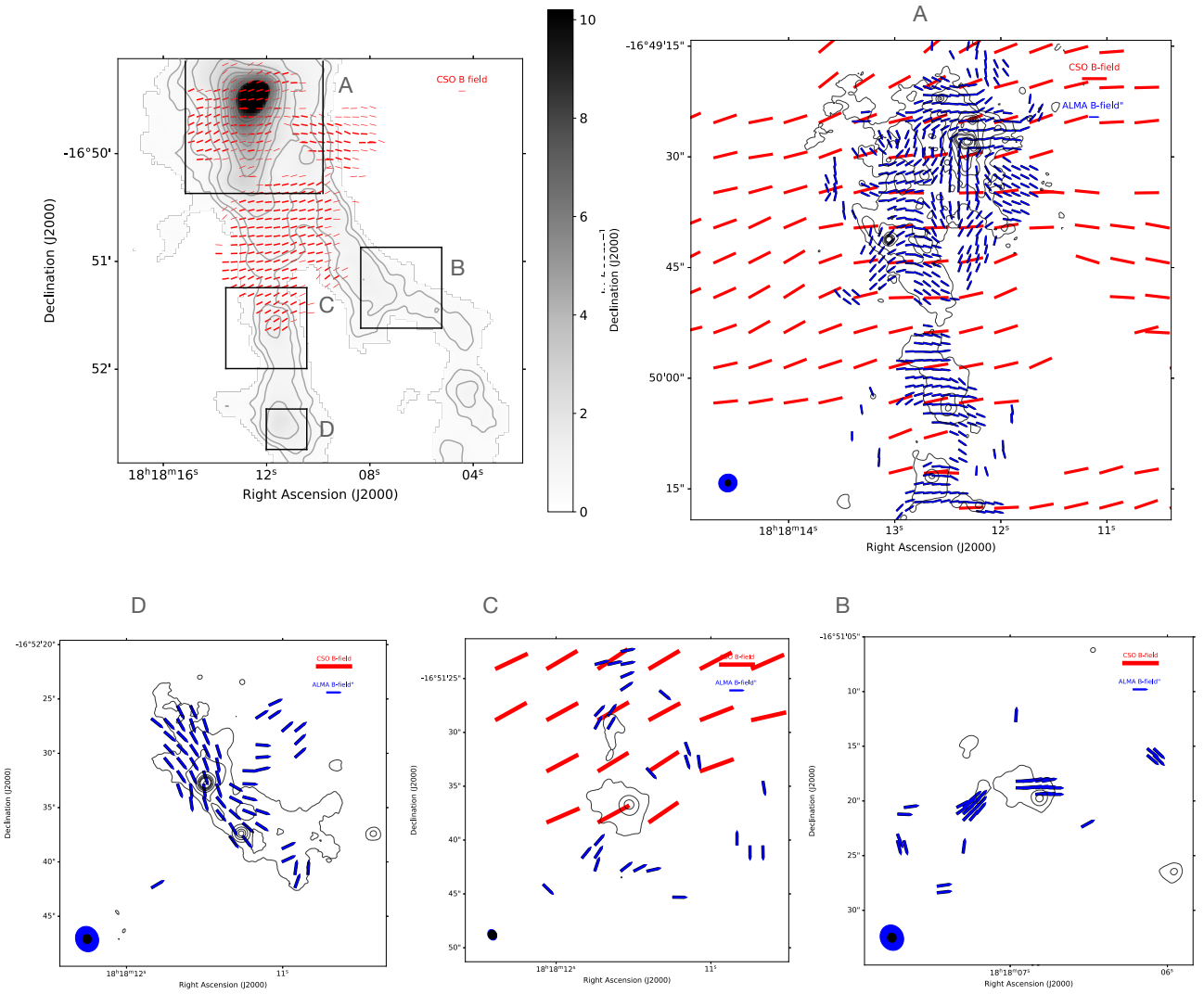

Figure 4.2: IRDC G14.2 Hub-N 350 μmCSO polarization (upper left) where we square the ALMA field of view shown in the rest of the panels. Red segments show the CSO B-field. Panel A: 1.1 mm ALMA polarization observation toward the densest millimeter core. Contours represent ALMA continuum emission showing 2, 7, 20, 40, 60, 80, 100, 200, 300 times rms noise ($\sim 20\times10^{-5}$Jy beam^{-1}), blue segments depict the B-field observed with ALMA ($\sim 2''$ a.r.) and red segments show the CSO B-field. Panels B,C and D: Similar to panel A for each of the remaining pointings.

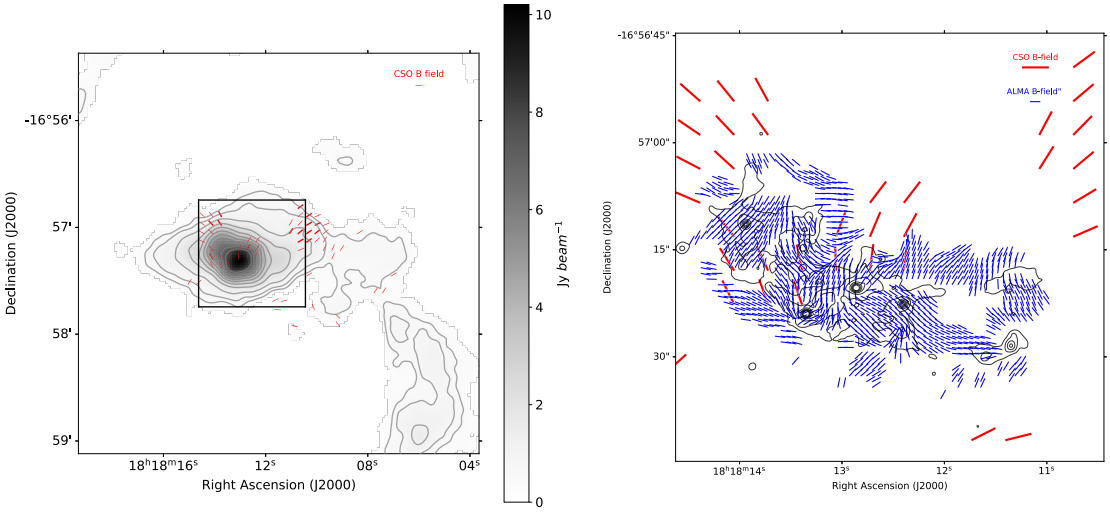

Figure 4.3: Similar to Figure 4.2 toward the Hub-S in the IRDC G14.2

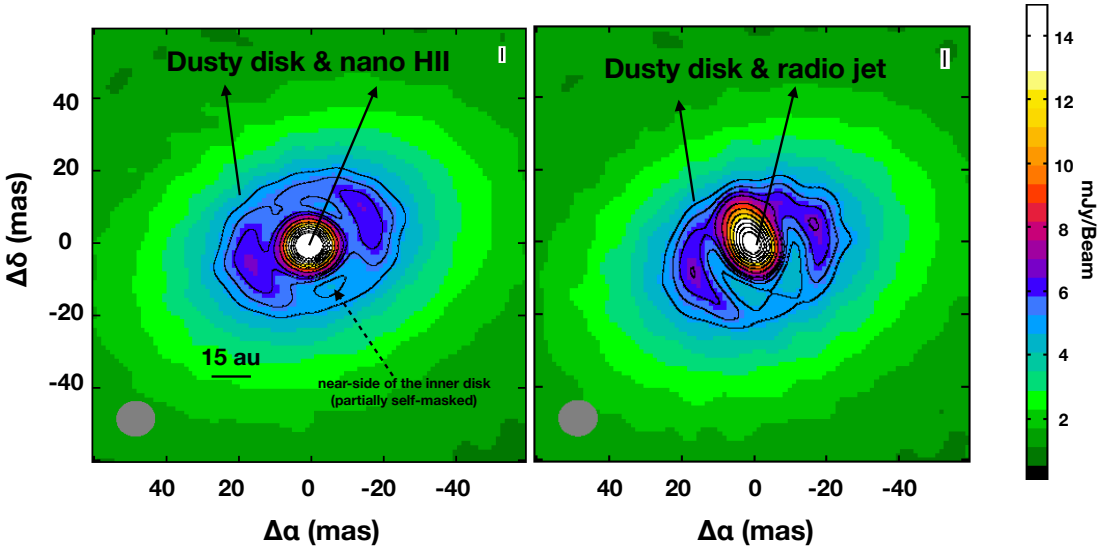

Figure 4.4: Synthetic ALMA image at 860 μmtoward the accretion disk surrounding GGD 27–MM1. We used the best fit model found in the Chapter 3 and we overlapped a circular (R=5 au; left panel) and elliptical (20x4 au; right panel) Gaussian source.

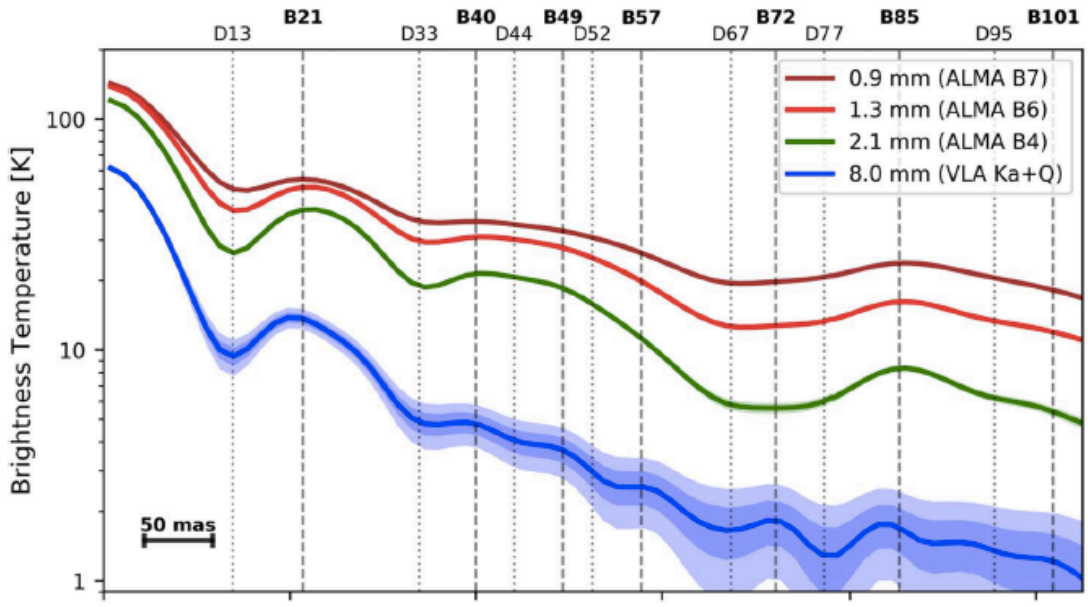

Figure 4.5: Brightness temperature as a function of the radius for HL Tau images at different wavelengths. Credits: Carrasco-González et al. (2019)

Bibliography

Añez-López, N. et al. (Jan. 2020a). "Modeling the Accretion Disk around the High-mass Protostar GGD 27-MM1". In: *ApJ* 888.1, 41, p. 41. DOI: 10.3847/1538-4357/ab5dbc. arXiv: 1911.12398 [astro-ph.SR].

Añez-López, N. et al. (Dec. 2020b). "Role of the magnetic field in the fragmentation process: the case of G14.225-0.506". In: *A&A* 644, A52, A52. DOI: 10.1051/0004-6361/202039152. arXiv: 2010.13503 [astro-ph.GA].

ALMA Partnership et al. (July 2015). "The 2014 ALMA Long Baseline Campaign: First Results from High Angular Resolution Observations toward the HL Tau Region". In: *ApJL* 808.1, L3, p. L3. DOI: 10.1088/2041-8205/808/1/L3. arXiv: 1503.02649 [astro-ph.SR].

Alves, Felipe O. et al. (Oct. 2020). "A case of simultaneous star and planet formation". In: *arXiv e-prints*, arXiv:2010.15135, arXiv:2010.15135. arXiv: 2010.15135 [astro-ph.EP].

Andersson, B. G., A. Lazarian, and John E. Vaillancourt (Aug. 2015). "Interstellar Dust Grain Alignment". In: *ARA&A* 53, pp. 501–539. DOI: 10.1146/annurev-astro-082214-122414.

Andre, P., D. Ward-Thompson, and M. Barsony (May 2000). "From Prestellar Cores to Protostars: the Initial Conditions of Star Formation". In: *Protostars and Planets IV*. Ed. by V. Mannings, A. P. Boss, and S. S. Russell, p. 59. arXiv: astro-ph/9903284 [astro-ph].

André, P. et al. (Jan. 2014). "From Filamentary Networks to Dense Cores in Molecular Clouds: Toward a New Paradigm for Star Formation". In: *Protostars and Planets VI*. Ed. by Henrik Beuther et al., p. 27. DOI: 10.2458/azu_uapress_9780816531240-ch002. arXiv: 1312.6232 [astro-ph.GA].

Andrews, Sean M. (Aug. 2020). "Observations of Protoplanetary Disk Structures". In: *ARA&A* 58, pp. 483–528. DOI: 10.1146/annurev-astro-031220-010302. arXiv: 2001.05007 [astro-ph.EP].

Andrews, Sean M. et al. (Aug. 2009). "Protoplanetary Disk Structures in Ophiuchus". In: *ApJ* 700.2, pp. 1502–1523. DOI: 10.1088/0004-637X/700/2/1502. arXiv: 0906.0730 [astro-ph.EP].

— (2010). "Protoplanetary Disk Structures in Ophiuchus. II. Extension to Fainter Sources". In: *ApJ* 723.2, pp. 1241–1254. DOI: 10.1088/0004-637X/723/2/1241. arXiv: 1007.5070 [astro-ph.SR].

Andrews, Sean M. et al. (2018). "The Disk Substructures at High Angular Resolution Project (DSHARP). I. Motivation, Sample, Calibration, and Overview". In: *ApJ* 869.2, L41, p. L41. DOI: 10.3847/2041-8213/aaf741. arXiv: 1812.04040 [astro-ph.SR].

Anglada, Guillem, Luis F. Rodríguez, and Carlos Carrasco-González (2018). "Radio jets from young stellar objects". In: *A&ARv* 26.1, 3, p. 3. DOI: 10.1007/s00159-018-0107-z. arXiv: 1806.06444 [astro-ph.SR].

Ansdell, M. et al. (May 2018). "ALMA Survey of Lupus Protoplanetary Disks. II. Gas Disk Radii". In: *ApJ* 859.1, 21, p. 21. DOI: 10.3847/1538-4357/aab890. arXiv: 1803.05923 [astro-ph.EP].

Attard, Michael et al. (Sept. 2009). "Magnetic Fields and Infall Motions in NGC 1333 IRAS 4". In: *ApJ* 702.2, pp. 1584–1592. DOI: 10.1088/0004-637X/702/2/1584. arXiv: 0907.1301 [astro-ph.SR].

Beltrán, M. T. and W. J. de Wit (Jan. 2016). "Accretion disks in luminous young stellar objects". In: *A&ARv* 24, 6, p. 6. DOI: 10.1007/s00159-015-0089-z. arXiv: 1509.08335.

Beltrán, M. T. et al. (Jan. 2011). "Rotating toroids in G10.62-0.38, G19.61-0.23, and G29.96-0.02". In: *A&A* 525, A151, A151. DOI: 10.1051/0004-6361/201015049. arXiv: 1010.0843.

Beltrán, M. T. et al. (Nov. 2014). "Filamentary structure and Keplerian rotation in the high-mass star-forming region G35.03+0.35 imaged with ALMA". In: *A&A* 571, A52, A52. DOI: 10.1051/0004-6361/201424031.

Beltrán, M. T. et al. (Oct. 2019). "ALMA resolves the hourglass magnetic field in G31.41+0.31". In: *A&A* 630, A54, A54. DOI: 10.1051/0004-6361/201935701. arXiv: 1908.01597 [astro-ph.GA].

Bonnell, Ian A. and Matthew R. Bate (Oct. 2002). "Accretion in stellar clusters and the collisional formation of massive stars". In: *MNRAS* 336.2, pp. 659–669. DOI: 10.1046/j.1365-8711.2002.05794.x.

Bonnell, Ian A. and Rowan J. Smith (Apr. 2011). "The Formation of Massive Stars". In: *Computational Star Formation*. Ed. by João. Alves et al. Vol. 270, pp. 57–64. DOI: 10.1017/S1743921311000184.

Bontemps, S. et al. (1996). "Evolution of outflow activity around low-mass embedded young stellar objects". In: *A&A* 311, pp. 858–872.

Burkert, Andreas, Matthew R. Bate, and Peter Bodenheimer (Aug. 1997). "Protostellar fragmentation in a power-law density distribution". In: *MNRAS* 289.3, pp. 497–504. DOI: 10.1093/mnras/289.3.497. arXiv: astro-ph/9706092 [astro-ph].

Busquet, G. et al. (Feb. 2013). "Unveiling a Network of Parallel Filaments in the Infrared Dark Cloud G14.225-0.506". In: *ApJL* 764, L26, p. L26. DOI: 10.1088/2041-8205/764/2/L26. arXiv: 1212.5917.

Busquet, G. et al. (Mar. 2016). "What Is Controlling the Fragmentation in the Infrared Dark Cloud G14.225-0.506?: Different Levels of Fragmentation in Twin Hubs." In: *ApJ* 819, 139, p. 139. DOI: 10.3847/0004-637X/819/2/139. arXiv: 1602.02500.

Busquet, G. et al. (Mar. 2019). "Unveiling a cluster of protostellar disks around the massive protostar GGD 27 MM1". In: *A&A* 623, L8, p. L8. DOI: 10.1051/0004-6361/201833687. arXiv: 1902.07581 [astro-ph.SR].

Calvet, N. et al. (Apr. 1992). "Irradiation of Accretion Disks around Young Objects. II. Continuum Energy Distribution". In: *RMxAA* 24, p. 27.

Calvet, N. et al. (Sept. 2005). "Disks in Transition in the Taurus Population: Spitzer IRS Spectra of GM Aurigae and DM Tauri". In: *ApJL* 630.2, pp. L185–L188. DOI: 10.1086/491652.

Calvet, Nuria et al. (Oct. 1991). "Irradiation of Accretion Disks around Young Objects. I. Near-Infrared CO Bands". In: *ApJ* 380, p. 617. DOI: 10.1086/170618.

Capitanio, L. et al. (Oct. 2017). "Three-dimensional mapping of the local interstellar medium with composite data". In: *A&A* 606, A65, A65. DOI: 10.1051/0004-6361/201730831. arXiv: 1706.07711.

Carrasco-González, C. et al. (Nov. 2010). "A Magnetized Jet from a Massive Protostar". In: *Science* 330, p. 1209. DOI: 10.1126/science.1195589. arXiv: 1011.6254 [astro-ph.GA].

Carrasco-González, C. et al. (June 2012). "Resolving the Circumstellar Disk around the Massive Protostar Driving the HH 80-81 Jet". In: *ApJL* 752, L29, p. L29. DOI: 10.1088/2041-8205/752/2/L29. arXiv: 1205.3302.

Carrasco-González, Carlos et al. (2016). "The VLA View of the HL Tau Disk: Disk Mass, Grain Evolution, and Early Planet Formation". In: *ApJL* 821.1, L16, p. L16. DOI: 10.3847/2041-8205/821/1/L16. arXiv: 1603.03731 [astro-ph.SR].

Carrasco-González, Carlos et al. (2019). "The Radial Distribution of Dust Particles in the HL Tau Disk from ALMA and VLA Observations". In: *ApJ* 883.1, 71, p. 71. DOI: 10.3847/1538-4357/ab3d33. arXiv: 1908.07140 [astro-ph.EP].

Cesaroni, Riccardo (2005). "Hot molecular cores". In: *Massive Star Birth: A Crossroads of Astrophysics*. Ed. by R. Cesaroni et al. Vol. 227. IAU Symposium, pp. 59–69. DOI: 10.1017/S1743921305004369.

Chandrasekhar, S. and E. Fermi (July 1953a). "Magnetic Fields in Spiral Arms." In: *ApJ* 118, p. 113. DOI: 10.1086/145731.

— (July 1953b). "Magnetic Fields in Spiral Arms." In: *ApJ* 118, p. 113. DOI: 10.1086/145731.

Chapman, Nicholas L. et al. (June 2013). "Alignment between Flattened Protostellar Infall Envelopes and Ambient Magnetic Fields". In: *ApJ* 770.2, 151, p. 151. DOI: 10.1088/0004-637X/770/2/151. arXiv: 1305.2922 [astro-ph.GA].

Chen, Hope How-Huan et al. (Dec. 2019a). "Droplets. II. Internal Velocity Structures and Potential Rotational Motions in Pressure-dominated Coherent Structures". In: *ApJ* 886.2, 119, p. 119. DOI: 10.3847/1538-4357/ab4ce9. arXiv: 1908.04367.

Chen, Huei-Ru Vivien et al. (2016). "A Hot and Massive Accretion Disk around the High-mass Protostar IRAS 20126+4104". In: *ApJ* 823.2, 125, p. 125. DOI: 10.3847/0004-637X/823/2/125. arXiv: 1604.00523 [astro-ph.GA].

Chen, Huei-Ru Vivien et al. (2019b). "Filamentary Accretion Flows in the Infrared Dark Cloud G14.225-0.506 Revealed by ALMA". In: *ApJ* 875.1, 24, p. 24. DOI: 10.3847/1538-4357/ab0f3e. arXiv: 1903.04376 [astro-ph.GA].

Cieza, Lucas A. et al. (July 2016). "Imaging the water snow-line during a protostellar outburst". In: *Nature* 535.7611, pp. 258–261. DOI: 10.1038/nature18612. arXiv: 1607.03757 [astro-ph.SR].

Cieza, Lucas A. et al. (Jan. 2019). "The Ophiuchus DIsc Survey Employing ALMA (ODISEA) - I: project description and continuum images at 28 au resolution". In: *MNRAS* 482.1, pp. 698–714. DOI: 10.1093/mnras/sty2653. arXiv: 1809.08844 [astro-ph.EP].

Cleeves, L. Ilsedore et al. (Nov. 2013). "Radionuclide Ionization in Protoplanetary Disks: Calculations of Decay Product Radiative Transfer". In: *ApJ* 777.1, 28, p. 28. DOI: 10.1088/0004-637X/777/1/28. arXiv: 1309.0018 [astro-ph.SR].

Commerçon, Benoît, Patrick Hennebelle, and Thomas Henning (Nov. 2011). "Collapse of Massive Magnetized Dense Cores Using Radiation Magnetohydrodynamics: Early Fragmentation Inhibition". In: *ApJL* 742.1, L9, p. L9. DOI: 10.1088/2041-8205/742/1/L9. arXiv: 1110.2955 [astro-ph.SR].

Crutcher, Richard M. et al. (Jan. 2004). "SCUBA Polarization Measurements of the Magnetic Field Strengths in the L183, L1544, and L43 Prestellar Cores". In: *ApJ* 600.1, pp. 279–285. DOI: 10.1086/379705. arXiv: astro-ph/0305604 [astro-ph].

Cudlip, W. et al. (Sept. 1982). "Far infrared polarimetry of W51A and M42". In: *MNRAS* 200, pp. 1169–1173. DOI: 10.1093/mnras/200.4.1169.

Cunningham, Andrew J. et al. (May 2018). "The effects of magnetic fields and protostellar feedback on low-mass cluster formation". In: *MNRAS* 476.1, pp. 771–792. DOI: 10.1093/mnras/sty154. arXiv: 1709.01277 [astro-ph.GA].

D'Alessio, P., N. Calvet, and L. Hartmann (May 2001). "Accretion Disks around Young Objects. III. Grain Growth". In: *ApJ* 553, pp. 321–334. DOI: 10.1086/320655. eprint: astro-ph/0101443.

D'Alessio, P. et al. (June 1998). "Accretion Disks around Young Objects. I. The Detailed Vertical Structure". In: *ApJ* 500, pp. 411–427. DOI: 10.1086/305702. eprint: astro-ph/9806060.

D'Alessio, P. et al. (Feb. 2006). "Effects of Dust Growth and Settling in T Tauri Disks". In: *ApJ* 638, pp. 314–335. DOI: 10.1086/498861. eprint: astro-ph/0511564.

D'Alessio, Paola, Nuria Calvet, and Lee Hartmann (1997). "The Structure and Emission of Accretion Disks Irradiated by Infalling Envelopes". In: *ApJ* 474.1, pp. 397–406. DOI: 10.1086/303433.

D'Alessio, Paola et al. (1999). "Accretion Disks around Young Objects. II. Tests of Well-mixed Models with ISM Dust". In: *ApJ* 527.2, pp. 893–909. DOI: 10.1086/308103. arXiv: astro-ph/9907330 [astro-ph].

Danielski, C. et al. (June 2018). "The empirical Gaia G-band extinction coefficient". In: *A&A* 614, A19, A19. DOI: 10.1051/0004-6361/201732327. arXiv: 1802.01670 [astro-ph.SR].

Dapp, Wolf B., Shantanu Basu, and Matthew W. Kunz (May 2012). "Bridging the gap: disk formation in the Class 0 phase with ambipolar diffusion and Ohmic dissipation". In: *A&A* 541, A35, A35. DOI: 10.1051/0004-6361/201117876. arXiv: 1112.3801 [astro-ph.SR].

Davidson, J. A. et al. (May 2011). "Magnetic Field Structure Around Low-mass Class 0 Protostars: B335, L1527, and IC348-SMM2". In: *ApJ* 732.2, 97, p. 97. DOI: 10.1088/0004-637X/732/2/97. arXiv: 1103.4370 [astro-ph.GA].

Davis Leverett, Jr. and Jesse L. Greenstein (Sept. 1951). "The Polarization of Starlight by Aligned Dust Grains." In: *ApJ* 114, p. 206. DOI: 10.1086/145464.

Davis, Leverett (1951a). "The Strength of Interstellar Magnetic Fields". In: *Phys. Rev.* 81 (5), pp. 890–891. DOI: 10.1103/PhysRev.81.890.2. URL: https://link.aps.org/doi/10.1103/PhysRev.81.890.2.

— (1951b). "The Strength of Interstellar Magnetic Fields". In: *Phys. Rev.* 81 (5), pp. 890–891. DOI: 10.1103/PhysRev.81.890.2. URL: https://link.aps.org/doi/10.1103/PhysRev.81.890.2.

De Buizer, J. M., M. Osorio, and N. Calvet (Dec. 2005). "Observations and Modeling of the 2-25 μm Emission from High-Mass Protostellar Object Candidates". In: *ApJ* 635, pp. 452–465. DOI: 10.1086/497259. eprint: astro-ph/0508376.

Dhabal, Arnab et al. (Feb. 2018). "Morphology and Kinematics of Filaments in the Serpens and Perseus Molecular Clouds". In: *ApJ* 853.2, 169, p. 169. DOI: 10.3847/1538-4357/aaa76b. arXiv: 1801.03155 [astro-ph.GA].

Dobbs, Clare L., Ian A. Bonnell, and Paul C. Clark (June 2005). "Centrally condensed turbulent cores: massive stars or fragmentation?" In: *MNRAS* 360.1, pp. 2–8. DOI: 10.1111/j.1365-2966.2005.08941.x. arXiv: astro-ph/0502479 [astro-ph].

Dolginov, A. Z. and I. G. Mitrofanov (Sept. 1976). "Orientation of Cosmic Dust Grains". In: *APSS* 43.2, pp. 291–317. DOI: 10.1007/BF00640010.

Dowell, C. Darren et al. (1998). "Submillimeter Array Polarimetry with Hertz". In: *ApJ* 504.1, pp. 588–598. DOI: 10.1086/306069.

Dowell, Charles D. et al. (2003). "SHARC II: a Caltech submillimeter observatory facility camera with 384 pixels". In: *PROCSPIE*. Ed. by Thomas G. Phillips and Jonas Zmuidzinas. Vol. 4855. Society of Photo-Optical Instrumentation Engineers (SPIE) Conference Series, pp. 73–87. DOI: 10.1117/12.459360.

Draine, B. T. and H. M. Lee (1984). "Optical Properties of Interstellar Graphite and Silicate Grains". In: *ApJ* 285, p. 89. DOI: 10.1086/162480.

Drążkowska, J. and Y. Alibert (Dec. 2017). "Planetesimal formation starts at the snow line". In: *A&A* 608, A92, A92. DOI: 10.1051/0004-6361/201731491. arXiv: 1710.00009 [astro-ph.EP].

Dullemond, C. P. and C. Dominik (2004). "The Global Structure of Protoplanetary Disks". In: *Extrasolar Planets: Today and Tomorrow*. Ed. by J. Beaulieu, A. Lecavelier Des Etangs, and C. Terquem. Vol. 321. Astronomical Society of the Pacific Conference Series, p. 361.

Dullemond, C. P., C. Dominik, and A. Natta (Oct. 2001). "Passive Irradiated Circumstellar Disks with an Inner Hole". In: *ApJ* 560.2, pp. 957–969. DOI: 10.1086/323057. arXiv: astro-ph/0106470 [astro-ph].

Dullemond, C. P., G. J. van Zadelhoff, and A. Natta (July 2002). "Vertical structure models of T Tauri and Herbig Ae/Be disks". In: *A&A* 389, pp. 464–474. DOI: 10.1051/0004-6361:20020608. arXiv: astro-ph/0204281 [astro-ph].

Dullemond, C. P. et al. (Jan. 2020). "Midplane temperature and outer edge of the protoplanetary disk around HD 163296". In: *A&A* 633, A137, A137. DOI: 10.1051/0004-6361/201936438. arXiv: 1911.12434 [astro-ph.EP].

Elmegreen, B. G. and C. J. Lada (1976). "Discovery of an extended (85 pc) molecular cloud associated with the M17 star-forming complex." In: *ApJ* 81, pp. 1089–1094. DOI: 10.1086/111990.

Espaillat, C. et al. (Feb. 2011). "A Spitzer IRS Study of Infrared Variability in Transitional and Pre-transitional Disks Around T Tauri Stars". In: *ApJ* 728.1, 49, p. 49. DOI: 10.1088/0004-637X/728/1/49. arXiv: 1012.3500 [astro-ph.SR].

Federrath, C. et al. (Dec. 2016). "The Link between Turbulence, Magnetic Fields, Filaments, and Star Formation in the Central Molecular Zone Cloud G0.253+0.016". In: *ApJ* 832.2, 143, p. 143. DOI: 10.3847/0004-637X/832/2/143. arXiv: 1609.05911 [astro-ph.GA].

Federrath, Christoph et al. (Aug. 2014). "Modeling Jet and Outflow Feedback during Star Cluster Formation". In: *ApJ* 790.2, 128, p. 128. DOI: 10.1088/0004-637X/790/2/128. arXiv: 1406.3625 [astro-ph.SR].

Fernández-López, M. et al. (Oct. 2011a). "A Rotating Molecular Disk Toward IRAS 18162-2048, the Exciting Source of HH 80-81". In: *ApJ* 142, 97, p. 97. DOI: 10.1088/0004-6256/142/4/97. arXiv: 1107.3176.

Fernández-López, M. et al. (Mar. 2011b). "Millimeter and Submillimeter High Angular Resolution Interferometric Observations: Dust in the Heart of IRAS 18162-2048". In: *ApJ* 141, 72, p. 72. DOI: 10.1088/0004-6256/141/3/72. arXiv: 1011.2237 [astro-ph.SR].

Fernández-López, M. et al. (Aug. 2014). "CARMA Large Area Star Formation Survey: Observational Analysis of Filaments in the Serpens South Molecular Cloud". In: *ApJL* 790.2, L19, p. L19. DOI: 10.1088/2041-8205/790/2/L19. arXiv: 1407.0755 [astro-ph.GA].

Fissel, Laura M. et al. (June 2016). "Balloon-Borne Submillimeter Polarimetry of the Vela C Molecular Cloud: Systematic Dependence of Polarization Fraction on Column Density and Local Polarization-Angle Dispersion". In: *ApJ* 824.2, 134, p. 134. DOI: 10.3847/0004-637X/824/2/134. arXiv: 1509.05298 [astro-ph.GA].

Fogel, Jeffrey K. J. et al. (2011). "Chemistry of a Protoplanetary Disk with Grain Settling and Lyα Radiation". In: *ApJ* 726.1, 29, p. 29. DOI: 10.1088/0004-637X/726/1/29. arXiv: 1011.0446 [astro-ph.SR].

Fontani, F. et al. (Sept. 2016). "Magnetically regulated fragmentation of a massive, dense, and turbulent clump". In: *A&A* 593, L14, p. L14. DOI: 10.1051/0004-6361/201629442. arXiv: 1608.08083 [astro-ph.GA].

Fontani, F. et al. (July 2018). "Fragmentation properties of massive protocluster gas clumps: an ALMA study". In: *A&A* 615, A94, A94. DOI: 10.1051/0004-6361/201832672. arXiv: 1804.02429 [astro-ph.GA].

Forgan, D. H. et al. (2016). "Self-gravitating disc candidates around massive young stars". In: *MNRAS* 463.1, pp. 957–964. DOI: 10.1093/mnras/stw1917. arXiv: 1608.05539 [astro-ph.SR].

Frau, P. et al. (Feb. 2015). "Formation of dense structures induced by filament collisions. Correlation of density, kinematics, and magnetic field in the Pipe nebula". In: *A&A* 574, L6, p. L6. DOI: 10.1051/0004-6361/201425234. arXiv: 1412.4778 [astro-ph.GA].

Gaia Collaboration et al. (2016). "The Gaia mission". In: *A&A* 595, A1, A1. DOI: 10.1051/0004-6361/201629272. arXiv: 1609.04153 [astro-ph.IM].

Gaia Collaboration et al. (2018). "Gaia Data Release 2. Summary of the contents and survey properties". In: *A&A* 616, A1, A1. DOI: 10.1051/0004-6361/201833051. arXiv: 1804.09365 [astro-ph.GA].

Galametz, Maud et al. (Aug. 2018). "SMA observations of polarized dust emission in solar-type Class 0 protostars: Magnetic field properties at envelope scales". In: *A&A* 616, A139, A139. DOI: 10.1051/0004-6361/201833004. arXiv: 1804.05801 [astro-ph.GA].

Galli, Daniele et al. (Aug. 2006). "Gravitational Collapse of Magnetized Clouds. I. Ideal Magnetohydrodynamic Accretion Flow". In: *ApJ* 647.1, pp. 374–381. DOI: 10.1086/505257. arXiv: astro-ph/0604573 [astro-ph].

Garufi, A. et al. (Dec. 2018). "Evolution of protoplanetary disks from their taxonomy in scattered light: spirals, rings, cavities, and shadows". In: *A&A* 620, A94, A94. DOI: 10.1051/0004-6361/201833872. arXiv: 1810.04564 [astro-ph.SR].

Ginsburg, Adam et al. (2019). "Orion SrcI's Disk Is Salty". In: *ApJ* 872.1, 54, p. 54. DOI: 10.3847/1538-4357/aafb71. arXiv: 1901.04489 [astro-ph.GA].

Girart, J. M. et al. (2001). "Star Formation Signatures in the Condensation Downstream of HH 80N". In: *ApJL* 562.1, pp. L91–L94. DOI: 10.1086/337995. arXiv: astro-ph/0110052 [astro-ph].

Girart, J. M. et al. (Sept. 2017). "The Circumestellar Disk of the B0 Protostar Powering the HH 80-81 Radio Jet". In: *ApJ* 847, 58, p. 58. DOI: 10.3847/1538-4357/aa81c9. arXiv: 1707.06463 [astro-ph.SR].

Girart, J. M. et al. (Apr. 2018). "Resolving the Polarized Dust Emission of the Disk around the Massive Star Powering the HH 80−81 Radio Jet". In: *ApJL* 856, L27, p. L27. DOI: 10.3847/2041-8213/aab76b. arXiv: 1803.06165 [astro-ph.SR].

Girart, Jose M. et al. (1994). "Ammonia Downstream from HH 80 North". In: *ApJL* 435, p. L145. DOI: 10.1086/187615.

Girart, Josep M., Ramprasad Rao, and Daniel P. Marrone (Aug. 2006). "Magnetic Fields in the Formation of Sun-Like Stars". In: *Science* 313.5788, pp. 812–814. DOI: 10.1126/science.1129093. arXiv: astro-ph/0609177 [astro-ph].

Girart, Josep M. et al. (June 2009). "Magnetic Fields in the Formation of Massive Stars". In: *Science* 324.5933, p. 1408. DOI: 10.1126/science.1171807.

Girichidis, Philipp et al. (June 2011). "Importance of the initial conditions for star formation - I. Cloud evolution and morphology". In: *MNRAS* 413.4, pp. 2741–2759. DOI: 10.1111/j.1365-2966.2011.18348.x. arXiv: 1008.5255 [astro-ph.SR].

Gold, T. (Feb. 1952a). "Polarization of Starlight". In: *Nature* 169.4295, p. 322. DOI: 10.1038/169322a0.

— (Jan. 1952b). "The alignment of galactic dust". In: *MNRAS* 112, p. 215. DOI: 10.1093/mnras/112.2.215.

Goldreich, P. and N. D. Kylafis (1981). "On mapping the magnetic field direction in molecular clouds by polarization measurements". In: *ApJL* 243, pp. L75–L78. DOI: 10.1086/183446.

— (1982). "Linear polarization of radio frequency lines in molecular clouds and circumstellar envelopes". In: *ApJ* 253, pp. 606–621. DOI: 10.1086/159663.

Gómez, Gilberto C. and Enrique Vázquez-Semadeni (Aug. 2014). "Filaments in Simulations of Molecular Cloud Formation". In: *ApJ* 791.2, 124, p. 124. DOI: 10.1088/0004-637X/791/2/124. arXiv: 1308.6298 [astro-ph.GA].

Gómez, Gilberto C., Enrique Vázquez-Semadeni, and Manuel Zamora-Avilés (Nov. 2018). "The magnetic field structure in molecular cloud filaments". In: *MNRAS* 480.3, pp. 2939–2944. DOI: 10.1093/mnras/sty2018. arXiv: 1801.03169 [astro-ph.GA].

Gómez, Y. et al. (Nov. 2003). "VLA and BIMA Observations toward the Exciting Source of the Massive HH 80-81 Outflow". In: *ApJ* 597, pp. 414–423. DOI: 10.1086/378403. eprint: astro-ph/0307511.

Gueth, F. and S. Guilloteau (Mar. 1999). "The jet-driven molecular outflow of HH 211". In: *A&A* 343, pp. 571–584.

Guillet, V. et al. (Feb. 2020). "Polarized emission by aligned grains in the Mie regime: Application to protoplanetary disks observed by ALMA". In: *A&A* 634, L15, p. L15. DOI: 10.1051/0004-6361/201937314. arXiv: 2001.08400 [astro-ph.GA].

Gutermuth, R. A. et al. (Oct. 2011). "A Correlation between Surface Densities of Young Stellar Objects and Gas in Eight Nearby Molecular Clouds". In: *ApJ* 739.2, 84, p. 84. DOI: 10.1088/0004-637X/739/2/84. arXiv: 1107.0966 [astro-ph.SR].

Gvaramadze, V. V. et al. (Apr. 2017). "IRAS 18153-1651: an H II region with a possible wind bubble blown by a young main-sequence B star". In: *MNRAS* 466.2, pp. 1857–1867. DOI: 10.1093/mnras/stw3257. arXiv: 1612.03916 [astro-ph.SR].

Hall, John S. (Feb. 1949). "Observations of the Polarized Light from Stars". In: *Science* 109.2825, pp. 166–167. DOI: 10.1126/science.109.2825.166.

Harsono, Daniel et al. (2018). "Evidence for the start of planet formation in a young circumstellar disk". In: *Nature Astronomy* 2, pp. 646–651. DOI: 10.1038/s41550-018-0497-x. arXiv: 1806.09649 [astro-ph.SR].

Hartigan, P. and C. J. Lada (1985). "CCD images of suspected Herbig-Haro objects." In: *ApJ* 59, pp. 383–396. DOI: 10.1086/191077.

Hartmann, L., G. Herczeg, and N. Calvet (Sept. 2016). "Accretion onto Pre-Main-Sequence Stars". In: *ARA&A* 54, pp. 135–180. DOI: 10.1146/annurev-astro-081915-023347.

Hartmann, Lee, Javier Ballesteros-Paredes, and Fabian Heitsch (Feb. 2012). "Rapid star formation and global gravitational collapse". In: *MNRAS* 420.2, pp. 1457–1461. DOI: 10.1111/j.1365-2966.2011.20131.x. arXiv: 1111.2582 [astro-ph.SR].

Heathcote, S., B. Reipurth, and A. C. Raga (Oct. 1998). "Structure, Excitation, and Kinematics of the Luminous Herbig-Haro Objects 80/81". In: *ApJ* 116, pp. 1940–1960. DOI: 10.1086/300548.

Heitsch, Fabian et al. (Nov. 2001). "Magnetic Field Diagnostics Based on Far-Infrared Polarimetry: Tests Using Numerical Simulations". In: *ApJ* 561.2, pp. 800–814. DOI: 10.1086/323489. arXiv: astro-ph/0103286 [astro-ph].

Hennebelle, P. et al. (Apr. 2011). "Collapse, outflows and fragmentation of massive, turbulent and magnetized prestellar barotropic cores". In: *A&A* 528, A72, A72. DOI: 10.1051/0004-6361/201016052. arXiv: 1101.1574 [astro-ph.GA].

Hildebrand, R. H. et al. (Sept. 2000). "A Primer on Far-Infrared Polarimetry". In: *PASP* 112, pp. 1215–1235. DOI: 10.1086/316613.

Hildebrand, R. H. et al. (May 2009). "Dispersion of Magnetic Fields in Molecular Clouds. I". In: *ApJ* 696, pp. 567–573. DOI: 10.1088/0004-637X/696/1/567. arXiv: 0811.0813.

Hildebrand, Roger H. (Sept. 1988). "Magnetic fields and stardust". In: *RASQJ* 29, pp. 327–351.

Hoang, Thiem and A. Lazarian (Nov. 2016). "A Unified Model of Grain Alignment: Radiative Alignment of Interstellar Grains with Magnetic Inclusions". In: *ApJ* 831.2, 159, p. 159. DOI: 10.3847/0004-637X/831/2/159. arXiv: 1605.02828 [astro-ph.GA].

Hosokawa, T. and K. Omukai (Jan. 2009). "Evolution of Massive Protostars with High Accretion Rates". In: *ApJ* 691, pp. 823–846. DOI: 10.1088/0004-637X/691/1/823. arXiv: 0806.4122.

Houde, Martin and John E. Vaillancourt (2007). "Astronomical Image Processing with Array Detectors". In: *PASP* 119.858, pp. 871–885. DOI: 10.1086/521109. arXiv: 0706.3481 [astro-ph].

Houde, Martin et al. (Dec. 2009). "Dispersion of Magnetic Fields in Molecular Clouds. II." In: *ApJ* 706.2, pp. 1504–1516. DOI: 10.1088/0004-637X/706/2/1504. arXiv: 0909.5227 [astro-ph.GA].

Huang, Jane et al. (Dec. 2018). "The Disk Substructures at High Angular Resolution Project (DSHARP). II. Characteristics of Annular Substructures". In: *ApJL* 869.2, L42, p. L42. DOI: 10.3847/2041-8213/aaf740. arXiv: 1812.04041 [astro-ph.EP].

Hughes, A. Meredith et al. (June 2009). "A Spatially Resolved Inner Hole in the Disk Around GM Aurigae". In: *ApJ* 698.1, pp. 131–142. DOI: 10.1088/0004-637X/698/1/131. arXiv: 0903.4455 [astro-ph.SR].

Humphreys, R. M. (Dec. 1978). "Studies of luminous stars in nearby galaxies. I. Supergiants and O stars in the Milky Way." In: *ApJ* 38, pp. 309–350. DOI: 10.1086/190559.

Ilee, J. D. et al. (Dec. 2018). "G11.92−0.61 MM 1: A Fragmented Keplerian Disk Surrounding a Proto-O Star". In: *ApJL* 869, L24, p. L24. DOI: 10.3847/2041-8213/aaeffc. arXiv: 1811.05267 [astro-ph.SR].

Inoue, Tsuyoshi and Yasuo Fukui (Sept. 2013). "Formation of Massive Molecular Cloud Cores by Cloud-Cloud Collision". In: *ApJL* 774.2, L31, p. L31. DOI: 10.1088/2041-8205/774/2/L31. arXiv: 1305.4655 [astro-ph.GA].

Isella, Andrea, John M. Carpenter, and Anneila I. Sargent (Aug. 2009). "Structure and Evolution of Pre-main-sequence Circumstellar Disks". In: *ApJ* 701.1, pp. 260–282. DOI: 10.1088/0004-637X/701/1/260. arXiv: 0906.2227 [astro-ph.SR].

Jaffe, D. T., R. Guesten, and D. Downes (Nov. 1981). "New H2O masers associated with far-infrared sources." In: *ApJ* 250, pp. 621–630. DOI: 10.1086/159409.

Jaffe, D. T., M. T. Stier, and G. G. Fazio (Jan. 1982). "A high-resolution far-infrared survey of a section of the galactic plane. I. The nature of the sources." In: *ApJ* 252, pp. 601–609. DOI: 10.1086/159587.

Jiménez-Serra, Izaskun et al. (July 2020). "The Ionized Warped Disk and Disk Wind of the Massive Protostar Monoceros R2-IRS2 Seen with ALMA". In: *ApJL* 897.2, L33, p. L33. DOI: 10.3847/2041-8213/aba050. arXiv: 2006.15853 [astro-ph.SR].

Johnston, K. G. et al. (Mar. 2013). "The standard model of low-mass star formation applied to massive stars: a multi-wavelength picture of AFGL 2591". In: *A&A* 551, A43, A43. DOI: 10.1051/0004-6361/201219657. arXiv: 1212.1719 [astro-ph.SR].

Johnston, K. G. et al. (Nov. 2015). "A Keplerian-like Disk around the Forming O-type Star AFGL 4176". In: *ApJL* 813, L19, p. L19. DOI: 10.1088/2041-8205/813/1/L19. arXiv: 1509.08469 [astro-ph.SR].

Kataoka, Akimasa et al. (July 2017). "The Evidence of Radio Polarization Induced by the Radiative Grain Alignment and Self-scattering of Dust Grains in a Protoplanetary Disk". In: *ApJL* 844.1, L5, p. L5. DOI: 10.3847/2041-8213/aa7e33. arXiv: 1707.01612 [astro-ph.EP].

Kenyon, S. J. and L. Hartmann (Dec. 1987). "Spectral Energy Distributions of T Tauri Stars: Disk Flaring and Limits on Accretion". In: *ApJ* 323, p. 714. DOI: 10.1086/165866.

Keto, Eric, George B. Field, and Eric G. Blackman (Mar. 2020). "A turbulent-entropic instability and the fragmentation of star-forming clouds". In: *MNRAS* 492.4, pp. 5870–5877. DOI: 10.1093/mnras/staa230. arXiv: 2001.02678 [astro-ph.GA].

Kirby, Larry et al. (2005). "Improved Data Reduction for Far-Infrared/Submillimeter Polarimetry". In: *PASP* 117.835, pp. 991–995. DOI: 10.1086/432783.

Kirk, Helen et al. (Apr. 2013). "Filamentary Accretion Flows in the Embedded Serpens South Protocluster". In: *ApJ* 766.2, 115, p. 115. DOI: 10.1088/0004-637X/766/2/115. arXiv: 1301.6792 [astro-ph.GA].

Kirk, Helen et al. (Apr. 2015). "The Role of Turbulence and Magnetic Fields in Simulated Filamentary Structure". In: *ApJ* 802.2, 75, p. 75. DOI: 10.1088/0004-637X/802/2/75. arXiv: 1501.05999 [astro-ph.GA].

Klassen, M. et al. (May 2016). "Simulating the Formation of Massive Protostars. I. Radiative Feedback and Accretion Disks". In: *ApJ* 823, 28, p. 28. DOI: 10.3847/0004-637X/823/1/28. arXiv: 1603.07345.

Koch, P. M., Y.-W. Tang, and P. T. P. Ho (Mar. 2012a). "Magnetic Field Strength Maps for Molecular Clouds: A New Method Based on a Polarization-Intensity Gradient Relation". In: *ApJ* 747, 79, p. 79. DOI: 10.1088/0004-637X/747/1/79. arXiv: 1201.4263.

Koch, Patrick M., Ya-Wen Tang, and Paul T. P. Ho (2012b). "Quantifying the Significance of the Magnetic Field from Large-scale Cloud to Collapsing Core: Self-similarity, Mass-to-flux Ratio, and Star Formation Efficiency". In: *ApJ* 747.1, 80, p. 80. DOI: 10.1088/0004-637X/747/1/80. arXiv: 1201.4313 [astro-ph.GA].

— (2013). "Interpreting the Role of the Magnetic Field from Dust Polarization Maps". In: *ApJ* 775.1, 77, p. 77. DOI: 10.1088/0004-637X/775/1/77. arXiv: 1308.6185 [astro-ph.GA].

Koch, Patrick M. et al. (Dec. 2014). "The Importance of the Magnetic Field from an SMA-CSO-combined Sample of Star-forming Regions". In: *ApJ* 797.2, 99, p. 99. DOI: 10.1088/0004-637X/797/2/99. arXiv: 1411.3830 [astro-ph.GA].

Koch, Patrick M. et al. (Mar. 2018). "Polarization Properties and Magnetic Field Structures in the High-mass Star-forming Region W51 Observed with ALMA". In: *ApJ* 855.1, 39, p. 39. DOI: 10.3847/1538-4357/aaa4c1. arXiv: 1801.08264 [astro-ph.GA].

Krumholz, Mark R. (Apr. 2006). "Radiation Feedback and Fragmentation in Massive Protostellar Cores". In: *ApJL* 641.1, pp. L45–L48. DOI: 10.1086/503771. arXiv: astro-ph/0603026 [astro-ph].

Krumholz, Mark R., Richard M. Crutcher, and Charles L. H. Hull (Apr. 2013). "Protostellar Disk Formation Enabled by Weak, Misaligned Magnetic Fields". In: *ApJL* 767.1, L11, p. L11. DOI: 10.1088/2041-8205/767/1/L11. arXiv: 1301.5648 [astro-ph.SR].

Kuiper, R. and T. Hosokawa (Aug. 2018). "First hydrodynamics simulations of radiation forces and photoionization feedback in massive star formation". In: *A&A* 616, A101, A101. DOI: 10.1051/0004-6361/201832638. arXiv: 1804.10211.

Kwon, J. et al. (June 2016). "Near-infrared Imaging Polarimetry of GGD 27: Circular Polarization and Magnetic Field Structures". In: *ApJ* 824, 95, p. 95. DOI: 10.3847/0004-637X/824/2/95.

Lada, Charles J. et al. (Mar. 2003). "The Dynamical State of Barnard 68: A Thermally Supported, Pulsating Dark Cloud". In: *ApJ* 586.1, pp. 286–295. DOI: 10.1086/367610. arXiv: astro-ph/0211507 [astro-ph].

Lai, Shih-Ping et al. (Nov. 2001). "Interferometric Mapping of Magnetic Fields in Star-forming Regions. I. W51 e1/e2 Molecular Cores". In: *ApJ* 561.2, pp. 864–870. DOI: 10.1086/323372. arXiv: astro-ph/0107322 [astro-ph].

Lallement, R. et al. (Sept. 2018). "Three-dimensional maps of interstellar dust in the Local Arm: using Gaia, 2MASS, and APOGEE-DR14". In: *A&A* 616, A132, A132. DOI: 10.1051/0004-6361/201832832. arXiv: 1804.06060.

Lambrechts, M. and A. Johansen (2012). "Rapid growth of gas-giant cores by pebble accretion". In: *A&A* 544, A32, A32. DOI: 10.1051/0004-6361/201219127. arXiv: 1205.3030 [astro-ph.EP].

Larson, Richard B. (Oct. 2003). "The physics of star formation". In: *Reports on Progress in Physics* 66.10, pp. 1651–1697. DOI: 10.1088/0034-4885/66/10/R03. arXiv: astro-ph/0306595 [astro-ph].

Lazarian, A. (July 2007). "Tracing magnetic fields with aligned grains". In: *JQSRT* 106, pp. 225–256. DOI: 10.1016/j.jqsrt.2007.01.038. arXiv: 0707.0858 [astro-ph].

Lazarian, A., E. Vishniac, and G. Kowal (Apr. 2009). "Model of Reconnection of Weakly Stochastic Magnetic Field and its Testing". In: *Numerical Modeling of Space Plasma Flows: ASTRONUM-2008*. Ed. by N. V. Pogorelov et al. Vol. 406. Astronomical Society of the Pacific Conference Series, p. 23. arXiv: 0812.4579 [astro-ph].

Li, H. et al. (2008). "Design and initial performance of SHARP, a polarimeter for the SHARC-II camera at the Caltech Submillimeter Observatory". In: *AOIP* 47.3, pp. 422–430. DOI: 10.1364/AO.47.000422. arXiv: 0707.0127 [astro-ph].

Li, Hua-Bai et al. (2015). "Self-similar Fragmentation Regulated by Magnetic Fields in a Massive Star Forming Filament". In: *Nature* 20.7548, pp. 422–430. DOI: 10.1038/nature14291.

Li, Pak Shing and Richard I. Klein (June 2019). "Magnetized interstellar molecular clouds - II. The large-scale structure and dynamics of filamentary molecular clouds". In: *MNRAS* 485.4, pp. 4509–4528. DOI: 10.1093/mnras/stz653. arXiv: 1901.04593 [astro-ph.GA].

Li, Z. Y. et al. (Jan. 2014). "The Earliest Stages of Star and Planet Formation: Core Collapse, and the Formation of Disks and Outflows". In: *Protostars and Planets VI*. Ed. by Henrik Beuther et al., p. 173. DOI: 10.2458/azu_uapress_9780816531240-ch008. arXiv: 1401.2219 [astro-ph.SR].

Li, Zhi-Yun, Ruben Krasnopolsky, and Hsien Shang (Sept. 2011). "Non-ideal MHD Effects and Magnetic Braking Catastrophe in Protostellar Disk Formation". In: *ApJ* 738.2, 180, p. 180. DOI: 10.1088/0004-637X/738/2/180. arXiv: 1106.2620 [astro-ph.GA].

Lin, Yuxin et al. (May 2017a). "Cloud Structure of Three Galactic Infrared Dark Star-forming Regions from Combining Ground- and Space-based Bolometric Observations". In: *ApJ* 840.1, 22, p. 22. DOI: 10.3847/1538-4357/aa6c67. arXiv: 1704.06448 [astro-ph.GA].

— (July 2017b). "Erratum: "Cloud Structure of Three Galactic Infrared Dark Star-forming Regions from Combining Ground and Space-based Bolometric Observations " (''https://doi.org/10.3847/1538-4357/aa6c67" >2017, ApJ, 840, 22</A>)". In: *ApJ* 843.2, 153, p. 153. DOI: 10.3847/1538-4357/aa7842.

Liu, Tie et al. (June 2018). "A Holistic Perspective on the Dynamics of G035.39-00.33: The Interplay between Gas and Magnetic Fields". In: *ApJ* 859.2, 151, p. 151. DOI: 10.3847/1538-4357/aac025. arXiv: 1803.09457 [astro-ph.GA].

Lopez-Rodriguez, Enrique et al. (Jan. 2020). "SOFIA/HAWC+ Traces the Magnetic Fields in NGC 1068". In: *ApJ* 888.2, 66, p. 66. DOI: 10.3847/1538-4357/ab5849. arXiv: 1907.06648 [astro-ph.GA].

Lu, Xing et al. (Mar. 2018). "Filamentary Fragmentation and Accretion in High-mass Star-forming Molecular Clouds". In: *ApJ* 855.1, 9, p. 9. DOI: 10.3847/1538-4357/aaad11. arXiv: 1801.05955 [astro-ph.GA].

Lynds, B. T. (May 1962). "Catalogue of Dark Nebulae." In: *ApJ* 7, p. 1. DOI: 10.1086/190072.

Macías, E. et al. (Sept. 2018). "Multiple Rings in the Transitional Disk of GM Aurigae Revealed by VLA and ALMA". In: *ApJ* 865, 37, p. 37. DOI: 10.3847/1538-4357/aad811. arXiv: 1808.01920 [astro-ph.SR].

Macías, Enrique et al. (2019). "Characterization of Ring Substructures in the Protoplanetary Disk of HD 169142 from Multiwavelength Atacama Large Millimeter/submillimeter Array Observations". In: *ApJ* 881.2, 159, p. 159. DOI: 10.3847/1538-4357/ab31a2. arXiv: 1907.07277 [astro-ph.SR].

Martí, J., L. F. Rodríguez, and B. Reipurth (Oct. 1993). "HH 80-81: A Highly Collimated Herbig-Haro Complex Powered by a Massive Young Star". In: *ApJ* 416, p. 208. DOI: 10.1086/173227.

Martí, Josep, Luis F. Rodríguez, and Bo Reipurth (1998). "Proper Motions of the Inner Condensations in the HH 80-81 Thermal Radio Jet". In: *ApJ* 502.1, pp. 337–341. DOI: 10.1086/305900.

Masqué, J. M. et al. (Nov. 2015). "Proper Motions of the Outer Knots of the HH 80/81/80N Radiojet". In: *ApJ* 814, 44, p. 44. DOI: 10.1088/0004-637X/814/1/44. arXiv: 1510.01769 [astro-ph.SR].

Masqué, Josep M. et al. (2011). "A Multi-wavelength Study of the Star-forming Core Ahead of HH 80N". In: *ApJ* 738.1, 43, p. 43. DOI: 10.1088/0004-637X/738/1/43. arXiv: 1106.2005 [astro-ph.SR].

Masqué, Josep M. et al. (2013). "Interferometric Observations of Nitrogen-bearing Molecular Species in the Star-forming Core Ahead of HH 80N". In: *ApJ* 776.1, 28, p. 28. DOI: 10.1088/0004-637X/776/1/28. arXiv: 1307.0761 [astro-ph.SR].

Maud, L. T. et al. (2019). "Substructures in the Keplerian disc around the O-type (proto-)star G17.64+0.16". In: *A&A* 627, L6, p. L6. DOI: 10.1051/0004-6361/201935633. arXiv: 1906.06548 [astro-ph.SR].

Maury, A. J. et al. (Jan. 2019). "Characterizing young protostellar disks with the CALYPSO IRAM-PdBI survey: large Class 0 disks are rare". In: *A&A* 621, A76, A76. DOI: 10.1051/0004-6361/201833537. arXiv: 1810.11221 [astro-ph.GA].

McCaughrean, Mark J., John T. Rayner, and Hans Zinnecker (Dec. 1994). "Discovery of a Molecular Hydrogen Jet near IC 348". In: *ApJL* 436, p. L189. DOI: 10.1086/187664.

McClure, M. K. et al. (2013). "Curved Walls: Grain Growth, Settling, and Composition Patterns in T Tauri Disk Dust Sublimation Fronts". In: *ApJ* 775.2, 114, p. 114. DOI: 10.1088/0004-637X/775/2/114. arXiv: 1308.3207 [astro-ph.EP].

McClure, M. K. et al. (Nov. 2016). "Mass Measurements in Protoplanetary Disks from Hydrogen Deuteride". In: *ApJ* 831.2, 167, p. 167. DOI: 10.3847/0004-637X/831/2/167. arXiv: 1608.07817 [astro-ph.SR].

McKee, C. F. and E. C. Ostriker (Sept. 2007). "Theory of Star Formation". In: *ARA&A* 45, pp. 565–687. DOI: 10.1146/annurev.astro.45.051806.110602. arXiv: 0707.3514.

McKee, Christopher F. and Jonathan C. Tan (Mar. 2002). "Massive star formation in 100,000 years from turbulent and pressurized molecular clouds". In: *Nature* 416.6876, pp. 59–61. DOI: 10.1038/416059a. arXiv: astro-ph/0203071 [astro-ph].

Men'shchikov, Alexander B., Thomas Henning, and Olaf Fischer (1999). "Self-consistent Model of the Dusty Torus around HL Tauri". In: *ApJ* 519.1, pp. 257–278. DOI: 10.1086/307333.

Mercimek, Seyma et al. (May 2017). "An Estimation of the Star Formation Rate in the Perseus Complex". In: *ApJ* 153.5, 214, p. 214. DOI: 10.3847/1538-3881/aa661f. arXiv: 1704.07596 [astro-ph.GA].

Mestel, L. and Jr. Spitzer L. (Jan. 1956). "Star formation in magnetic dust clouds". In: *MNRAS* 116, p. 503. DOI: 10.1093/mnras/116.5.503.

Meyer, D. M. A. et al. (2018). "Forming spectroscopic massive protobinaries by disc fragmentation". In: *MNRAS* 473.3, pp. 3615–3637. DOI: 10.1093/mnras/stx2551. arXiv: 1710.01162 [astro-ph.SR].

Moeckel, Nickolas and Andreas Burkert (July 2015). "The Formation of Filamentary Bundles in Turbulent Molecular Clouds". In: *ApJ* 807.1, 67, p. 67. DOI: 10.1088/0004-637X/807/1/67. arXiv: 1402.2614 [astro-ph.GA].

Molinari, S. et al. (July 2010). "Clouds, filaments, and protostars: The Herschel Hi-GAL Milky Way". In: *A&A* 518, L100, p. L100. DOI: 10.1051/0004-6361/201014659. arXiv: 1005.3317 [astro-ph.GA].

Monsch, Kristina et al. (July 2018). "Dense Gas Kinematics and a Narrow Filament in the Orion A OMC1 Region Using NH_3". In: *ApJ* 861.2, 77, p. 77. DOI: 10.3847/1538-4357/aac8da. arXiv: 1806.01847 [astro-ph.GA].

Motogi, Kazuhito et al. (2019). "The First Bird's-eye View of a Gravitationally Unstable Accretion Disk in High-mass Star Formation". In: *ApJL* 877.2, L25, p. L25. DOI: 10.3847/2041-8213/ab212f. arXiv: 1905.12983 [astro-ph.SR].

Mouschovias, T. Ch. and Jr. Spitzer L. (Dec. 1976). "Note on the collapse of magnetic interstellar clouds." In: *ApJ* 210, p. 326. DOI: 10.1086/154835.

Mouschovias, Telemachos Ch. (Jan. 1987). "Star formation in magnetic interstellar clouds: I. Interplay between theory and observations." In: *Physical Processes in Interstellar Clouds*. Ed. by G. E. Morfill and M. Scholer. Vol. 210. NATO Advanced Study Institute (ASI) Series C, pp. 453–489.

— (May 1991). "Magnetic Braking, Ambipolar Diffusion, Cloud Cores, and Star Formation: Natural Length Scales and Protostellar Masses". In: *ApJ* 373, p. 169. DOI: 10.1086/170035.

Murray, Norman and Philip Chang (Feb. 2012). "Star Formation in Massive Clusters via Bondi Accretion". In: *ApJ* 746.1, 75, p. 75. DOI: 10.1088/0004-637X/746/1/75. arXiv: 1106.3083 [astro-ph.GA].

Myers, Andrew T. et al. (Apr. 2013). "The Fragmentation of Magnetized, Massive Star-forming Cores with Radiative Feedback". In: *ApJ* 766.2, 97, p. 97. DOI: 10.1088/0004-637X/766/2/97. arXiv: 1211.3467 [astro-ph.SR].

Myers, Philip C. (Aug. 2009). "Filamentary Structure of Star-forming Complexes". In: *ApJ* 700.2, pp. 1609–1625. DOI: 10.1088/0004-637X/700/2/1609. arXiv: 0906.2005 [astro-ph.GA].

Myhill, Elizabeth A. and William M. Kaula (Feb. 1992). "Numerical Models for the Collapse and Fragmentation of Centrally Condensed Molecular Cloud Cores". In: *ApJ* 386, p. 578. DOI: 10.1086/171040.

Nagel, E. et al. (2013). "The Effect of Sublimation Temperature Dependencies on Disk Walls Around T Tauri Stars". In: *RMxAA* 49, pp. 43–52. arXiv: 1210.2323 [astro-ph.SR].

Naghizadeh-Khouei, J. and D. Clarke (July 1993). "On the statistical behaviour of the position angle of linear polarization". In: *A&A* 274, p. 968.

Nakano, T. (Jan. 1983). "Nonconservation of magnetic flux in star formation". In: *PASJ* 35.1, pp. 87–90.

Ohashi, Satoshi et al. (Dec. 2016). "Dense Core Properties in the Infrared Dark Cloud G14.225-0.506 Revealed by ALMA". In: *ApJ* 833.2, 209, p. 209. DOI: 10.3847/1538-4357/833/2/209. arXiv: 1610.08581 [astro-ph.GA].

Osorio, M., S. Lizano, and P. D'Alessio (Nov. 1999). "Hot Molecular Cores and the Formation of Massive Stars". In: *ApJ* 525, pp. 808–820. DOI: 10.1086/307929.

Osorio, M. et al. (Mar. 2009). "Collapsing Hot Molecular Cores: A Model for the Dust Spectrum and Ammonia Line Emission of the G31.41+0.31 Hot Core". In: *ApJ* 694, pp. 29–45. DOI: 10.1088/0004-637X/694/1/29. arXiv: 0811.4096.

Osorio, M. et al. (Aug. 2014). "Imaging the Inner and Outer Gaps of the Pre-transitional Disk of HD 169142 at 7 mm". In: *ApJL* 791, L36, p. L36. DOI: 10.1088/2041-8205/791/2/L36. arXiv: 1407.6549 [astro-ph.SR].

Osorio, M. et al. (July 2016). "A Dwarf Transitional Protoplanetary Disk around XZ Tau B". In: *ApJL* 825, L10, p. L10. DOI: 10.3847/2041-8205/825/1/L10. arXiv: 1606.03118 [astro-ph.SR].

Ostriker, Eve C., James M. Stone, and Charles F. Gammie (Jan. 2001). "Density, Velocity, and Magnetic Field Structure in Turbulent Molecular Cloud Models". In: *ApJ* 546.2, pp. 980–1005. DOI: 10.1086/318290. arXiv: astro-ph/0008454 [astro-ph].

Padoan, Paolo et al. (May 2001). "The Turbulent Shock Origin of Proto-Stellar Cores". In: *ApJ* 553.1, pp. 227–234. DOI: 10.1086/320636. arXiv: astro-ph/0011122 [astro-ph].

Palau, Aina et al. (Jan. 2013). "Early Stages of Cluster Formation: Fragmentation of Massive Dense Cores down to <~1000 AU". In: *ApJ* 762.2, 120, p. 120. DOI: 10.1088/0004-637X/762/2/120. arXiv: 1211.2666 [astro-ph.GA].

Palau, Aina et al. (Apr. 2014). "Fragmentation of Massive Dense Cores Down to <~1000 AU: Relation between Fragmentation and Density Structure". In: *ApJ* 785.1, 42, p. 42. DOI: 10.1088/0004-637X/785/1/42. arXiv: 1401.8292 [astro-ph.GA].

Palau, Aina et al. (2020). "In search for an observational correlation between the fragmentation level and the magnetic field properties of massive dense cores". In: *ApJ*. arXiv: 2010.12099 [astro-ph.GA].

Palmeirim, P. et al. (Feb. 2013). "Herschel view of the Taurus B211/3 filament and striations: evidence of filamentary growth?" In: *A&A* 550, A38, A38. DOI: 10.1051/0004-6361/201220500. arXiv: 1211.6360 [astro-ph.SR].

Patel, N. A. et al. (Sept. 2005). "A disk of dust and molecular gas around a high-mass protostar". In: *Nature* 437, pp. 109–111. DOI: 10.1038/nature04011. eprint: astro-ph/0509637.

Pattle, Kate et al. (July 2019). "JCMT BISTRO Survey Observations of the Ophiuchus Molecular Cloud: Dust Grain Alignment Properties Inferred Using a Ricean Noise Model". In: *ApJ* 880.1, 27, p. 27. DOI: 10.3847/1538-4357/ab286f. arXiv: 1906.03391 [astro-ph.GA].

Peretto, N. et al. (Jan. 2014). "SDC13 infrared dark clouds: Longitudinally collapsing filaments?" In: *A&A* 561, A83, A83. DOI: 10.1051/0004-6361/201322172. arXiv: 1311.0203 [astro-ph.GA].

Pillai, T. et al. (Jan. 2015). "Magnetic Fields in High-mass Infrared Dark Clouds". In: *ApJ* 799.1, 74, p. 74. DOI: 10.1088/0004-637X/799/1/74. arXiv: 1410.7390 [astro-ph.GA].

Pillai, Thushara G. S. et al. (Aug. 2020). "Magnetized filamentary gas flows feeding the young embedded cluster in Serpens South". In: *Nature Astronomy*. DOI: 10.1038/s41550-020-1172-6.

Planck Collaboration et al. (Apr. 2015). "Planck intermediate results. XXII. Frequency dependence of thermal emission from Galactic dust in intensity and polarization". In: *A&A* 576, A107, A107. DOI: 10.1051/0004-6361/201424088. arXiv: 1405.0874 [astro-ph.GA].

Planck Collaboration et al. (Feb. 2016). "Planck intermediate results. XXXV. Probing the role of the magnetic field in the formation of structure in molecular clouds". In: *A&A* 586, A138, A138. DOI: 10.1051/0004-6361/201525896. arXiv: 1502.04123 [astro-ph.GA].

Povich, M. S. and B. A. Whitney (May 2010). "Evidence for Delayed Massive Star Formation in the M17 Proto-OB Association". In: *ApJL* 714, pp. L285–L289. DOI: 10.1088/2041-8205/714/2/L285. arXiv: 1004.1712.

Povich, M. S. et al. (July 2016). "Rapid Circumstellar Disk Evolution and an Accelerating Star Formation Rate in the Infrared Dark Cloud M17 SWex". In: *ApJ* 825, 125, p. 125. DOI: 10.3847/0004-637X/825/2/125. arXiv: 1604.06497.

Qiu, Keping and Qizhou Zhang (2009). "Discovery of Extremely High Velocity "Molecular Bullets" in the HH 80-81 High-Mass Star-Forming Region". In: *ApJ* 702.1, pp. L66–L71. DOI: 10.1088/0004-637X/702/1/L66. arXiv: 0907.5040 [astro-ph.GA].

Qiu, Keping et al. (2019). "CO Multi-line Observations of HH 80-81: A Two-component Molecular Outflow Associated with the Largest Protostellar Jet in Our Galaxy". In: *ApJ* 871.2, 141, p. 141. DOI: 10.3847/1538-4357/aaf728. arXiv: 1812.03501 [astro-ph.GA].

Racine, R. (May 1968). "Stars in reflection nebulae". In: *ApJ* 73, p. 233. DOI: 10.1086/110624.

Rafikov, Roman R. (Nov. 2016). "Protoplanetary Disk Heating and Evolution Driven by Spiral Density Waves". In: *ApJ* 831.2, 122, p. 122. DOI: 10.3847/0004-637X/831/2/122. arXiv: 1601.03009 [astro-ph.EP].

Rao, R. et al. (July 1998). "High-Resolution Millimeter-Wave Mapping of Linearly Polarized Dust Emission: Magnetic Field Structure in Orion". In: *ApJL* 502.1, pp. L75–L78. DOI: 10.1086/311485. arXiv: astro-ph/9805288 [astro-ph].

Reipurth, B., S. A. Rodney, and S. Heathcote (Dec. 2008). "Star Formation in Sagittarius: The Lynds 291 Cloud". In: *Handbook of Star Forming Regions, Volume II*. Ed. by B. Reipurth, p. 578.

Reynolds, S. P. (1986). "Continuum Spectra of Collimated, Ionized Stellar Winds". In: *ApJ* 304, p. 713. DOI: 10.1086/164209.

Rivera-Ingraham, A. et al. (June 2016). "Galactic cold cores. VII. Filament formation and evolution: Methods and observational constraints". In: *A&A* 591, A90, A90. DOI: 10.1051/0004-6361/201526263. arXiv: 1603.09177 [astro-ph.GA].

Rodriguez, L. F. et al. (Feb. 1980). "Radio observations of water vapor, hydroxyl, silicon monoxide, ammonia, carbon monoxide, and compact H II regions in the vicinities of suspected Herbig-Haro objects". In: *ApJ* 235, pp. 845–865. DOI: 10.1086/157687.

Rodríguez-Kamenetzky, A. et al. (Dec. 2017). "The Highly Collimated Radio Jet of HH 80-81: Structure and Nonthermal Emission". In: *ApJ* 851, 16, p. 16. DOI: 10.3847/1538-4357/aa9895. arXiv: 1711.02554 [astro-ph.HE].

Rosenfeld, Katherine A. et al. (Sept. 2013). "A Spatially Resolved Vertical Temperature Gradient in the HD 163296 Disk". In: *ApJ* 774.1, 16, p. 16. DOI: 10.1088/0004-637X/774/1/16. arXiv: 1306.6475 [astro-ph.SR].

Rubinstein, A. E. et al. (June 2018). "A Cavity of Large Grains in the Disk around the Group II Herbig Ae/Be Star HD 142666". In: *ApJ* 860.1, 7, p. 7. DOI: 10.3847/1538-4357/aabfba. arXiv: 1804.07343 [astro-ph.SR].

Saito, H. et al. (Dec. 1999). "A Study of the Molecular Cloud toward the H {II} Regions S35 and S37 with NANTEN". In: *PASJ* 51, pp. 819–835. DOI: 10.1093/pasj/51.6.819.

Sánchez-Monge, Á. et al. (Sept. 2014). "A necklace of dense cores in the high-mass star forming region G35.20-0.74 N: ALMA observations". In: *A&A* 569, A11, A11. DOI: 10.1051/0004-6361/201424032. arXiv: 1406.4081.

Sandford, Scott A. and Louis J. Allamandola (1993). "Condensation and Vaporization Studies of CH 3OH and NH 3 Ices: Major Implications for Astrochemistry". In: *ApJ* 417, p. 815. DOI: 10.1086/173362.

Sanhueza, Patricio et al. (Dec. 2019). "The ALMA Survey of 70 μm Dark High-mass Clumps in Early Stages (ASHES). I. Pilot Survey: Clump Fragmentation". In: *ApJ* 886.2, 102, p. 102. DOI: 10.3847/1538-4357/ab45e9. arXiv: 1909.07985 [astro-ph.GA].

Sanna, A. et al. (2019). "Discovery of a sub-Keplerian disk with jet around a 20 M young star. ALMA observations of G023.01-00.41". In: *A&A* 623, A77, A77. DOI: 10.1051/0004-6361/201833411. arXiv: 1805.09842 [astro-ph.SR].

Santos, Fábio P. et al. (2016). "Magnetically Dominated Parallel Interstellar Filaments in the Infrared Dark Cloud G14.225-0.506". In: *ApJ* 832.2, 186, p. 186. DOI: 10.3847/0004-637X/832/2/186. arXiv: 1609.08052 [astro-ph.GA].

Sault, R. J., P. J. Teuben, and M. C. H. Wright (1995). "A Retrospective View of MIRIAD". In: *Astronomical Data Analysis Software and Systems IV*. Ed. by R. A. Shaw, H. E. Payne, and J. J. E. Hayes. Vol. 77. Astronomical Society of the Pacific Conference Series, p. 433. arXiv: astro-ph/0612759 [astro-ph].

Segura-Cox, Dominique M. et al. (Feb. 2016). "The VLA Nascent Disk and Multiplicity Survey: First Look at Resolved Candidate Disks around Class 0 and I Protostars in the Perseus Molecular Cloud". In: *ApJL* 817.2, L14, p. L14. DOI: 10.3847/2041-8205/817/2/L14. arXiv: 1601.03040 [astro-ph.SR].

Segura-Cox, Dominique M. et al. (Oct. 2018). "The VLA Nascent Disk and Multiplicity Survey of Perseus Protostars (VANDAM). V. 18 Candidate Disks around Class 0 and I Protostars in the Perseus Molecular Cloud". In: *ApJ* 866.2, 161, p. 161. DOI: 10.3847/1538-4357/aaddf3. arXiv: 1808.10438 [astro-ph.SR].

Segura-Cox, Dominique M. et al. (Oct. 2020). "Four annular structures in a protostellar disk less than 500,000 years old". In: *Nature* 586.7828, pp. 228–231. DOI: 10.1038/s41586-020-2779-6. arXiv: 2010.03657 [astro-ph.EP].

Seifried, D. et al. (2016). "Revealing the dynamics of Class 0 protostellar discs with ALMA". In: *MNRAS* 459.2, pp. 1892–1906. DOI: 10.1093/mnras/stw785. arXiv: 1601.02384 [astro-ph.SR].

Shakura, N. I. and R. A. Sunyaev (1973). "Reprint of 1973A&A....24..337S. Black holes in binary systems. Observational appearance." In: *A&A* 500, pp. 33–51.

Sheehan, Patrick D. et al. (Oct. 2020). "The VLA/ALMA Nascent Disk and Multiplicity (VANDAM) Survey of Orion Protostars. III. Substructures in Protostellar Disks". In: *ApJ* 902.2, 141, p. 141. DOI: 10.3847/1538-4357/abbad5. arXiv: 2010.00606 [astro-ph.SR].

Shu, Frank H., Susana Lizano, and Fred C. Adams (1987). "Star formation in molecular cloud cores". In: *Star Forming Regions*. Ed. by Manuel Peimbert and Jun Jugaku. Vol. 115. IAU Symposium, pp. 417–433.

Simon, M., A. Dutrey, and S. Guilloteau (Dec. 2000). "Dynamical Masses of T Tauri Stars and Calibration of Pre-Main-Sequence Evolution". In: *ApJ* 545.2, pp. 1034–1043. DOI: 10.1086/317838. arXiv: astro-ph/0008370 [astro-ph].

Simon, M. et al. (Aug. 2017). "Dynamical Masses of Low-mass Stars in the Taurus and Ophiuchus Star-forming Regions". In: *ApJ* 844.2, 158, p. 158. DOI: 10.3847/1538-4357/aa78f1. arXiv: 1706.03505 [astro-ph.SR].

Skalidis, Raphael and Konstantinos Tassis (Oct. 2020). "High-accuracy estimation of magnetic field strength in the interstellar medium from dust polarization". In: *arXiv e-prints*, arXiv:2010.15141, arXiv:2010.15141. arXiv: 2010.15141 [astro-ph.GA].

Smith, Rowan J., Simon C. O. Glover, and Ralf. S. Klessen (Dec. 2014). "On the nature of star-forming filaments - I. Filament morphologies". In: *MNRAS* 445.3, pp. 2900–2917. DOI: 10.1093/mnras/stu1915. arXiv: 1407.6716 [astro-ph.GA].

Smith, Rowan J. et al. (Feb. 2016). "On the nature of star-forming filaments - II. Subfilaments and velocities". In: *MNRAS* 455.4, pp. 3640–3655. DOI: 10.1093/mnras/stv2559. arXiv: 1509.03321 [astro-ph.GA].

Soam, Archana et al. (Sept. 2019). "Magnetic Fields in the Infrared Dark Cloud G34.43+0.24". In: *ApJ* 883.1, 95, p. 95. DOI: 10.3847/1538-4357/ab39dd. arXiv: 1908.03624 [astro-ph.GA].

Soler, Juan D. (Sept. 2019). "Using Herschel and Planck observations to delineate the role of magnetic fields in molecular cloud structure". In: *A&A* 629, A96, A96. DOI: 10.1051/0004-6361/201935779. arXiv: 1909.04862 [astro-ph.GA].

Spitzer, Lyman (1978). *Physical processes in the interstellar medium*. DOI: 10.1002/9783527617722.

Stein, Wayne (Apr. 1966). "Infrared Radiation from Interstellar Grains". In: *ApJ* 144, p. 318. DOI: 10.1086/148606.

Sugitani, K. et al. (June 2011). "Near-infrared-imaging Polarimetry Toward Serpens South: Revealing the Importance of the Magnetic Field". In: *ApJ* 734.1, 63, p. 63. DOI: 10.1088/0004-637X/734/1/63. arXiv: 1104.2977 [astro-ph.SR].

Sugiyama, Koichiro et al. (Aug. 2017). "The shortest periodic and flaring flux variability of a methanol maser emission at 6.7 GHz in G 014.23-00.50". In: *PASJ* 69.4, 59, p. 59. DOI: 10.1093/pasj/psx034. arXiv: 1704.02807 [astro-ph.SR].

Takahashi, S. Z., Y. Tsukamoto, and S. Inutsuka (2016). "A revised condition for self-gravitational fragmentation of protoplanetary discs". In: *MNRAS* 458.4, pp. 3597–3612. DOI: 10.1093/mnras/stw557. arXiv: 1603.01402 [astro-ph.SR].

Tan, J. C. et al. (2014). "Massive Star Formation". In: *Protostars and Planets VI*. Ed. by Henrik Beuther et al., pp. 149–172. DOI: 10.2458/azu_uapress_9780816531240-ch007. arXiv: 1402.0919 [astro-ph.GA].

Tang, Ya-Wen et al. (July 2009). "Evolution of Magnetic Fields in High-Mass Star Formation: Linking Field Geometry and Collapse for the W51 e2/e8 Cores". In: *ApJ* 700.1, pp. 251–261. DOI: 10.1088/0004-637X/700/1/251. arXiv: 0905.1996 [astro-ph.SR].

Tang, Ya-Wen et al. (June 2019). "Gravity, Magnetic Field, and Turbulence: Relative Importance and Impact on Fragmentation in the Infrared Dark Cloud G34.43+00.24". In: *ApJ* 878.1, 10, p. 10. DOI: 10.3847/1538-4357/ab1484. arXiv: 1903.12397 [astro-ph.GA].

Tapia, C. and S. Lizano (Nov. 2017). "Emission from Magnetized Accretion Disks around Young Stars". In: *ApJ* 849.2, 136, p. 136. DOI: 10.3847/1538-4357/aa8f9b. arXiv: 1711.04803 [astro-ph.SR].

Tazzari, M. et al. (Oct. 2017). "Physical properties of dusty protoplanetary disks in Lupus: evidence for viscous evolution?" In: *A&A* 606, A88, A88. DOI: 10.1051/0004-6361/201730890. arXiv: 1707.01499 [astro-ph.EP].

Terebey, S., F. H. Shu, and P. Cassen (Nov. 1984). "The collapse of the cores of slowly rotating isothermal clouds". In: *ApJ* 286, pp. 529–551. DOI: 10.1086/162628.

Testi, L. et al. (2014). "Dust Evolution in Protoplanetary Disks". In: *Protostars and Planets VI*. Ed. by Henrik Beuther et al., pp. 339–361. DOI: 10.2458/azu_uapress_9780816531240-ch015. arXiv: 1402.1354 [astro-ph.SR].

Tobin, John J. et al. (2018). "The VLA/ALMA Nascent Disk and Multiplicity (VANDAM) Survey of Perseus Protostars. VI. Characterizing the Formation Mechanism for Close Multiple Systems". In: *ApJ* 867.1, 43, p. 43. DOI: 10.3847/1538-4357/aae1f7. arXiv: 1809.06434 [astro-ph.SR].

Tobin, John J. et al. (Nov. 2020). "The VLA/ALMA Nascent Disk and Multiplicity (VANDAM) Survey of Orion Protostars IV. Unveiling the Embedded Intermediate-Mass Protostar and Disk within OMC2-FIR3/HOPS-370". In: *arXiv e-prints*, arXiv:2011.01160, arXiv:2011.01160. arXiv: 2011.01160 [astro-ph.GA].

Trinidad, M. A. et al. (May 2003). "Observations of Water Masers and Radio Continuum Emission in AFGL 2591". In: *ApJ* 589, pp. 386–396. DOI: 10.1086/374618.

Van Loo, Sven, Eric Keto, and Qizhou Zhang (July 2014). "Core and Filament Formation in Magnetized, Self-gravitating Isothermal Layers". In: *ApJ* 789.1, 37, p. 37. DOI: 10.1088/0004-637X/789/1/37. arXiv: 1405.1013 [astro-ph.SR].

Vázquez-Semadeni, Enrique, Alejandro González-Samaniego, and Pedro Colín (May 2017). "Hierarchical star cluster assembly in globally collapsing molecular clouds". In: *MNRAS* 467.2, pp. 1313–1328. DOI: 10.1093/mnras/stw3229. arXiv: 1611.00088 [astro-ph.GA].

Vázquez-Semadeni, Enrique et al. (Dec. 2009). "High- and Low-Mass Star-Forming Regions from Hierarchical Gravitational Fragmentation. High Local Star Formation Rates with Low Global Efficiencies". In: *ApJ* 707.2, pp. 1023–1033. DOI: 10.1088/0004-637X/707/2/1023. arXiv: 0904.4515 [astro-ph.GA].

Vázquez-Semadeni, Enrique et al. (Dec. 2019). "Global hierarchical collapse in molecular clouds. Towards a comprehensive scenario". In: *MNRAS* 490.3, pp. 3061–3097. DOI: 10.1093/mnras/stz2736. arXiv: 1903.11247 [astro-ph.GA].

Wang, Yang et al. (2006). "Water Masers Associated with Infrared Dark Cloud Cores". In: *ApJL* 651.2, pp. L125–L128. DOI: 10.1086/508939.

Ward-Thompson, D. et al. (May 2018). "VizieR Online Data Catalog: LDN 1495 SCUBA-2 and Herschel data (Ward-Thompson+, 2016)". In: *VizieR Online Data Catalog*, J/MNRAS/463/1008, J/MNRAS/463/1008.

Wardle, Mark and Cindy Ng (Feb. 1999). "The conductivity of dense molecular gas". In: *MNRAS* 303.2, pp. 239–246. DOI: 10.1046/j.1365-8711.1999.02211.x. arXiv: astro-ph/9810468 [astro-ph].

Weaver, Erik, Andrea Isella, and Yann Boehler (Feb. 2018). "Empirical Temperature Measurement in Protoplanetary Disks". In: *ApJ* 853.2, 113, p. 113. DOI: 10.3847/1538-4357/aaa481. arXiv: 1801.03478 [astro-ph.EP].

Whittet, D. C. B. et al. (Feb. 2008). "The Efficiency of Grain Alignment in Dense Interstellar Clouds: a Reassessment of Constraints from Near-Infrared Polarization". In: *ApJ* 674.1, pp. 304–315. DOI: 10.1086/525040. arXiv: 0711.2536 [astro-ph].

Williams, G. M. et al. (May 2018). "Gravity drives the evolution of infrared dark hubs: JVLA observations of SDC13". In: *A&A* 613, A11, A11. DOI: 10.1051/0004-6361/201731587. arXiv: 1801.07253 [astro-ph.GA].

Williams, J. P. and L. A. Cieza (Sept. 2011). "Protoplanetary Disks and Their Evolution". In: *ARA&A* 49, pp. 67–117. DOI: 10.1146/annurev-astro-081710-102548. arXiv: 1103.0556 [astro-ph.GA].

Williams, Jonathan P. et al. (Apr. 2019). "The Ophiuchus DIsk Survey Employing ALMA (ODISEA): Disk Dust Mass Distributions across Protostellar Evolutionary Classes". In: *ApJL* 875.2, L9, p. L9. DOI: 10.3847/2041-8213/ab1338. arXiv: 1904.06471 [astro-ph.SR].

Wolfire, M. G. and J. P. Cassinelli (Aug. 1987). "Conditions for the formation of massive stars". In: *ApJ* 319, pp. 850–867. DOI: 10.1086/165503.

Xu, Y. et al. (2011). "Trigonometric Parallaxes of Massive Star-forming Regions. VIII. G12.89+0.49, G15.03-0.68 (M17), and G27.36-0.16". In: *ApJ* 733.1, 25, p. 25. DOI: 10.1088/0004-637X/733/1/25. arXiv: 1103.3139 [astro-ph.GA].

Yang, Haifeng et al. (2017). "Scattering-produced (sub)millimetre polarization in inclined discs: optical depth effects, near-far side asymmetry and dust settling". In: *MNRAS* 472.1, pp. 373–388. DOI: 10.1093/mnras/stx1951. arXiv: 1705.05432 [astro-ph.SR].

Yorke, Harold W. and Peter Bodenheimer (Nov. 1999). "The Formation of Protostellar Disks. III. The Influence of Gravitationally Induced Angular Momentum Transport on Disk Structure and Appearance". In: *ApJ* 525.1, pp. 330–342. DOI: 10.1086/307867.

Zapata, L. A. et al. (Jan. 2019). "An Asymmetric Keplerian Disk Surrounding the O-type Protostar IRAS16547−4247". In: *ApJ* 872, p. 176. arXiv: 1901.04896 [astro-ph.SR].

Zhang, Ke, Geoffrey A. Blake, and Edwin A. Bergin (2015). "Evidence of Fast Pebble Growth Near Condensation Fronts in the HL Tau Protoplanetary Disk". In: *ApJL* 806.1, L7, p. L7. DOI: 10.1088/2041-8205/806/1/L7. arXiv: 1505.00882 [astro-ph.EP].

Zhang, Ke et al. (Sept. 2019). "Systematic Variations of CO Gas Abundance with Radius in Gas-rich Protoplanetary Disks". In: *ApJ* 883.1, 98, p. 98. DOI: 10.3847/1538-4357/ab38b9. arXiv: 1908.03267 [astro-ph.EP].

Zhang, Qizhou et al. (Sept. 2014). "Magnetic Fields and Massive Star Formation". In: *ApJ* 792.2, 116, p. 116. DOI: 10.1088/0004-637X/792/2/116. arXiv: 1407.3984 [astro-ph.GA].

Zhu, Zhaohuan et al. (2011). "Transitional and Pre-transitional Disks: Gap Opening by Multiple Planets?" In: *ApJ* 729.1, 47, p. 47. DOI: 10.1088/0004-637X/729/1/47. arXiv: 1012.4395 [astro-ph.SR].

Zhu, Zhaohuan et al. (June 2019). "One Solution to the Mass Budget Problem for Planet Formation: Optically Thick Disks with Dust Scattering". In: *ApJL* 877.2, L18, p. L18. DOI: 10.3847/2041-8213/ab1f8c. arXiv: 1904.02127 [astro-ph.EP].